Synthesis and Physicochemical Characterisation of Metal-Organic Frameworks and Metal-Organic Polyhedra Composed from Extended Organic Ligands

A thesis submitted to the University of Dublin for the degree of Doctor of Philosophy

Kevin David Byrne

School of Chemistry
University of Dublin
2020

Declarations

I declare that this thesis has not been submitted as an exercise for a degree at this or any other university and it is entirely my own work.

I agree to deposit this thesis in the University's open access institutional repository or allow the library to do so on my behalf, subject to Irish Copyright Legislation and Trinity College Library conditions of use and acknowledgement.

……

Kevin David Byrne

Summary

The research presented in this thesis concentrates on the synthesis of advanced materials known as metal organic polyhedra (MOPs) and metal organic frameworks (MOFs). The resulting materials were structurally characterised using single crystal X-ray diffraction methods and further characterised using a range of complementary techniques. These materials were then applied to guest binding and encapsulation, gas sorption and catalytic OER activities.

Chapter 1 summarises the available literature which relates to the work in this thesis. The reader is introduced to the relevant materials, their classifications, synthesis, properties and where they have been applied.

Chapter 2 focuses on synthesis using 3,3',3''-(benzene-1,3,5-triyltris(ethyne-2,1-diyl))tribenzoic acid (**H_3L1**) with Cu^{2+} ions for the synthesis of crystals of **1**, $[Cu_{36}(\mathbf{L1})_{24}(DMF)_8(H_2O)_{28}]$. **1** is shown to be composed of isostructural spherical coordination molecules **1A** and **1B**. The molecules have cross-sectional diameters of *ca.* 5 nm across and are among the largest synthetic coordination cage type molecules which are crystallographically characterised. It is shown that **1** can be solubilised by utilising 4-(3-phenylpropyl)pyridine making single molecules accessible. Photophysical studies were carried out using 7-amino-4-methylcoumarin (AMC) as a guest molecule.

Chapter 3 centres on the synthesis using 4,4',4''-(benzene-1,3,5-triyltris(ethyne-2,1-diyl))tribenzoic acid (**H_3L2**) with Co^{2+} ions to synthesise **2**, $Me_2NH_2[Co_5(\mathbf{L2})_3(\mu_3\text{-}OH)_2(H_2O)_2(DMF)_2]$. The polymeric structure of **2** takes the form of a porous honeycomb-type network and the structure is twofold interpenetrated with a measured BET surface area of 1755 m^2/g. **2** was investigated as a catalyst for water oxidation at neutral pH. Under photocatalytic conditions, high turnover frequencies and turnover numbers of 1.482 s^{-1} and 248 were achieved, respectively. Similarly, under electrocatalytic conditions in carbon paste (CP) electrodes, the compound reveals overpotentials of 0.405 and 0.755 V to reach 1 and 10 mA/cm^2, respectively (for the 40% **2**/CP electrodes). Further, it was demonstrated that a material whose structural attributes match closely to that of **2** could be synthesised under electrochemical conditions on the surface of fluorine doped tin oxide (FTO) glass electrodes. These **2**/FTO electrodes demonstrated catalytic activity in relation to

electrochemical water oxidation. Bulk electrolysis experiments and the subsequent electrode characterisations on both, the **2**/CP and **2**/FTO electrodes, show that these systems are exceptionally stable for prolonged periods of time under the applied conditions.

Chapter 4 extends the use of 4,4',4''-(benzene-1,3,5-triyltris(ethyne-2,1-diyl))tribenzoic acid (**H_3L2**) for the synthesis of an isoreticular series of mixed-metal MOFs, [$MnCo_2$(**L2**)$_2$(H_2O)$_2$] (**3**), [$CoZn_2$(**L2**)$_2$(DMF)$_2$] (**4**) and [$ZnCo_2$(**L2**)$_2$(DMF)$_2$] (**5**). The fundamental aim was for the synthesised materials to show potentials for use as OER catalysts. Therefore, we decided to mainly focus these synthetic activities around the incorporation of transition metal ions which have previously been shown as components of other proven OER catalysts such as Co^{II} and Mn^{II}. These materials were characterised using a range of complimentary techniques including single-crystal X-ray diffraction, EDX spectroscopy, UV-vis-NIR spectroscopic studies, XPS and computational modelling. Preliminary photo-induced water oxidation studies using **3** and **4** highlight their potential in this field of study. In particular the presence of **3** in a reaction mixture showed significantly increased oxygen production.

Chapter 5 looks at the synthesis of MOFs using an elongated ligand, 5,5'-((5'-(4-((4-carboxyphenyl)ethynyl)phenyl)-[1,1':3',1''-terphenyl]-4,4''-diyl)-bis(ethyne-2,1-diyl))benzoic acid (**H_3L3**). This was used to synthesise compound **6,** [Zn_4(μ_4-O)(**L3**)$_2$]. Compound **6** was found to be composed of two interwoven rutile (**rtl**) nets. This topology is rarely found among MOFs when 6-connected {Zn_4O} SBUs are combined with 3-connecting ligands. Particularly noteworthy properties of **6** are the low density (0.266 g/cm^3), large pore sizes (up to *ca.* 22.8 Å) and the BET surface area of 3028 m^2/g. The H_2 gas sorption studies give rise to a large H_2 uptake of 332 cm^3/g at 756 Torr and 77 K, which corresponds to an uptake of 2.9 wt% which is among the best gravimetric H_2 uptakes for MOFs at low pressures.

Chapter 6 describes the experimental details for the work performed.

Chapter 7 concludes on the work carried out and based on the questions that emerge from this research it provides details of possible future directions that could be explored.

Acknowledgements

There are many people that helped me get where I am today. First and foremost I would like to thank my parents David and Mary. I owe them everything and would not be here today if it were not for the love and time they invested in me throughout my entire life. I would also like to thank my girlfriend Julia, sister Laura and the rest of my family.

I would especially like to thank my PhD supervisor Prof. Wolfgang Schmitt for all his help, patience (lots), hard work and guidance throughout this project and the thesis. I would like to thank Dr. Nianyong Zhu (Jom) and Dr. Gerard Tobin. This project builds on the foundations they laid in the research group during their previous work.

This research would not have been possible without the support and contributions from the following people in the Schmitt group, for that I am eternally thankful; Ximo provided direction, guidance and help throughout many aspects of the project with a particular focus on the electrochemical studies. Rory and Amal for their photocatalytic measurements. Swetanshu for his diligent computational modelling. Sebastien for the help with the gas sorption analysis as well as theoretical BET surface area and pore size distribution calculations. Éadaoin and Zubair for their spectroscopy work. Friedrich and Xiao-Ping for their topological analysis. Debo for the many discussions about chemistry and politics! Friedrich, Amal and Jom for their crystallography work. To everyone else in the Schmitt group, past and present members including Muhamed, Mariah, Greg, Joe, Colm, Paul, Luana, Ako, Aneela, Anna, Donal, Camelia, Adam P. and Adam D., thank you very much for all the help, it has been a pleasure to work with you all.

In addition, this work could not have been completed without collaborations with the following scientists with expertise in other research areas; Dr. Danny Fox and his supervisor Prof. Hongzhou Zhang for their 'many' electron and atomic force microscopy experiments. Dr. Ross Lundy and his supervisor Prof. Mick Morris for the XPS experiments. Dr. Matthew Lennox and Prof. Tina Düren for the theoretical gas sorption simulations. I would also like to acknowledge the many contributions from the technical and support staff in the School of Chemistry. In particular I would like to thank Dr. John O'Brien and Dr. Manuel Reuther for their all-round work and assistance with analytical techniques, especially NMR, and also to Dr. Brendan Twamley for his extensive time-consuming crystallographic work which was crucial to much of the project. Also, I would like to thank Martin Feeney, Dr Gary Hessman, Peter Brien, Patsy Greene, Tom Conroy, Dr. Noelle Scully, Fred Cowzer, Kieron Galvin, Teresa McDonnell, Dr. Sinead Boyce, Maria Copley, Anne Marie Farrell and all the other support staff. Finally, I would like to thank Science Foundation Ireland (SFI) for supporting me financially and making this research possible.

Table of Contents

Abbreviations

1-MCP	1-Methylcyclopropene
1D	One dimensional
2D	Two dimensional
3D	Three dimensional
5-FU	5-Fluorouracil
AWGs	Atmospheric water generators
BET	Brunauer–Emmett–Teller
BUT	Beijing University of Technology
CN	Coordination network
CP	Coordination polymer (Chapter 1) / Carbon paste (Chapters 3, 6 and 7)
cub	Cube
cuo	Cuboctaheron
CUS	Coordinatively unsaturated sites
DCM	Dichloromethane
dia	Diamond
DLS	Dynamic light scattering
DMF	Dimethylformamide
DMSO-d	Deuterated dimethyl sulfoxide
DOE	US Department of Energy
DUT	Dresden University of Technology
EDX	Energy-dispersive X-ray spectroscopy
fcu	Face centered cubic
ftw	Neovius minimal surface

HER	Hydrogen evolution reaction
HKUST	Hong Kong University of Science and Technology
HRC	Hydrogen reduction catalyst
HSAB	Hard and soft Lewis acid and base theory
ico	Icosahedron
IR	Infrared spectroscopy
IRMOF	Iso-reticular metal-organic framework
LMCT	Ligand to metal charge transfer
LSV	Linear sweep voltammetry
MAF	Metal azolate framework
MeOH	Methanol
MIL	Matériaux de l'Institut Lavoisier
MLCT	Metal to ligand charge transfer
MOCN	Metal-organic coordination network
MOF	Metal-organic framework
MOM	Metal-organic material
MOP	Metal-organic polyhedron
MOS	Metal-organic surfaces
m.p.	Melting point
NENU	Northeast Normal University
NHE	Normal hydrogen electrode
NLDFT	Non-linear density functional theory
NMR	Nuclear magnetic resonance spectroscopy
NU	Northwestern University

oct	Octahedron
OER	Oxygen evolution reaction
PCN	Porous coordination network
PCP	Porous coordination polymer
pcu	Primitive cubic
POM	Polyoxometalate
POMOF	Polyoxometalate-based metal-organic framework
PS	Photosensitiser
PSM	Post-synthetic modification
PTFE	Polytetrafluoroethylene
pts	Platinum sulfide topology
PXRD	Powder X-ray diffraction
RBF	Round bottomed flask
RCSR	Reticular chemistry structure resource
S.A.	Surface area
SBU	Secondary building unit
SCXRD	Single crystal X-ray diffraction
SIFSIX	SiF_6^{2-} based MOFs
SS	Steady state
STEM	Scanning transmission electron microscopy
tbo	Twisted boracite topology
TCNQ	Tetracyanoquinodimethane
TEM	Transmission electron microscopy
tet	Tetrahedron
TGA	Thermogravimetric analysis

THF	Tetrahydrofuran
TOF	Turn over frequency
TON	Turn over number
UiO	University of Oslo
UMC	Undercoordinated metal centre
WOC	Water oxidation catalyst
XRD	X-ray diffraction
ZIF	Zeolitic imidazolate framework

Chapter 1

Introduction

1 Introduction

1.1 Motivation

The world of today faces many economic and ecological difficulties which will magnify with the expected growth in the global population. According to the United Nations, the global population will pass 9.6 billion people by 2050 and will reach 11 billion by 2100. To overcome the challenges that this will bring there is a need for the development of new and innovative solutions. The emission of excess CO_2 into the atmosphere that contributes to trapping heat is showing its influence on the climate causing an increase in extreme weather events as well as warming across the planet.[1] This warming is at its greatest magnitude at the poles[2] and has led to a melting of polar icecaps and glaciers, leading to rising sea levels.[3]

The transport sector is Europe's largest producer of CO_2 and a growing source of emissions globally as economic development is leading many people to move to more energy intensive modes of transport.[4] If CO_2 emissions are to be kept in check then the development of new energy sources are necessary. Both electric (which rely on battery technologies) and hydrogen vehicles (which rely on hydrogen production and storage technologies) are currently being developed as replacements for vehicles powered by fossil fuels. Hydrogen technologies require the development of new ways to both produce hydrogen as well as to store it efficiently and safely. Even with current efforts to reduce new emissions, the quantity of CO_2 that has already been emitted is predicted to cause devastating climate change. In the year 1970 the atmospheric CO_2 levels were at 327 ppm, by the 18th of April 2019, the CO_2 concentration in the atmosphere had reached 413 ppm.[5] Therefore, it will be necessary to not only reduce emissions but also to capture significant CO_2 quantities from the atmosphere. To help to overcome these challenges, the development of selected coordination compounds, composed of various organic and inorganic components and with well-defined structural architectures were identified as being potentially useful. This chapter will introduce and discuss two related classes of coordination compounds, known as metal organic frameworks (MOFs) and metal organic polyhedra (MOPs) providing an overview of relevant literature references. Attention will be directed to the units that assemble, to form these polymeric as well as some discrete molecular structures; the resulting key properties of the materials will be discussed. Their uses for various applications will be reviewed.

1.2 Porous inorganic and hybrid materials

The name coordination compound derives from the coordination bond.[6] This type of bonding was considered to form from the donation of electron pairs from ligands to metal ions. Coordination compounds are generally referred to as 'complexes'. These compounds have been used in pigments since ancient times.[7] The presence of transition metals in these complexes often leads to absorptions in the visible range of the electromagnetic spectrum by various mechanisms including metal to ligand charge transfer (MLCT), ligand to metal charge transfer (LMCT) and d-d transitions giving colours to these complexes. Examples of these pigments include aureolin ($K_3[Co(NO_2)_6]$) a yellow dye, and Prussian blue ($Fe_7(CN)_{18}$).

An interesting group of porous compounds were identified in 1756, when Axel Fredrik Cronstedt observed the production of steam upon heating a mineral known as stilbite. He coined the term 'Zeolite' which is used to describe this group of aluminosilicates today.[8] The materials can be extracted from the ground or synthesised cheaply for industrial puposes.[9] Their unique structures, in particular their porosities have led to many of them finding applications in a wide variety of different industries. They have been used for 'cracking' and reforming of petrochemicals, to remove Ca^{2+} from water, drying agents and even as absorbents for cat litter. These tectosilicates in which SIO_4^{4-} tetrahedra are 3-dimesionally lined are inorganic in nature (they do not contain C-C bonds) and highly porous, revealing surface areas of up to several hundred m^2/g.[10,11] Representative zeolite structures are shown in (**Figure 1.2.1**). Structurally related mesoporous silcas, i.e. SBA-15 or MCM-41 have larger nanoscopic pore and reach surface areas of 900 and 2400 m^2/g respectively.[12,13]

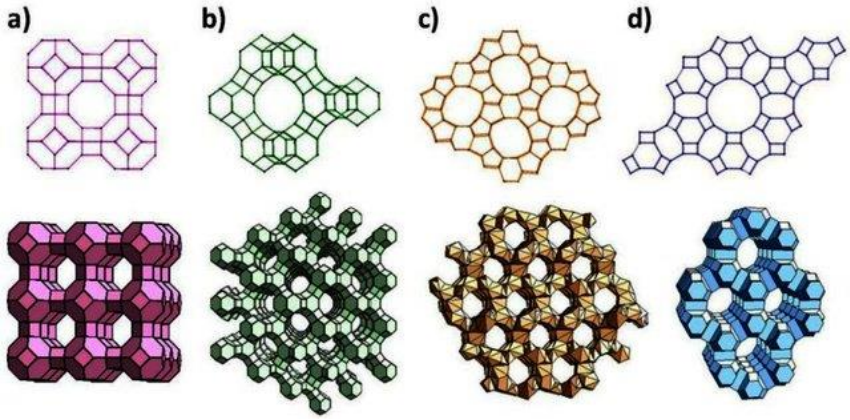

Figure 1.2.1: Representative zeolite frameworks showing pore openings). **a)** Zeolite A (3D, 4.2 Å pores), **b)** Zeolite Y (3D, 7.4 Å pores), **c)** Zeolite L (1D, 7.1 Å pores) and **d)** ZSM-5 (silicalite) (2D, 5.3 × 5.6 Å and 5.1 × 5.5 Å pores). Reproduced from reference 14.

1.3 Ordered coordination compounds with porosity

1.3.1 Metal-organic frameworks

The synthesis and characterisation of hybrid inorganic-organic materials currently comprises a highly vibrant area of science and includes metal-organic frameworks (MOFs) as a component class of materials. IUPAC has defined a MOF as; "a coordination network with organic ligands containing potential voids".[15] The term represents a class of normally ordered porous materials consisting of metal ions or clusters coordinated to multitopic organic linker molecules forming extended two or three dimensional structures. Examples of these can be seen in **Figure 1.3.1**. MOF like structures were first proposed by Hoskins and Robson in 1989[16] and a practical approach for their design and synthesis using crystal engineering was later developed[17–19] building on the concept of crystal engineering which was first proposed in 1971[20] by Schmidt to describe the rules being developed to design crystals with predetermined architectures. Unlike zeolites, which are also naturally occurring, MOFs were thought to be exclusively synthetic, until recently when minerals with "metal-organic framework like structures" were discovered.[21]

To better understand the diverse class of materials assigned to the MOF label it helps to reduce their component building units into simple geometric shapes such as triangles, squares and prisms. These are then divided into the inorganic and organic parts. The inorganic building blocks in MOFs consisting of metal ions or clusters are commonly referred to as secondary building units (SBUs) and the organic linker molecules are known

as organic SBUs or ligands (**Figure 1.3.2**).[22] These simplified descriptors are important in MOF systems where both, the nature and geometry of the components, as well as their 3 dimensional arrangement impart strong influence on the properties of the resulting MOFs.[23]

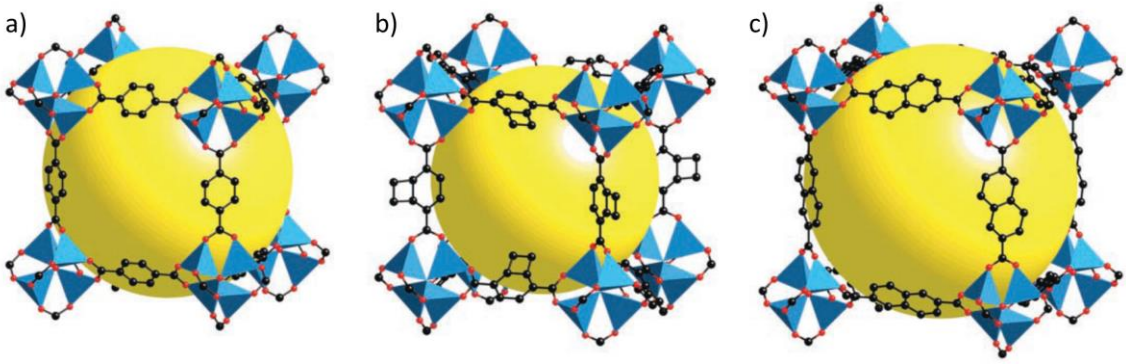

Figure 1.3.1: Single crystal X-ray structures of three MOFs, **a)** MOF-5, **b)** IRMOF-6 (isoreticular metal organic framework) and **c)** IRMOF-8 showing single cube fragments of their extended structures. This series of MOFs is composed of teranuclear {Zn_4O} SBUs with octahedral topology and linear organic linkers. Colour scheme: C (black), O (red), Zn (blue polyhedra) and voids (yellow spheres). Hydrogen atoms have been excluded for clarity. Reproduced from reference 24.

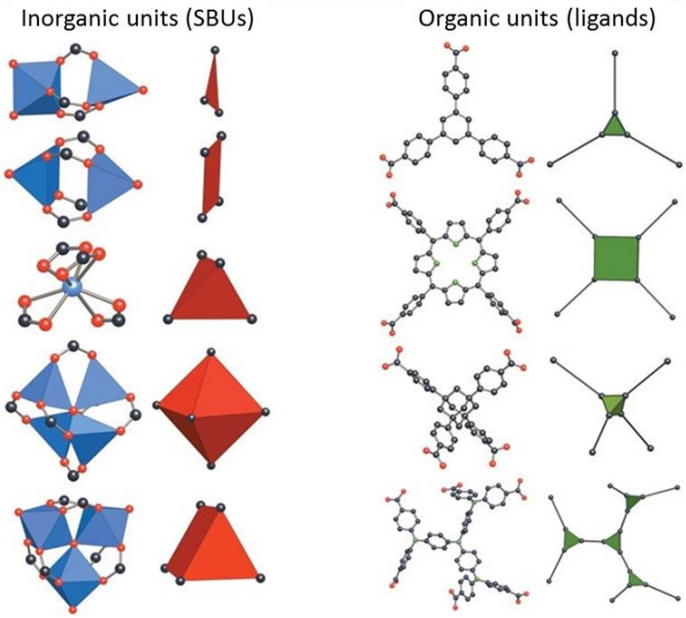

Figure 1.3.2: Examples of common SBUs and their corresponding simplified geometric shapes. Reproduced from reference 22. Colour scheme: C (black), O (red), N (green), Metal (blue/blue polyhedra). Simplified geometries of inorganic SBUs (red) and organic SBUs (green).

A wide variety of inorganic SBUs have been used for the synthesis of MOFs, composed of main group metals,[25,26] transition metals,[27,28] lantanides[29–33] and actinides.[34,35] These, combined with the near infinite variety of organic ligands that can be synthesised, leads to a vast number of possible MOF structures with different properties. A search for journal articles with the term 'MOF' reveals that in the last two decades there have been more than 20,000 papers published in the field of science currently reaching up to 3000 publications per year on the subject (**Figure 1.3.3**). It should further be noted that a series of researchers use different terminologies to describe similar types of compounds including porous coordination polymers (PCPs), coordination networks, etc. Thus, the number of research articles published in this scientific area might even be higher.

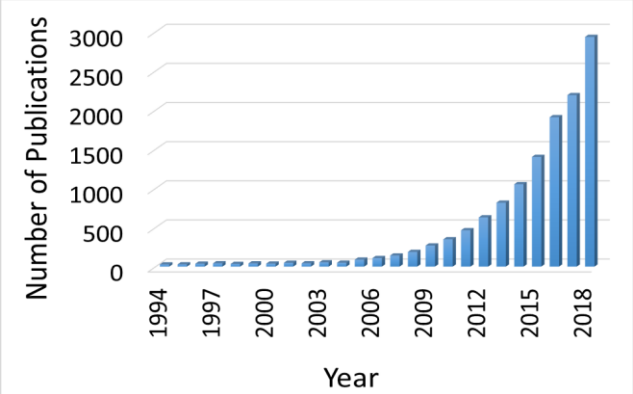

Figure 1.3.3: Number of publications containing the term 'MOF' per year from 1994 to 2018. Source: scientific citation indexing website 'Web of Science'.[36]

1.3.2 Metal-organic polyhedra

Another related fast-developing and exciting area is that of metal-organic polyhedra (MOPs), also often referred to as molecular coordination-cages,[37] molecular containers[38] and nano-balls.[39] Examples of MOPs are shown in **Figure 1.3.4**. Broadly speaking, MOPs and MOFs are structurally related metallo-supramolecular materials that are constructed from the structurally similar sets of inorganic SBUs and organic ligands. The self-assembly principles of these components, ultimately determines the type of material that is formed. While MOFs are 2D or 3D extended networks, MOPs are discrete molecular species. Both compounds generally contain well defined cavities. While individual MOPs form ordered structures on the molecular scale, the same type of MOP may exist in both solid structures and as discrete molecules in solution. As for MOFs, MOPs are often classified according to their structural topologies composed of structurally reduced SBUs as nodes.

Fujita and Stang are two researchers that were instrumental in the development of the field of coordination cages, publishing early MOPs in 1995[40] Over the following decades many other publications followed.[39,41–66] The compounds reveal interesting attributes for gas storage,[60] catalysis,[63,64] sensing,[41,65] molecular separations,[66] and guest uptake/release.[43]

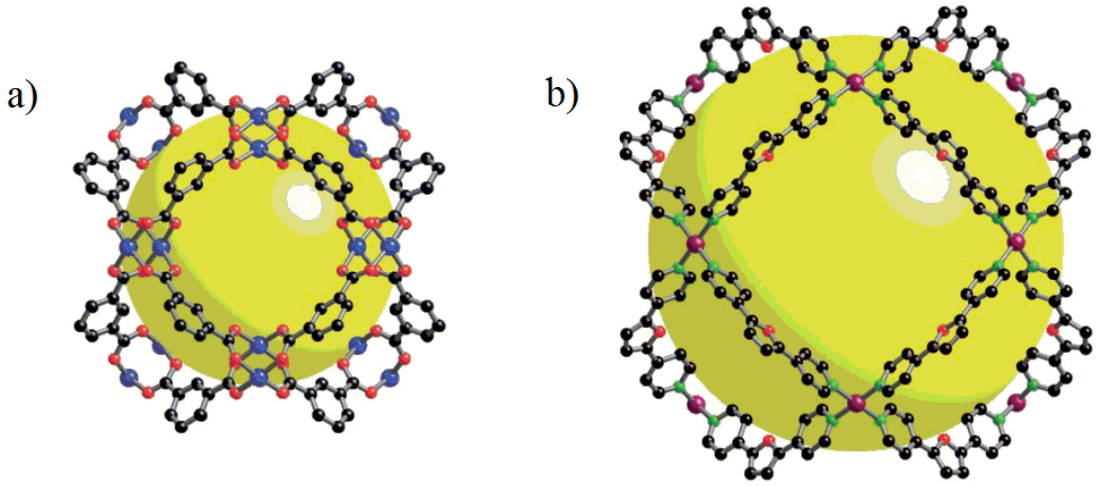

Figure 1.3.4: Two MOPs with cuboctahedral topologies **a)** MOP-1, **b)** Pd_{12}(,5-bis(4-pyridyl)furan)$_{24}$ MOP. Colour scheme: C (black), O (red), N (green), Cu (blue), Pd (purple) and inner cavities represented as (yellow spheres). Reproduced from reference 67.

1.3.3 Classification of extended coordination compounds

As new disciplines of science emerge, there is a need for new defining terminologies to facilitate scientific discussion of the concepts and results, as stated by Antoine Lavoisier in April 1787 at a public meeting of the Academy of Science. Here he stated that;

"As ideas are preserved and communicated by means of words, it necessarily follows that we cannot improve the language of any science, without at the same time improving the science itself; neither can we, on the other hand, improve a science without improving the language or nomenclature which belongs to it."[68]

The initial emergence of multiple terms to describe identical or related concepts undergoes a transition period and as a scientific field evolves some terms become more dominant than others. The word MOF has firmly established itself as a widely used term among many researchers but there are multiple other terminologies often used to refer to the same or similar classes of materials as well as various sub-classes of coordination compounds, often with slightly different definitions. The many terms in use include but are not limited to coordination polymer (CP),[25,69,70] metal-organic material (MOM),[71] coordination network (CN),[72] porous coordination polymer (PCP),[73,74] porous coordination network (PCN),[75–77] microporous coordination polymer (MCP),[78,79] and metal-organic coordination network (MOCN).[80–82]

To provide a more unambiguous definition for what precisely each of these commonly used terms mean, a IUPAC expert group was established in 2009 with the aim of giving clear definitions to some of the terminologies commonly used in the literature and provide a guideline of terms to be used. In 2013 this group gave their recommendations.[15] Coordination polymers were defined as "coordination compounds with repeating coordination entities extending in 1, 2 or 3 dimensions". A sub-group within these, termed as coordination networks was defined as "a coordination compound extending, through repeating coordination entities, in 1 dimension, but with cross-links between two or more individual chains, loops or spiro-links, or a coordination compound extending through repeating coordination entities in 2 or 3 dimensions." Within the group coordination networks, the MOF sub-group was defined, representing porous, extended

2D and 3D structures. A Venn diagram that aims to simplify the categories of various coordination compounds including MOPs as molecular species is shown in **Figure 1.3.5**.

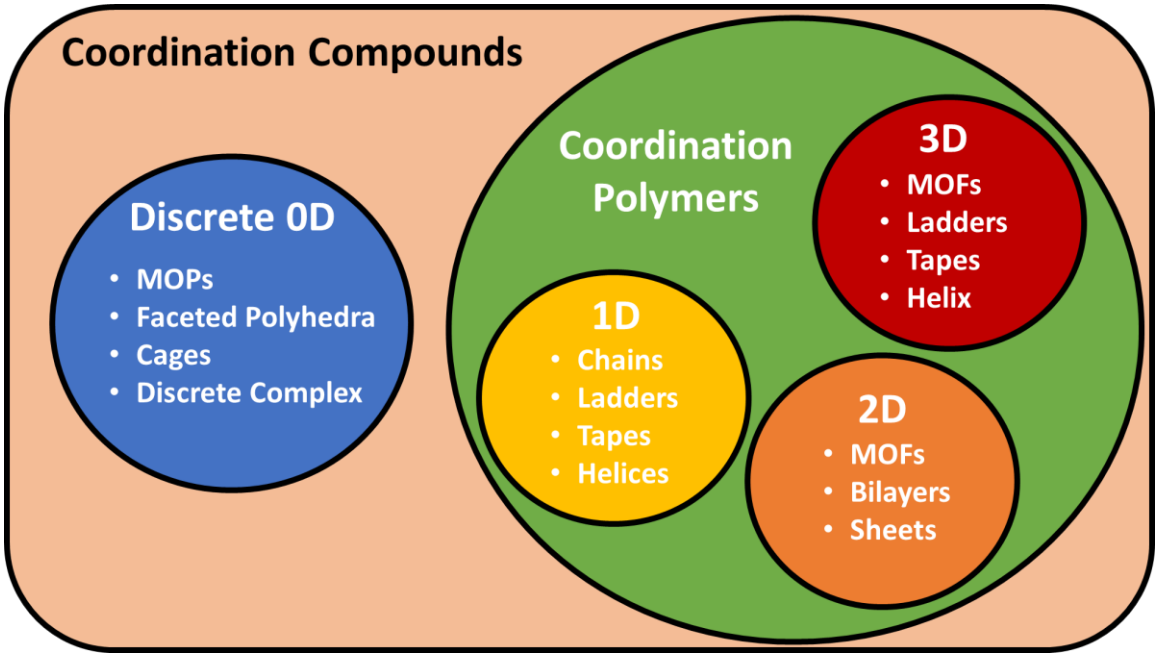

Figure 1.3.5: Venn diagram representation showing the relationships between several classifications of coordination compounds. Adapted from reference 71.

1.3.4 Framework descriptions and topology

A central challenge has been associated with the description of the structures of MOFs and other coordination polymers. To simplify structural description the concept of simplified nets is used to define the topology of a given framework. The nets can be characterised by abstract mathematical descriptors originally developed by Schläfli for the description of complex polyhedra and then further developed for use in extended networks by Wells.[83,84] Later, descriptors modelled on those used to specify zeolites[85] were used for 2D and 3D MOF structures and consist of three, bold lower case letters which relate to the corresponding inorganic default networks or the shape of the frameworks, e.g. **dia** (diamond) or **pts** (platinum sulfide). These have since become widely used in the description of MOFs[86] and are known as reticular chemistry structure resource (RCSR) symbols.[86] The structures are categorised according to this topological nomenclature and listed in the RCSR database.[87] The nets of two well-known MOFs are shown in **Figure 1.3.6**. MOF-5 has a 6-connected net consisting of bridging ditopic ligands and six connected

octahedral $\{Zn_4O\}$ SBUs resulting in a **pcu** net (primitive cubic)[88] while HKUST-1 (Hong Kong University of Science and Technology) has a 3,4-connected net with three connected ligands and 4 connected $\{Cu\}_2$ SBUs resulting in a twisted boracite type, **tbo** net.[89]

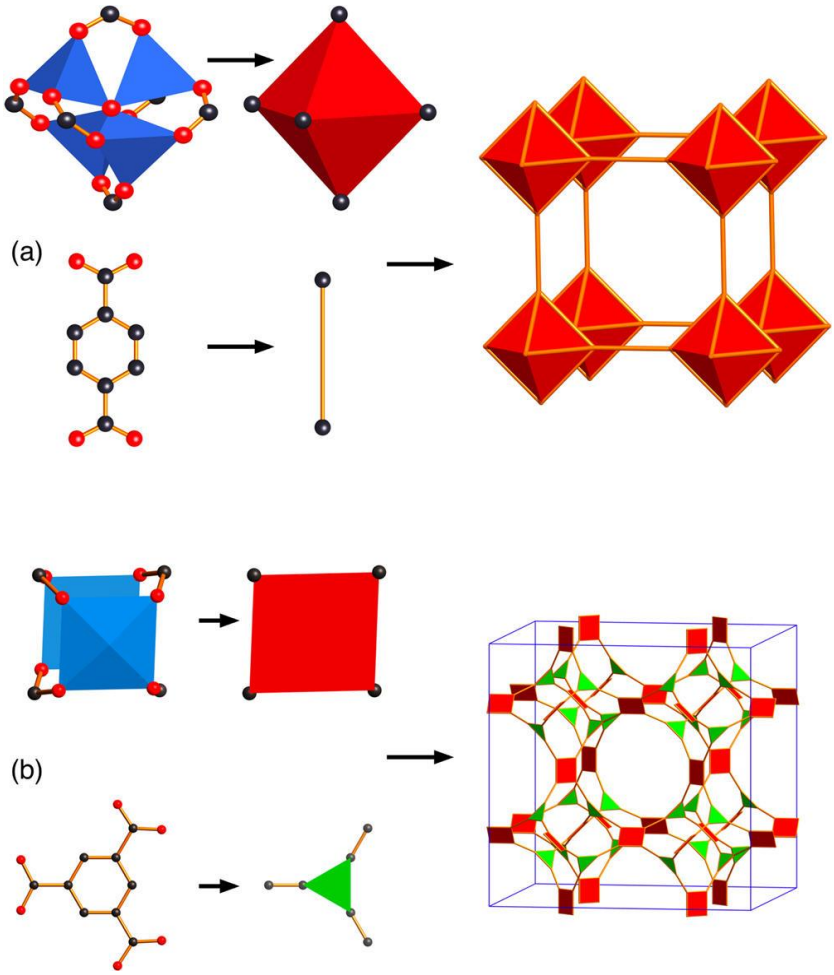

Figure 1.3.6: (a) The components of MOF-5[88] showing the $\{Zn_4O(-CO_2)_6\}$ SBU as an octahedron and the ditopic terephthalate ligand as a rod; the assembly results in a **pcu** net. (b) The components of HKUST-1[89] showing a $\{Cu_2(-CO_2)_4\}$ 'paddle wheel' SBU as a square and the tritopic trimesate ligand as a triangle. Their assembly results in a **tbo** net. Reproduced from reference 90**.**

MOPs are often described according to their shape and the linkages between their building units. MOPs can be grouped based on two important angles as proposed by O'Keeffe and Yaghi.[67] The angle 'η' is the angle between the direct linkages of the inorganic SBUs. The second angle 'ϑ', is the angle between the direct linkages of the ligands. The combination of both angles can then be used to sort MOPs into categories based on their shapes. Representations of these groups and their topologies are shown in **Figure 1.3.7**.

Following these principles and like for MOFs, three-letter RCSR symbols are also applied to describe MOPs.[87] Some common examples of these shape categories include **tet** (tetrahedron), **oct** (octahedron), **cub** (cube), **cuo** (cuboctahedron) and **ico** (icosahedron).

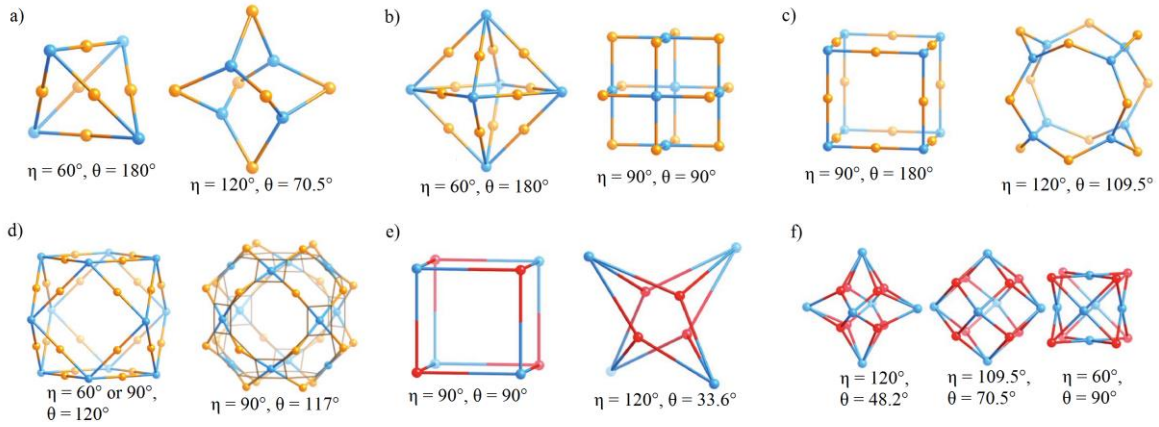

Figure 1.3.7: Representations showing structure topologies of MOPs. **a)** Tetrahedron: two different configurations of four, trivalent SBUs (blue); **b)** Octahedron: two different configurations of six tetravalent SBUs (blue); **c)** Cube: two different configurations of eight trivalent SBUs (blue);, **d)** Cuboctahedron: two different configurations of twelve tetravalent SBUs (blue); **e)** Heterocube: two different configurations of eight trivalent SBUs (red/blue); **f)** Rhombic dodecahedron: three different configurations of eight trivalent SBUs (red) linked to six tetravalent SBUs (blue). Reproduced from reference 67.

1.4 Synthesis of MOFs and MOPs

The synthesis of MOFs and MOPs can be challenging. Favourable reaction conditions for individual reactants need to be discovered for variable ligand(s)-metal(s) combinations and usually single crystals should be obtained to allow structural elucidation. The synthesis of MOFs often does not lead exclusively to the synthesis of the desired product or default structure.

1.4.1 Reticular synthesis

The word "reticular" is defined as "having the form of a net or netlike". This definition, along with the term "reticular synthesis" was first introduced by Yaghi *et al* in a highly cited *Nature* article published in 2003.[22] The article describes "reticular synthesis" as "the process of assembling judiciously designed rigid molecular building blocks into predetermined ordered structures (networks), which are held together by strong bonding". In reticular synthesis the SBU remains unaltered throughout the construction process. By modifying the length of the organic ligand and using the same SBU, a series of MOFs with the same topologies but different pore sizes can be synthesised. This is referred to as an 'iso-reticular' series ('iso reticular' = same net).[91] This conventional synthetic approach enables the fine tuning of pore sizes depending on the extent of the organic SBUs and desired application of the material (**Figure 1.4.1**). Yaghi and co-workers distinguish this underlying synthetic concept from a supramolecular assembly as the building blocks involved in reticular synthesis being linked by relatively strong coordination bonds.

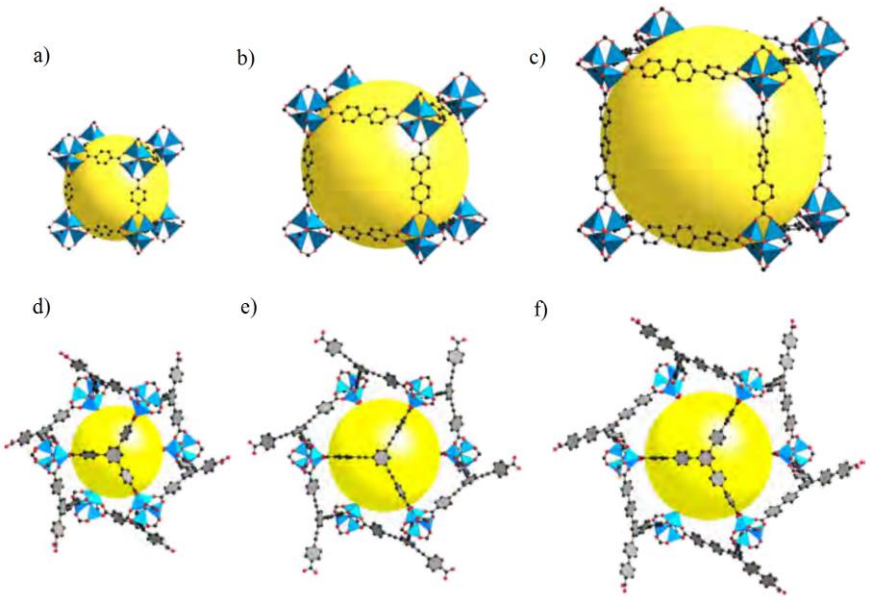

Figure 1.4.1: Representations of two different series of isoreticular MOFs. a) IR-MOF-1 (also known as MOF-5) b) IR-MOF-10, c) IR-MOF-15, d) MOF-177, e) MOF-180, f) MOF-200. Adapted from references 91 and 92.

As for MOFs, extending ligand lengths and reassembling the same structure type is one strategy to expand the size of the pores in MOPs whilst maintaining the key properties of the molecular species. The approach is comparable to iso-reticular synthetic approaches for MOFs.

An alternative strategy open to certain classes of MOPs which employ bent ligands, involves variation of the binding angles of the organic ligands. By widening the angle closer to 180°, the formation of larger MOP structures is favoured. Research into a series of M_nL_{2n} MOPs constructed from square planar Pd^{2+} complexes and bent ditopic N-donor ligands, has shown this to be a viable and applicable strategy (**Figure 1.4.2**). Thus, within the series of molecular species, the M_6L_{12} octahedron has an ideal angle between ligand N-donor groups of 90° whilst bend angles between 127° and 131°, favour the formation of a $M_{12}L_{24}$ cuboctahedron.[54] At angles between 131° to 149° a $M_{24}L_{48}$ rhombicuboctahedron is assembled.[47,93] When the bend angle exceeds 149° the larger $M_{30}L_{60}$ icosidodecahedron is formed.[59]

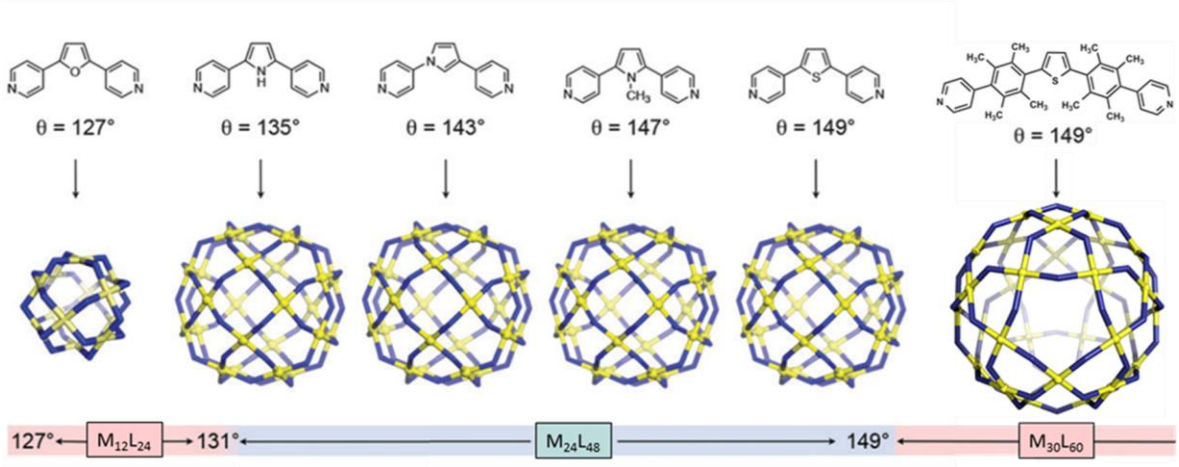

Figure 1.4.2: Representations of a series of M_nL_{2n} MOPs constructed from square planar Pd^{2+} units and bent ditopic N-donor ligands. Adapted from references 59 and 93.

1.4.2 Methods of synthesis

The solvothermal synthesis method remains the most widely used approach for the synthesis of new MOFs as it provides a means to overcome thermodynamic barriers associated with the formation of network structures and solubility issues of the reactants; it has a tendency to produce reasonably-sized crystals which are required to characterise the resulting structures using single crystal X-ray diffraction (SCXRD) characterisation.[94]

Synthetic methods include electrochemical,[95–99] microwave-assisted,[100–102] mechanochemical[103,104] and sonochemical[105,106] methods as well as syntheses under ambient conditions,[107–110] at elevated temperature,[111,112] or using vapour diffusion[113] methods. The latter method proceeds for instance *via* the slow diffusion of base into the reaction solution leading to the deprotonation of the carboxylate-based ligands and slow crystallisation (**Figure 1.4.5**, **b)**). This was applied for instance in the original synthesis archetype MOFs, such as MOF-5.[88]

Different synthetic methods as summarised in **Figure 1.4.3**, are chosen based on the nature of the desired compound, morphology and field of application. Methods such as microwave-assisted, mechanochemical and sonochemical approaches are often used for the scale-up production of a MOF once the structure has been elucidated.

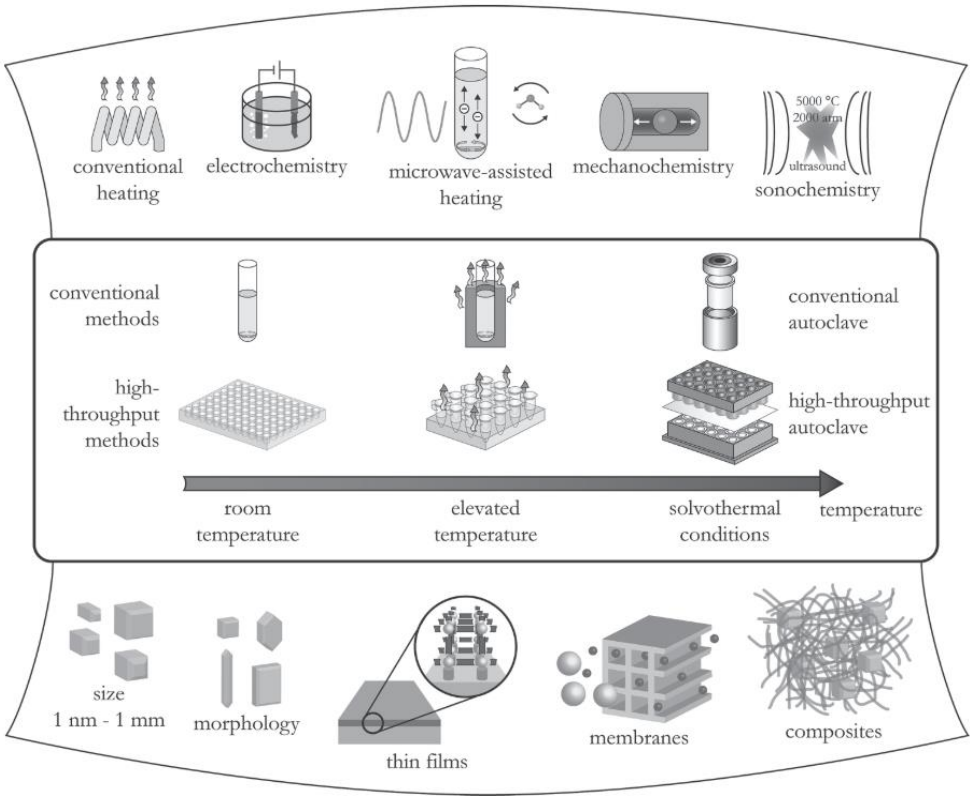

Figure 1.4.3: Overview of possible synthesis methods at various reaction temperatures and final reaction products in MOF synthesis. Reproduced from reference 112.

If crystalline material of sufficient quality for SCXRD is not produced, the structure of the material can be extremely difficult or impossible to determine with reasonable certainty. Crystallisation is an extremely sensitive process which is often only successful after extensive trial and error. This trial and error approach represents a limiting factor in MOF and MOP synthesis. Furthermore, applied synthetic approaches often do not lead to the exclusive formation of the desired product. Separation of the desired crystals from other products is often necessary.

Solvothermal methods allow variation of a large number of possible synthetic parameters. Temperature, pressure, time, pH and concentrations of reactants can be varied leading to a wide range of different compounds that can be synthesised. The parameters may be modified to change not only the type of compound formed but also the size and morphology of forming crystals. This method has proved itself to be particularly useful for the synthesis of hybrid inorganic-organic materials including MOFs. The method involves a sealed Teflon-lined vessel containing the reagents and solvents which are heated

for prolonged periods of time to elevated temperatures, often above the boiling point of the solvents (**Figure 1.4.4**).

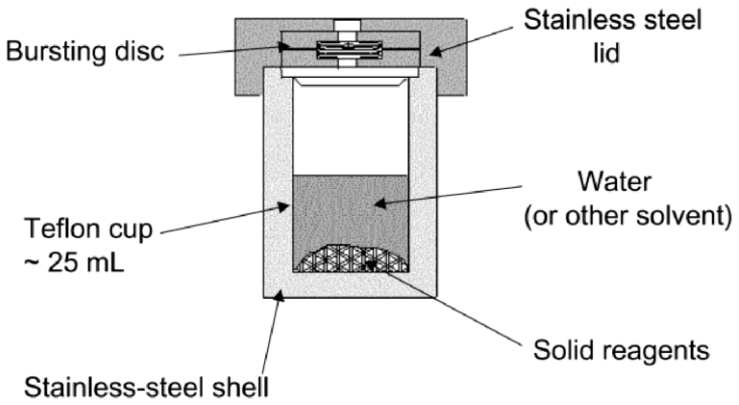

Figure 1.4.4: Schematic of a Teflon-lined stainless-steel autoclave used for solvothermal synthesis. Reproduced from reference 114.

Solvothermal synthesis approaches to MOFs are often preformed in dialkylformamide type solvents. This approach is known to proceed through slow solvent decomposition resulting in the *in-situ* formation of dialkylamines and the deprotonation of carboxylic acid based ligands, assisting SBU and crystal formation (**Figure 1.4.5**, **a)**). By definition, during solvothermal synthesis, the temperature of the reaction media should exceed the boiling point of the solvent.[94] However, in the literature the term is also often used to refer to reactions in sealed vessels at elevated temperatures that remain below boiling point of the solvent.[69,115,116]

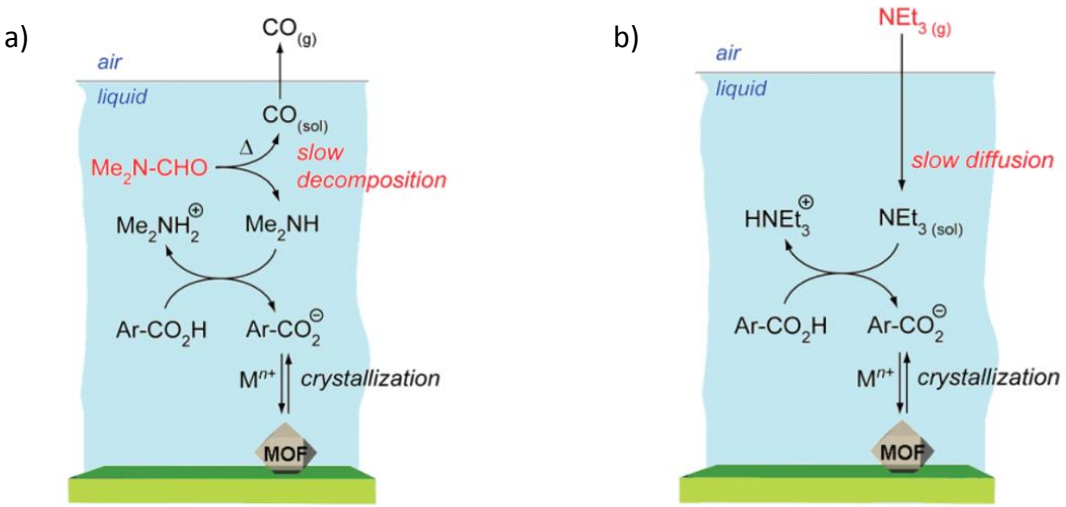

Figure 1.4.5: MOF synthesis upon **a)** slow thermal decomposition of N,N-dimethylformamide, **b)** vapour diffusion of base. Reproduced from reference 95.

1.4.3 Electrochemical synthesis and MOF deposition

MOFs can also be synthesised using electrochemical deposition methods on conductive surfaces.[117] The technique can be used to synthesise adherent, microporous MOF layers on top of conductive substrates at room temperature, at atmospheric pressure and often within significantly shorter time periods than those required for solvothermal syntheses. Electrochemical methods are further attractive due to their general cost effectiveness.

Generally, two methods, anodic and cathodic synthesis deposition approaches are applied. Cathodic depositions of MOFs makes use of solutions containing all the starting materials needed for the synthesis (metal ions and organic ligands). The mechanism of cathodic electrodeposition is attributed to a shift in the pH of the reaction media in the proximity of the electrode surface. It proceeds *via* the production of a "pro-base" at the cathode. Often oxoanions, such as nitrite ions, that derive from the reduction of nitrate ions and act as pro-bases. Their presence results in the local formation of hydroxide ions which deprotonate the carboxylic acid ligands.[95] The oxoanions can reduce water in the solution producing oxide or hydroxide ions which may also be directly required as ligands for the generation of certain SBUs. The solvated metal ions in solution are attracted by the negative potential at the substrate surface and the local presence of deprotonated ligands can trigger the self-assembly, growth and deposition of MOF crystals which are confined to the conductive substrate surface (**Figure 1.4.7**). The consequent growth of MOFs at the conductive surface allows for facile surface functionalisation as required, which constitutes an important research area in materials science. The synthetic approach is particularly applicable for electro-catalytic studies using MOFs as surface-found catalysts.

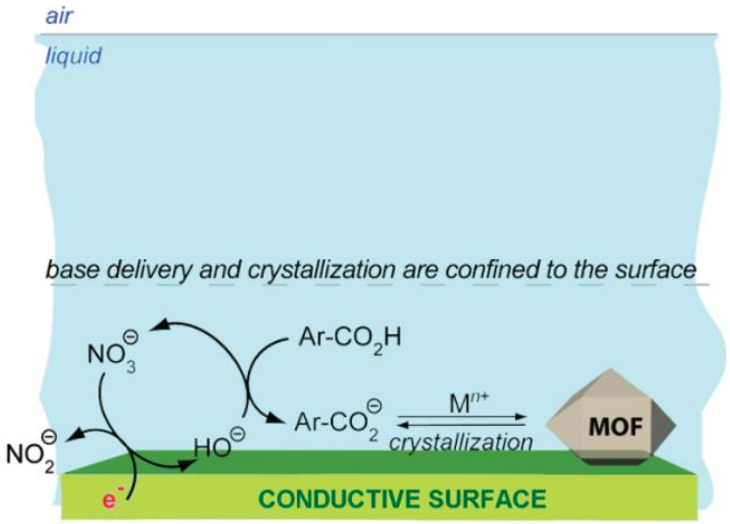

Figure 1.4.7: Schematic approach for the cathodic electrodeposition of crystalline MOFs at conductive surfaces, reproduced from reference 95.

Anodic depositions of MOFs use solutions containing only the organic ligands without metal cations initially present in the reaction media. The latter are generated by anode oxidation whereby the nature of the anode material determines the composition and structure of the synthesised MOF material.[118] The general mechanism of anodic deposition can be divided into four phases: nucleation, growth of islands, intergrowth and detachment.[96]

At first, metal ions are released into the ligand solution from the anode due to the applied oxidising potential. When a critical concentration of reagents is reached, MOF nuclei form in solution and at the lateral boundary of the anode surface (nucleation step).

It has been observed that new nuclei tend to accumulate adjacent to existing ones, leading to the growth of islands. This process prevails as the electrode area directly around existing nuclei gives rise to higher current densities whereas areas that are covered by nuclei reveal increased electrical resistance. Thus, higher concentrations of metal ions at the nuclei-surface boundary promote the formation of secondary nuclei and the growth of islands.

Nuclei continue to form and grow leading to intergrown layers of MOFs which coat the anode surface. For materials of sufficient pore size, metal ions can diffuse through the pores, facilitating MOF formation even after the entire anode surface appears covered (intergrowth). However, the organic ligands may also be too large to diffuse through to the

anode surface and thus growth of the MOF may not take place beneath an existing MOF layer.

During the final phase, parts of the MOF layer may lose their adhesion to the anode and are released into the solution to form dispersions. Generally this occurs when the MOF layer becomes 'undercut' by the dissolution of the anode material or due to internal structural forces within the growing MOF layer or strains at the boundary (detachment).

It is worth noting that the intrinsic properties of the conductive surface, temperature, pressure, applied potentials and additives have a strong influence on MOF formation and growth.[99,119–121]

1.4.4 Post-synthetic modification

Post-synthetic modification (PSM) approaches extend the synthetic methods to generate various MOFs and MOPs for targeted applications.[122–125]

Ligand exchange within MOFs can be exploited as a means to introduce new functional groups into MOFs under mild conditions. Studies have shown reversible ligand exchange in MOFs whereby the crystalline or molecular structure and porosity of the material stays intact[122,126,127] or becomes modified if desired.[128] Post-synthetic ligand exchange reactions can be achieved conveniently when replacing ligands of a similar size and that reveal comparable binding properties. Thus, dispersion of a MOF in a ligand solution for several days at room temperature can deliver quantitative ligand exchange, whereby heating may be applied to assist the exchange reactions that proceed at various rates depending on the solvent systems. It has been shown that even highly stable MOFs can undergo ligand exchange under selected solvent conditions.[129,123,130] PSM methods can be used to synthesise MOFs, that are not readily accessible using traditional direct methods.

Comparable PSM methods can be exploited for the synthesis of MOPs that are structurally related to MOFs. It has been shown that Cu(II) paddle-wheel based MOPs with cuboctahedral topology can be converted into other MOPs using partial or complete organic ligand substitution involving soluble or insoluble MOP precursors. The resulting MOPs that largely maintain the topological aspects of the precursor species can be isolated as crystalline products (**Figure 1.4.8**).[49] PSM methods are comparable to "dynamic, covalent scrambling approaches" reported for porous organic molecular frameworks where individual organic components can be exchanged due to the reversibility and dynamic nature of certain bond formation/cleavage reactions, e.g. post-synthetic modifications involving the reversible formation and hydrolysis of imine bonds.[131]

Metal ion exchange reactions using preformed MOFs as substrates, are complimentary to ligand exchange approaches. In MOFs and MOPs, heterometals can be introduced or anchored at chelating sites of the organic ligands,[132,133] as well as incorporated into the inorganic SBUs by metal exchange.[134,135] Depending on the MOF system, partial or quantitative exchange is observed whereby the topology of the parent framework is maintained.[125,135–141] Metal exchange, incorporating Li^+ ions into MOF SBUs

as well as exchanging counter ions, has been shown to modify H_2, CO_2 and CH_4 gas uptake properties in MOFs.[142–145]

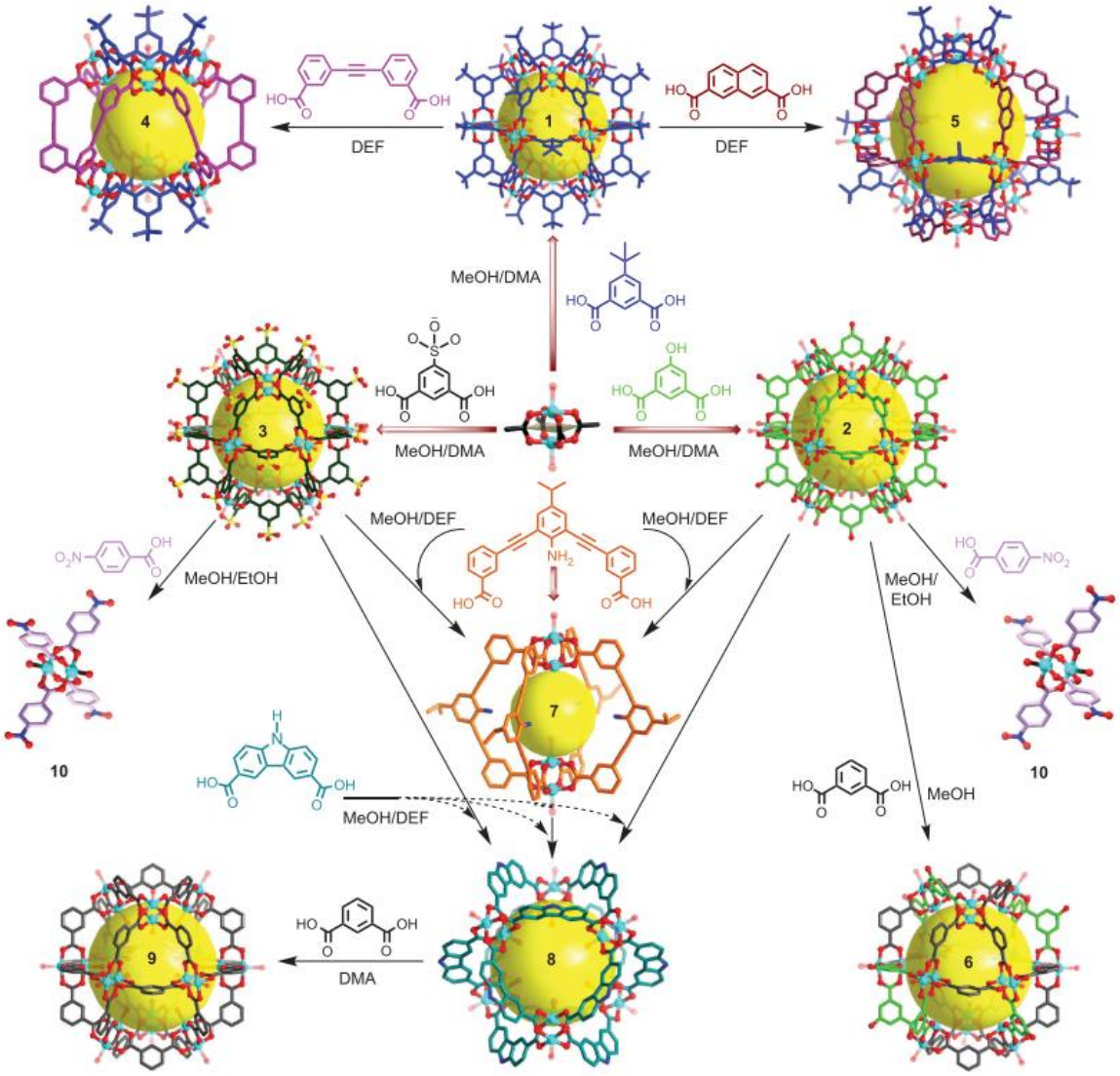

Figure 1.4.8: Schematic representation of the synthesis of MOPs using post-synthetic methods. Compounds 1–3 were synthesised directly from $Cu_2(OAc)_4{\cdot}xH_2O$ and the corresponding carboxylic acid ligands in appropriate solvents; Their transformations into MOPs 4–9 and to dinuclear species 10 are facilitated through ligand substitution reactions. All H atoms, uncoordinated solvent molecules, part atoms of coordinated terminal solvent molecules, and Na^+ ions have been omitted for clarity. Colour scheme: Cu (cyan), O (red), N (blue), S (yellow), C (represented in the same colour as the corresponding structural formula of the ligands). The yellow spheres represent the free space inside each molecular cage. Reproduced from reference 49.

Highly stable MOFs, such as Zr-based MOFs have been shown to be particularly tolerant to post-synthetic modifications; in some cases selected SBUs can undergo structural rearragments.[124,146] Thus, by application of a combination of ligand and metal exchange processes, it is possible to generate heterometallic MOFs that are composed of various different inorganic and organic SBUs using monometallic MOF starting materials. Such multi-component assemblies can be synthesised by sequential modification of metal clusters and organic linkers within preformed MOFs.[132,147] The approach allows certain network topologies to be post-synthetically altered (**Figure 1.4.9**).[133,148]

Many MOPs can be viewed as disassembled units that can be used for the construction of MOFs.[71,51,149–153] The assembly of MOFs from MOP precursors by interlinking MOPs has been shown to be possible.[51] However, it is often synthetically difficult due to the low solubility of neutral MOPs (e.g. the low solubility of $\{Cu_2\}$-based MOPs shown in **Figure 1.4.8**).[149]

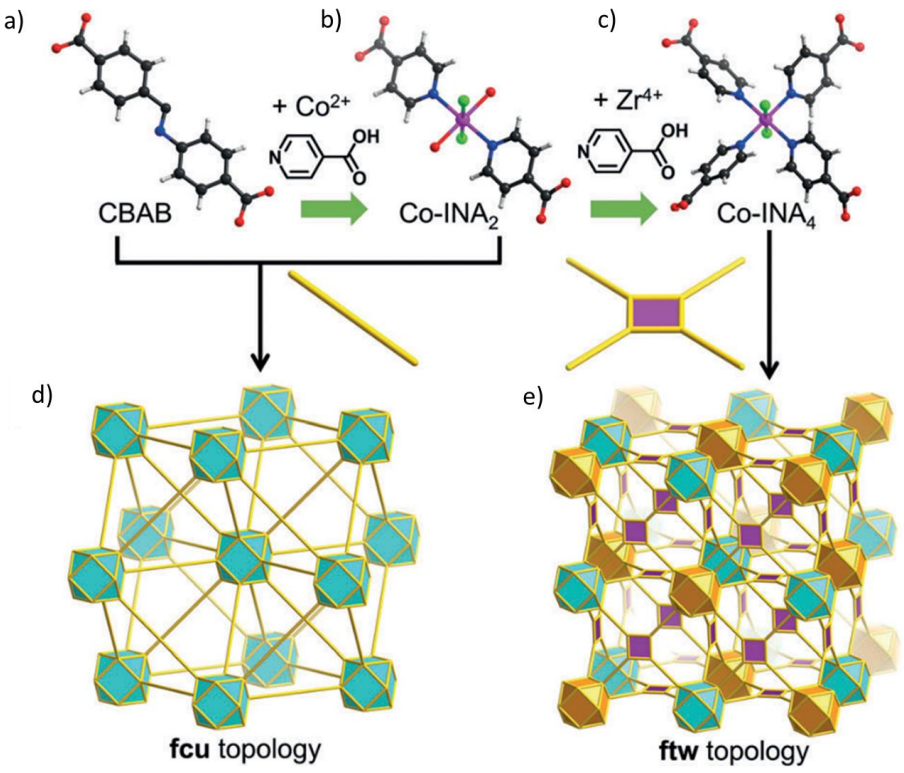

Figure 1.4.9: PSM topological transformation involving the introduction of ligands and nodes. **a), b, c)** Linkers and their topological representations; **d), e)** Modification of MOF with **fcu** topology to form a new structure with **ftw** topology. The Zr-SBUs are represented as teal cuboctahedrons while the additional Zr-SBUs are represented as orange cuboctahedrons. Adapted from reference 133.

Using PSM methods it has been shown that some MOPs can be assembled into 1D polymers and 2D and 3D MOFs through the introduction of secondary bridging ligands. Additionally, MOFs can be disassembled into their component units by exchange methods using non-bridging, terminal capping ligands. This approach was first demonstrated using a $\{Cu_2\}$ paddle wheel based system.[154] Within the SBU, four carboxylate functionalities bind to the equatorial sites leaving two apical sites with coordinated solvent molecules. The latter can be displaced by more strongly coordinating ligands allowing the introduction of new ligands. MOPs containing these SBUs can be post-synthetically interconnected by bridging ligands or disassembled by capping ligands which bind to the outer apical sites at the $\{Cu_2\}$ SBUs (**Figure 1.4.10**).

It is further noteworthy, that it is possible to alter crystal morphologies of MOFs post-synthetically by consecutive crystal dissolution and regrowth processes.[155] Such approaches have recently been reviewed.

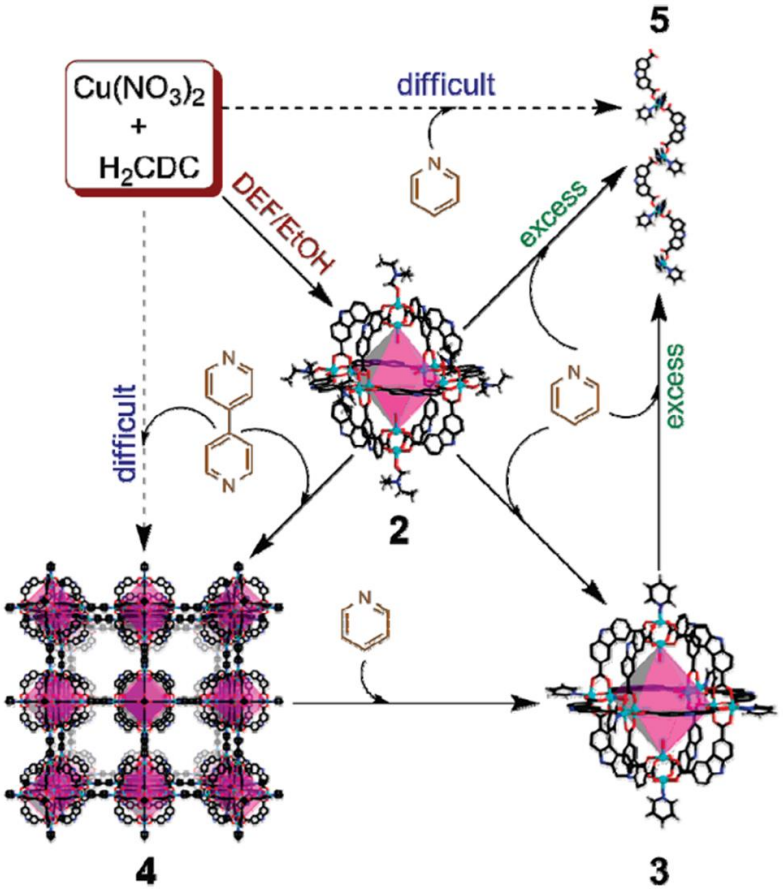

Figure 1.4.10: Interconversion between MOPs (**2** & **3**), MOFs (**4**) and 1D polymers (**5**). Most H atoms have been omitted for clarity. Colour scheme: Cu (teal), O (red), N (blue), C (black). Reproduced from reference 154.

1.5 Structural aspects of MOFs and MOPs

1.5.1 Hydrolytic stability

The stability of MOFs and MOPs depends on the components from which they are constructed and how they interact. Thus, their stability varies greatly. However certain attributes often lead to increased stabilities. Stability in MOFs and MOPs is now being widely investigated as it is a key requirement when considering their use in various applications.[156] Many archetype MOFs constructed from Cu^{2+} and Zn^{2+} ions, proved to be unsuitable for various applications due to their lack of hydrolytic, thermal or oxidative stability under the conditions encountered during use. A good example for limited hydrolytic stability is represented by the Zn-based MOF-5, which revealed exceptional gas uptake characteristics, however, it gradually degrades when exposed to moisture. Hydrolytic stability is of particular concern for many MOFs and MOPs especially as exposure to some levels of water is unavoidable. The hydrolytic degradation of MOF-5, HKUST-1 and other MOFs, involves a series of substitution reactions whereby coordinated organic ligands are displaced by water molecules (**Figure 1.5.1**)[157,158] Constructing materials using kinetically labile metal ions that facilitate strong coordination bonds between SBUs and ligands can result in water-stable compounds.

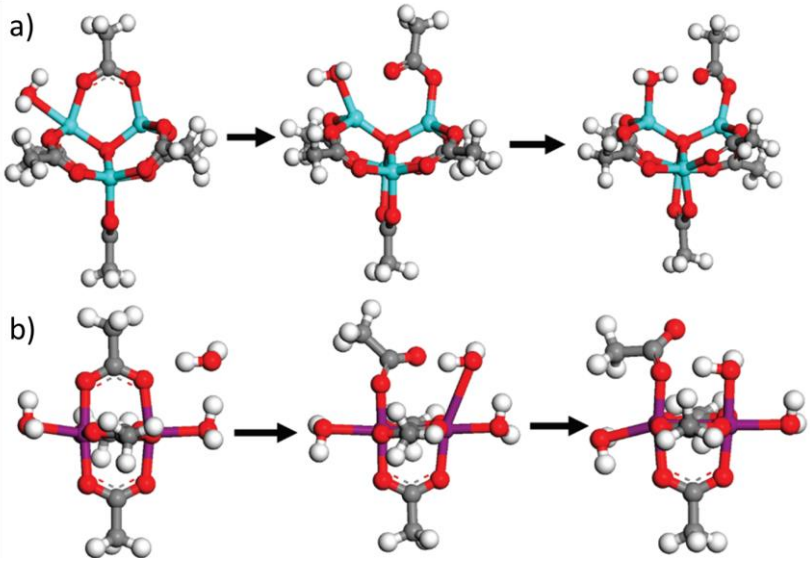

Figure 1.5.1: Hydrolytic degradation mechanisms of SBUs involving ligand/H_2O substitution reactions; Mechanisms were derived from computational simulations using simplified clusters. **a)** $[Zn_4O(C_2H_3O_2)_4]$ as a model complex for the $\{Zn_4O\}$ SBU undergoing a substitution reaction with H_2O, **b)** Hydrolytic degradation of $[Cu_2(C_2H_3O_2)_4(H_2O)_2]$ as a model complex for the $\{Cu_2\}$ SBU. Reproduced from reference 157.

The hydrolytic stability of MOFs and MOPs can be predicted by investigating the strength of the bonds that form the structure. The strengths of coordination bonds are related to the orbital overlap between metal ion orbitals and ligand orbitals and the electron configuration. Systems in which anti-bonding molecular orbitals remain unoccupied reveal higher hydrolytic stability and remain inert to ligand exchange reactions. Broadly, the strength of a coordination bond relates to the charge and the radii of the metal ions whereby highly charged small metal ions give rise to increased stabilities.

The expected stability can be judged using the hard and soft Lewis acid and base (HSAB) theory. The concept states that hard Lewis bases (e.g. carboxylates) form strong bonds with hard Lewis acids (e.g. K^+, Al^{3+}, In^{3+}, Zr^{4+}). While soft Lewis bases (e.g. imidazole) form strong bonds with soft Lewis acids (e.g. Cu^+, Pd^{2+}, Cd^{2+}, Te^{4+}). Thus, examples of water stable materials constructed from hard acids and hard bases include the Zr^{4+} containing UiO-66[159] (University of Oslo) and the In^{3+} containing BUT-70[160] (Beijing University of Technology) MOFs. Examples of water stable materials constructed from soft acids and soft bases include many Pd^{2+} containing coordination cages including [Pd(Me_4en)$_2$(1,3,5-tris(isonicotinoyloxyethyl)cyanurate)$_2$][161] whilst corresponding Pt^{2+} systems often reveal higher kinetic lability towards hydrolytic substitution reactions.

Highly connected SBUs in MOFs tend to impart stability to the materials preventing gradual dissociation of the inorganic SBUs from the framework.[162,163] Examples of highly connected MOFs include the before mentioned UiO Zr-based MOFs and PCN-601 that is composed of 8-connected {Ni_8} SBUs and 4-connected porphyrin ligands.

Coordinatively unsaturated sites (CUS) are positions on the metallic nodes of MOFs or MOPs that derive from binding sites that are occupied by labile solvent molecules. Whilst these sites are often essential for catalytic activity, they do not significantly contribute or even reduce the overall hydrolytic stability of the materials. However, CUS can be used as binding positions for additional ligands to increase the stability of the compounds and modify their properties.[164,165]

The thermal stability of a MOF is intrinsically limited by the decomposition of the organic ligands. To synthesise MOFs that retain their structural integrity on removal of constitutional solvent molecules, highly connected nodes and rigid ligands are desirable.

1.5.2 Surface Areas, Densities and Porosity

MOFs can possess exceptionally low densities which are related to their porous nature. A MOF with the lowest density was initially provided by MOF-399, published in 2011 which has a density of 0.126 g/cm^3.[166] An even lower density was achieved in 2017 by NU-1301 revealing a density of 0.124 g/cm^3.[167] Among the first application directed properties explored for the use of MOFs, were gas storage and purification capabilities. In MOFs the network connectivity of the building units determine key characteristics of the materials. By using suitable ligands, any various desired porosity types can be obtained providing microporous to macroporous networks with remarkable surface areas (S.A.). MOFs reveal the highest achievable surface areas of any material, reaching theoretical values of up to 14,600 m^2/g.[168]

Two commonly used methods to calculate surface areas of MOFs are Langmuir and Brunauer–Emmett–Teller (BET) methods. Langmuir surface area calculates the surface area of a material assuming it becomes covered by a monolayer of adsorbate. The method tends to overestimate the actual available surface area since multiple adsorbate layers are often condensed within the pores of MOFs. MOF-210 holds the record value achieving a Langmuir S.A. of 10,400 m^2/g.[92] The BET method is often considered to be more reliable as it allows for consideration of multi-layer condensation. Since 2012, the highest measured BET S.A. was achieved by NU-110 (7140 m^2/g) which was recently surpassed by DUT-60 revealing a S.A. of 7839 m^2/g (**Table 1.5.1**).[169]

Geometric surface areas, calculated from the crystallographic data are also widely used to characterise the framework structures. Sometimes the measurement of the BET and Langmuir surface area is not possible due to framework collapse upon removal of solvent molecules upon activation.[170] However, calculated surface areas can provide insights into the nature of the materials providing guidance for experiments and applications under which the framework structure remains intact, i.e. heterogeneous catalysis in solution using MOF substrates.

Starting from IRMOF-74-I which is formed by a combination of the dioxidoterephthalate ligand with Zn^{2+} or Mg^{2+} ions, Yaghi *et al* were able to form a series of iso-reticular MOFs by lengthening the ligand structure (**Figure 1.5.2**). This approach resulted in increasing channel diameters of up to 98 Å in IRMOF-74-XI.[171]

Table 1.5.1: Summary of BET and geometric surface areas as well as specific pore volumes for selected highly porous MOFs. Geometric surface areas are calculated based on crystallographic data. Adapted from references 168 and 169.

MOF Name	BET Surface Area (m^2/g)	Geometric Surface Area (m^2/g)	Pore Volume (cm^3/g)
MOF-5	3800	N/A	1.55
MIL-101c	4230	N/A	2.15
MOF-177	4750	N/A	1.59
DUT-6	4460	4760	2.16
NU-100	6140	5740	2.82
MOF-210	6240	5740	3.60
DUT-76	6344	5150	3.25
DUT-32	6411	5410	3.16
NU-109	7010	6020	3.75
NU-110	7140	6160	4.40
DUT-60	7839	6200	5.02

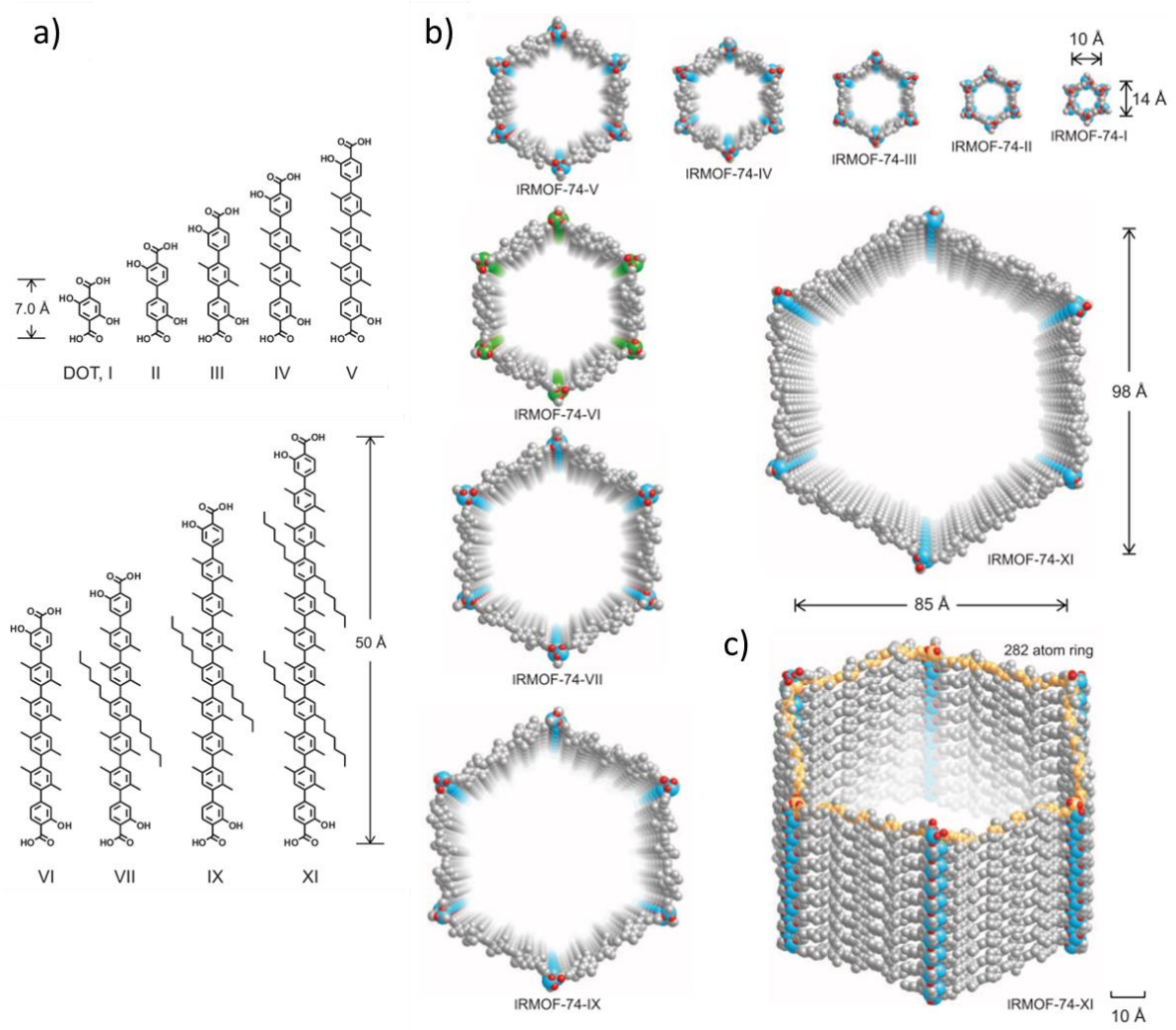

Figure 1.5.2: a) Chemical structures of the organic ligands used in the synthesis. **b)** Perspective views down the hexagonal channels of each MOF in the series. **c)** Perspective side view of the hexagonal channel in IRMOF-74-XI. Adapted from reference 171.

Several MOPs also possess large measured and geometric surface areas that give rise to porosity. Simulations of the surface areas of such molecular species suggest that surface areas of MOPs are generally comparable to MOFs. However when measured the materials generally show lower stabilities and tend to reveal lower surface areas than their related 3D connected MOFs. In 2011, Zhou and co-workers published a $\{Cu_2\}$ paddlewheel based MOP with a BET surface area of 160 m^2/g (Langmuir surface area of 181 m^2/g).[172] In 2015, Chunhua and co-workers reported two Co-based MOPs which were shown to have BET surface areas of 410 m^2/g and 558 m^2/g.[173] In 2018, two Cu-based and Cr-based MOPs composed of carbazoledicarboxylate ligands revealed measured BET surface areas of 657 m^2/g and 1235 m^2/g, respectively.[60] The latter is the highest measured BET surface area for a MOP. Whilst the surface area can be regarded as high, it is significantly lower than that of DUT-60 or of related MOFs.

In 2016, Fujita and co-workers published a M_nL_{2n} type MOP composed of 30 Pd^{2+} ions and 60 ligands was published (**Figure 1.5.3**).[59] These types of cages display large single voids in their interior. This particular MOP a remarkable outer diameter of 8.2 nm (82 Å) and an inner void volume of 157,000 $Å^3$. It is the largest cavity inside a MOP, however, the surface area was not reported.

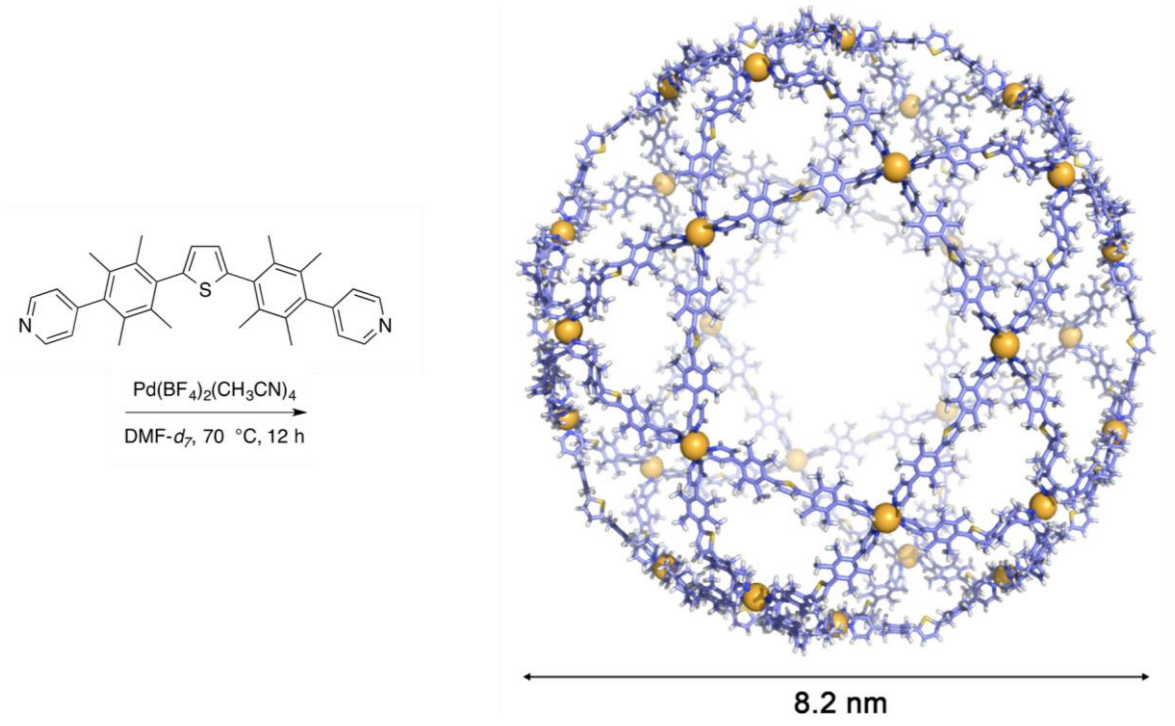

Figure 1.5.3: Synthesis and X-ray crystallographic structure of $Pd_{30}L_{60}$ MOP which has an icosidodecahedral symmetry. Adapted from reference 59.

1.5.3 Catenation, interpenetration and interweaving

Framework catenation is a frequently observed phenomenon in MOFs and it refers to the intergrowth and prevalence of two or more networks composed of the same or different components within a compound. Catenation in MOFs derives from the presence of a significant accessible void volume that results in a single framework structure. The available space can then accommodate the growth of one or more additional nets within the framework. There are no chemical bonds between these nets. However, supramolecular interactions, such as hydrogen bonds, π-π interactions and van der Waals forces can promote the formation of interpenetrated compounds, often significantly adding to the stability of MOFs.[174–178]

As a result of catenation, a single net in a catenated MOF cannot be separated from the rest of the framework structure without the breakage of chemical bonds. Catenated frameworks can be divided into two sub-types: interpenetrated and interwoven frameworks.[179] Within interpenetrated frameworks the nets are maximally displaced from each other, while in interwoven frameworks the distance between nets is minimised (**Figure 1.5.4**).[180]

Catenation approaches can be is used as a synthetic method to control specific pore sizes. Catenation generally results in a decrease in the accessible pore volume for gas molecules due to additional space requirements of the additional nets.[164,181] The underlying synthetic approach has been used to vary pore sizes to synthesise MOFs that are highly selective for a particular type of gas molecule.[178] In 2011, Kim and co-workers published a 2-fold interpenetrated version of the Zn-based MOF, MOF-5. It exhibited a lower pore volume compared with single-net structure of MOF-5 and revealed inferior H_2 uptakes at high pressure (100 bar at 77 K). However the interpenetrated MOF-5 showed superior H_2 uptakes in the low pressure regimes (At 1 atm and 77 K it had a 54% greater H_2 uptake than single-net MOF-5) and revealed significantly enhanced water and heat stability.[176]

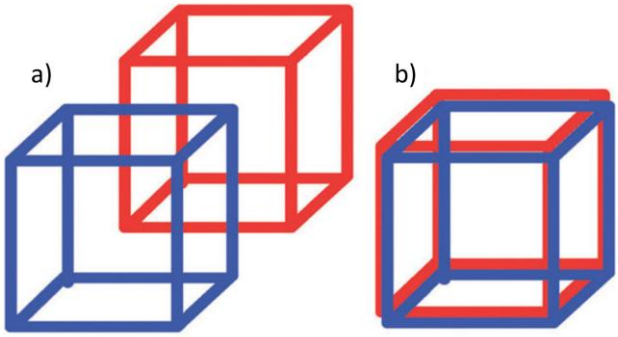

Figure 1.5.4: Simplified representations of two forms of catenated MOFs; **a)** Interpenetration and **b)** interweaving. Different nets are shown in red and blue. Reproduced from reference 180.

1.5.4 Defects

While defects in many MOFs inherently occur, they may not be directly detectable or visible through single crystal diffraction studies. Defects however can introduce significant changes to various properties of a MOF including reactivity and porosity. UiO-66 provides a well-studied MOF composed of Zr_6 SBUs and terephthalic acid ligands and is known to contain regular defects in the form of missing carboxylate ligands leaving 'open' metal sites at the SBU which results in unique physicochemical attributes. These open sites or undercoordinated metal centres (UMCs) have been shown to make this type of MOF more hydrophilic enhancing H_2O and CO_2 uptakes[182] as well as increasing the available space in the pores within the MOFs thereby increasing their pore volumes.[183] UMCs can result in unique catalytic effects which are not observable in corresponding homogeneous phases. Further, defect sites leave binding sites and space for post-synthetic functionalisation.[184] Defects can be introduced in MOFs by design. Methods have been developed to control the number of defects formed by varying the temperature during MOF formation[185] as well as by using modulators[183,186] which can even reduce the number of entire inorganic SBUs in the structure. Another method to introduce defects into a framework structure is by using selective mixed ligand systems during the synthesis of the MOF. This was shown in 2011 by Yaghi *et al*. using MOF-5 which is conventionally synthesised from a mixture of Zn^{2+} ions and terephthalic acid.[187] By replacing a fraction of the of the terephthalates with monofunctional carboxylates containing a capping group (in

this case 4-(dodecyloxy)benzoate), defects can purposefully be introduced, resulting in the formation of amorphous MOFs containing meso- and macropores (**Figure 1.5.5**).

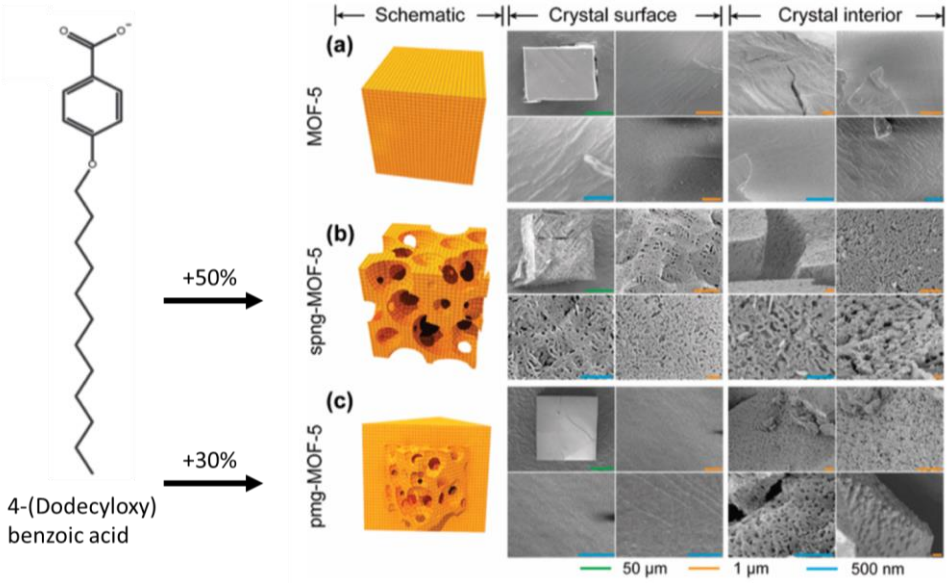

Figure 1.5.5: SEM observations of mesopores in **(a)** MOF-5, **(b)** spng-MOF-5, and **(c)** pmg-MOF-5 upon use of 4-(dodecyloxy)benzoate. Adapted from reference 187.

1.6 Potential applications of MOFs and MOPs

1.6.1 Gas storage and purification

Porous materials play many important roles in chemistry and engineering.[188] While it is important for investigators to synthesise novel materials, it is equally important to explore applications for which those materials could be suited. Initially MOFs were regarded as being suitable for gas storage applications due to their high surface areas and their tuneable pore structures.

1.6.2 Hydrogen storage

For widespread commercial applications in vehicles, fuel sources are required to have high volumetric and gravimetric energy densities. Hydrogen is a fuel source with the highest energy densities by weight producing nearly three times the amount of energy when burned compared to petrol (33.3 kWh/kg vs. 12.8 kWh/kg) (**Table 1.6.1**). Its combustion in air produces only water as a product, making it an attractive choice for sustainable and eco-friendly alternatives to fossil fuels.[189] However, it lacks volumetric density which currently hinders its widespread use. To overcome this difficulty new innovative ways to store hydrogen are being developed globally. Since 2002 the US Department of Energy (DOE) has funded successive research initiatives into the subject, setting rising benchmarks and significantly accelerating hydrogen storage research including the development of MOFs for this application.[24,92,115,190,191]

With extremely high surface areas as well as low densities, MOFs show excellent capacity for gravimetric H_2 storage. Hydrogen uptake capacity in MOFs seems to approximately increase with increasing surface area which is limited by the maximum theoretical S.A. possible in MOFs.[192,193] Additional approaches to increase the H_2 uptake capacity involve the introduction of undercoordinated metal centres (UMCs) which can result in increased uptake characteristics, especially at lower pressures as UMCs offer strong binding sites for H_2 molecules.[194–196] Doping approaches, i.e. doping with alkali metal cations, have been shown to increase H_2 uptakes despite simultaneously reducing BET surface areas.[197] MOF-based absorbents are able to reach DOE storage targets at low temperatures but it remains challenging to reach satisfactory values at ambient temperature.

Table 1.6.1: Specific energy (energy density by mass) and energy density (by volume) of fuels (container weights and volumes excluded). Reproduced from reference 189.

Fuel	Specific energy (kWh/kg)	Energy density (kWh/dm^3)
Liquid hydrogen	33.3	2.37
Hydrogen (200 bar)	33.3	0.53
Liquid natural gas	13.9	5.6
Natural gas (200 bar)	13.9	2.3
Petrol	12.8	9.5
Diesel	12.6	10.6
Coal	8.2	7.6
NH_3BH_3	6.5	5.5
Methanol	5.5	4.4
Wood	4.2	3.0
Electricity (Li-ion battery)	0.55	1.69

The first MOF which was discovered to have noteworthy hydrogen storage capability was MOF-5. In 2003 uptakes of 4.5 wt% (1 bar, 78 K) and 1 wt% (20 bar, 298 K) were reported for MOF-5.[24] Since then, extensive investigations into MOFs as hydrogen storage materials were conducted. Another significant benchmark was set in 2007 using a structurally related, high-surface area Zn-MOF, MOF-177, achieving an uptake of 7.5 wt% at 60 bar and 77 K.[190]

Materials derived from MOFs have also been tested for H_2 uptake capacity. In 2011, A highly stable porous carbon material which was synthesised from ZIF-8 upon thermolysis was shown to have a moderate hydrogen storage capacity of 2.77 wt% at 77 K and at 1 atm.[191] One MOF with the highest hydrogen storage capacity, is MOF-210 (BET S.A. 6240 m^2/g) which has shown a gravimetric H_2 uptake of 17.6 wt% at 80 bar and 77 K which is far better than any zeolite or porous carbon based material.[92] However, this still fails to reach the overall DOE H_2 storage target of 5.5 wt% uptake with a density of 40 g/L, below 100 bar at an operating temperature of 233 K or higher.

Current research activities into H_2 storage maintain the objective to achieve these targets but are restricted by the fact that the H_2–surface interactions are not strong enough and thus restrict H_2 binding at elevated temperatures. Therefore, recent research focuses on introducing more strongly binding adsorption sites into MOFs. Open metal sites are known to increase the enthalpy of H_2-adsobent interactions which should approximately be above 15 kJ/mol to facilitate strong adsorption at higher temperatures.[198] In 2014, a

MOF with open metal sites, Ni_2(*m*-dobdc), was shown to facilitate an exceptional H_2 uptake of 12.1 g/L at 100 bar and 298 K, revealing a significant increase when compared to the uptake characteristics of MOF-5 (**Figure 1.6.1**). The high density of undercoodinated 'open' Ni^{2+} sites leads to polarisation of H_2 molecules upon sorption and results in a binding enthalpy of 13.7 kJ/mol.[199]

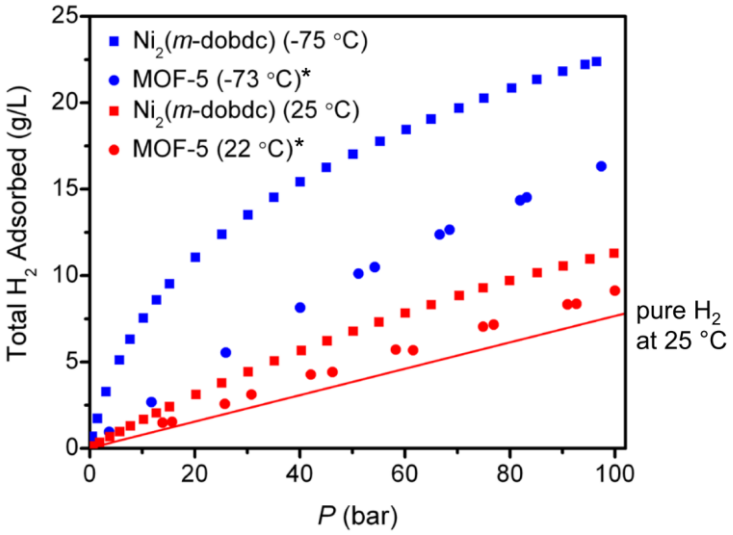

Figure 1.6.1: High pressure H_2 adsorption using [Ni_2(*m*-dobdc)] and MOF-5 in comparison to pure H_2 at 25°C. Reproduced from reference 200.

1.6.3 CO_2 and CH_4 capture and storage

With rising levels of atmospheric CO_2, it is becoming apparent that there will be a need to reduce CO_2 emissions. Moreover concepts to actively remove CO_2 from the atmosphere are discussed. Certain MOFs have shown promise for such 'Direct Air Capture' applications.

One of the early families of MOFs, published by Zaworotko,[201] now abbreviated by the term SIFSIX (**Figure 1.6.2**), have more recently been shown to have excellent selective CO_2 adsorption properties. Over a decade after the structures were first published, it was discovered that certain structural variants of these MOFs, which contain pyrazine linkers, display selective CO_2 uptakes at extremely low CO_2 pressures of *ca.* 40 Pa. The selective CO_2 uptake has been attributed to the pore size of the MOFs (*ca.* 3.5 Å) which are very close to the kinetic diameter of CO_2 molecules (3.30 Å) but too small to permit the uptake of N_2. Moreover, the cavity and channel surfaces in these porous materials strongly interact with the CO_2 molecules leading to relatively high adsorption enthalpies and allowing CO_2 to be easily separated from dry air even at low concentrations (**Figure 1.6.3**). Efforts are now being directed to the use of these and other MOFs to capture atmospheric CO_2.[202–205]

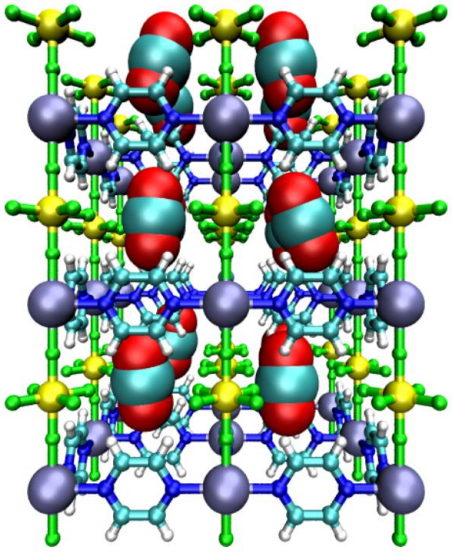

Figure 1.6.2: Molecular illustration of the pyrazine-based SIFSIX-3-Zn framework at CO_2 saturation showing rows of CO_2 molecules located in the pores. View in the direction of the crystallographic c-axis of the modelled 3×3×3 unit cell system. Colour scheme: C (cyan), H (white), N (blue), O (red), F (green), Si (yellow), Zn (grey/lavender). Reproduced from reference 206.

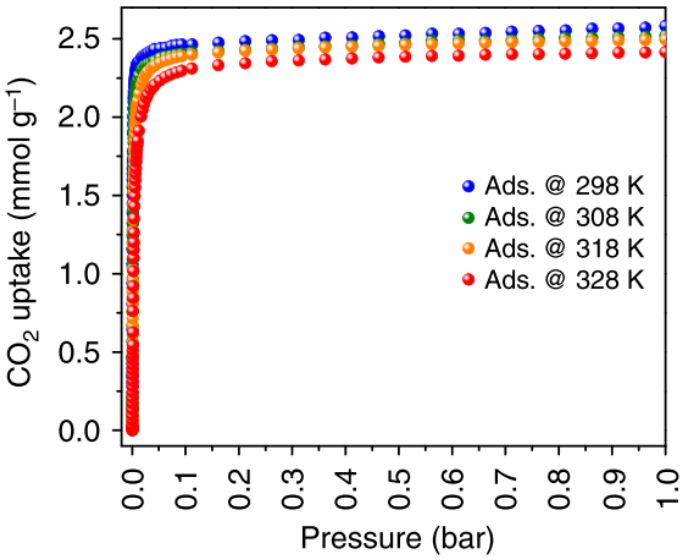

Figure 1.6.3: CO_2 adsorption isotherms at variable temperatures for SIFSIX-3-Cu showing strong uptakes at low pressures. Reproduced from reference 205.

Another strategy, whereby single molecules of CO_2 are trapped in pores between two dinuclear $\{Cu_2\}$ paddle wheel SBUs has been employed for MOPs, MOFs and related composite materials.[207] The introduction of functional reagents, such as lithium alkoxides has been proposed to significantly improve CO_2 binding capabilities.[208]

Many MOFs have a high affinity for the adsorption of H_2O, which hampers their suitability for adsorption of atmospheric CO_2.[202,209,210] The H_2O concentration in the atmosphere is significantly higher that the CO_2 concentration and H_2O molecules have smaller kinetic diameters than CO_2 molecules (2.65 vs 3.30 Å), thus they tend to penetrate microporous materials and bind firmly to charged or polarisable surfaces. Amine-functionalised MOFs containing large void channels have been developed for the capture CO_2 under wet atmospheric conditions revealing exceptionally high capture capabilities. The atmospheric water assists the CO_2 capture to form carbamates.[211,212] However the limited hydrolytic stability of the MOFs (containing UMCs) currently prohibits commercial use.

CH_4/natural gas storage is currently being assessed as a potential application for many MOFs.[152,192,204,213–215] In 2008, Zhou and co-workers published a MOF containing nanoscopic cages, PCN-14, which reveal a CH_4 adsorption capacity of 230 cm^3/cm^3 at 290 K and 65 bar, which at the time exceeded the DOE adsorption target of 180 cm^3/cm^3 and was a record capacity value for CH_4 storage materials.[152] Storage of CH_4 in MOFs has been

shown to have enough commercial potential that the initial results prompted BASF to invest in the technology and to develop MOF-based natural gas storage systems which are undergoing testing in vehicles since 2013.[216] A comparative study in 2014 of six MOFs showed HKUST-1 to have the greatest CH_4 uptake capacity of 267 cm^3/cm^3 at 298 K and 65 bar.[217]

MOPs are also being explored for CH_4 adsorption applications. In 2018, an octahedral Cr-based MOP was shown to have a reasonable BET surface area of 1235 m^2/g and good CH_4 uptake of 194 cm^3/g at 65 bar while the equivalent Mo-based MOP revealed an increased volumetric capacity of 150 cm^3/cm^3.[60]

1.6.4 Water capture from the air

Demand for fresh water is projected to increase substantially over the next decade and it is unlikely that the current supply sources will be able to meet future requirements.[218] There is an abundance of water on the planet. However most of this is located in ice caps/glaciers or is too salty to consume. Desalination and decontamination plants can produce fresh water but are expensive to build and can only be located near bodies of water.[219,220] Generating water locally where it is needed, is a major challenge. Atmospheric water generators (AWGs) are not restricted to specific locations and allow water production where desalination and other water recovery approaches are restricted. Current AWGs however usually operate by chilling air below its dew point requiring unsustainable quantities of energy.[221]

As a result of the discovery of hydrolytically stable MOFs that reveal high water sorption capacities, selected MOFs are now tested for their ability to capture atmospheric water.[222–226] Under ideal conditions certain MOFs have been shown to absorb H_2O at 200 wt-%.[225] The maximum H_2O adsorption capacity in MOFs is related to the accessible pore volumes of the material (**Figure 1.6.4**). Water vapour capture using MOFs has led to the initial development of demonstration devices for atmospheric water capture and extraction.[226] A difficulty associated with the widespread use of MOFs is that it can be challenging to remove the absorbed water molecules from the pores after adsorption. This requires either subjecting the MOF to vacuum or heat, or both, which can be energy intensive. However, this problem may be overcome by systems that use direct sunlight for the heating process whilst H_2O capture proceeds during the night.[224] A judicative selection

of a suitable MOF can lead to reversible water uptake/release facilitated by small temperature differences (**Figure 1.6.5**).[222]

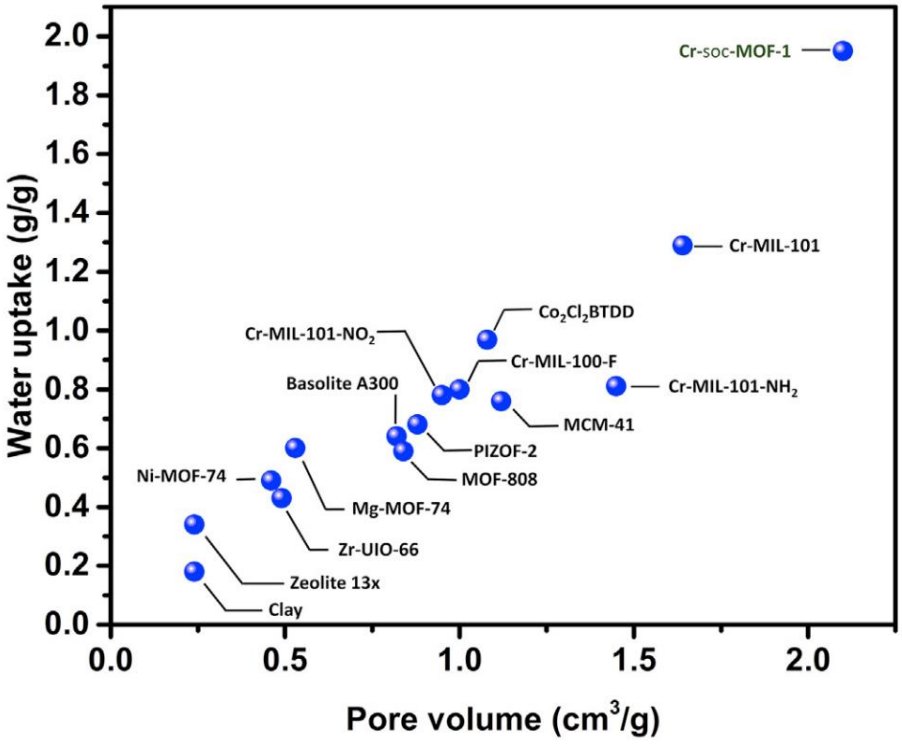

Figure 1.6.4: Correlation between water uptake capacities and pore volumes for selected MOFs. Reproduced from reference 225.

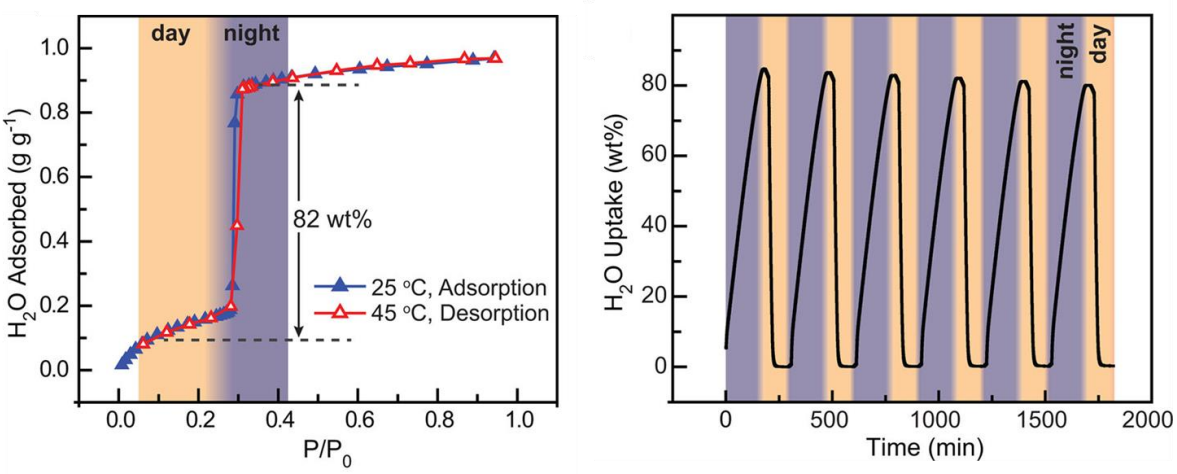

Figure 1.6.5: Reversible uptake and release of H_2O by the Co_2Cl_2(BTDD) MOF BTDD = bis(1H-1,2,3-triazolo[4,5-b],[4',5'-i])dibenzo[1,4]dioxin). Cycling between simulated night (25°C) and day (45°C) conditions to facilitate the adsorption and desorption of H_2O respectively. Reproduced from reference 222.

1.6.5 Solution-based guest molecule encapsulation and release

The use of MOFs and MOPs as container materials for the absorption and release of different guest molecules is being extensively explored and selected examples underline the potential of the class of materials. The high costs of these materials however remains a major hindrance to their commercialisation.

In 2011, it was shown that it was possible to encapsulate 5-fluorouracil (5-FU), an anti-cancer therapeutic into the pores of a MOF ($[Cu_{24}(5\text{-}NH_2\text{-}m\text{BDC})_{24}(bpy)_6(H_2O)_{12}]\cdot 72DMA$) which was constructed by interlinking MOP-15 precursors using bridging 5-NH_2-*m*BDC ligands. After absorption of the 5-FU into the MOF, they were shown to be slowly released from the MOF when placed into phosphate buffered aqueous solutions.[227] In 2012, Yaghi and co-workers succeeded in the encapsulation of a range of materials, including some proteins, into MOFs in the IRMOF-74 series. These MOFs are constructed from extended ditopic ligands and contain some of the largest recorded pore diameters of any MOFs. The studies included the encapsulation of vitamin-B_{12} (largest section 27 Å across) in IRMOF-74-IV, MOP-18 (largest section 34 Å across) in IRMOF-74-V, myoglobin (largest section 44 Å across) in IRMOF-74-VII-oeg and green fluorescent protein (largest section 45 Å across) in IRMOF-74-IX.[171] In 2014, Costas, Ribas and co-workers used a three-dimensional Zn(II)-porphyrin-Pd(II)-based MOP, which contains a distinct cavity, for the encapsulation of different sized fullerenes (**Figure 1.6.6**). The researchers investigated the uptakes of C_{60}, C_{70}, C_{76}, C_{78} and C_{84} fullerenes and were able to selectively purify C_{60} fullerenes from a mixture of fullerenes.[66] In 2015, a Co(II) calixarene-based MOP was used to encapsulate ibuprofen, a non-steroidal anti-inflammatory medication commonly used for pain relief. It was then demonstrated that ibuprofen could slowly be released in phosphate buffered saline solution giving rise to improved drug delivery profiles and elongating the therapeutic activity time of the medication.[173]

In 2016 it was announced that MOFs were being examined for commercial suitability relating to the absorption, storage and then slow release of 1-methylcyclopropene (1-MCP) in the presence of certain fruits. 1-MCP binds to the ethylene receptors on the surface of fruits delaying their ripening and therefore allowing extended preservation.[228] In 2017 this was followed by a study using commercially available MOFs Basolite C300 and Basolite A520 to absorb and release 1-MCP and ethylene (another molecule involved in fruit ripening). The research suggests that the MOFs are useful for the

delivery of these bioactive compounds.[229] In 2017, Stoddart and co-workers used a non-toxic, biocompatible MOF synthesised from γ-cyclodextrin and alkali metals for the slow release of ibuprofen and were able to show its potential as an effective drug delivery system.[230]

In 2018, a series of superhydrophobic MOFs containing of first-row transition metal ions such as Co^{2+}, Ni^{2+}, and Zn^{2+}, were synthesised and converted into pellets which were shown to float on the surface of water. Using organic solvents/oil mixtures they were shown to efficiently absorb the oils at a maximum uptake capacity of 385 wt%. Moreover, the materials were reusable without losing their superhydrophobicity.[134]

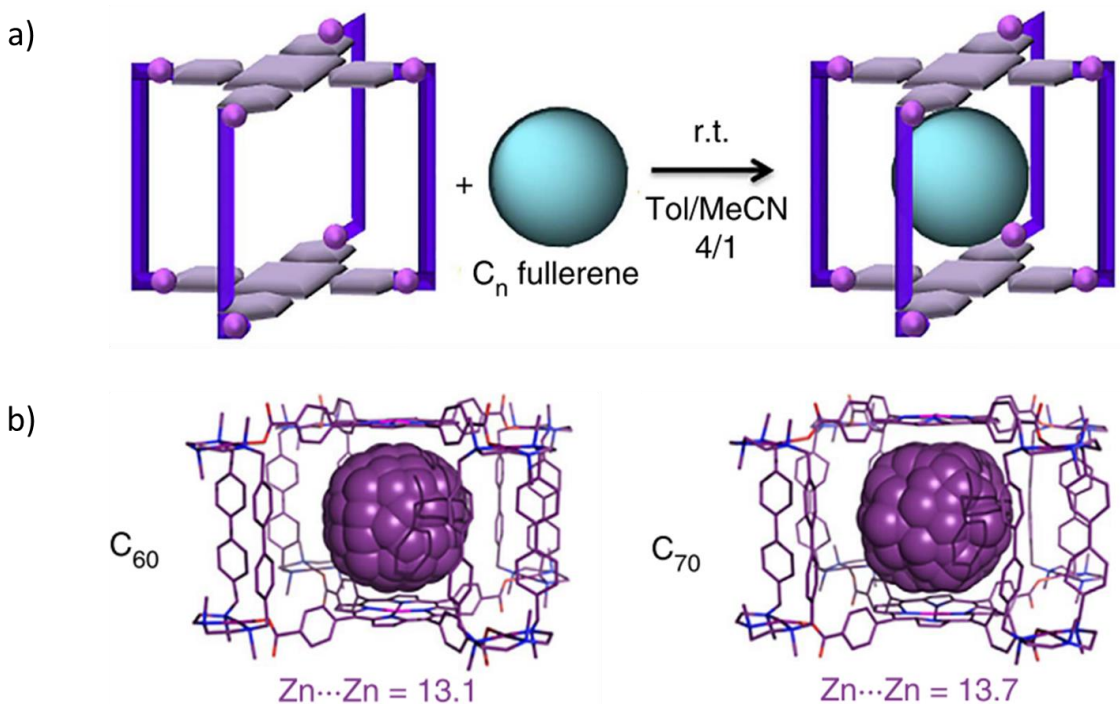

Figure 1.6.6: a) Simplified representation of a Zn(II)-porphyrin-Pd(II)-based MOP being used for the encapsulation and separation of fullerenes. **b)** X-ray diffraction analysis of fullerene host–guest compounds. Zn-Zn distances in opposite-located porphyrins given in Å. Adapted from reference 66.

1.6.6 Catalysis

Catalysts are required to lower the activation energy of reactions. The use of MOFs for catalysis is currently a 'hot' topic with many new publications on the subject. MOPs have also been used as catalysts, but they appear to have been used to a lesser extent than MOFs. There are two types of catalysts: homogeneous and heterogeneous catalysts. Homogenous catalysts are typically small metal coordination complexes containing either open metal sites or coordination sites that are vacant on the metal or else bound by very weakly coordinating molecule(s). Solvents are usually required and they are dissolved in the reaction medium. Homogeneous Catalysts can be highly active at room temperature due to the fact that all catalytic sites are exposed to dissolved reagents in the medium and they are often quite selective. However, they often lack stability, especially at higher temperatures and are difficult to recycle. Heterogeneous catalysts usually take the form of solid metals or metal oxides. While heterogeneous catalysts tend to be quite stable even at higher temperatures their selectivity is often poor and they have low surface areas exposed to the reaction medium reducing their overall activity. They are usually easy to separate from the reaction medium and highly recyclable.

MOFs are heterogeneous catalysts, however they do also share many properties with homogenous catalysts potentially combining properties from both catalyst types. MOPs have been used as both heterogeneous and homogenous catalysts. They can both show the high surface areas and selectivities of homogeneous catalysts combined with the stability and recyclability of heterogeneous catalysts. MOFs have been shown to catalyse reactions by keeping reactants close together within their pores[231,232] or by directly catalysing reactions using 'open' metal sites contained within MOFs.[233,234] The 'open' metal sites can either be on the SBUs themselves, part of the linker molecules[235] or else on guest molecules contained within the MOF or MOP.[236]

MOFs and also MOPs are now being used to catalyse a diverse set of reactions including for multicomponent coupling reactions,[237] Aldol–Tishchenko reactions,[238] amidation reactions,[239] bromination reactions,[240] allylic oxidations,[241] Diels−Alder cyclisations,[241] cyclopropanation reactions,[172] oxidation of alkanes and alkenes,[242,243] oxidative dehydrogenation,[124,244] sulfide oxidation,[233] oxidative coupling reactions,[245] acetylenic acid cyclisation,[63] as well as many other types of catalysis. Water reduction and oxidation catalysis are also being explored using MOFs (**Sections 1.6.6.3** & **1.6.6.4**).

While the interest in using MOFs for catalysis remains extremely appealing among researchers, it is clear that they have limitations due to their lesser chemical and thermal stabilities when compared to zeolites and many other porous inorganic catalysts which must be addressed if MOFs are to be widely used.

Composites involving stable but catalytically inactive MOFs with encapsulated species are now being investigated for their catalytic activities. In 2015, Zhou and co-workers were able to encapsulate 3 different enzymes inside the 5.5 nm diameter pores of a stable MOF known as PCN-333(Al). They were able to load the MOF with large amounts of enzymes which they attributed to a strong interaction between the MOF and the enzymes. They then compared the catalytic activities to those of the same free enzymes and also those encapsulated in mesoporous silica and found that the enzymes maintained much greater activity in the MOF during recycling experiments. The researchers point to the fact that each cavity in the MOF holds only one enzyme and this prevents enzyme agglomeration as the reason for the enhanced activity observed.[246] In 2018, Farha et al synthesised a Zr_6-based MOF constructed from tetratopic pyrene-based ligands in a solution of Pt nanoparticles leading to their encapsulation in the framework. It was then successfully used for alkene hydrogenation catalysis. The MOF-nanoparticle composite prohibited the agglomeration of the nanoparticles during catalysis which is normally observed, inhibiting the reduction in catalytic activity normally observed.[108]

1.6.6.1 Electrical conductivity of MOFs

The use of MOFs in electrocatalysis has only commenced. Progress has been hampered by the low charge carrier mobilities within MOFs which are composed of non-conjugated, redox inactive ligands which are chelating to metal ions (with conductivities in the range of $<10^{-10}$ S/cm).[247] These systems offer a low density of charge carriers and no low-energy charge transport pathways. To overcome the electronically insulating nature of MOFs, various resolutions have been proposed. Electrocatalytic setups generally aim to minimise the thickness of electrochemically deposited MOFs on the electrode surface to decrease the electron transport distance. The development of intrinsically more conductive MOFs that enable electrical conductivity through highly conjugated frameworks is subject of various investigations and different synthetic approaches have been pursued.[248]

The first 'conductive' MOF, $Cu[Cu(pdt)_2]$ (pdt = 2,3-pyrazinedithiol) was published in 2009 by Takishi *et al.* and revealed a measured conductivity of 6×10^{-4} S/cm at 300 K (**Figure 1.6.7**, **a)**).[70] There has been considerable improvements since then. The most obvious approach to influence electrical conductivity in MOFs involves the incorporation of organic ligands that give rise to high charge carrier transport. Thus organic moieties that are used for organic conductors, semiconductors or related devices are introduced.

MOFs containing organic moieties with fully π-conjugated ligand systems including, double and triple bonded systems, have been shown to have increased conductivity versus structurally similar materials, composed of non-conjugated ligand moieties(**Figure 1.6.7**, **d)**).[248,249–258]

Further, it has been shown using structurally identical MOFs that those connected through metal-sulphur bonds have greater conductivity than comparable materials that are stabilised by metal-oxygen bonds.[259,260] Guest molecules can be introduced into frameworks to bridge between SBUs and create alternative pathways for charges to flow increasing the conductivity of the frameworks. This approach has been used to modify the conductivity of HKUST-1 MOF. The conductivity of this $\{Cu_2\}$-based MOF increased from 10^{-8} to 0.07 S/cm upon introduction of bridging tetracyanoquinodimethane (TCNQ) molecules (**Figure 1.6.7**, **b)**).[261] Different metal coordination environments, as well as the nature of the metal ions in SBUs, distinctly influence the charge mobility of electrons in the MOF.[260,262]

While inter-net π-π interactions in MOFs are known to increase the stability of frameworks, it has been shown that charge carriers can also pass through spaces between closely located interacting aromatic systems whereby the degree of orbital overlap influences the electrical conductivity of the material (**Figure 1.6.7**, **c)**).[263–266]

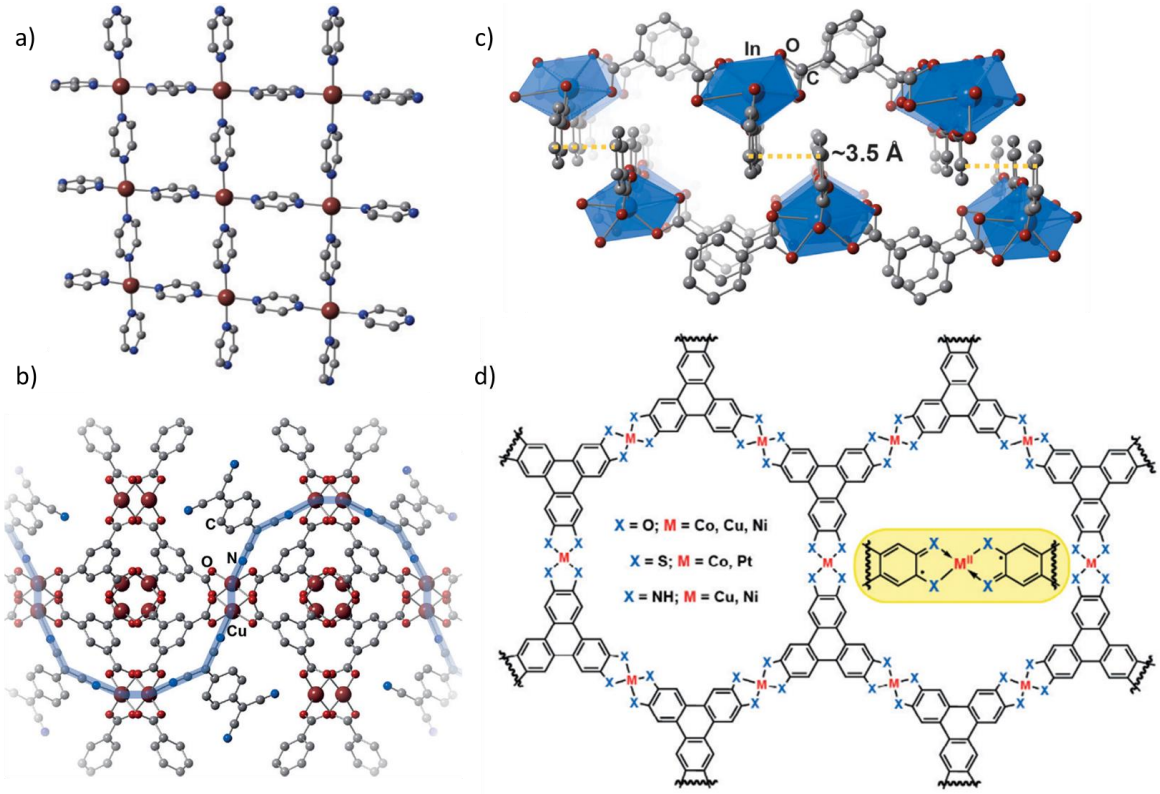

Figure 1.6.7: A series of strategies to increase the conductivity of MOFs. **a)** Structure of the first conductive MOF published by Takishi et al. in 2009 containing 2,3-pyrazinedithiol ligands. **b)** Structure of HKUST-1 containing bridging conductive TCNQ molecules, **c)** Ln(III)/isopthalate MOF that shows a measurable increase in conductivity over similar MOFs that lack π-π interactions, **d)** Structure of hexagonal 2D MOFs based on triphenylene-derived ligands. The inset shows the oxidized radical anion form of the ligands, that are expected to be found in such neutral frameworks that can contain various M(II) ions. Images reproduced from reference 267.

1.6.6.2 Water splitting

With fossil fuel reserves shrinking and the impact of their unrestricted use leading to significant changes to the earth's climate, it has become clear that alternative sources of energy are needed. With regard to transportation, clean alternatives to replace petrol and diesel are essential. The two main replacements currently being proposed are electric (battery) and liquid hydrogen powered vehicles.

The sustainability of both options depends on the way electricity and energy sources are generated. Water splitting by electrolysis for the production of molecular hydrogen is regarded as a clean method of production. Unfortunately, commercial electrolysis of water currently only accounts for around 3-4% of total hydrogen production globally. The remainder is produced from fossil-fuels, mainly through steam reforming from hydrocarbons.[268]

Renewable energy sources as well as nuclear power could be used to produce the energy needed to drive electrolysis of water for the production of H_2 fuel. To encourage the widespread application of this electrolysis for H_2 fuel production, associated investment and operational costs must be reduced. To achieve this, the development of relatively inexpensive, stable and active catalysts to improve the energy efficiency of the electrolysis process are required.

The overall process of water splitting requires that electron transfer events are coupled to catalytic units at the anode that are able to mediate the four electron four proton coupled splitting of H_2O (oxidation) and that the protons and electrons are then recombined forming H_2 at using a separate catalyst at the cathode (reduction) (**Figure 1.6.8**). The water oxidation step is particularly challenging due to its high energy demand (ΔG = 4.92 eV) and it is widely accepted as the bottleneck in water electrolysis.[269,270]

$$4H^+ + 4e^- \longrightarrow 2H_2 \qquad E^0 = 0.00 \text{ eV}$$

$$2H_2O \longrightarrow O_2 + 4H^+ + 4e^- \qquad E^0 = -1.23 \text{ eV}$$

Figure 1.6.8: Reduction and oxidation half-equations for water electrolysis.

Solar energy is an attractive power source but in order to utilise it to a satisfactory potential, effective means to harness and store solar energy must be developed. Using

solar energy to split water into H_2 and O_2, which can be recombined at later stages (releasing the chemical energy), provides a practical way to achieve this.

In a photochemical system, a photosensitiser (PS) is used to absorb light upon excitation and oxidation. It receives an electron from the water oxidation catalyst (WOC) which facilitates the oxidation of bound water molecules forming O_2. The resulting protons then diffuse through the solution to the hydrogen reduction catalyst (HRC) were they are reduced to form H_2 gas (**Figure 1.6.9**).

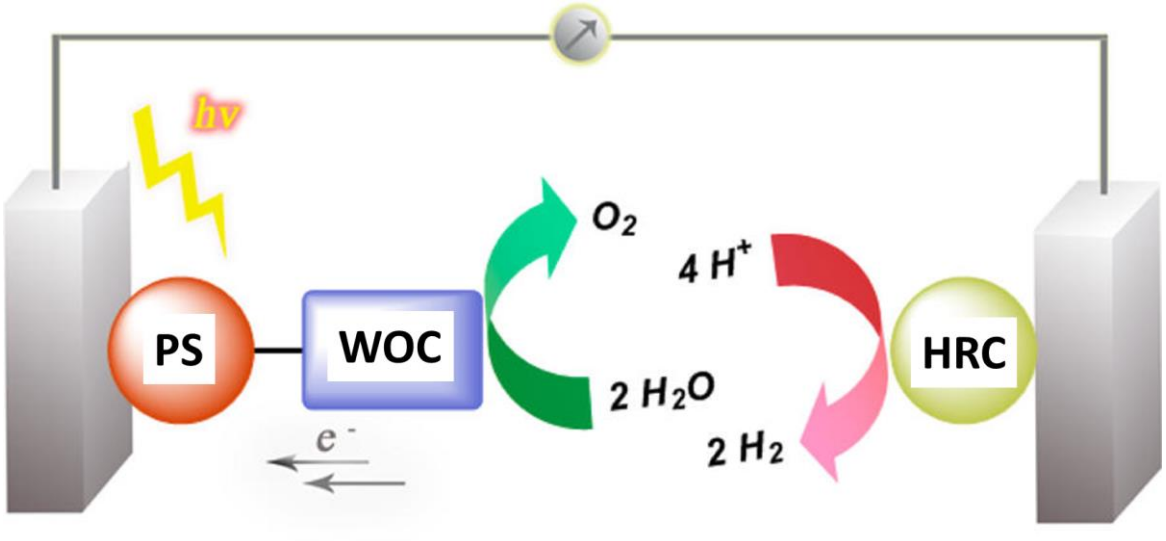

Figure 1.6.9: Schematic representation of a molecular assembly for catalytic H_2O splitting, consisting of a photosensitiser (PS), a water oxidation catalyst (WOC) and a hydrogen reduction catalyst (HRC), which facilitates the production of H_2 gas. Reproduced from reference 271.

Binding sites on both the WOC and HRC are essential for activity, allowing them to interact with the substrates of the solution. The sites on molecular catalysts may contain weakly bound solvent molecules or sites with labile organic ligands attached. Integration of the individual components in a photocatalytic system is essential to ensure that the overall catalytic process proceeds efficiently. Thus, a PS with satisfactory redox potential must absorb light of a sufficient energy to cause the WOC to be oxidised. Precious metal-based catalysts, such as Pt-based catalysts, are currently still considered to be the best water oxidation and hydrogen reduction catalysts, however, their widespread use is hampered by their high cost and low abundance.[272,273] Research to develop low-cost, earth abundant replacement catalysts is ongoing.

1.6.6.3 Hydrogen evolution reaction (HER) catalysis

MOFs as well as their composites have shown promise to be used in hydrogen evolution catalysis.[104,109-118] Generally, most hydrogen evolution reaction (HER) catalysis experiments using MOFs are performed in acidic solutions due to lower energy requirements and improved catalytic performances.

In 2015, two cobalt-based MOFs, MOS 1 and MOS 2, constructed from conjugated benzenehexathiol and triphenylene-2,3,6,7,10,11-hexathiolate ligands were shown to have significant HER catalytic activity under a wide range of different pH conditions. MOS 1 the more active MOF of the two revealed onset potential of 280 mV vs. SHE and a Tafel slope of 149 mV/dec at pH 1.3.[256] The observed activity was partly attributed to the electrical conductivity that resulted from the thiol-based ligand system. More recently a 2D cobalt(II)-based MOF containing a pentanuclear $\{Co_5\}$ SBU was shown to be catalytically active.[274] MOF composites were prepared using graphene. The best composite gave rise to an onset overpotential (the extra potential needed above the thermodynamic redox potential to catalyse the reaction) of 125 mV and a Tafel slope of 91 mV/dec in 0.5 M H_2SO_4. Remarkably, after 1000 catalytic CV cycles the catalytic activity was unchanged.[274]

Polyoxometalates (POM)s represent a class of materials that can readily undergo multi-electron reduction and oxidation processes which makes them excellent HRC candidates.[283] They can also display excellent HER activity when incorporated into MOFs most likely due to the assembly of active POM species to form MOFs with high surface areas.

In 2011, Keggin type polyoxometalate-based metal-organic frameworks (POMOFs) were shown to be robust HER catalysts in acidic conditions.[284] In 2015, a POMOF referred to as NENU-500 (Northeast Normal University) was shown to be highly active revealing an onset overpotential of 180 mV in 0.5 M H_2SO_4 and maintaining its electrocatalytic activity beyond 2000 cycles.[285]

MOFs can also be used for hydrogen reduction catalysis as light harvesting matrixes in conjunction with other catalysts that are encapsulated within the pores. In 2015, it was shown by Lin *et al.* that a catalytically active Wells-Dawson type POM can be encapsulated in the pores of a light harvesting MOF, facilitating its use as a photochemical WRC. Using visible light and methanol as the sacrificial electron donor a turn over number (TON) of 79

after 14 hours was achieved. When triethanolamine was used as the sacrificial electron donor instead, the TON increased to 307 after 14 hours (**Figure 1.6.10**).[276]

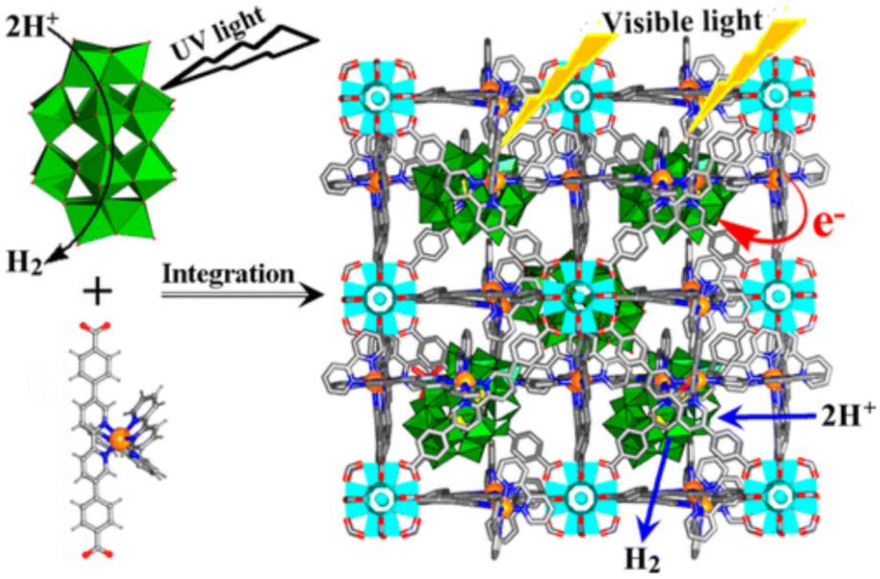

Figure 1.6.10: Light harvesting Zr-based MOF and encapsulated Wells-Dawson POM catalysts for photochemical hydrogen evolution catalysis. Reproduced from reference 276.

1.6.6.4 Oxygen evolution reaction catalysis

Catalysing the oxygen evolution reaction is key to all water splitting technologies for energy conversion. The previously discussed strategies for HER efficiency will ultimately be limited by the electrical potential determined by its counterpart response, the oxygen evolution reaction (OER) which occurs at the anode is highly endergonic and is considered to be one of the bottle neck processes in artificial water splitting.[286] The high cost of advanced precious metal based catalysts currently obstructs the widespread use and commercialisation of electrochemical OER. Another difficulty arises from the strongly oxidising intermediates and conditions which often lead to the decomposition of the catalyst during the oxidation of H_2O. The OER proceeds *via* removal of four electrons from two water molecules to generate one molecule of dioxygen. The process is slow and usually requires a large overpotential to achieve a reasonable reaction rate and current density.[287] Many oxidation studies use high pH conditions as these are thermodynamically favourable for water oxidation. However, highly alkaline conditions can lead to rapid degradation of the catalyst as well as photosensitisers that may be used in photocatalytic systems.

Many WOCs containing earth abundant transition metals such as cobalt, iron, copper and manganese have been reported.[127–138] The earliest work using MOFs as WOCs was published in 2011 and led by Lin *et al.*. They modified the well-known UiO-67 MOF[298,299] by replacing some of the linker molecules with iridium based water oxidation catalysts. The resulting frameworks show catalytic activity giving rise to a turn over frequency (TOF) of 4.8 h^{-1} vs. 37 h^{-1} for the free homogeneous catalyst at pH 1.

However this performance is lower than that of the corresponding homogeneously dissolved Ir(III) complexes. The authors justified this by proposing that the catalytic water oxidation is only taking place on the surface of the MOF as the Ce^{4+} ions of the oxidant are too large to enter the pores of the MOFs.[300] Since then a number of improved MOF-based catalyst have been reported. In 2016, a Co(II)-based azolate framework, MAF-X27-OH was prepared from a precursor derivative MAF-X27-Cl *via* post-synthetic ion exchange. After the ion exchange, the electrochemical water oxidation activity of the new material drastically increased. MAF-X27-Cl reached an overpotential of 387 mV at 10 mA/cm^2 at pH 14. The potential decreased to 292 mV at 10 mA/cm^2 for MAF-X27-OH under the same conditions.[301] It was proposed that the ion exchange alters the reaction mechanism to

proceed intramolecularly *via* an intraframework coupling pathway as shown in **Figure 1.6.11**.

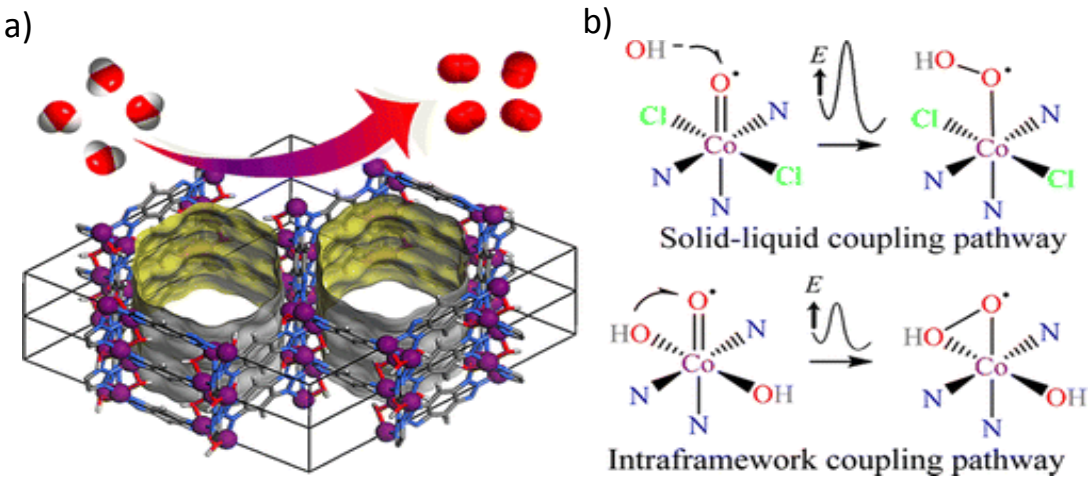

Figure 1.6.11: a) Three-dimensional coordination network and pore surface structures of MAF-X27-OH. **b)** Solid–liquid coupling pathway for MAF-X27-Cl (top) and the intraframework coupling pathway for MAF-X27-OH (bottom). Reproduced from reference 301.

Cobalt acetate is known to be a highly active WOC that is unfortunately also unstable in water under oxidising conditions. In 2017, a MOF composed of acetate-derived $\{Co_2\}$ paddle-wheel SBUs and $\{Fe_3\}$ SBUs was synthesised in a stepwise process from a MOF composed of mononuclear $\{Fe\}$ and trinuclear $\{Fe_3\}$ SBUs. When tested for OER activity, the original water stable $\{Fe/Fe_3\}$-based framework revealed an overpotential of 460 at 1 mA/cm^2 and a Tafel slope of 137 mV/dec at pH 13. The mixed-metal $\{Co_2\text{-}Fe_3\}$-based MOF was also found to be water stable and gave rise to an improved overpotential of 283 mV at 10 mA/cm^2 and a Tafel slope of only 43 mV/dec at pH 13.[302] It was also found that exchange of all Fe(III) centres by Co(II) ions to form a $\{Co_2\text{-}Co_3\}$ framework results in a loss of stability in water. A separate study reported in the same year, found that a MOF containing a cubane type $\{Co_4\}$ SBU was able to facilitate overpotentials of 408 mV and 500 mV to achieve 10 mA/cm^2 vs. RHE at pH = 14 and 13 respectively.[303]

In 2016, a MOF containing trinuclear, triangular {Fe_3} SBUs, known as MIL-101(Fe) was shown to have reasonable photocatalytic water oxidation properties, achieving a maximum TON of 27.3 after 10 minutes and a TOF of 0.1 s^{-1} at pH 10. Other related iron-based MOFs; MIL-88(Fe) and MIL-53(Fe) and the amine functionalised derivatives were also tested under the same conditions but were found to have lower activities than MIL-101(Fe).[304]

In 2017, Ni(II) coordination in a Al(III) 2-aminoterephthalate MOF was shown to catalyse both, the H_2 and O_2 evolution reactions under photocatalytic conditions producing 16.5 and 155 µmol/h of the gases, respectively.[305]

In 2018 a cobalt(II)/imidazolate-based MOF, referred to as ZIF-L, was grown on flexible conductive carbon cloth by a liquid deposited method and then used for water oxidation. An overpotential of 330 mV at 20 mA/cm^2 (pH = 14) was achieved. The system revealed good stability and a relatively low Tafel slope of 106.6 mV/dec was recorded.[306]

Several other MOFs have been synthesised and used successfully for water oxidation catalysis in recent years.[307–310]

As for the HER, it is possible to use encapsulated guest molecules in the pores of MOFs to catalyse the OER. In 2018, two cobalt based POMs, $K_7[Co^{II}Co^{III}W_{11}O_{39}(H_2O)]$ and $Na_{10}[Co_4(PW_9O_{34})_2(H_2O)_2]$ were encapsulated in the MIL-100(Fe) MOF which is composed of trinuclear {Fe_3} SBUs and trimesate ligands. The system was used for photochemical water oxidation (**Figure 1.6.12**).[311] MIL-100, itself, was found to be inactive for water oxidation catalysis under photocatalytic conditions. However, the POM/MOF system revealed increased activity in comparison to the activity the individual POMs. Noteworthy is the improvement of the TOFs upon POM incorporation into the MOF, increasing from 0.48 to 0.53 s^{-1} for $K_7[Co^{II}Co^{III}W_{11}O_{39}(H_2O)]$ POM and from 4 x 10^{-3} s^{-1} to 9.2 x 10^{-3} s^{-1} for $Na_{10}[Co_4(PW_9O_{34})_2(H_2O)_2]$.

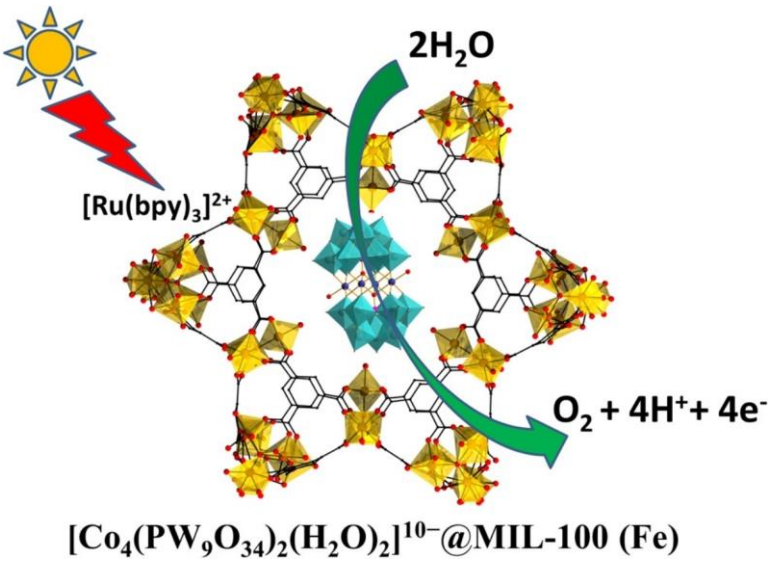

Figure 1.6.12: Representation of the photocatalytic water oxidation upon POM incorporation in MIL-100(Fe). Reproduced from reference 311.

MOF-derived materials, instead of MOFs, have also been investigated for OER catalysis. Some of these systems show exceptionally high activity and arguably some, appear commercially more viable than any MOF catalysts.[312–314]

In 2014 a Co(II)/naphthalenedicarboxylate based MOF was grown directly on Cu foil using solvothermal synthesis methods forming a pillar-like morphology. The material was then carbonised by heating it in an N_2 atmosphere forming porous carbon nanowire assemblies containing Co_3O_4 particles (**Figure 1.6.13**).[312] This composite material was then used for water oxidation studies at pH 13 and showed a higher activity than IrO_2, Co_3O_4 and the precursor MOF. Tafel slopes of 142 mV/dec, and 123 mV/dec were recorded for the precursor MOF and Co_3O_4, respectively. In contrast the MOF-derived carbon/Co_3O_4 material revealed a significantly lower Tafel slope of 70 mV/dec.

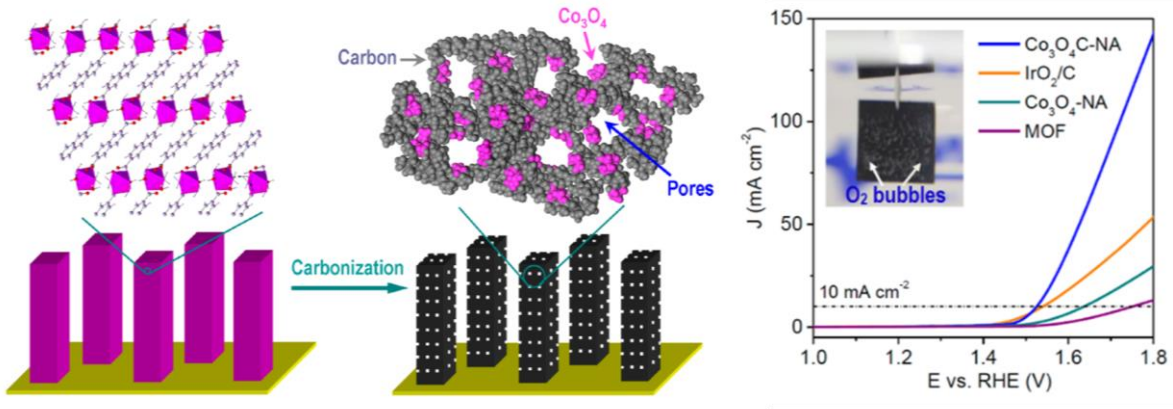

Figure 1.6.13: *Left*: Fabrication of hybrid porous carbon nanowires containing Co_3O_4 materials; *Right*: Linear sweep voltammogram showing the relative water oxidation activity of these nanowires compared to IrO_2, Co_3O_4 and the reagent MOF. Adapted from reference 312.

This summary of results demonstrates that more innovations are needed to improve the armamentarium of active compounds if water splitting either by electrolysis or by photochemical means is to become a widely established practice. Despite many advances in this field, the general performance of most MOF based catalysts reported remains still far from satisfactory and the application of MOFs as electro- or photo-catalysts is still in its emerging stages.[315]

1.7 Aims and Objectives

Following on from the materials discussed in the previous sections of this chapter the fundamental aims of this project were to synthesise tri-functional ligands for the synthesis of novel, highly augmented MOPs and MOFs. In particular the aim was directed towards stable materials containing polynuclear SBUs that could be applied to oxidation catalysis. The Co and Mn based materials were envisaged to be used in electro- and photo-catalytic water oxidation. From a structural perspective we were keen to investigate effects that result from the rotational freedom of the acetylene moieties and the structural flexibility of the extended ligands. The synthetic methods were directed towards crystalline materials allowing detailed structural analysis.

For these purposes the following ligands were used;

H_3L1 = 3,3',3''-(benzene-1,3,5-triyltris(ethyne-2,1-diyl))tribenzoic acid

H_3L2 = 4,4',4''-(benzene-1,3,5-triyltris(ethyne-2,1-diyl))tribenzoic acid

H_3L3 = 5,5'-((5'-(4-((4-carboxyphenyl)ethynyl)phenyl)-[1,1':3',1''-terphenyl]-4,4''-diyl)bis-(ethyne-2,1-diyl))benzoic acid

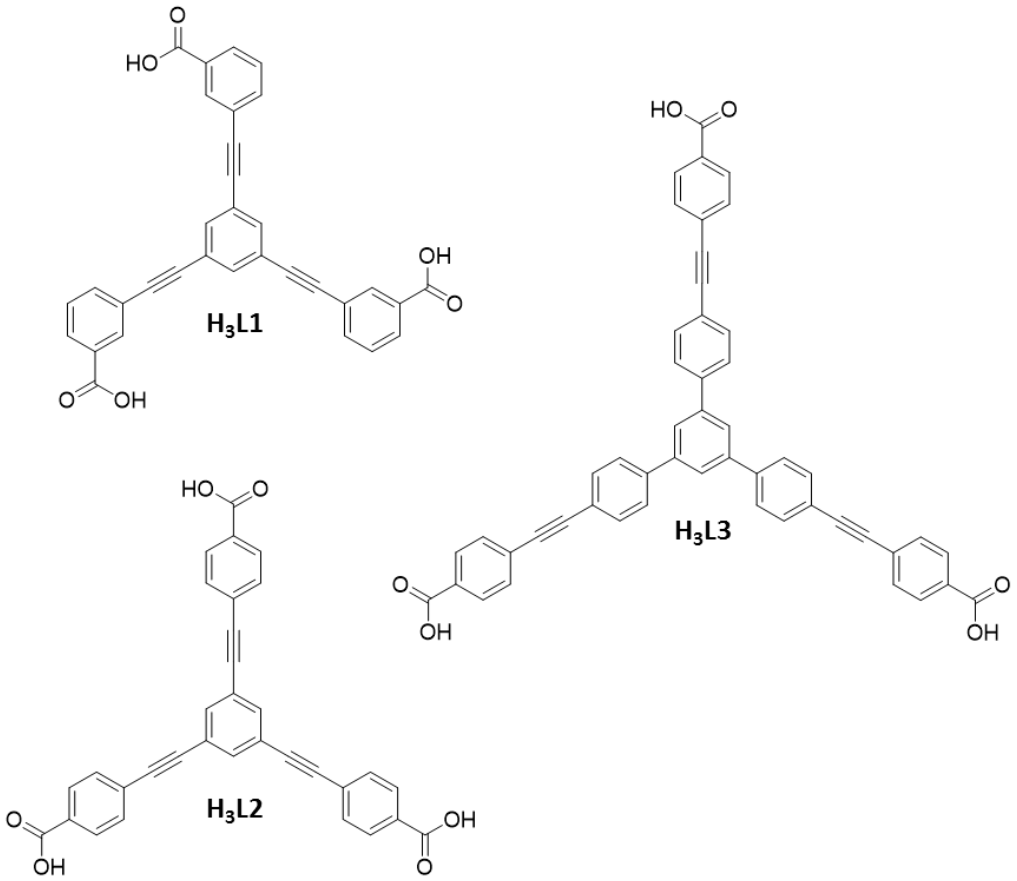

The results will include ligand synthesis, structural and physicochemical characterisations of the materials as well as catalytic water oxidation studies.

To achieve these aims, we set out to pursue the following objectives:

- To develop synthetic strategies to produce novel advanced coordination materials incorporating structurally related tri-functional carboxylate ligands in combination with transition metal ions.
- To resolve the structure of each of the resulting materials using appropriate analytical techniques.
- To investigate the physico-chemical attributes of each material, including for guest binding, guest encapsulation, gas sorption and catalytic OER activity.

1.8 References

1 M.S.L.J., *The Economist explains: The 2°C limit on global warming*, 2018.

2 J. Huang, X. Zhang, Q. Zhang, Y. Lin, M. Hao, Y. Luo, Z. Zhao, Y. Yao, X. Chen, L. Wang, S. Nie, Y. Yin, Y. Xu and J. Zhang, *Nat. Clim. Chang.*, 2017, **7**, 875–879.

3 C. C. Hay, E. Morrow, R. E. Kopp and J. X. Mitrovica, *Nature*, 2015, **517**, 481–484.

4 G. Archer, T. Earl, E. Bannon, J. Poliscanova, N. Muzi and S. Alexandridou, *CO2 EMISSIONS FROM CARS: the facts*, European Federation for Transport and Environment AISBL, Brussels, 2018.

5 Carbon Dioxide Consentration at Mauna Loa Observatory, https://scripps.ucsd.edu/programs/keelingcurve/, (accessed 18 April 2019).

6 *IUPAC Compendium of Chemical Terminology Gold Book*, IUPAC, 2.3.3 ed., 2014.

7 M. V. Orna, A. W. Kozlowski, A. Baskinger and T. Adams, in *Coordination Chemistry*, 1994, 165–176.

8 A. F. Cronstedt, *Kongl Vetenskaps Acad. Handl. Stock.*, 1756, **17**, 120.

9 R. Virta, *Geotimes: Mineral Resource of the Month*, 2008.

10 R. Virta, *Earth Magazine, Mineral Resource of the Month: Zeolites*, 2014.

11 M. Pérez-Page, J. Makel, K. Guan, S. Zhang, J. Tringe, R. H. R. Castro and P. Stroeve, *Ceram. Int.*, 2016, **42**, 15423–15431.

12 N. Thanabodeekij, S. Sadthayanon, E. Gulari and S. Wongkasemjit, *Mater. Chem. Phys.*, 2006, **98**, 131–137.

13 V. Chaudhary and S. Sharma, *J. Porous Mater.*, 2017, **24**, 741–749.

14 Y. Zheng, X. Li and P. K. Dutta, *Sensors*, 2012, **12**, 5170–5194.

15 S. R. Batten, N. R. Champness, X.-M. Chen, J. Garcia-Martinez, S. Kitagawa, L. Öhrström, M. O'Keeffe, M. Paik Suh and J. Reedijk, *Pure Appl. Chem.*, 2013, **85**, 1715–1724.

16 B. F. Hoskins and R. Robson, *J. Am. Chem. Soc.*, 1989, **111**, 5962–5964.

17 G. R. Desiraju, *Crystal Engineering: The Design of Organic Solids*, Elsevier, Amsterdam, 1989.

18 L. R. MacGillivray, S. Subramanian and M. J. Zaworotko, *J. Chem. Soc. Chem. Commun.*, 1994, 1325.

19 O. M. Yaghi and H. Li, *J. Am. Chem. Soc.*, 1995, **117**, 10401–10402.

20 G. M. J. Schmidt, *Pure Appl. Chem.*, 1971, **27**, 647–678.

21 I. Huskić, I. V. Pekov, S. V. Krivovichev and T. Friščić, *Sci. Adv.*, 2016, **2**, e1600621.

22 O. M. Yaghi, M. O'Keeffe, N. W. Ockwig, H. K. Chae, M. Eddaoudi and J. Kim, *Nature*, 2003, **423**, 705–714.

23 A. Schoedel, M. Li, D. Li, M. O'Keeffe and O. M. Yaghi, *Chem. Rev.*, 2016, **116**, 12466–12535.

24 N. L. Rosi, *Science*, 2003, **300**, 1127–1129.

25 K. M. Fromm, *Coord. Chem. Rev.*, 2008, **252**, 856–885.

26 M. Servati Gargari, V. Stilinović, A. Bauzá, A. Frontera, P. McArdle, D. Van Derveer, S. W. Ng and G. Mahmoudi, *Chem. - A Eur. J.*, 2015, **21**, 17951–17958.

27 L. K. Macreadie, E. J. Mensforth, R. Babarao, K. Konstas, S. G. Telfer, C. M. Doherty, J. Tsanaktsidis, S. R. Batten and M. R. Hill, *J. Am. Chem. Soc.*, 2019, **141**, 3828–3832.

28 X. Wei, S. Wang, Z. Hua, L. Chen and J. Shi, *ACS Appl. Mater. Interfaces*, 2018, **10**, 25422–25428.

29 Q. Yao, A. Bermejo Gómez, J. Su, V. Pascanu, Y. Yun, H. Zheng, H. Chen, L. Liu, H. N. Abdelhamid, B. Martín-Matute and X. Zou, *Chem. Mater.*, 2015, **27**, 5332–5339.

30 Z.-H. Yan, M.-H. Du, J. Liu, S. Jin, C. Wang, G.-L. Zhuang, X.-J. Kong, L.-S. Long and L.-S. Zheng, *Nat. Commun.*, 2018, **9**, 3353.

31 G. Tobin, S. Comby, N. Zhu, R. Clérac, T. Gunnlaugsson and W. Schmitt, *Chem. Commun.*, 2015, **51**, 13313–13316.

32 X. Guo, G. Zhu, Z. Li, F. Sun, Z. Yang and S. Qiu, *Chem. Commun.*, 2006, **1**, 3172–3174.

33 W. Yang, Z.-Q. Bai, W.-Q. Shi, L.-Y. Yuan, T. Tian, Z.-F. Chai, H. Wang and Z.-M. Sun, *Chem. Commun.*, 2013, **49**, 10415.

34 J. Andreo, E. Priola, G. Alberto, P. Benzi, D. Marabello, D. M. Proserpio, C. Lamberti and E. Diana, *J. Am. Chem. Soc.*, 2018, **140**, 14144–14149.

35 E. A. Dolgopolova, A. M. Rice and N. B. Shustova, *Chem. Commun.*, 2018, **54**, 6472–6483.

36 Search of journal publications containing the term 'MOF', http://wcs.webofknowledge.com, (accessed 29 January 2019).

37 J. S. Wright, A. J. Metherell, W. M. Cullen, J. R. Piper, R. Dawson and M. D. Ward, *Chem. Commun.*, 2017, **53**, 4398–4401.

38 S. Zarra, D. M. Wood, D. a Roberts and J. R. Nitschke, *Chem. Soc. Rev.*, 2014, **44**, 419–432.

39 I. A. Bhat, D. Samanta and P. S. Mukherjee, *J. Am. Chem. Soc.*, 2015, **137**, 9497–9502.

40 M. Fujita, D. Oguro, M. Miyazawa, H. Oka, K. Yamaguchi and K. Ogura, *Nature*, 1995, **378**, 469–471.

41 K. Byrne, M. Zubair, N. Zhu, X. P. Zhou, D. S. Fox, H. Zhang, B. Twamley, M. J. Lennox, T. Düren and W. Schmitt, *Nat. Commun.*, 2017, **8**, 15268.

42 Y.-T. Lai, E. Reading, G. L. Hura, K.-L. Tsai, A. Laganowsky, F. J. Asturias, J. A. Tainer, C. V. Robinson and T. O. Yeates, *Nat. Chem.*, 2014, **6**, 1065–1071.

43 M. Han, R. Michel, B. He, Y.-S. Chen, D. Stalke, M. John and G. H. Clever, *Angew. Chem. Int. Ed.*, 2013, **52**, 1319–1323.

44 A. Mallick, B. Garai, D. D. Díaz and R. Banerjee, *Angew. Chem. Int. Ed.*, 2013, **52**, 13755–13759.

45 Q.-F. Sun, T. Murase, S. Sato and M. Fujita, *Angew. Chem. Int. Ed.*, 2011, **50**, 10318–10321.

46 J. Wang, C. He, P. Wu, J. Wang and C. Duan, *J. Am. Chem. Soc.*, 2011, **133**, 12402–12405.

47 Q.-F. Sun, J. Iwasa, D. Ogawa, Y. Ishido, S. Sato, T. Ozeki, Y. Y. Sei, K. Yamaguchi and M. Fujita, *Science*, 2010, **328**, 1144–1147.

48 T. Kikuchi, S. Sato and M. Fujita, *J. Am. Chem. Soc.*, 2010, **132**, 15930–15932.

49 J.-R. Li and H.-C. Zhou, *Nat. Chem.*, 2010, **2**, 893–898.

50 M. Yoshizawa, J. K. Klosterman and M. Fujita, *Angew. Chem. Int. Ed.*, 2009, **48**, 3418–3438.

51 Perry, V. C. Kravtsov, G. J. McManus and M. J. Zaworotko, *J. Am. Chem. Soc.*, 2007, **129**, 10076–10077.

52 A. Carné-Sánchez, J. Albalad, T. Grancha, I. Imaz, J. Juanhuix, P. Larpent, S. Furukawa and D. Maspoch, *J. Am. Chem. Soc.*, 2019, **141**, 4094–4102.

53 H. Furukawa, J. Kim, K. E. Plass and O. M. Yaghi, *J. Am. Chem. Soc.*, 2006, **128**, 8398–8399.

54 M. Tominaga, K. Suzuki, T. Murase and M. Fujita, *J. Am. Chem. Soc.*, 2005, **127**, 11950–11951.

55 J. Bai, A. V. Virovets and M. Scheer, *Science*, 2003, **300**, 781–783.

56 N. Takeda, K. Umemoto, K. Yamaguchi and M. Fujita, *Nature*, 1999, **398**, 794–796.

57 B. Olenyuk, J. A. Whiteford, A. Fechtenkötter and P. J. Stang, *Nature*, 1999, **398**, 796–799.

58 K. Umemoto, K. Yamaguchi and M. Fujita, *J. Am. Chem. Soc.*, 2000, **122**, 7150–7151.

59 D. Fujita, Y. Ueda, S. Sato, H. Yokoyama, N. Mizuno, T. Kumasaka and M. Fujita, *Chem*, 2016, **1**, 91–101.

60 C. A. Rowland, G. R. Lorzing, E. J. Gosselin, B. A. Trump, G. P. A. Yap, C. M. Brown and E. D. Bloch, *J. Am. Chem. Soc.*, 2018, **140**, 11153–11157.

61 C. C. Givelet, P. I. Dron, J. Wen, T. F. Magnera, M. Zamadar, K. Čépe, H. Fujiwara, Y. Shi, M. R. Tuchband, N. Clark, R. Zbořil and J. Michl, *J. Am. Chem. Soc.*, 2016, **138**, 6676–6687.

62 D. Fujita, Y. Ueda, S. Sato, N. Mizuno, T. Kumasaka and M. Fujita, *Nature*, 2016, **540**, 563–566.

63 Q.-Q. Wang, S. Gonell, S. H. A. M. Leenders, M. Dürr, I. Ivanović-Burmazović and J. N. H. Reek, *Nat. Chem.*, 2016, **8**, 225–230.

64 W. Cullen, M. C. Misuraca, C. A. Hunter, N. H. Williams and M. D. Ward, *Nat. Chem.*, 2016, **8**, 231–236.

65 X. Yan, T. R. Cook, P. Wang, F. Huang and P. J. Stang, *Nat. Chem.*, 2015, **7**, 342–348.

66 C. García-Simón, M. Garcia-Borràs, L. Gómez, T. Parella, S. Osuna, J. Juanhuix, I. Imaz, D. Maspoch, M. Costas and X. Ribas, *Nat. Commun.*, 2014, **5**, 5557.

67 D. J. Tranchemontagne, Z. Ni, M. O'Keeffe and O. M. Yaghi, *Angew. Chem. Int. Ed.*, 2008, **47**, 5136–5147.

68 A. L. Lavoisier, *Elements of Chemistry, In a New Systematic Order, Containing all the Modern Discoveries*, 1787.

69 I. M. Hauptvogel, V. Bon, R. Grünker, I. a. Baburin, I. Senkovska, U. Mueller and S. Kaskel, *Dalt. Trans.*, 2012, **41**, 4172.

70 S. Takaishi, M. Hosoda, T. Kajiwara, H. Miyasaka, M. Yamashita, Y. Nakanishi, Y. Kitagawa, K. Yamaguchi, A. Kobayashi and H. Kitagawa, *Inorg. Chem.*, 2009, **48**, 9048–9050.

71 J. J. Perry IV, J. A. Perman and M. J. Zaworotko, *Chem. Soc. Rev.*, 2009, **38**, 1400.

72 S. Seth and A. J. Matzger, *Cryst. Growth Des.*, 2017, **17**, 4043–4048.

73 T. Kitao, Y. Tokunaga, D. Umeyama, C. R. Kim, T. Uemura and S. Kitagawa, *Inorganica Chim. Acta*, 2015, **424**, 221–225.

74 C. S. Hawes, K. Byrne, W. Schmitt and T. Gunnlaugsson, *Inorg. Chem.*, 2016, **55**, 11570–11582.

75 K. Ohara, M. Kawano, Y. Inokuma and M. Fujita, *J. Am. Chem. Soc.*, 2010, **132**, 30–31.

76 J. Martí-Rujas, N. Islam, D. Hashizume, F. Izumi, M. Fujita and M. Kawano, *J. Am. Chem. Soc.*, 2011, **133**, 5853–5860.

77 M. Zhang, Y. P. Chen and H. C. Zhou, *CrystEngComm*, 2013, **15**, 9544–9552.

78 J. K. Schnobrich, K. Koh, K. N. Sura and A. J. Matzger, *Langmuir*, 2010, **26**, 5808–5814.

79 S. R. Caskey and A. J. Matzger, *Inorg. Chem.*, 2008, **47**, 7942–7944.

80 S. Laokroekkiat, M. Hara, S. Nagano and Y. Nagao, *Langmuir*, 2016, **32**, 6648–6655.

81 D. Kühne, F. Klappenberger, R. Decker, U. Schlickum, H. Brune, S. Klyatskaya, M. Ruben and J. V. Barth, *J. Am. Chem. Soc.*, 2009, **131**, 3881–3883.

82 T. Lin, G. Kuang, X. S. Shang, P. N. Liu and N. Lin, *Chem. Commun.*, 2014, **50**, 15327–15329.

83 M. J. Bucknum and E. A. Castro, *MATCH Commun. Math. Comput. Chem.*, 2005, **54**, 89–119.

84 S. Kaskel, *The Chemistry of Metal–Organic Frameworks*, Wiley-VCH, 1st edn., 2016.

85 C. Baerlocher, L. B. McCusker and D. H. Olson, *Atlas of Zeolite Framework Types*, Elsevier B.V., 6th edn., 2007.

86 M. O'Keeffe, M. A. Peskov, S. J. Ramsden and O. M. Yaghi, *Acc. Chem. Res.*, 2008, **41**, 1782–1789.

87 Reticular Chemistry Structure Resource (RCSR) Database, http://rcsr.anu.edu.au, (accessed 13 April 2019).

88 H. Li, M. Eddaoudi, M. O'Keeffe and O. M. Yaghi, *Nature*, 1999, **402**, 276–279.

89 S. S. Y. Chui, S. M. F. Lo, J. P. H. Charmant, a G. Orpen and I. D. Williams, *Science*, 1999, **283**, 1148–1150.

90 M. Li, D. Li, M. O'Keeffe and O. M. Yaghi, *Chem. Rev.*, 2014, **114**, 1343–1370.

91 M. Eddaoudi, J. Kim, N. Rosi, D. Vodak, J. Wachter, M. O'Keeffe and O. M. Yaghi, *Science*, 2002, **295**, 469–472.

92 H. Furukawa, N. Ko, Y. B. Go, N. Aratani, S. B. Choi, E. Choi, A. O. Yazaydin, R. Q. Snurr, M. O'Keeffe, J. Kim and O. M. Yaghi, *Science*, 2010, **329**, 424–428.

93 K. Harris, D. Fujita and M. Fujita, *Chem. Commun.*, 2013, **49**, 6703.

94 S. H. Feng and G. H. Li, in *Modern Inorganic Synthetic Chemistry*, Eds. R. Xu and Y. Xu, Elsevier, 2017, pp. 73–104.

95 M. Li and M. Dincă, *J. Am. Chem. Soc.*, 2011, **133**, 12926–12929.

96 N. Campagnol, T. R. C. Van Assche, M. Li, L. Stappers, M. Dincă, J. F. M. Denayer, K. Binnemans, D. E. De Vos and J. Fransaer, *J. Mater. Chem. A*, 2016, **4**, 3914–3925.

97 A. Martinez Joaristi, J. Juan-Alcañiz, P. Serra-Crespo, F. Kapteijn and J. Gascon, *Cryst. Growth Des.*, 2012, **12**, 3489–3498.

98 M. Li and M. Dincă, *Chem. Mater.*, 2015, **27**, 3203–3206.

99 N. Campagnol, T. Van Assche, T. Boudewijns, J. Denayer, K. Binnemans, D. De Vos and J. Fransaer, *J. Mater. Chem. A*, 2013, **1**, 5827–5830.

100 J. Klinowski, F. A. Almeida Paz, P. Silva and J. Rocha, *Dalt. Trans.*, 2011, **40**, 321–330.

101 G. H. Albuquerque and G. S. Herman, *Cryst. Growth Des.*, 2017, **17**, 156–162.

102 Z. Ni and R. I. Masel, *J. Am. Chem. Soc.*, 2006, **128**, 12394–12395.

103 A. Pichon and S. L. James, *CrystEngComm*, 2008, **10**, 1839.

104 M. Klimakow, P. Klobes, A. F. Thünemann, K. Rademann and F. Emmerling, *Chem. Mater.*, 2010, **22**, 5216–5221.

105 W.-J. Son, J. Kim, J. Kim and W.-S. Ahn, *Chem. Commun.*, 2008, 6336.

106 M. Bigdeli and A. Morsali, *Ultrason. Sonochem.*, 2015, **27**, 416–422.

107 D. J. Tranchemontagne, J. R. Hunt and O. M. Yaghi, *Tetrahedron*, 2008, **64**, 8553–8557.

108 H. Noh, C.-W. Kung, T. Islamoglu, A. W. Peters, Y. Liao, P. Li, S. J. Garibay, X. Zhang, M. R. DeStefano, J. T. Hupp and O. K. Farha, *Chem. Mater.*, 2018, **30**, 2193–2197.

109 N. Getachew, Y. Chebude, I. Diaz and M. Sanchez-Sanchez, *J. Porous Mater.*, 2014, **21**, 769–773.

110 L. Na, L. Zhang, W. Zhang and R. Hua, *Synth. React. Inorganic, Met. Nano-Metal*

Chem., 2015, **45**, 1463–1466.

111 Y. Bai, Y. Dou, L.-H. Xie, W. Rutledge, J.-R. Li and H.-C. Zhou, *Chem. Soc. Rev.*, 2016, **45**, 2327–2367.

112 N. Stock and S. Biswas, *Chem. Rev.*, 2012, **112**, 933–969.

113 J. Kim, B. Chen, T. M. Reineke, H. Li, M. Eddaoudi, D. B. Moler, M. O'Keeffe and O. M. Yaghi, *J. Am. Chem. Soc.*, 2001, **123**, 8239–8247.

114 R. I. Walton, *Chem. Soc. Rev.*, 2002, **31**, 230–238.

115 D. Saha, R. Zacharia, L. Lafi, D. Cossement and R. Chahine, *Chem. Eng. J.*, 2011, **171**, 517–525.

116 M. Almáši, V. Zeleňák, R. Gyepes, A. Zukal and J. Čejka, *Colloids Surfaces A Physicochem. Eng. Asp.*, 2013, **437**, 101–107.

117 G. Genesio, J. Maynadié, M. Carboni and D. Meyer, *New J. Chem.*, 2018, **42**, 2351–2363.

118 B. F. Sels, L. Alaerts, J. Fransaer, D. E. De Vos, R. Ameloot and L. Stappers, *Chem. Mater.*, 2009, **21**, 2580–2582.

119 H. Zhu, H. Liu, I. Zhitomirsky and S. Zhu, *Mater. Lett.*, 2015, **142**, 19–22.

120 S. D. Worrall, H. Mann, A. Rogers, M. A. Bissett, M. P. Attfield and R. A. W. Dryfe, *Electrochim. Acta*, 2016, **197**, 228–240.

121 T. Mitra, F. Moreau, A. Nevin, C. U. Perotto, A. Summerfield, E. S. Davies, E. A. Gibson, T. L. Easun and M. Schröder, *Chem. Sci.*, 2018, 6572–6579.

122 H. J. Park, Y. E. Cheon and M. P. Suh, *Chem. - A Eur. J.*, 2010, **16**, 11662–11669.

123 M. Kim, J. F. Cahill, Y. Su, K. A. Prather and S. M. Cohen, *Chem. Sci.*, 2012, **3**, 126–130.

124 H. G. T. Nguyen, N. M. Schweitzer, C.-Y. Chang, T. L. Drake, M. C. So, P. C. Stair, O. K. Farha, J. T. Hupp and S. T. Nguyen, *ACS Catal.*, 2014, **4**, 2496–2500.

125 S. J. D. Smith, B. P. Ladewig, A. J. Hill, C. H. Lau and M. R. Hill, *Sci. Rep.*, 2015, **5**, 15–18.

126 J. Seo, C. Bonneau, R. Matsuda, M. Takata and S. Kitagawa, *J. Am. Chem. Soc.*, 2011, **133**, 9005–9013.

127 M.-H. Zeng, S. Wan, M. Kurmoo, J. Yang and Z. Yin, *Coord. Chem. Rev.*, 2017, **378**, 500–512.

128 T. Li, M. T. Kozlowski, E. A. Doud, M. N. Blakely and N. L. Rosi, *J. Am. Chem. Soc.*, 2013, **135**, 11688–11691.

129 A. F. Gross, E. Sherman, S. L. Mahoney and J. J. Vajo, *J. Phys. Chem. A*, 2013, **117**, 3771–3776.

130 R. J. Wakeham, M. Taddei, A. R. Barron, A. Koutsianos and E. Andreoli, *Angew. Chem. Int. Ed.*, 2018, **57**, 11706–11710.

131 S. Jiang, J. T. A. Jones, T. Hasell, C. E. Blythe, D. J. Adams, A. Trewin and A. I. Cooper, *Nat. Commun.*, 2011, **2**, 207.

132 S. Yuan, Y.-P. Chen, J.-S. Qin, W. Lu, L. Zou, Q. Zhang, X. Wang, X. Sun and H.-C. Zhou, *J. Am. Chem. Soc.*, 2016, **138**, 8912–8919.

133 S. Yuan, J.-S. Qin, J. Su, B. Li, J. Li, W. Chen, H. Drake, P. Zhang, D. Yuan, J. Zuo and H.-C. Zhou, *Angew. Chem. Int. Ed.*, 2018, 1–7.

134 K. P. Rao, M. Higuchi, J. Suryachandram and S. Kitagawa, *J. Am. Chem. Soc.*, 2018, **140**, 13786–13792.

135 Y. Han, J.-R. Li, Y. Xie and G. Guo, *Chem. Soc. Rev.*, 2014, **43**, 5952–5981.

136 M. Lalonde, W. Bury, O. Karagiaridi, Z. Brown, J. T. Hupp and O. K. Farha, *J. Mater. Chem. A*, 2013, **1**, 5453–5468.

137 B. Tu, Q. Pang, D. Wu, Y. Song, L. Weng and Q. Li, *J. Am. Chem. Soc.*, 2014, **136**, 14465–14471.

138 C. K. Brozek and M. Dincă, *Chem. Soc. Rev.*, 2014, **43**, 5456–5467.

139 Y. Noori and K. Akhbari, *RSC Adv.*, 2017, **7**, 1782–1808.

140 M. J. Kalmutzki, N. Hanikel and O. M. Yaghi, *Sci. Adv.*, 2018, **4**, eaat9180.

141 D. G. Truhlar, J. T. Hupp, T. C. Wang, O. K. Farha, R. C. Klet and L. E. Fernandez, *Chem. Mater.*, 2016, **28**, 1213–1219.

142 Y.-L. Huang, L. Jiang and T.-B. Lu, *Chempluschem*, 2016, **81**, 780–785.

143 Y. Liu, Z. U. Wang and H.-C. Zhou, *Greenh. Gases Sci. Technol.*, 2012, **2**, 239–259.

144 Y. S. Bae, B. G. Hauser, O. K. Farha, J. T. Hupp and R. Q. Snurr, *Microporous Mesoporous Mater.*, 2011, **141**, 231–235.

145 B. Liu, R. Zhang, C. Y. Pan and H. L. Jiang, *Inorg. Chem.*, 2017, **56**, 4263–4266.

146 S. Yuan, Y.-P. Chen, J. Qin, W. Lu, X. Wang, Q. Zhang, M. Bosch, T.-F. Liu, X. Lian and H.-C. Zhou, *Angew. Chem. Int. Ed.*, 2015, **54**, 14696–14700.

147 S. Yuan, J. S. Qin, J. Li, L. Huang, L. Feng, Y. Fang, C. Lollar, J. Pang, L. Zhang, D. Sun, A. Alsalme, T. Cagin and H. C. Zhou, *Nat. Commun.*, 2018, **9**, 1-11.

148 G. González Miera, A. Bermejo Gómez, P. J. Chupas, B. Martín-Matute, K. W. Chapman and A. E. Platero-Prats, *Inorg. Chem.*, 2017, **56**, 4576–4583.

149 A. C. Sudik, A. P. Côté, A. G. Wong-Foy, M. O'Keeffe and O. M. Yaghi, *Angew. Chem. Int. Ed.*, 2006, **45**, 2528–2533.

150 J. T. Hupp and K. R. Poeppelmeler, *Science*, 2005, **309**, 2008–2009.

151 G. Férey, C. Mellot-Draznieks, C. Serre, F. Millange, J. Dutour, S. Surblé and I. Margiolaki, *Science*, 2005, **309**, 2040–2042.

152 S. Ma, D. Sun, J. M. Simmons, C. D. Collier, D. Yuan and H.-C. Zhou, *J. Am. Chem. Soc.*, 2008, **130**, 1012–1016.

153 H. Chun, *J. Am. Chem. Soc.*, 2008, **130**, 800–801.

154 J.-R. Li, D. J. Timmons and H.-C. Zhou, *J. Am. Chem. Soc.*, 2009, **131**, 6368–6369.

155 T. He, X. Xu, B. Ni, H. Lin, C. Li, W. Hu and X. Wang, *Angew. Chem. Int. Ed.*, 2018, **57**, 10148–10152.

156 S. Yuan, L. Feng, K. Wang, J. Pang, M. Bosch, C. Lollar, Y. Sun, J. Qin, X. Yang, P. Zhang, Q. Wang, L. Zou, Y. Zhang, L. Zhang, Y. Fang, J. Li and H.-C. Zhou, *Adv. Mater.*, 2018, **30**, 1704303.

157 J. J. Low, A. I. Benin, P. Jakubczak, J. F. Abrahamian, S. A. Faheem and R. R. Willis, *J. Am. Chem. Soc.*, 2009, **131**, 15834–15842.

158 H. Furukawa, F. Gándara, Y.-B. Zhang, J. Jiang, W. L. Queen, M. R. Hudson and O. M. Yaghi, *J. Am. Chem. Soc.*, 2014, **136**, 4369–4381.

159 X. Liu, N. K. Demir, Z. Wu and K. Li, *J. Am. Chem. Soc.*, 2015, **137**, 6999–7002.

160 Z.-J. Guo, J. Yu, Y.-Z. Zhang, J. Zhang, Y. Chen, Y. Wu, L.-H. Xie and J.-R. Li, *Inorg. Chem.*, 2017, **56**, 2188–2197.

161 T. H. Noh, E. Heo, K. H. Park and O.-S. Jung, *J. Am. Chem. Soc.*, 2011, **133**, 1236–1239.

162 T.-F. Liu, D. Feng, Y.-P. Chen, L. Zou, M. Bosch, S. Yuan, Z. Wei, S. Fordham, K. Wang and H.-C. Zhou, *J. Am. Chem. Soc.*, 2015, **137**, 413–419.

163 K. Wang, X.-L. Lv, D. Feng, J. Li, S. Chen, J. Sun, L. Song, Y. Xie, J.-R. Li and H. C. Zhou, *J. Am. Chem. Soc.*, 2016, **138**, 914–919.

164 N. Zhu, M. J. Lennox, G. Tobin, L. Goodman, T. Düren and W. Schmitt, *Chem. - A Eur. J.*, 2014, **20**, 3595–3599.

165 Z. Chang, D.-S. Zhang, Q. Chen, R.-F. Li, T.-L. Hu and X.-H. Bu, *Inorg. Chem.*, 2011, **50**, 7555–7562.

166 H. Furukawa, Y. B. Go, N. Ko, Y. K. Park, F. J. Uribe-Romo, J. Kim, M. O'Keeffe and O. M. Yaghi, *Inorg. Chem.*, 2011, **50**, 9147–9152.

167 P. Li, N. A. Vermeulen, C. D. Malliakas, D. A. Gómez-Gualdrón, A. J. Howarth, B. L. Mehdi, A. Dohnalkova, N. D. Browning, M. O'Keeffe and O. K. Farha, *Science*, 2017, **356**, 624–627.

168 O. K. Farha, I. Eryazici, N. C. Jeong, B. G. Hauser, C. E. Wilmer, A. A. Sarjeant, R. Q. Snurr, S. T. Nguyen, A. Ö. Yazaydin and J. T. Hupp, *J. Am. Chem. Soc.*, 2012, **134**, 15016–15021.

169 D. I. M. Hönicke, D. I. Senkovska, D. V. Bon, D. I. A. Baburin, N. Bönisch, S. Raschke, D. J. D. Evans and P. D. S. Kaskel, *Angew. Chem. Int. Ed.*, 2018, **57**, 13780–13783.

170 R. A. Dodson, A. G. Wong-Foy and A. J. Matzger, *Chem. Mater.*, 2018, **30**, 6559–6565.

171 H. Deng, S. Grunder, K. E. Cordova, C. Valente, H. Furukawa, M. Hmadeh, F. Gandara, A. C. Whalley, Z. Liu, S. Asahina, H. Kazumori, M. O'Keeffe, O. Terasaki, J. F. Stoddart and O. M. Yaghi, *Science*, 2012, **336**, 1018–1023.

172 W. Lu, D. Yuan, A. Yakovenko and H.-C. Zhou, *Chem. Commun.*, 2011, **47**, 4968.

173 S. Du, T.-Q. Yu, W. Liao and C. Hu, *Dalt. Trans.*, 2015, **44**, 14394–14402.

174 J. L. C. Rowsell and O. M. Yaghi, *J. Am. Chem. Soc.*, 2006, **128**, 1304–1315.

175 D. Sun, S. Ma, Y. Ke, T. M. Petersen and H. C. Zhou, *Chem. Commun.*, 2005, 2663–2665.

176 H. Kim, S. Das, M. G. Kim, D. N. Dybtsev, Y. Kim and K. Kim, *Inorg. Chem.*, 2011, **50**, 3691– 3696.

177 M. Dincă, A. Dailly, C. Tsay and J. R. Long, *Inorg. Chem.*, 2008, **47**, 11–13.

178 S. Ma, X. Sen Wang, D. Yuan and H. C. Zhou, *Angew. Chem. Int. Ed.*, 2008, **47**, 4130–4133.

179 J. L. C. Rowsell and O. M. Yaghi, *Angew. Chem. Int. Ed.*, 2005, **44**, 4670–4679.

180 S. S. Han, J. L. Mendoza-Cortés and W. A. Goddard III, *Chem. Soc. Rev.*, 2009, **38**, 1460.

181 S. S. Han, D.-H. Jung and J. Heo, *J. Phys. Chem. C*, 2013, **117**, 71–77.

182 P. Ghosh, Y. J. Colón and R. Q. Snurr, *Chem. Commun.*, 2014, **50**, 11329–11331.

183 H. Wu, Y. S. Chua, V. Krungleviciute, M. Tyagi, P. Chen, T. Yildirim and W. Zhou, *J. Am. Chem. Soc.*, 2013, **135**, 10525–10532.

184 G. C. Shearer, J. G. Vitillo, S. Bordiga, S. Svelle, U. Olsbye and K. P. Lillerud, *Chem. Mater.*, 2016, **28**, 7190–7193.

185 M. R. DeStefano, T. Islamoglu, S. J. Garibay, J. T. Hupp and O. K. Farha, *Chem. Mater.*, 2017, **29**, 1357–1361.

186 G. C. Shearer, S. Chavan, S. Bordiga, S. Svelle, U. Olsbye and K. P. Lillerud, *Chem. Mater.*, 2016, **28**, 3749–3761.

187 K. M. Choi, H. J. Jeon, J. K. Kang and O. M. Yaghi, *J. Am. Chem. Soc.*, 2011, **133**, 11920–11923.

188 A. G. Slater and A. I. Cooper, *Science*, 2015, **348**, aaa8075–aaa8075.

189 P. P. Edwards, V. L. Kuznetsov, W. I. F. David and N. P. Brandon, *Energy Policy*, 2008, **36**, 4356–4362.

190 H. Furukawa, M. A. Miller and O. M. Yaghi, *J. Mater. Chem.*, 2007, **17**, 3197.

191 H.-L. Jiang, B. Liu, Y.-Q. Lan, K. Kuratani, T. Akita, H. Shioyama, F. Zong and Q. Xu, *J. Am. Chem. Soc.*, 2011, **133**, 11854–11857.

192 A. Schoedel, Z. Ji and O. M. Yaghi, *Nat. Energy*, 2016, **1**, 16034.

193 H. W. Langmi, J. Ren, B. North, M. Mathe and D. Bessarabov, *Electrochim. Acta*, 2014, **128**, 368–392.

194 J. L. C. Rowsell and O. M. Yaghi, *J. Am. Chem. Soc.*, 2006, **128**, 1304–1315.

195 L. Wang and R. T. Yang, *Energy Environ. Sci.*, 2008, **1**, 268.

196 Q. Yang and C. Zhong, *J. Phys. Chem. B*, 2006, **110**, 655–658.

197 K. L. Mulfort and J. T. Hupp, *Inorg. Chem.*, 2008, **47**, 7936–7938.

198 S. K. Bhatia and A. L. Myers, *Langmuir*, 2006, **22**, 1688–1700.

199 M. T. Kapelewski, S. J. Geier, M. R. Hudson, D. Stück, J. A. Mason, J. N. Nelson, D. J. Xiao, Z. Hulvey, E. Gilmour, S. A. FitzGerald, M. Head-Gordon, C. M. Brown and J. R. Long, *J. Am. Chem. Soc.*, 2014, **136**, 12119–12129.

200 J. R. Long, *DOE Hydrogen and Fuel Cells Program Review: Hydrogen Storage in Metal-Organic Frameworks*, 2015.

201 S. Subramanian and M. J. Zaworotko, *Angew. Chem. Int. Ed.*, 1995, **34**, 2127–2129.

202 C. A. Trickett, A. Helal, B. A. Al-Maythalony, Z. H. Yamani, K. E. Cordova and O. M. Yaghi, *Nat. Rev. Mater.*, 2017, **2**, 17045.

203 B. Zheng, R. Yun, J. Bai, Z. Lu, L. Du and Y. Li, *Inorg. Chem.*, 2013, **52**, 2823–2829.

204 C. Serre, G. Maurin, P. L. Llewellyn, C. Zhong, Q. Yang, A. D. Wiersum, T. Devic, F. Ragon and V. Guillerm, *Chem. Commun.*, 2012, **48**, 9831.

205 O. Shekhah, Y. Belmabkhout, Z. Chen, V. Guillerm, A. Cairns, K. Adil and M. Eddaoudi, *Nat. Commun.*, 2014, **5**, 1–7.

206 K. A. Forrest, T. Pham and B. Space, *CrystEngComm*, 2017, **19**, 3338–3347.

207 J.-R. Li, J. Yu, W. Lu, L.-B. Sun, J. Sculley, P. B. Balbuena and H.-C. Zhou, *Nat. Commun.*, 2013, **4**, 1538.

208 J. Hu, J. Liu, Y. Liu and X. Yang, *J. Phys. Chem. C*, 2016, **120**, 10311–10319.

209 J. Yao, D. Li and H. Wang, in *Eco- and Renewable Energy Materials*, Springer Berlin Heidelberg, Berlin, Heidelberg, 2013, vol. 2, pp. 233–257.

210 J. Liu, Y. Wang, A. I. Benin, P. Jakubczak, R. R. Willis and M. D. LeVan, *Langmuir*, 2010, **26**, 14301–14307.

211 R. W. Flaig, T. M. Osborn Popp, A. M. Fracaroli, E. A. Kapustin, M. J. Kalmutzki, R. M. Altamimi, F. Fathieh, J. A. Reimer and O. M. Yaghi, *J. Am. Chem. Soc.*, 2017, **139**, 12125–12128.

212 A. Masala, J. G. Vitillo, G. Mondino, C. A. Grande, R. Blom, M. Manzoli, M. Marshall and S. Bordiga, *ACS Appl. Mater. Interfaces*, 2017, **9**, 455–463.

213 I. Spanopoulos, P. Xydias, C. D. Malliakas and P. N. Trikalitis, *Inorg. Chem.*, 2013, **52**, 855–862.

214 Y. He, W. Zhou, G. Qian and B. Chen, *Chem. Soc. Rev. Chem. Soc. Rev*, 2014, **43**, 5657–5678.

215 Q. Yang, P. Lama, S. Sen, M. Lusi, K.-J. Chen, W. Gao, M. Shivanna, T. Pham, N. Hosono, S. Kusaka, J. J. Perry, S. Ma, B. Space, L. J. Barbour, S. Kitagawa and M. J. Zaworotko, *Angew. Chem. Int. Ed.*, 2018, **57**, 5684–5689.

216 BASF, *Chem. Soc. Rev.*, 2014, **43**, 6173–6174.

217 Y. Peng, V. Krungleviciute, I. Eryazici, J. T. Hupp, O. K. Farha and T. Yildirim, *J. Am. Chem. Soc.*, 2013, **135**, 11887–11894.

218 *United Nations World Water Assessment Programme. UN World Water Development Report: Managing Water under Uncertainty and Risk*, 2012, vol. 1.

219 M. Elimelech and W. A. Phillip, *Science*, 2011, **333**, 712–717.

220 M. A. Shannon, P. W. Bohn, M. Elimelech, J. G. Georgiadis, B. J. Mariñas and A. M. Mayes, *Nature*, 2008, **452**, 301–310.

221 A. Lee, M.-W. Moon, H. Lim, W.-D. Kim and H.-Y. Kim, *Langmuir*, 2012, **28**, 10183–10191.

222 A. J. Rieth, S. Yang, E. N. Wang and M. Dincă, *ACS Cent. Sci.*, 2017, **3**, acscentsci.7b00186.

223 Z. Chen, P. Li, X. Zhang, P. Li, M. C. Wasson, T. Islamoglu, J. F. Stoddart and O. K. Farha, *J. Am. Chem. Soc.*, 2019, **141**, 2900–2905.

224 H. Kim, S. Yang, S. R. Rao, S. Narayanan, E. A. Kapustin, H. Furukawa, A. S. Umans, O. M. Yaghi and E. N. Wang, *Science*, 2017, **356**, 430–434.

225 S. M. Towsif Abtab, D. Alezi, P. M. Bhatt, A. Shkurenko, Y. Belmabkhout, H. Aggarwal, Ł. J. Weseliński, N. Alsadun, U. Samin, M. N. Hedhili and M. Eddaoudi, *Chem*, 2018, **4**, 94–105.

226 H. Kim, S. R. Rao, E. A. Kapustin, L. Zhao, S. Yang, O. M. Yaghi and E. N. Wang, *Nat. Commun.*, 2018, **9**, 1191.

227 H.-N. Wang, X. Meng, G.-S. Yang, X.-L. Wang, K.-Z. Shao, Z.-M. Su and C.-G. Wang, *Chem. Commun.*, 2011, **47**, 7128.

228 J. Urquhart, World's first commercial MOF keeps fruit fresh, https://www.chemistryworld.com/news/worlds-first-commercial-mof-keeps-fruit-fresh/1017469.article.

229 S. Chopra, S. Dhumal, P. Abeli, R. Beaudry and E. Almenar, *Postharvest Biol. Technol.*, 2017, **130**, 48–55.

230 K. J. Hartlieb, D. P. Ferris, J. M. Holcroft, I. Kandela, C. L. Stern, M. S. Nassar, Y. Y. Botros and J. F. Stoddart, *Mol. Pharm.*, 2017, **14**, 1831–1839.

231 T.-Y. Zhou, B. Auer, S. J. Lee and S. G. Telfer, *J. Am. Chem. Soc.*, 2019, **141**, 1577–1582.

232 X. Li, J. Wu, C. He, Q. Meng and C. Duan, *Small*, 2019, **1804770**, 1804770.

233 R. Limvorapitux, H. Chen, M. L. Mendonca, M. Liu, R. Q. Snurr and S. T. Nguyen, *Catal. Sci. Technol.*, 2019, **9**, 327–335.

234 J. Ye, L. Gagliardi, C. J. Cramer and D. G. Truhlar, *J. Catal.*, 2018, **360**, 160–167.

235 Y. Zhang, X. Yang and H.-C. Zhou, *Polyhedron*, 2018, **154**, 189–201.

236 J.-S. Qin, S. Yuan, C. Lollar, J. Pang, A. Alsalme and H.-C. Zhou, *Chem. Commun.*, 2018, **54**, 4231–4249.

237 G.-J. Chen, C.-Q. Chen, X.-T. Li, H.-C. Ma and Y.-B. Dong, *Chem. Commun.*, 2018, **54**, 11550–11553.

238 G. Bauer, D. Ongari, X. Xu, D. Tiana, B. Smit and M. Ranocchiari, *J. Am. Chem. Soc.*, 2017, **139**, 18166–18169.

239 L. T. M. Hoang, L. H. Ngo, H. L. Nguyen, H. T. H. Nguyen, C. K. D. Nguyen, B. T. Nguyen, Q. T. Ton, H. K. D. Nguyen, K. E. Cordova and T. Truong, *Chem. Commun.*, 2015, **51**, 17132–17135.

240 J. Pang, S. Yuan, D. Du, C. Lollar, L. Zhang, M. Wu, D. Yuan, H.-C. Zhou and M. Hong, *Angew. Chem. Int. Ed.*, 2017, **56**, 14622–14626.

241 Y. Ueda, H. Ito, D. Fujita and M. Fujita, *J. Am. Chem. Soc.*, 2017, **139**, 6090–6093.

242 M. Tonigold, Y. Lu, B. Bredenkötter, B. Rieger, S. Bahnmüller, J. Hitzbleck, G. Langstein and D. Volkmer, *Angew. Chem. Int. Ed.*, 2009, **48**, 7546–7550.

243 L. Hamidipour and F. Farzaneh, *React. Kinet. Mech. Catal.*, 2013, **109**, 67–75.

244 Z. Li, A. W. Peters, V. Bernales, M. A. Ortuño, N. M. Schweitzer, M. R. DeStefano, L. C. Gallington, A. E. Platero-Prats, K. W. Chapman, C. J. Cramer, L. Gagliardi, J. T. Hupp and O. K. Farha, *ACS Cent. Sci.*, 2017, **3**, 31–38.

245 N. Van Velthoven, S. Waitschat, S. M. Chavan, P. Liu, S. Smolders, J. Vercammen, B. Bueken, S. Bals, K. P. Lillerud, N. Stock and D. E. De Vos, *Chem. Sci.*, 2019, **10**, 3616–3622.

246 D. Feng, T.-F. Liu, J. Su, M. Bosch, Z. Wei, W. Wan, D. Yuan, Y.-P. Chen, X. Wang, K. Wang, X. Lian, Z.-Y. Gu, J. Park, X. Zou and H.-C. Zhou, *Nat. Commun.*, 2015, **6**, 5979.

247 S. K. Bhardwaj, N. Bhardwaj, R. Kaur, J. Mehta, A. L. Sharma, K.-H. Kim and A. Deep, *J. Mater. Chem. A*, 2018, **6**, 14992–15009.

248 E. M. Miner, T. Fukushima, D. Sheberla, L. Sun, Y. Surendranath and M. Dincă, *Nat. Commun.*, 2016, **7**, 10942.

249 T. Kambe, R. Sakamoto, K. Hoshiko, K. Takada, M. Miyachi, J. H. Ryu, S. Sasaki, J. Kim, K. Nakazato, M. Takata and H. Nishihara, *J. Am. Chem. Soc.*, 2013, **135**, 2462–2465.

250 R. Gutzler and D. F. Perepichka, *J. Am. Chem. Soc.*, 2013, **135**, 16585–16594.

251 T. Kusamoto, K. Ishizaka, K. Hoshiko, T. Shimojima, R. Sakamoto, Z. Wang, H. Nishihara, T. Kambe, F. Liu, N. Fukui, T. Pal, T. Hirahara and S. Hasegawa, *J. Am. Chem. Soc.*, 2014, **136**, 14357–14360.

252 M. G. Campbell, D. Sheberla, S. F. Liu, T. M. Swager and M. Dincă, *Angew. Chem. Int. Ed.*, 2015, **54**, 4349–4352.

253 M. G. Campbell, S. F. Liu, T. M. Swager and M. Dincă, *J. Am. Chem. Soc.*, 2015, **137**, 13780–13783.

254 X. Huang, P. Sheng, Z. Tu, F. Zhang, J. Wang, H. Geng, Y. Zou, C. Di, Y. Yi , Y. Sun, W. Xu and D. Zhu, *Nat. Commun.*, 2015, **6**, 7408.

255 R. Dong, M. Pfeffermann, H. Liang, Z. Zheng, X. Zhu, J. Zhang and X. Feng, *Angew. Chem. Int. Ed.*, 2015, **54**, 12058–12063.

256 A. J. Clough, J. W. Yoo, M. H. Mecklenburg and S. C. Marinescu, *J. Am. Chem. Soc.*, 2015, **137**, 118–121.

257 M. Campbell and M. Dincă, *Sensors*, 2017, **17**, 1108.

258 W. Li, L. Sun, J. Qi, P. Jarillo-Herrero, M. Dincă and J. Li, *Chem. Sci.*, 2017, **8**, 2859–2867.

259 B. J. Holliday and T. M. Swager, *Chem. Commun.*, 2005, 23.

260 L. Sun, T. Miyakai, S. Seki and M. Dincă, *J. Am. Chem. Soc.*, 2013, **135**, 8185–8188.

261 A. A. Talin, A. Centrone, A. C. Ford, M. E. Foster, V. Stavila, P. Haney, R. A. Kinney, V. Szalai, F. El Gabaly, H. P. Yoon, F. Léonard and M. D. Allendorf, *Science*, 2014, **343**, 66–69.

262 Y. Kobayashi, B. Jacobs, M. D. Allendorf and J. R. Long, *Chem. Mater.*, 2010, **22**, 4120–4122.

263 H. Dong, X. Fu, J. Liu, Z. Wang and W. Hu, *Adv. Mater.*, 2013, **25**, 6158–6183.

264 T. C. Narayan, T. Miyakai, S. Seki and M. Dincă, *J. Am. Chem. Soc.*, 2012, **134**, 12932–12935.

265 S. S. Park, E. R. Hontz, L. Sun, C. H. Hendon, A. Walsh, T. Van Voorhis and M. Dincă, *J. Am. Chem. Soc.*, 2015, **137**, 1774–1777.

266 T. Panda and R. Banerjee, *Proc. Natl. Acad. Sci. India Sect. A - Phys. Sci.*, 2014, **84**, 331–336.

267 L. Sun, M. G. Campbell and M. Dincă, *Angew. Chem. Int. Ed.*, 2016, **55**, 3566–3579.

268 G. V. Research, *Hydrogen Generation Market Size, Share & Trends Analysis Report By Application (Coal Gasification, Steam Methane Reforming), By Technology, By System (Merchant, Captive), And Segment Forecasts*, 2018.

269 M. Blasco-Ahicart, J. Soriano-López, J. J. Carbó, J. M. Poblet and J. R. Galan-Mascaros, *Nat. Chem.*, 2018, **10**, 24–30.

270 W. A. A. Arafa, M. D. Kärkäs, B. L. Lee, T. Åkermark, R. Z. Liao, H. M. Berends, J. Messinger, P. E. M. Siegbahn and B. Åkermark, *Phys. Chem. Chem. Phys.*, 2014, **16**, 11950–11964.

271 M. D. Kärkäs, O. Verho, E. V. Johnston and B. Åkermark, *Chem. Rev.*, 2014, **114**, 11863–12001.

272 T. M. Laine, M. D. Kärkäs, R. Z. Liao, T. Åkermark, B. L. Lee, E. A. Karlsson, P. E. M. Siegbahn and B. Åkermark, *Chem. Commun.*, 2015, **51**, 1862–1865.

273 S. Mukhopadhyay, R. S. Singh, A. Biswas and D. S. Pandey, *Chem. Commun.*, 2016, **52**, 3840–3843.

274 J. Tian, M. Fu, D. Huang, X. Wang, Y. Wu, J. Y. Lu and D.-S. Li, *Inorg. Chem. Commun.*, 2018, **95**, 73–77.

275 H. Wang, F. Yin, G. Li, B. Chen and Z. Wang, *Int. J. Hydrogen Energy*, 2014, **39**, 16179–16186.

276 Z.-M. Zhang, T. Zhang, C. Wang, Z. Lin, L.-S. Long and W. Lin, *J. Am. Chem. Soc.*, 2015, **137**, 3197–3200.

277 X.-J. Kong, Z. Lin, Z.-M. Zhang, T. Zhang and W. Lin, *Angew. Chem. Int. Ed.*, 2016, **55**, 6411–6416.

278 F. Yin, X. Zhang, X. He and H. Wang, in *Metal-Organic Frameworks and their Applications in Hydrogen and Oxygen Evolution Reactions*, InTech, 2016.

279 H. Wang, Q. L. Zhu, R. Zou and Q. Xu, *Chem*, 2017, **2**, 52–80.

280 Y. P. Wu, W. Zhou, J. Zhao, W. W. Dong, Y. Q. Lan, D. S. Li, C. Sun and X. Bu, *Angew. Chem. Int. Ed.*, 2017, **56**, 13001–13005.

281 S. Y. Han, D. L. Pan, H. Chen, X. B. Bu, Y. X. Gao, H. Gao, Y. Tian, G. S. Li, G. Wang, S. L. Cao, C. Q. Wan and G. C. Guo, *Angew. Chem. Int. Ed.*, 2018, **57**, 9864–9869.

282 Y.-Q. Lan, F.-M. Zhang, J.-L. Sheng, Z.-D. Yang, X.-J. Sun, H.-L. Tang, M. Lu, H. Dong, F.-C. Shen and J. Liu, *Angew. Chem. Int. Ed.*, 2018, 1–6.

283 S.-S. Wang and G.-Y. Yang, *Chem. Rev.*, 2015, **115**, 4893–4962.

284 B. Nohra, H. El Moll, L. M. Rodriguez Albelo, P. Mialane, J. Marrot, C. Mellot-Draznieks, M. O'Keeffe, R. Ngo Biboum, J. Lemaire, B. Keita, L. Nadjo and A. Dolbecq, *J. Am. Chem. Soc.*, 2011, **133**, 13363–13374.

285 Y.-Q. Lan, L.-P. Guo, X.-J. Bo, J.-S. Qin, W. Guan, Y.-F. Li, Z.-M. Su, Y.-Y. Wang, H.-C. Zhou and D.-Y. Du, *J. Am. Chem. Soc.*, 2015, **137**, 7169–7177.

286 J. Soriano-López, D. G. Musaev, C. L. Hill, J. R. Galán-Mascarós, J. J. Carbó and J. M. Poblet, *J. Catal.*, 2017, **350**, 56–63.

287 L. Han, S. Dong and E. Wang, *Adv. Mater.*, 2016, **28**, 9266–9291.

288 S. M. Barnett, K. I. Goldberg and J. M. Mayer, *Nat. Chem.*, 2012, **4**, 498–502.

289 A. K. Poulsen, A. Rompel and C. J. McKenzie, *Angew. Chem. Int. Ed.*, 2005, **44**, 6916–6920.

290 S. J. Folkman, J. Soriano-Lopez, J. R. Galán-Mascarós and R. G. Finke, *J. Am. Chem. Soc.*, 2018, **140**, 12040–12055.

291 Q. Yin, J. M. Tan, C. Besson, Y. V Geletii, D. G. Musaev, A. E. Kuznetsov, Z. Luo, K. I. Hardcastle and C. L. Hill, *Science*, 2010, **328**, 342–345.

292 H. Lei, A. Han, F. Li, M. Zhang, Y. Han, P. Du, W. Lai and R. Cao, *Phys. Chem. Chem. Phys.*, 2014, **16**, 1883–1893.

293 D. Ressnig, M. Shalom, J. Patscheider, R. Moré, F. Evangelisti, M. Antonietti and G. R. Patzke, *J. Mater. Chem. A*, 2015, **3**, 5072–5082.

294 J. L. Fillol, Z. Codolà, I. Garcia-Bosch, L. Gàmez, J. J. Pla and M. Costas, *Nat. Chem.*, 2011, **3**, 807–813.

295 F. Evangelisti, P. E. Car, O. Blacque and G. R. Patzke, *Catal. Sci. Technol.*, 2013, **3**, 3117– 3129.

296 S. Shrestha and P. K. Dutta, *ACS Omega*, 2018, **3**, 11972–11981.

297 Z. Chen and T. J. Meyer, *Angew. Chem. Int. Ed.*, 2013, **52**, 700–703.

298 J. H. Cavka, S. Jakobsen, U. Olsbye, N. Guillou, C. Lamberti, S. Bordiga and K. P. Lillerud, *J. Am. Chem. Soc.*, 2008, **130**, 13850–13851.

299 M. J. Katz, Z. J. Brown, Y. J. Colón, P. W. Siu, K. A. Scheidt, R. Q. Snurr, J. T. Hupp and O. K. Farha, *Chem. Commun.*, 2013, **49**, 9449.

300 C. Wang, Z. Xie, K. E. Dekrafft and W. Lin, *J. Am. Chem. Soc.*, 2011, **133**, 13445–13454.

301 X. F. Lu, P. Q. Liao, J. W. Wang, J. X. Wu, X. W. Chen, C. T. He, J. P. Zhang, G. R. Li and X. M. Chen, *J. Am. Chem. Soc.*, 2016, **138**, 8336–8339.

302 J. Q. Shen, P. Q. Liao, D. D. Zhou, C. T. He, J. X. Wu, W. X. Zhang, J. P. Zhang and X. M. Chen, *J. Am. Chem. Soc.*, 2017, **139**, 1778–1781.

303 J. Jiang, L. Huang, X. Liu and L. Ai, *ACS Appl. Mater. Interfaces*, 2017, **9**, 7193–7201.

304 L. Chi, Q. Xu, X. Liang, J. Wang and X. Su, *Small*, 2016, **12**, 1351–1358.

305 Y. An, Y. Liu, P. An, J. Dong, B. Xu, Y. Dai, X. Qin, X. Zhang, M. H. Whangbo and B. Huang, *Angew. Chem. Int. Ed.*, 2017, **56**, 3036–3040.

306 Z. Wei, W. Zhu, Y. Li, Y. Ma, J. Wang, N. Hu, Y. Suo and J. Wang, *Inorg. Chem.*, 2018, **57**, 8422–8428.

307 F. Song, W. Li and Y. Sun, *Inorganics*, 2017, **5**, 40.

308 C. Wang, J. L. Wang and W. Lin, *J. Am. Chem. Soc.*, 2012, **134**, 19895–19908.

309 Y. Horiuchi, T. Toyao, K. Miyahara, L. Zakary, D. Do Van, Y. Kamata, T. H. Kim, S. W. Lee and M. Matsuoka, *Chem. Commun.*, 2016, **52**, 5190–5193.

310 K. Meyer, M. Ranocchiari and J. A. Van Bokhoven, *Energy Environ. Sci.*, 2015, **8**, 1923–1937.

311 W. A. Shah, A. Waseem, M. A. Nadeem and P. Kögerler, *Appl. Catal. A Gen.*, 2018, **567**, 132–138.

312 T. Y. Ma, S. Dai, M. Jaroniec and S. Z. Qiao, *J. Am. Chem. Soc.*, 2014, **136**, 13925–13931.

313 S. Li, S. Peng, L. Huang, X. Cui, A. M. Al-Enizi and G. Zheng, *ACS Appl. Mater. Interfaces*, 2016, **8**, 20534–20539.

314 L. Lux, K. Williams and S. Ma, *CrystEngComm*, 2015, **17**, 10–22.

315 A. Dhakshinamoorthy, Z. Li and H. Garcia, *Chem. Soc. Rev.*, 2018, **47**, 8134–8172.

Chapter 2

Ultra-large supramolecular coordination cages composed of endohedral Archimedean and Platonic bodies

2 Ultra-large supramolecular coordination cages composed of endohedral Archimedean and Platonic bodies

2.1 Introduction

Molecular coordination cages and metal-organic frameworks (MOFs) can be regarded as related metallo-supramolecular materials that consist of metal ions or polynuclear complexes linked through organic ligands to form extended networks or molecular species with defined cavities.[1–4] In the last decades, the former class of compound received significant scientific attention.[5-16] Preparative efforts were primarily directed towards the synthesis of new cage topologies with controllable inner cavities whose chemical, geometrical and electronic attributes can give rise to space-restricted properties that are exploitable in catalytic processes,[5,6,17,18] for separations,[19,20] drug delivery[21] and sensing.[22,23] Most prominent synthetic approaches to functional capsules generally take advantage of kinetically stable building units with defined ligand-accessible coordination sites which direct the self-assembly into hollow structures, for example, in the presence of pyridine or imine ligands.[5,6,9,24] Other concepts to hollow molecular entities employ 'reticular', topological considerations of inorganic and organic nodes which are generally applicable to MOFs,[25] and result in metal-organic polyhedra (MOP).[10] In this context dinuclear {Cu_2} acetate-based 'paddlewheel' complexes represent versatile secondary building units (SBUs) with well-understood functional group compatibility,[10,26] but limitations that often arise from the insolubility of the resulting neutral MOP.[27]

Among the most intriguing developments in the field of supramolecular chemistry are examples that show how molecular cages can provide avenues to synthetic macromolecules with enzyme-type characteristics,[28–31] demonstrating how hollow local binding environments influence the transition states and ultimately the performances of catalytic transformations. However, as new research strands are emerging and target guests are becoming more complex, achievements are hampered by a limited availability of capsules with large-diameter inner cavities whose dimensions, pore openings, surface properties and ligand characteristics allow the uptake and release of desired species at appropriate diffusion rates.[32–36] Representative large-

diameter cages have been reported by Stang, Fujita and co-workers.[32–36] Furthermore, species with various distinctive inner binding sites that regulate intermolecular interactions between multiple reactants are expected to result in enhanced reaction rates and selectivities or may be applicable for the preparation of multifunctional supramolecular materials. Thus assembly principles that produce highly porous 'super-cages' with endohedral, 'onion'-type sub-shells or that are composed of multiple smaller sub-cages, are anticipated to provide a new class of functional molecular hosts.[37–41]

In this chapter it is demonstrated how the rotational flexibility of an extended, tri-functional ligand, 3,3',3''-(benzene-1,3,5-triyltris(ethyne-2,1-diyl)tribenzoic acid (**H_3L1**), can be exploited to prepare {Cu_2}-based coordination cages with exceptionally large cross-sectional diameters and which are composed of outer- and inner-located Archimedean and Platonic bodies. The molecular species represent a highly augmented MOP whose complexity and topological characteristics compare to key structural attributes of MOFs. Whilst the conformational *anti, anti*-arrangement of two benzoate moieties of the **H_3L1** ligand gives rise to a 120^o binding geometry that promotes the formation of the outer shell, the rotational flexibility of the third alkyne-benzoate moiety promotes the formation of inner cages and allows the inner-located dinuclear {Cu_2} complexes to adopt variable arrangements. The labile coordination sites of the SBUs facilitate the post-synthetic interaction with co-ligands that solubilise the nanoscopic molecular species or with smaller guest molecules. The molecules described here are amongst the largest carboxylate-stabilised cages reported. The studies are supported by X-ray crystallography, electron microscopy, atomic force microscopy, dynamic light scattering and vibrational, UV-vis, steady-state, and time-resolved fluorescence spectroscopy.

2.2 Ligand synthesis and characterisation

The ligand discussed in this chapter, 3,3',3''-(benzene-1,3,5-triyltris(ethyne-2,1-diyl))tribenzoic acid, (**H_3L1**) was synthesised in a 4-step synthesis using a modified, synthetic procedure for the isomeric compound, 4,4',4''-(benzene-1,3,5-triyltris(ethyne-2,1-diyl)tribenzoic acid (**Scheme 2.2.1**).[42,43]

Step one involves a Sonogashira coupling reaction to produce 1,3,5-tris((trimethylsilyl)ethynyl)benzene.[44] For this purpose, 1,3,5-tribromobenzene was dissolved with ethynyltrimethylsilane in a THF:TEA solution. $[Pd^{II}(PPh_3)_2Cl_2]$ and CuI were added to the mixture and it was heated to 80°C for 16 hours under N_2. The solvent was removed under vacuum, the crude product dissolved in CH_2Cl_2 and washed 3 times with an aqueous NH_3 solution. A silica column was eluded with hexane yielding pure 1,3,5-tris((trimethylsilyl)ethynyl)benzene. Step two concerns the removal of the silyl groups. This was achieved by dissolving the 1,3,5-tris((trimethylsilyl)ethynyl)benzene in CH_2Cl_2 and mixing it at 35°C for 4 hours with a concentrated K_2CO_3-MeOH solution. The solvent was removed under vacuum and the crude product was washed with a 1 M HCl solution, followed by H_2O and then purified using a silica column with a CH_2Cl_2 mobile phase yielding pure 1,3,5-triethynylbenzene.

In step three a second Sonogashira coupling reaction was carried out combining 1,3,5-triethynylbenzene and ethyl 3-iodobenzoate and refluxing the reaction mixture at 80°C for 24 hours in a THF:TEA mixture. The crude product was dissolved in CH_2Cl_2 and washed 3 times with an aqueous NH_3 solution before being purified by column chromatography using a THF:hexane solution (2:1 by volume) to yield pure triethyl 3,3',3''-(benzene-1,3,5-triyltris(ethyne-2,1-diyl))tribenzoate. The final step involves a base-catalysed de-esterification to remove the methyl groups and form the free carboxylic acid. This was achieved using excess LiOH in a solvent mixture of THF:H_2O (1:1) and was carried out over 3 hours at 35°C. The THF solvent of the reaction mixture was removed under vacuum leaving an aqueous solution. The reaction mixture was acidified using a 1 M HCl solution which resulted in the precipitation of the crude product. This was washed with deionised H_2O, dried under vacuum and then purified by column chromatography using a THF mobile phase and yielding pure 3,3',3''-(benzene-1,3,5-triyltris(ethyne-2,1-diyl)tribenzoic acid, **H_3L1**.

A combination of ^{1}H-NMR, ^{13}C-NMR spectroscopy, single crystal X-ray analysis and a range of other techniques including FT-IR spectroscopy and mass spectrometry experiments confirmed the formation of **H_3L1**.

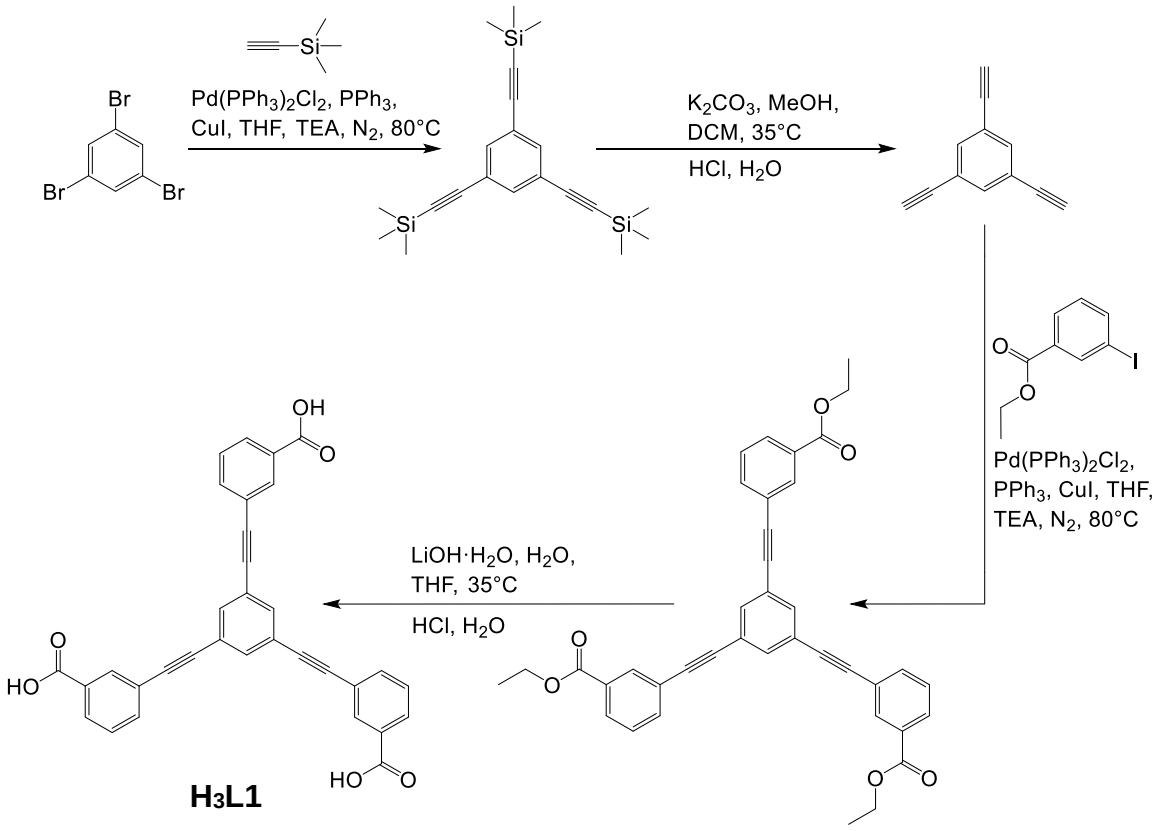

Scheme 2.2.1: Synthetic procedure used for the preparation of **H_3L1**.

2.2.1 NMR spectroscopy of **H_3L1**

^{1}H-NMR experiments in deuterated dimethyl sulfoxide of **H_3L1** (**Figure 2.2.2**) give rise to two singlet signals at 8.11 and 7.80 ppm whose integration accounts for three H-atoms each located at H(1) and H(2), respectively (see numbering scheme in **Figure 2.2.2**). Two doublet signals found at 7.94 and 7.62 ppm, can be attributed to the H-atoms located at H(3) and H(4) respectively. A single triplet signal at 7.43 ppm derives from remaining three H-atoms (H(5)). The ^{13}C-NMR experiments reveal eleven distinct carbon signals which correspond to the eleven distinct carbon positions in the structure of **H_3L1** (**Figure 2.2.3**).

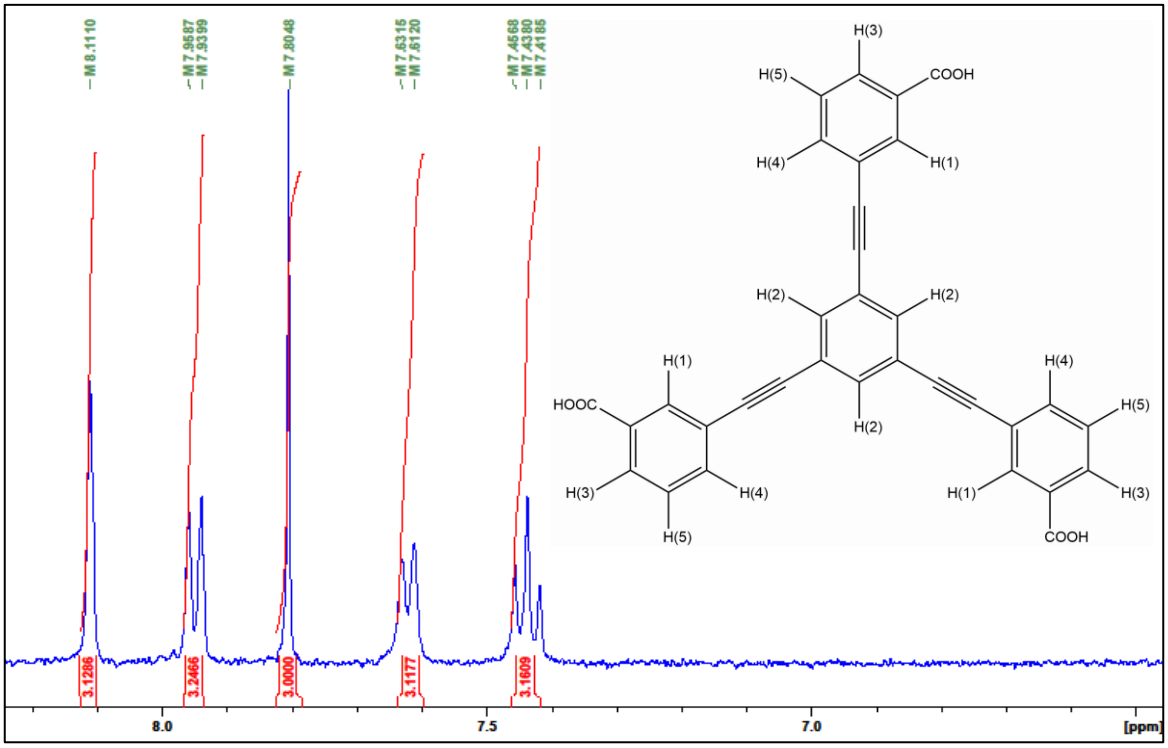

Figure 2.2.2: ^{1}H-NMR spectrum of **H_3L1** in DMSO-d_6.

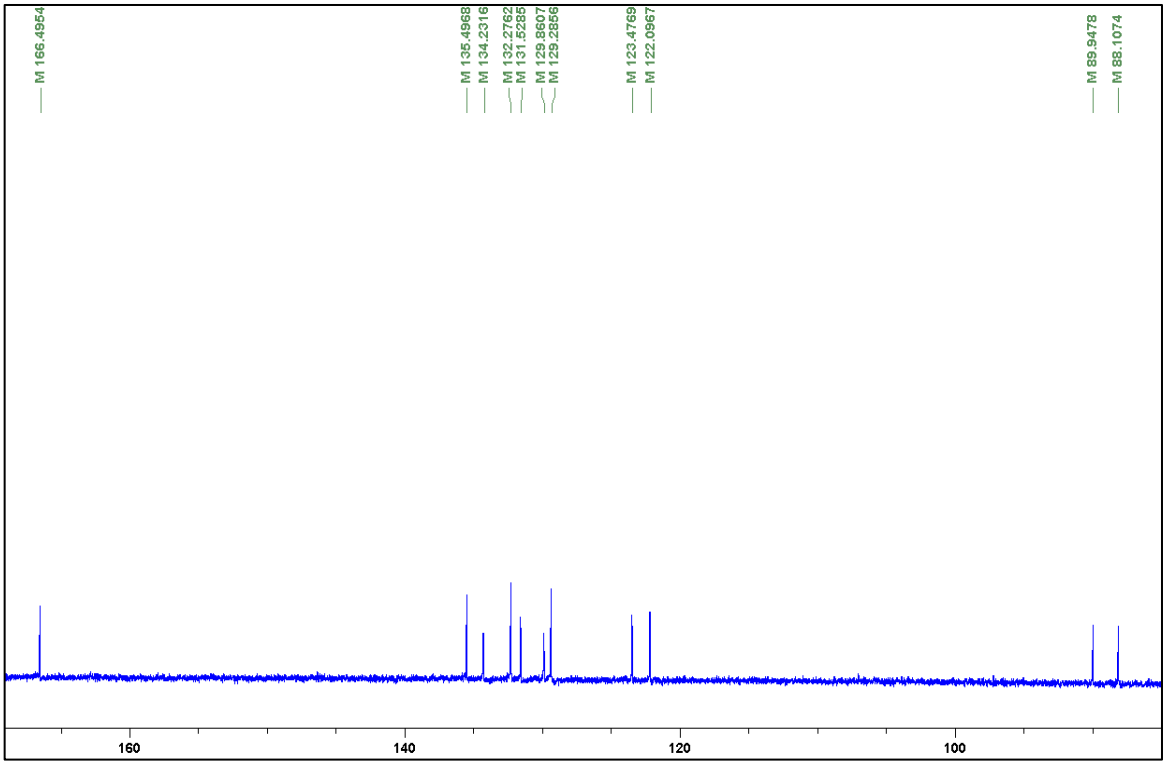

Figure 2.2.3: ^{13}C-NMR spectrum of **H_3L1** in DMSO-d_6.

2.2.2 X-ray characterisation for **H_3L1**

To crystallise **H_3L1,** a powdered sample (20 mg, 0.0392 mmol) was dissolved in a solution of DMF (1 mL) and trifluoroacetic acid (30 µL) at 100°C. The solution was cooled to 20 °C and colourless single crystals of **H_3L1** formed over a period of 2 days. **H_3L1** crystallises in the hexagonal space group $P6_5$. In the crystal structure, each molecule of **H_3L1** (**Figure 2.2.4**) co-crystallises with three DMF molecules giving a constitutional formula of $C_{33}H_{18}O_6$·3DMF. All molecules pack in layers in a planar arrangement parallel to the *ab* plane. We see that that each of the carboxylic acid groups on molecules of **H_3L1** form hydrogen–bonds with DMF molecules which vary in distance from the centre of the carboxylate O atom to the centre of the DMF O atom from 2.492 to 2.577 Å. These vary between 1.683 to 1.754 Å from the calculated carboxylate hydrogen atom centre to the DMF oxygen atom centre which are typical distances for hydrogen bonds (**Figure 2.2.5**, **a)**).[45] One carboxylic acid and DMF hydrogen-bond pairing is disordered over two positions. Additionally, there are parallel displacement π-π stacking interactions between neighbouring layers with edge to centroid distances in stacking phenyl rings of between 3.3 and 3.8 Å, typical distances for this type of interaction (**Figure 2.2.5**, **b)**).[46] The layers pack in an *A,B,C,D,E,F* fashion in the *c*-direction with each succeeding layer rotated by 60° in the *ab* plane in relation to the previous layer. The seventh layer repeats the packing sequence (**Figure 2.2.5**, **c)**). Thus, a 6_5 screw axis extends in the direction of the crystallographic *c*-axis.

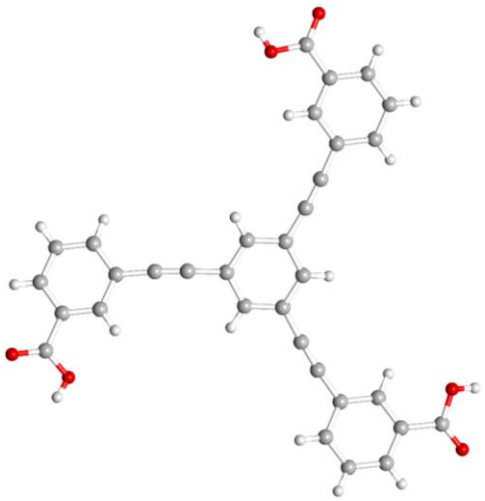

Figure 2.2.4: Crystal structure showing a single molecule of **H_3L1** with view down the crystallographic *c*-axis (disorder in the structure removed for clarity).

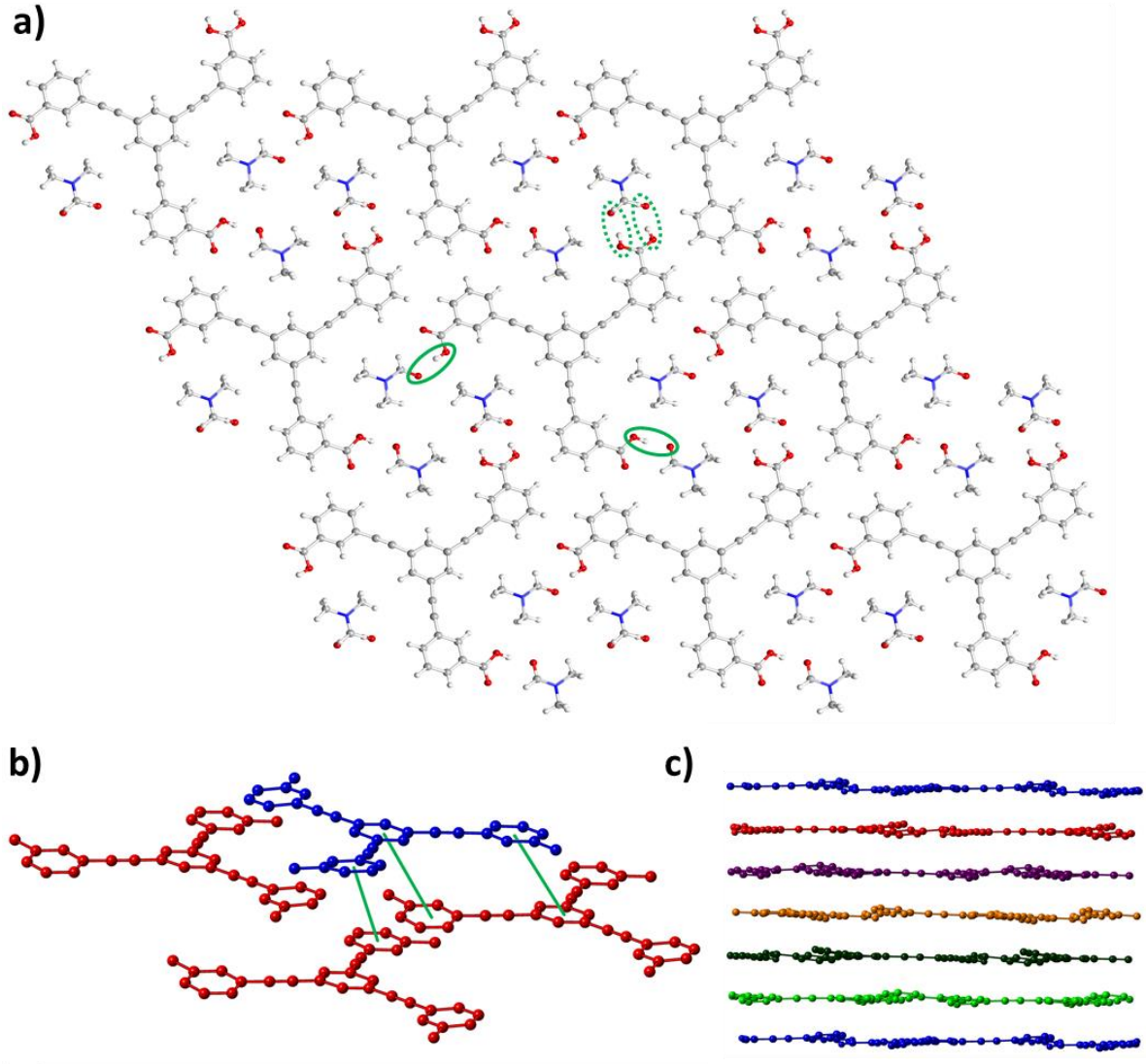

Figure 2.2.5: Packing diagrams of **H_3L1**. **a)** View in the direction of the crystallographic *c*-axis showing one layer of **H_3L1** and DMF molecules with hydrogen bonded atoms highlighted by green circles (dotted green circles were used to highlight the disordered hydrogen bond positions which are each present 50% of the time). **b) H_3L1** molecules in different layers (top (blue), bottom (red)) highlighting the parallel displacement π-π stacking between packing layers (green lines). Only carbon atoms are shown for clarity. **c)** View in the crystallographic *a*-direction showing layers of ligand packing across the *ab* plane. All the atoms in the same layer and repeating layers have the same colour, highlighting the repeating layers in the packing sequence *A,B,C,D,E,F*.

Table 2.3.1: Crystallographic data for **H_3L1**.

Identification code	**H_3L1**
Empirical formula	$C_{42}H_{39}N_3O_9$
Formula weight	729.76
Temperature/K	100(2)
Crystal system	Hexagonal
Space group	*P6$_5$*
a/Å	18.4176(4)
b/Å	18.4176(4)
c/Å	19.3354(4)
α/°	90
β/°	90
γ/°	120
Volume/Å^3	5680.0(3)
Z	6
ρ_{calc}g/cm^3	1.280
μ/mm^{-1}	0.091
F(000)	2304.0
Crystal size/mm^3	0.188 × 0.156 × 0.156
Radiation	MoKα (λ = 0.71073)
2Θ range for data collection/°	3.31 to 60.896
Index ranges	-26 ≤ h ≤ 26, -26 ≤ k ≤ 25, -27 ≤ l ≤ 27
Reflections collected	79432
Independent reflections	11393 [Rint = 0.0520, Rsigma = 0.0332]
Completeness to theta = 30.448°	99.7%
Absorption correction	SADABS
Refinement method	Full-matrix least-squares on F2
Data/restraints/parameters	11393/3/507
Goodness-of-fit on F^2	1.050
Final R indexes [I>=2σ (I)]	R1 = 0.0595, wR2 = 0.1538
Final R indexes [all data]	R1 = 0.0968, wR2 = 0.1793
Largest diff. peak/hole / e Å^{-3}	1.44/-0.41
Flack parameter	0.5(15)

2.3 $[Cu_{36}(\mathbf{L1})_{24}(H_2O)_{28}(DMF)_8]$ (**1**)

2.3.1 Synthesis and structural characterisation of $[Cu_{36}(\mathbf{L1})_{24}(H_2O)_{28}(DMF)_8]$ (**1**)

Crystals of $[Cu_{36}(\mathbf{L1})_{24}(H_2O)_{28}(DMF)_8]$ form reproducibly when **H_3L1** and $Cu(NO_3)_2{\cdot}3H_2O$ are reacted in DMF at 100°C for 5 days. Whilst equimolar Cu(II):**H_3L1** ratios favour the formation of merohedrally twinned crystals, higher Cu(II) concentrations promote the formation of blue rod-shaped crystals of **1**. The characteristic blue colour of **1** allows a facile identification of the compound using an optical microscope and the crystals were manually separated from an insoluble co-precipitating green powder. Single-crystal diffraction experiments demonstrate that **1** crystallises in the space group *C*2/*m* in the monoclinic crystal system with the molecular formula $[Cu_{36}(\mathbf{L1})_{24}(H_2O)_{28}(DMF)_8]$.[47]

At the initial stages of the project we were particularly interested in the rotational flexibility associated with the acetylene moiety of **H_3L1**, which was expected to produce a number of isomeric coordination compounds.[48] This rotational freedom is a feature of extended ligands that incorporate acetylene moieties and distinguishes these linker-types from less-extended sterically restrained derivatives.

The structure of **1** is composed of molecular coordination cages resulting from the self-assembly involving 96 components. These include 36 Cu atoms (18 $\{Cu_2\}$ SBUs), 24 **L1** ligands as well as 36 bound solvent molecules (**Figure 2.3.1)**. The rotational flexibility of the acetylene moiety results in two different isomers of **1**, **1A** and **1B** (**Figure 2.3.2 a)** & **b)**). The outer shells of the structures are identical but there are differences in the rotation of the inner-cage located phenyl rings. Both molecular cages reveal endohedral, onion-type arrangements with an inner octahedral SBU arrangement surrounded by an outer cuboctahedral topology (**Figure 2.3.2, c)** & **d)**).

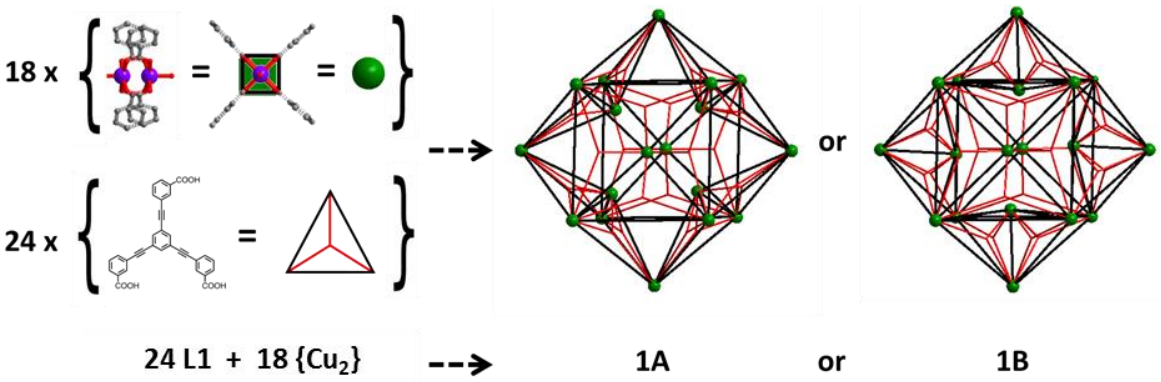

Figure 2.3.1: Schematic representation of the formation of the coordination cages **1A** and **1B**. With the 18 $\{Cu_2\}$ SBUs represented as green spheres and the 24 **L1** ligands as red lines within black triangles. The 36 bound solvent molecules are excluded for clarity.

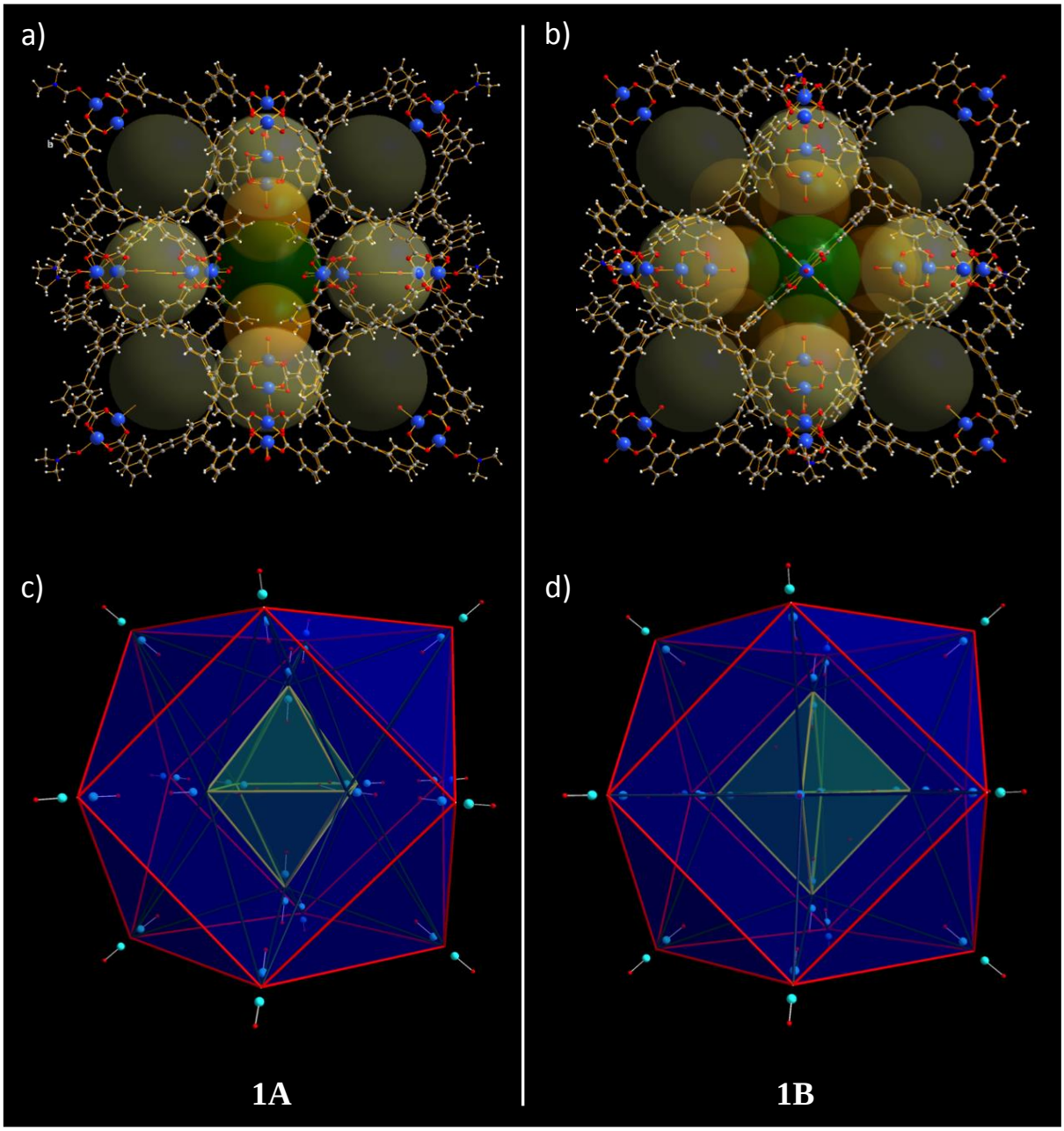

Figure 2.3.2: a), b) Structures of **1A** and **1B** with voids inside the molecules highlighted by transparent yellow and green (for the central void) spheres. **c), d)** Simplified models of **1A** and **1B** respectively. The {Cu_2} units represent the nodal vertices. The endohedral arrangement of Archimedean and Platonic bodies in each cage is shown; inner octahedra are rotated in their basal planes by *ca*. 45° in **1A** compared to **1B**. Colour scheme: Cu (blue/cyan), O (red), N (dark blue), C (grey) and H (white).

The secondary building units (SBUs) of the coordination cages are dinuclear {Cu_2} 'paddlewheel' complexes in which O-donor atoms of *syn, syn*-bidentate carboxylate groups of the deprotonated organic ligand **H_3L1** provide the basal plane of the square pyramidal coordination polyhedra; O-donor atoms of coordinating H_2O and DMF molecules bind in the apical positions (**Figure 2.3.3, a**). The observed structural characteristics of the {Cu_2} units closely compare to those observed in other MOPs and MOFs.[12,26,48,50,51] The Cu-O bond lengths of the outer located {Cu_2} units in **1** involving the carboxylate functionalities vary between 1.939(5) and 1.985(6) Å whilst Cu-O bond distances of the coordinating solvent molecules range between 2.106(5) and 2.166(7) Å. The inner carboxylates show greater variation in Cu-O bond lengths varying from 1.894(16) to 2.121(9) Å whilst Cu-O bond distances involving the coordinating solvent molecules range between 2.150(13) and 2.184(15) Å. The outer-sphere with cuboctahedral topology of the cages in **1** is composed of 12 {Cu_2} SBUs and is characterised by largest cross-sectional diameters of *ca.* 48-50 Å depending on the direction of view (distance between O-atoms of opposite-located, coordination solvent molecules). The outer-shell structure results from an *anti*-alignment of adjacent benzoate moieties of **L1** (red-coloured ligand representation in **Figure 2.3.3, b)**) whereby both benzoate rings adopt approximately co-planar arrangement with respect to the central aromatic ring. The third benzoate moiety of the **L1** ligand links the outer-shell to six further dinuclear {Cu_2} units which are located in the inner cavity. The six {Cu_2} SBUs in the inside of the sphere are disordered over 18 different positions; each inner phenyl ring of the **L1** ligand adopts three possible different orientations (blue-coloured ligand representation in **Figure 2.3.3, b)**). Due to this rotational flexibility of the acetylene moieties different octahedral {Cu_2} arrangements within the cuboctahedral shell are observed whereby two structurally distinguishable, isomeric forms **1A** and **1B** are possible. Thus, the key difference between **1A** and **1B** results from the orientation of the inner octahedral polygons, which are rotated in their basal planes by *ca.* 45^o, with respect to each other. Both cages in **1** are characterised by an endohedral arrangement of Archimedean (cuboctahedral) and Platonic (octahedral) bodies, thus we classify these molecular species as a type of supramolecular Keplerate (**Figure 2.3.2**, **c)** & **d)**).[49] Based on the refinement of the crystal structure and relative atom occupancies it is clear that **1A** is the dominant structural form in **1**.

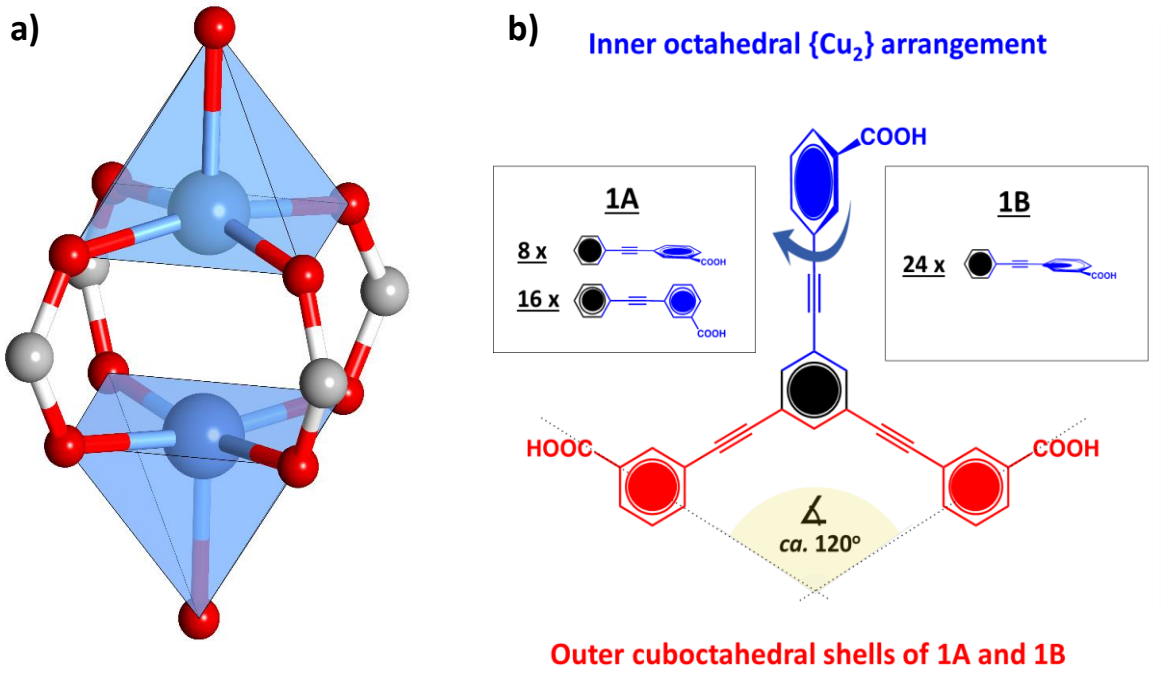

Figure 2.3.3: a) Representation of the {Cu_2} SBU showing four bridging carboxylates from **L1** ligands and two coordinated apical solvent molecules. Colour scheme: Cu (blue), O (red) and C (grey). **b)** Possible arrangement of the benzoate moieties of the **H_3L1** ligand in **1A** and **1B**.

1A results when some benzoate moieties that point to the inside of the coordination cage adopt approximately a co-planar arrangement (a *syn, syn*-binding mode) with respect to the central phenyl ring in **L1**. The building units of this species can be represented as four 'super-paddlewheel' cages[49,52–56] that assemble with two capping units containing square topology as schematically represented in **Figure 2.3.4**, **a)** & **b)** as yellow and red subunits. **1B** results when all benzoate moieties which point to the inside of the coordination cage are arranged approximately perpendicular to the central aromatic ring (a *syn, anti*-binding mode). This conformation results in an octahedral arrangement of the inner six {Cu_2} units that locate below the centres of the square faces of the cuboctahedral polygon. The formation of **1B** can schematically be visualised considering two capping units with square topology and four 'open'-subunits as represented in **Figure 2.3.4**, **a)** & **c)** as yellow and green subunits. The formal assembly of the latter 'open'-subunits gives rise to the remaining four square faces of the cuboctahedral polygon at their fusion points. In **1A** only two {Cu_2} units locate below square faces (yellow units in **Figure 2.3.4**) of the outer cuboctahedral polygon leaving the remaining four faces open, while in **1B** all six inner {Cu_2} units locate directly below square faces.

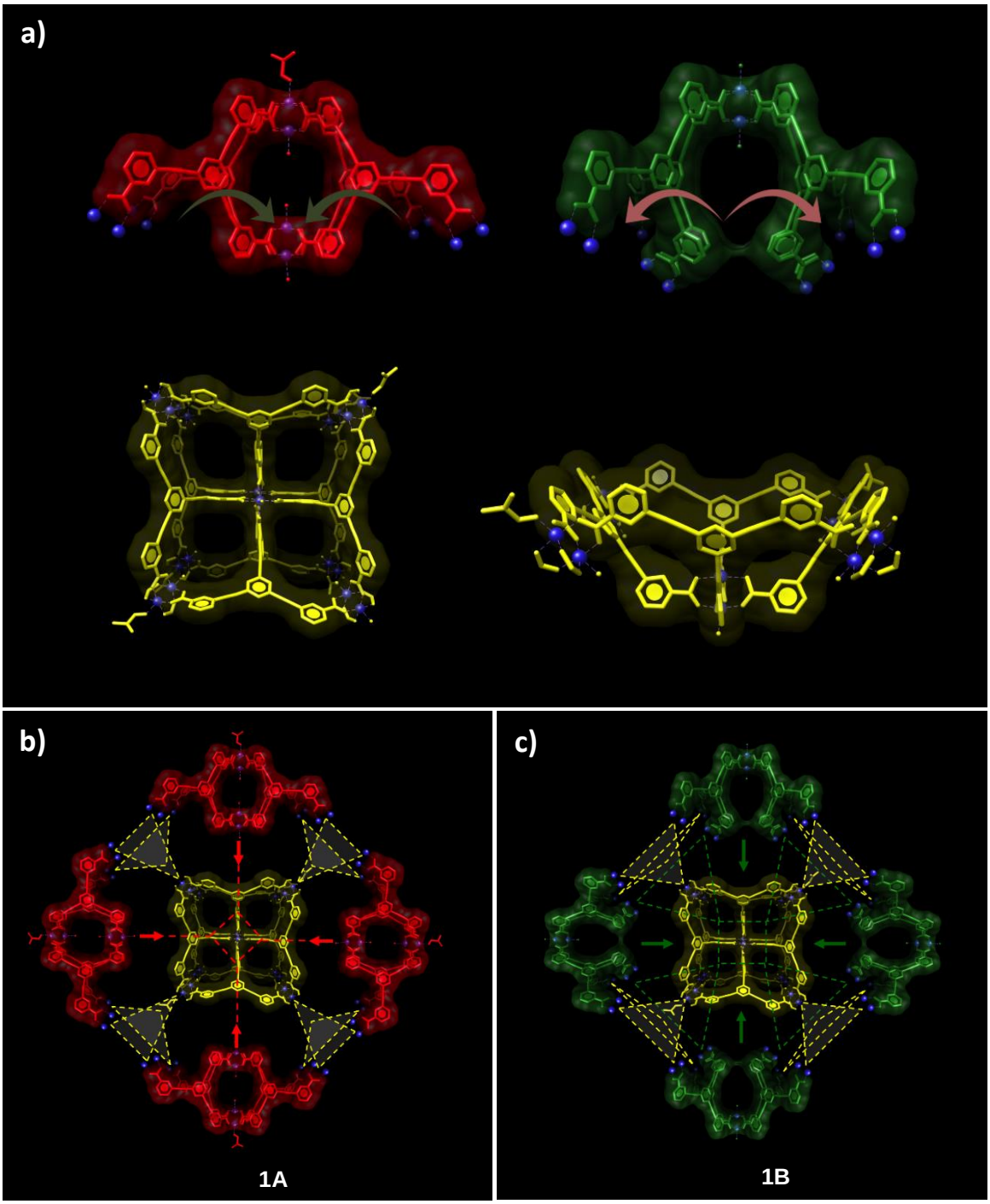

Figure 2.3.4: Sub-cages and building units of **1**. **a)** Structural motifs in **1A** and **1B**. **b)** & **c)** Building principles of **1A** and **1B**. Intersected lines indicate fusion points. Yellow lines give rise to the formation of square faces of the cuboctahedron (yellow units in **a)**); Green and red lines indicate the position of the inner-located $\{Cu_2\}$ units that form part of the inner octahedron. In **1A** only two $\{Cu_2\}$ units locate below square face (yellow units in **b)**) leaving the remaining four faces open while in **1B** all six inner $\{Cu_2\}$ units locate directly below square faces.

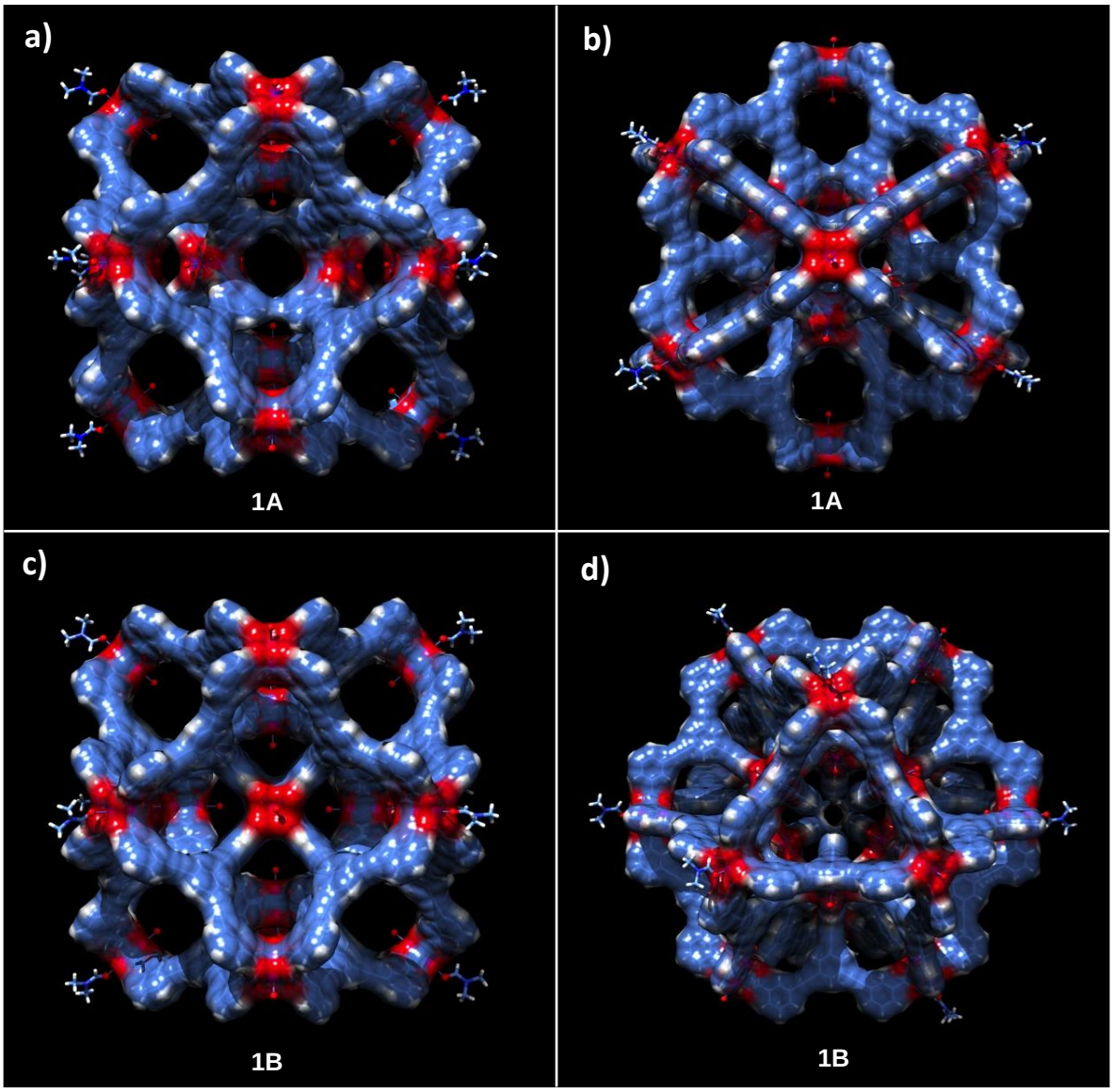

Figure 2.3.5: Space-filling representations of **1**, coordinating solvent molecules are shown in non-space-filling representations. **a)**, **b)** Molecular structure of **1A** shown from two different perspectives. **c)**, **d)** Molecular structure of **1B** shown from two different perspectives. Colour scheme: $\{Cu_2\}$ SBU with O-donor coordination (red), C (blue), N (dark blue), H (white).

This endohedral arrangement in **1** results in various, defined, interconnected void spaces with multiple binding sites and thus the structures and potential binding abilities are rather distinctive to those of large, single-volume cages. These cavities can be clearly seen in the space filling representations of **1A** and **1B** (**Figure 2.3.5**). Indeed, the structures presented here resemble structural characteristics of extended MOFs and marry attributes of large-diameter cages with the presence of multiple small cages that can give rise to enhanced binding abilities.

The individual coordination cages in the crystal structure form distorted hexagonal arrangements within the crystallographic (001) plane and pack directly on top of each other in the direction of the crystallographic *c*-axis (**Figures 3.3.6** & **3.3.7**). Despite this relatively dense packing of the molecular entities the compound is characterised by an exceptionally large solvent accessible void volume that accounts for more of than 70% of the unit cell volume. Considering the packing arrangement, a significant part of the void space that can give rise to porosity can be attributed to the inner void structure of the molecular species.

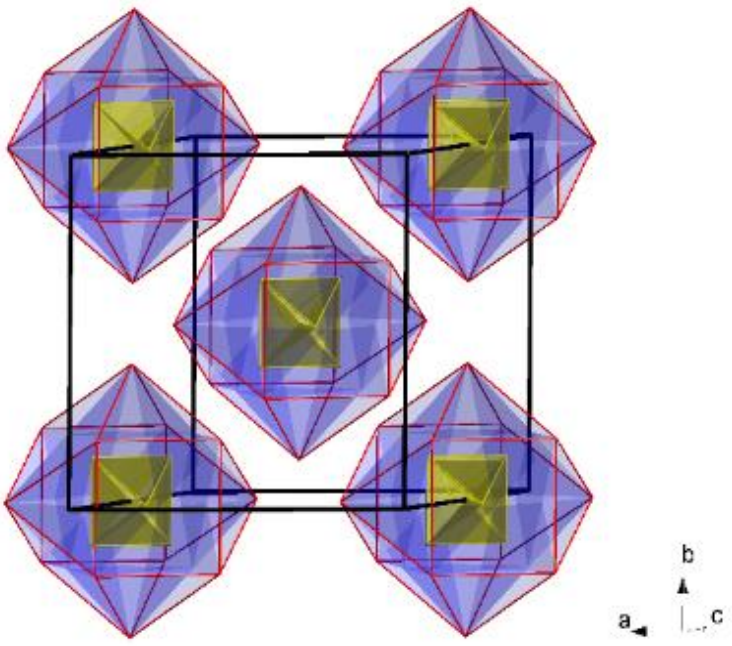

Figure 2.3.6: Unit cell representation of **1** with simplified representations of **1** species; disordered atom positions are omitted for clarity.

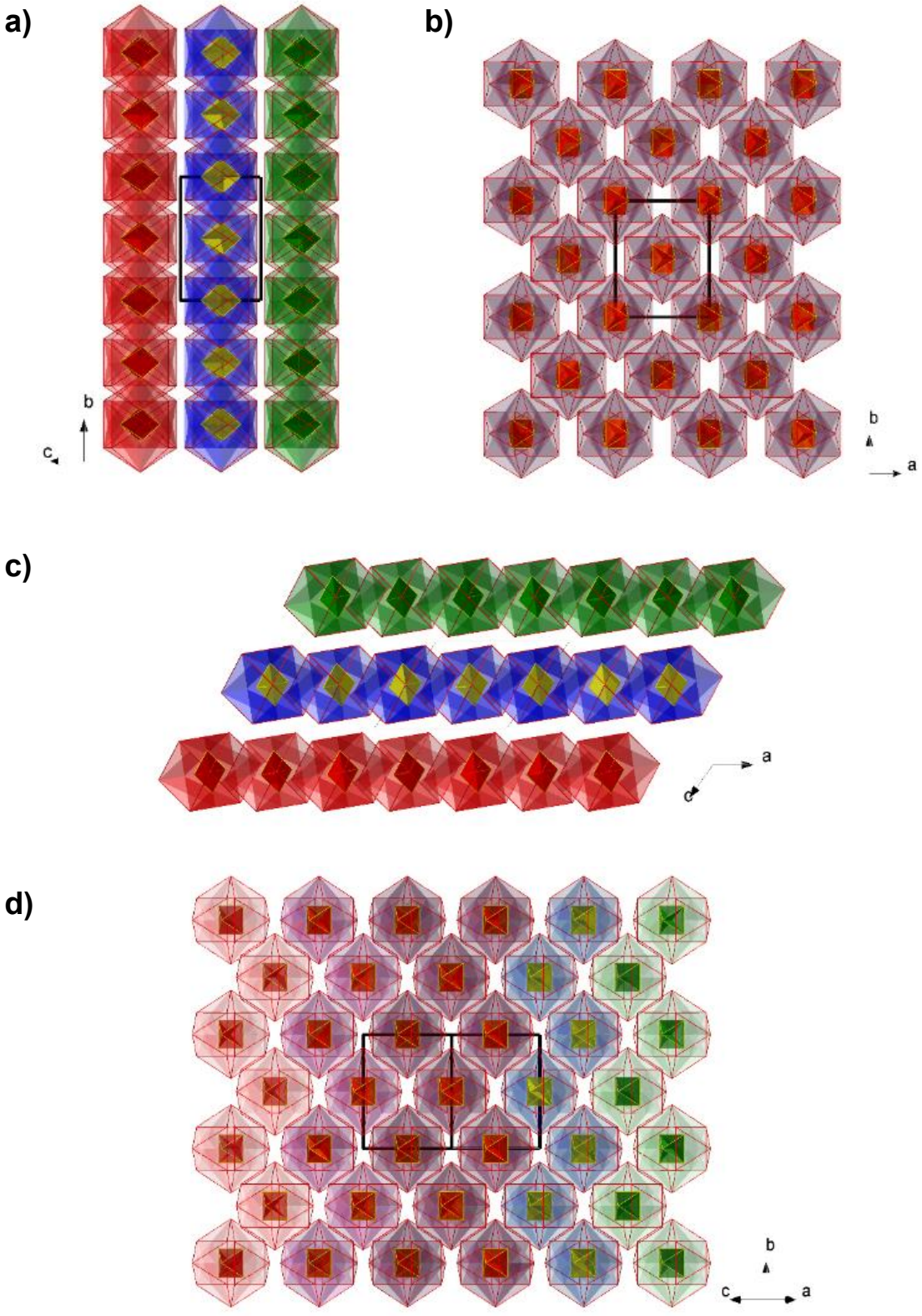

Figure 2.3.7: Packing diagrams of **1**. **a)** View in the direction of the crystallographic a-axis. **b)** View in the direction of the crystallographic c-axis. **c)** View in the direction of the crystallographic b-axis. **d)** View in the [101] direction.

Table 2.3.2: Selected bond distances for the coordination environment found in **1**.

Atoms	Distance [Å]	Atoms	Distance [Å]
Cu(1)-O(1A)	**1.958(4)**	Cu(13)-O(38I)	**1.919(15)**
Cu(1)-O(27J)	**1.958(5)**	Cu(14)-O(39F)	**1.910(16)**
Cu(2)-O(2A)	**1.960(4)**	Cu(14)-O(39I)	**1.912(16)**
Cu(2)-O(2R)	**1.967(6)**	Cu(15)-O(38H)	**2.028(14)**
Cu(2)-O(28J)	**1.969(5)**	Cu(15)-O(38K)	**2.019(14)**
Cu(3)-O(1D)	**1.956(4)**	Cu(15)-O(38M)	**2.121(9)**
Cu(3)-O(1P)	**1.972(4)**	Cu(15)-O(38R)	**2.092(6)**
Cu(3)-O(27A)	**1.939(5)**	Cu(16)-O(39H)	**2.025(14)**
Cu(3)-O(27M)	**1.951(4)**	Cu(16)-O(39K)	**2.048(16)**
Cu(4)-O(2D)	**1.965(4)**	Cu(16)-O(39M)	**2.055(11)**
Cu(4)-O(2P)	**1.960(5)**	Cu(16)-O(39R)	**2.052(7)**
Cu(4)-O(28A)	**1.947(5)**	Cu(17)-O(38C)	**1.917(15)**
Cu(4)-O(28M)	**1.979(5)**	Cu(17)-O(38L)	**1.896(16)**
Cu(5)-O(1G)	**1.955(5)**	Cu(18)-O(39C)	**1.903(16)**
Cu(5)-O(27D)	**1.961(5)**	Cu(18)-O(39L)	**1.894(16)**
Cu(6)-O(2G)	**1.962(4)**	Cu(19)-O(38N)	**1.992(12)**
Cu(6)-O(28D)	**1.952(5)**	Cu(19)-O(38Q)	**1.942(18)**
Cu(7)-O(1J)	**1.963(5)**	Cu(19)-O(38S)	**1.945(17)**
Cu(7)-O(1M)	**1.955(5)**	Cu(20)-O(39N)	**1.920(13)**
Cu(7)-O(1R)	**1.985(6)**	Cu(20)-O(39Q)	**1.934(16)**
Cu(7)-O(27G)	**1.945(6)**	Cu(20)-O(39S)	**1.970(17)**
Cu(8)-O(2J)	**1.940(5)**		
Cu(8)-O(2M)	**1.971(5)**	Cu(1)-O(1W)	**2.166(7)**
Cu(8)-O(28G)	**1.963(6)**	Cu(2)-O(2W)	**2.123(10)**
		Cu(3)-O(30)	**2.106(5)**
Cu(9)-O(38B)	**2.002(13)**	Cu(4)-O(4W)	**2.131(6)**
Cu(9)-O(38E)	**1.998(13)**	Cu(5)-O(5W)	**2.148(8)**
Cu(9)-O(38O)	**1.980(14)**	Cu(6)-O(6W)	**2.143(8)**
Cu(9)-O(38P)	**2.029(9)**	Cu(7)-O(70)	**2.163(5)**
Cu(10)-O(39B)	**2.012(14)**	Cu(8)-O(8W)	**2.133(7)**
Cu(10)-O(39E)	**1.971(15)**	Cu(9)-O(9W)	**2.158(16)**
Cu(10)-O(39O)	**1.989(15)**	Cu(10)-O(10W)	**2.160(16)**
Cu(10)-O(39P)	**2.015(10)**	Cu(11)-O(11W)	**2.184(15)**
Cu(11)-O(38A)	**1.989(16)**	Cu(12)-O(12W)	**2.150(13)**
Cu(11)-O(38D)	**1.988(16)**	Cu(13)-O(13W)	**2.161(17)**
Cu(11)-O(38G)	**1.997(15)**	Cu(14)-O(14W)	**2.170(17)**
Cu(11)-O(38J)	**2.003(15)**	Cu(15)-O(15W)	**2.160(15)**
Cu(12)-O(39A)	**1.952(15)**	Cu(16)-O(16W)	**2.178(14)**
Cu(12)-O(39D)	**1.975(16)**	Cu(17)-O(17W)	**2.174(17)**
Cu(12)-O(39G)	**1.936(15)**	Cu(18)-O(18W)	**2.174(16)**
Cu(12)-O(39J)	**1.978(17)**	Cu(19)-O(19W)	**2.172(17)**
Cu(13)-O(38F)	**1.916(15)**	Cu(20)-O(20W)	**2.159(16)**

Table 2.3.3: Crystallographic data for **1.**

Identification code	**1**
Empirical formula	$C_{816}H_{472}Cu_{36}N_8O_{180}$
Formula weight	15555.43
Temperature/K	215(2)
Crystal system	Monoclinic
Space group	*C2/m*
a/Å	54.9305(18)
b/Å	55.3715(18)
c/Å	44.3760(16)
α/°	90
β/°	125.723
γ/°	90
Volume/Å^3	109578(7)
Z	2
ρ_{calc}g/cm^3	0.471
μ/mm^{-1}	0.596
F(000)	15816
Crystal size/mm^3	0.48 × 0.2 × 0.2
Radiation	CuKα (λ = 1.54178)
2Θ range for data collection/°	1.272 to 50.624
Index ranges	-55 ≤ h ≤ 54, -55 ≤ k ≤ 55, -41 ≤ l ≤ 43
Reflections collected	433251
Independent reflections	58046 [R_{int} = 0.0992]
Completeness to theta = 50.624°	99.0%
Absorption correction	Semi-empirical from equivalents
Max. and min. transmission	0.7500 and 0.3118
Refinement method	Full-matrix least-squares on F2
Data/restraints/parameters	58046 / 2663 / 2719
Goodness-of-fit on F^2	1.339
Final R indexes [I>=2σ (I)]	R1 = 0.1280, wR2 = 0.3635
Final R indexes [all data]	R1 = 0.1741, wR2 = 0.3915
Largest diff. peak/hole / e Å^{-3}	0.934 and -0.688
Total Potential Solvent Accessible Void Vol. (Å^3) per unit cell, (%)	77291 Å; *ca.* 70.5%
CCDC No.	1491341

2.3.2 Topological analysis of **1A** and **1B**

A topological consideration of the molecules and their empirical composition, $\{Cu_2\}_{18}$(**L1**)$_{24}$ = $\{Cu_2\}_3$(**L1**)$_4$, underpins their relationship to neutral 'A_3X_4'-stoichiometric MOFs that assemble from SBUs with square and triangular nodes to form, for instance the edge-transitive default topologies that can be described by the RCSR symbols **tbo** and **pto** (for example, those found in HKUST-1 and MOF-14).[50,51] A numeration of this special class of (4,3)-connected nets in which each 4-connected node is connected to four 3-connected nodes has been given by Wells.[53]

The topology of **1** was analysed and simplified representations were constructed for each isomer (**Figure 2.3.8**). Both isomers are molecular structures with (3,4,4)-sub-connectivity. There are 3-nodal substructures (**L1**) connected to two sets of topologically distinguishable 4-connected nodes ($\{Cu_2\}$ SBUs. The topology of the outer-shell of the cages is best described as a cuboctahedron (**cuo**), whereby the centres of the Cu–Cu axes in the $\{Cu_2\}$ units represent the nodal vertices.

1A and **1B** can be represented with a unique set of point symbols, $4^6\cdot(4\cdot6^2\cdot8^3)\cdot(4^2\cdot6)$ and $(4^2\cdot6^2\cdot8^2)\cdot(4^4\cdot6^2)\cdot(4^2\cdot6)$ respectively. The different point symbols result from the outer and inner $\{Cu_2\}$ SBUs and further relate to the observed tilting between the central and outer phenyl rings of the **L1** ligand.

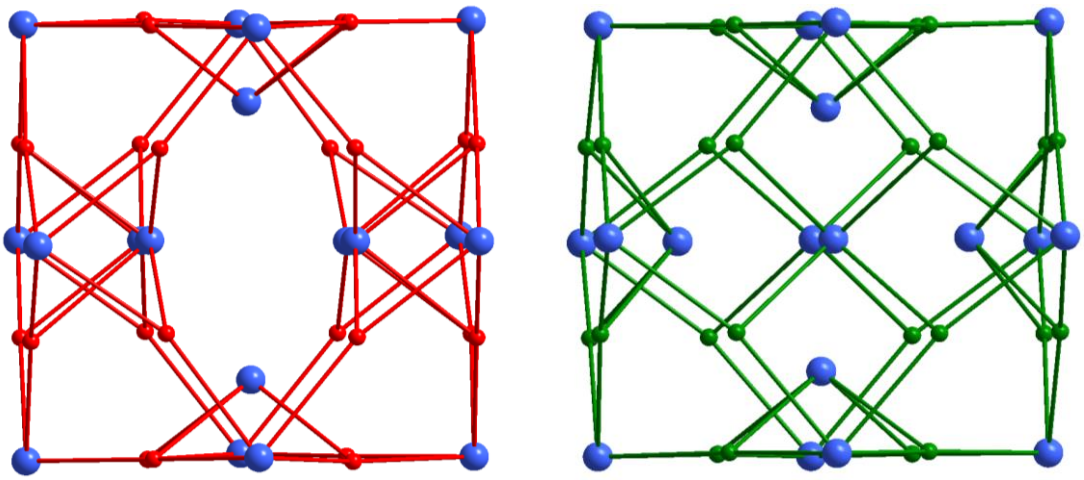

Figure 2.3.8: Topological representations of **1A** (red) and **1B** (green). The $\{Cu_2\}$ SBUs are shown as blue spheres and **L1** is shown as red and green spheres respectively.

2.3.3 Further solid state characterisation of **1**

2.3.3.1 X-ray powder diffraction

To characterise **1** by X-ray powder diffraction, crystals of **1** were ground into a powder while kept in DMF to reduce the possibility of structure collapse upon desolvation and capillary forces. A PXRD pattern was measured using an APEX II DUO X-ray diffractometer to characterise the phase-purity of the synthesised material (**Figure 2.3.9**). The PXRD pattern was measured in a capillary at 220 K to obtain low-angle signals and to avoid loss of crystallinity associated with solvent evaporation from the sample. The experimental pattern is characterised by prominent diffraction peaks at 4.14°, 5.03° and 6.80°. A broad set of signals which overlap with each other are observed at 7.60°, 7.92° and 8.22° in the measured pattern. Two intense broad signals can be seen in the measured pattern at 10.38° and 10.61°. The experimental pattern is less refined than the simulated pattern which can be attributed to the nature of the weakly diffracting material. However, both patterns show similarities indicating possible phase purity of the synthesised material and in addition provide further evidence for the accuracy of the refined crystal structure.

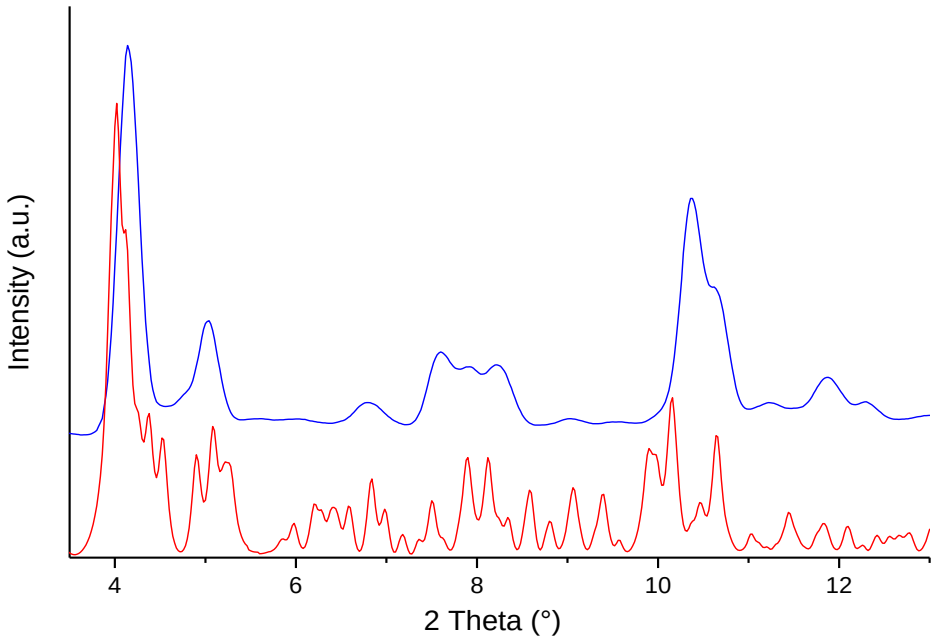

Figure 2.3.9: PXRD patterns of **1**, with the measured pattern in blue and the calculated pattern in red (based on the single crystal X-ray data refinement).

2.3.3.2 FT-IR spectroscopy

The FT-IR spectrum of **1** reveals signals which derive from the coordinating organic ligand **L1** as well as both coordinating and non-coordinating solvent molecules in the pores of the crystals (**Figure 2.3.10**). A broad signal centred at 3417 cm^{-1} in the spectrum of **1** results from hydrogen bonding involving solvent molecules. A weak signal is detected at 3066 cm^{-1} and most likely derives from the aromatic C-H bonds on the **L1** ligand while a more prominent signal at 2929 cm^{-1} corresponds to C-H stretches of DMF solvent molecules. A strong stretch at 1652 cm^{-1} derives from the C=O stretch of DMF. Signals at 1626 and 1594 cm^{-1} derive from aromatic C=C bond vibrations. Asymmetric and symmetric carboxylate stretches are observed at 1594 and 1430 cm^{-1}, respectively ($\Delta_{asy-sym}$ = 164 cm^{-1}).[57–60]

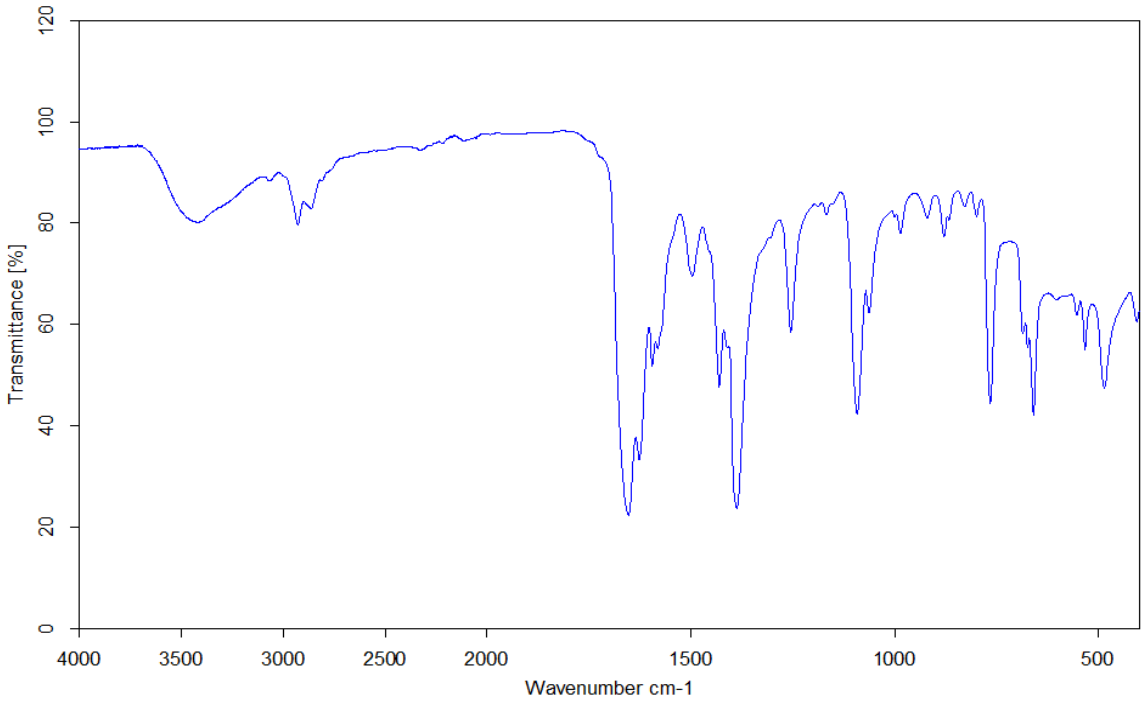

Figure 2.3.10: FT-IR spectrum of **1**.

2.3.3.3 Scanning electron microscopy and energy dispersive X-ray spectroscopy

Crystals of **1** were stored in $CHCl_3$, dried in air for 24 hours and then deposited on Si/SiO_2 wafers and analysed using Energy-Dispersive X-ray (EDX) spectroscopy. The elemental atomic percentages predicted from the crystal structure (C, N, O, Cu) were found to match closely to the observed proportions (**Table 2.3.4**). Additional signals that derive from Si- and O-atoms derive from the Si/SiO_2 sample holder in the background and a minor Cl-derived signal was observed indicating that some $CHCl_3$ is likely still present in the pores of the crystal structure (**Figure 2.3.11**).

Table 2.3.4: Expected and observed atomic ratios by EDX. Expected Atomic % calculated for the molecular formula Cu_{36}(**L1**)$_{24}(H_2O)_8(DMF)_{28}$.

Element	C	N	O	Cu
Expected Atomic %	78.2	2.5	16.1	3.2
Observed Atomic %	77.8	2.5	16.0	3.7

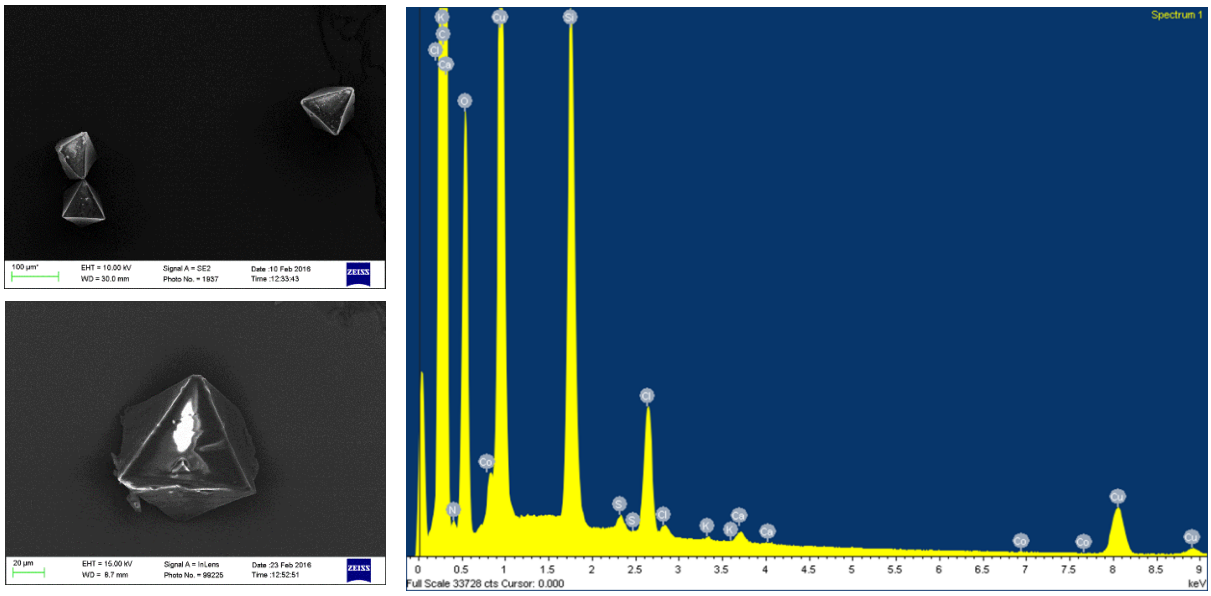

Figure 2.3.11: EDX spectroscopy of crystals of **1**. Sample stored in $CHCl_3$, dried in air and deposited on a Si/SiO_2 surface.

2.3.3.4 Thermogravimetric analysis

For thermogravimetric analyses (TGA) crystals of **1** were removed from their DMF storage solutions and placed briefly onto filter paper to remove excess solvent prior to the deposition in the TGA crucible. The measurement was performed under an N_2 gas flow (20 mL/min) at a heating rate of 3°C per minute (**Figure 2.3.12**). It reveals an initial weight loss of *ca.* 79% between 25 and 90°C which can be attributed to the loss of H_2O and DMF solvent molecules in the pores of the cage as well as constitutional solvent molecules located in between the molecular entities. The total potential solvent accessible void volume was calculated from the crystallographic data to represent 70.5% of the unit cell volume of **1**. Therefore it is likely that a significant amount of solvent could be contained within the structure of **1**. Further thermogravimetric steps commencing at *ca.* 300°C are associated with the decomposition of the organic **L1** ligand.

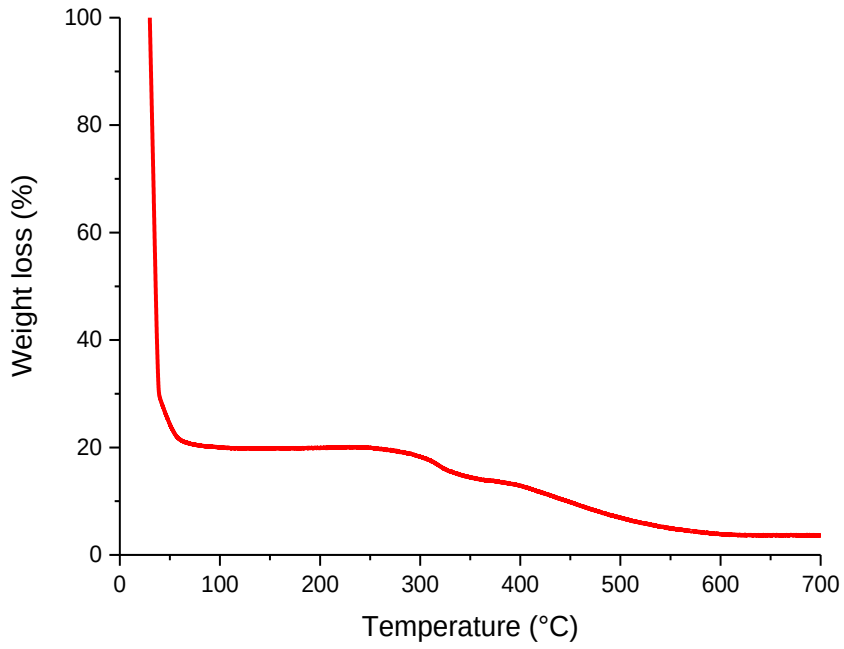

Figure 2.3.12: Thermogravimetric analyses (TGA) using crystals of **1**.

2.3.4 Theoretical gas sorption, BET surface area and pore size distribution

Bulk crystals of **1** rapidly lose crystallinity upon desolvation, and the associated structural changes hamper gas storage measurements. Computational BET studies to evaluate the potential porosity and surface areas of the compound were conducted considering the structure of **1A**.

The adsorption of N_2 at 77 K was simulated using grand canonical Monte Carlo simulations implemented in the MuSiC software package[61] and using translation, rotation and energy-biased insertion and deletion moves. All simulations were allowed at least 8 x 10^6 equilibration steps, followed by 12 x 10^6 production steps for each pressure point. The system was treated as rigid, with MOP atoms kept fixed at their crystallographic positions. Lennard-Jones parameters for the framework atoms were taken from the DREIDING force field[62] with the exception of Cu, for which UFF parameters[63] were used. Nitrogen was simulated as a rigid molecule using the TraPPE model,[64] incorporating both Lennard-Jones parameters and partial charges. Previous work has shown that nitrogen-MOF electrostatic contributions play only a minor role in nitrogen adsorption[65] and, as such, only the electrostatic interactions between nitrogen molecules were included in our simulations. The BET surface area was calculated following the consistency criteria of Rouquerol and co-workers[66] using a pressure range of $0.004 < P/P_0 < 0.06$. The data was simulated using a cif-file of **1** in which disordered atom positions were deleted to represent **1A**. All constitutional solvent molecules were removed whilst coordinated solvent molecules (DMF and H_2O) were retained. The adsorption of N_2 gives rise to a type-I isotherm and a maximum BET surface area of 4126 m^2/g. The calculated pore volume is 1.63 cm^3/g (**Figure 2.3.13, a), b)**).

The pore size distribution (PSD) was calculated following the method of Gelb and Gubbins,[67] in which the largest diameter spheres which may be successfully inserted into the structure without overlap with any of the framework atoms are recorded. The helium pore volume was determined with the Poreblazer tool set[68] using standard helium Lennard-Jones parameters (σ = 2.51 Å, ε/k_B = 10.22 K).[69] The pore-size distribution gives defined pores whose diameters range between *ca.* 6 to 16 Å (**Figure 2.3.13, c)**).

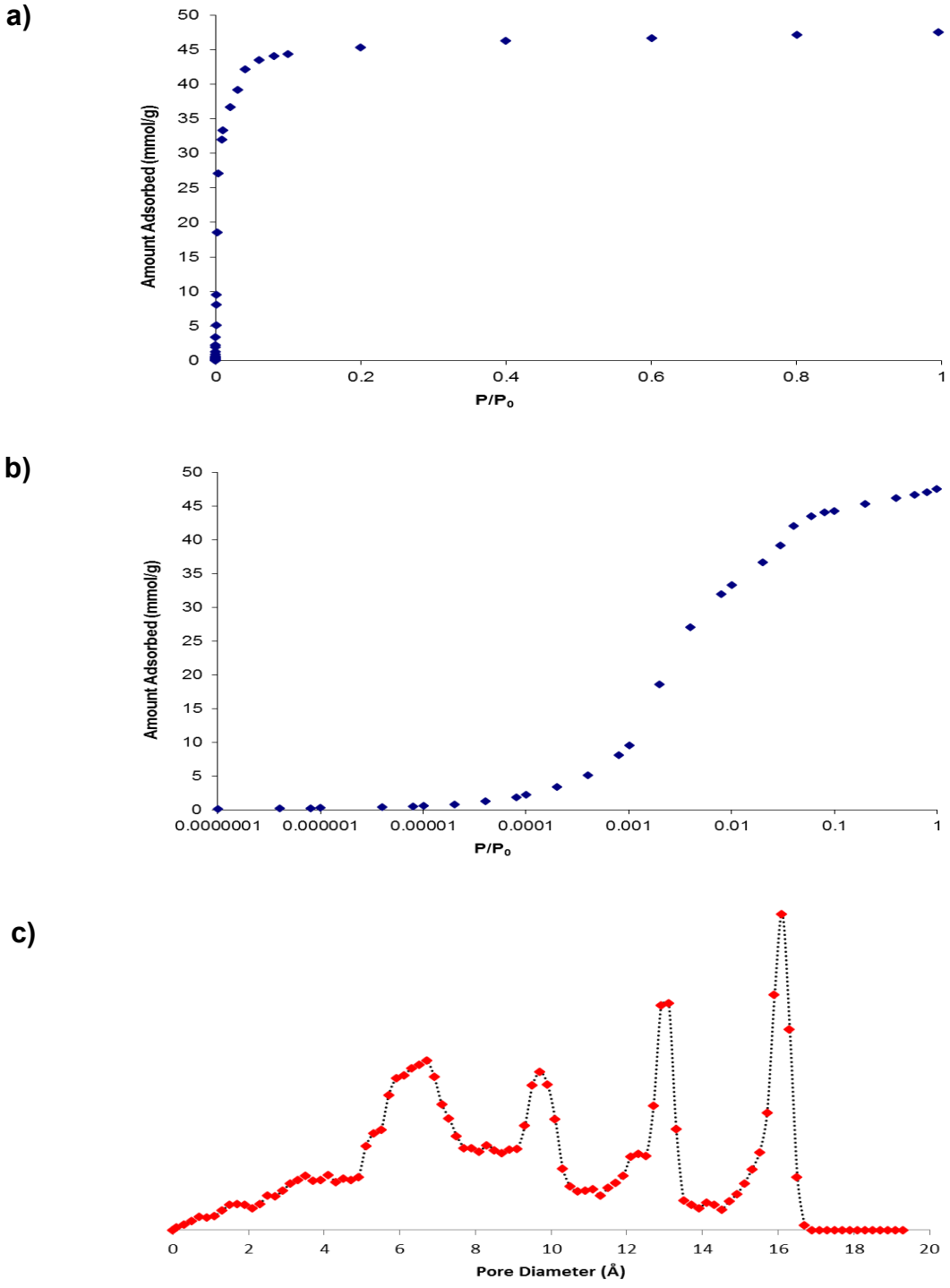

Figure 2.3.13: Theoretical calculation of the BET surface area and pore-size distribution of **1A. a), b)** Simulated N_2 adsorption isotherm at 77 K. **c)** Simulated pore size distribution of **1A**.

2.4 Dissolution and characterisation of **1**

Charge-neutral {Cu_2}-based coordination cages are known to display low solubilities which hamper their use in homogeneous host–guest systems.[27,52] Indeed, **1** is also insoluble in most common polar and non-polar solvents. Ligand-modification and post-synthetic functionalisation using pyridine and its derivatives are known strategies to influence the solubility of {Cu_2}-based coordination cages and cluster species that possess labile coordination sites.[54–56]

One observes, when long-chain, hydrophobic pyridines such as 4-(3-phenylpropyl)pyridine (PPP) are introduced, that crystals of **1** slowly dissolve in chloroform, dimethylformamide or toluene. The pyridines are expected to have a high affinity to interact with the apical sites of the {Cu_2} units and as such are generally expected to exchange with coordinating solvent molecules at these {Cu_2} binding sites, breaking-up the crystal packing structure and solubilising the molecular entities.

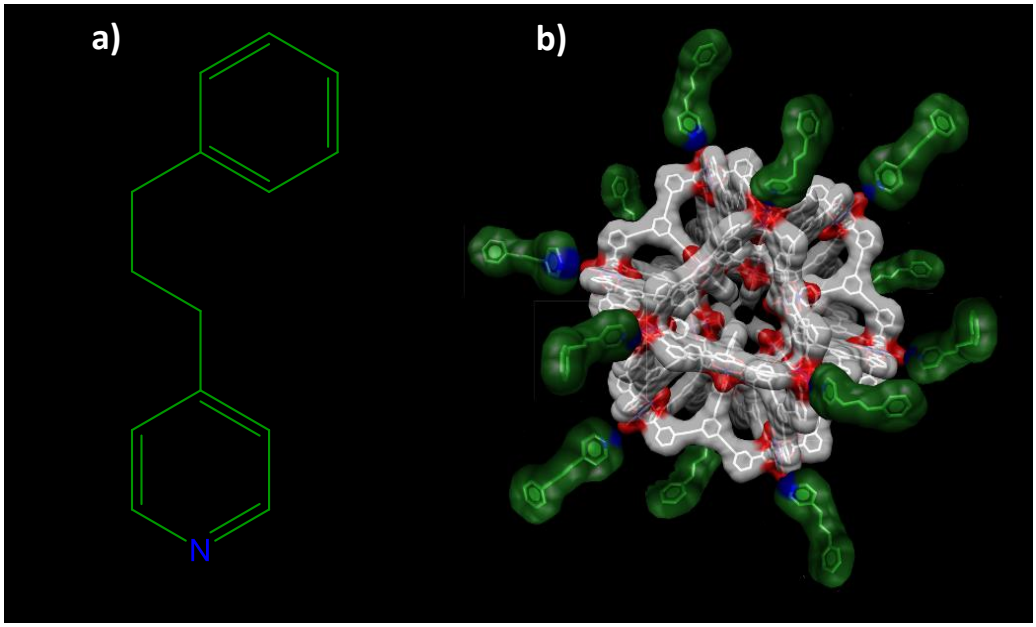

Figure 2.4.1: Representations of **a)** 4-(3-phenylpropyl)pyridine (PPP), **b) 1A** showing the possible functionalization using PPP.

2.4.1 Solution characterisation of **1** dissolved using 4-(3-phenylpropyl)pyridine (PPP)

Dynamic light scattering (DLS) experiments were conducted using a $CHCl_3$ solution (3 mL) which contained **1** (ca. 1 x 10^{-3} g) and excess 4-(3-phenylpropyl)pyridine (PPP, 100 µL) (**Figure 2.4.2**). The studies were performed using a Malvern Zeta Sizer Nano ZS analyser, with corrections carried out only for the solvent refractive index and viscosity. A single sharp signal is observed, centred at 5.62 nm, which is indicative of a well-defined, mono-disperse molecular species. This is consistent with the structural model in which PPP binds to individual molecules of **1**.

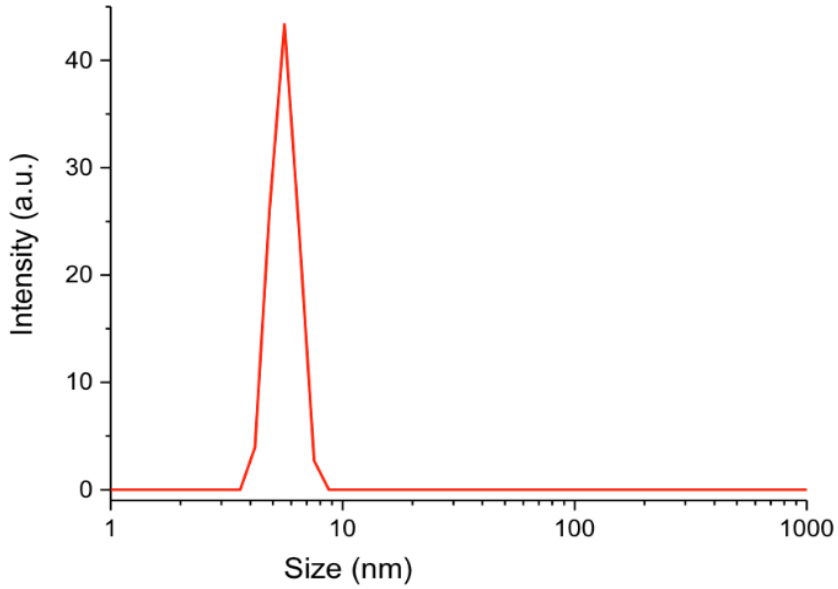

Figure 2.4.2 Dynamic light scattering of a saturated solution of **1**/PPP in $CHCl_3$.

2.4.2 Microscopy analyses of dried PPP/$CHCl_3$ solutions of **1**

Transmission electron microscopy (TEM) and scanning transmission electron microscopy (STEM) experiments were carried out using a $CHCl_3$ solution (2 mL) containing **1** (1 x 10^{-3} g) and excess 4-(3-phenylpropyl)pyridine (PPP, 100 µL). *Ca.* 0.15 mL of the former solution was drop-casted onto lacy carbon coated copper grids, which were then dried in air overnight. The samples were imaged using a titan field emission transmission electron microscope operating at an accelerating voltage of 80 kV (**Figures 3.4.3 – 3.4.5**).

The electron micrographs of **1**/PPP/$CHCl_3$ solutions that were drop-casted on TEM grids, identify uniform, monodisperse particles whose sizes agree well with a cross-sectional diameter of *ca.* 6 nm. These particles are consistent with the structural model in which PPP ligands bind to the molecular species confirming that single molecular species of the cages are experimentally accessible. EDX mapping was performed on the spherical particles of **1**/PPP observed using STEM and TEM microscopy using an acceleration voltage of 80 kV (**Figure 2.4.4**, **e) inset**). A Cu signal was seen overlapping with the particles further verifying that the objects contain Cu. For energy dispersive X-ray (EDX) spectroscopy analyses, a **1**/PPP/$CHCl_3$ solution that was also used for the TEM sample preparation was drop-casted onto a Si_4N_3 grid and analysed using a Zeiss Ultra Plus scanning electron microscope (SEM). A typical analysis (Atomic %) was found to give C 78.5%, O 18.9%, Cu 2.6%. These results in an experimental C/Cu ratio of 5.66 which corresponds with the expected ratio for the molecular formula Cu_{36}(*m*-BTEB)$_{24}$(PPP)$_{20}$(H_2O)$_{16}$ suggesting that *ca.* 20 PPP molecules interact with the individual capsular entities. While it can be expected that the PPP molecules primarily attach at the periphery of the cages, it is also feasible that some of these pyridine derivatives may possibly enter the cages.

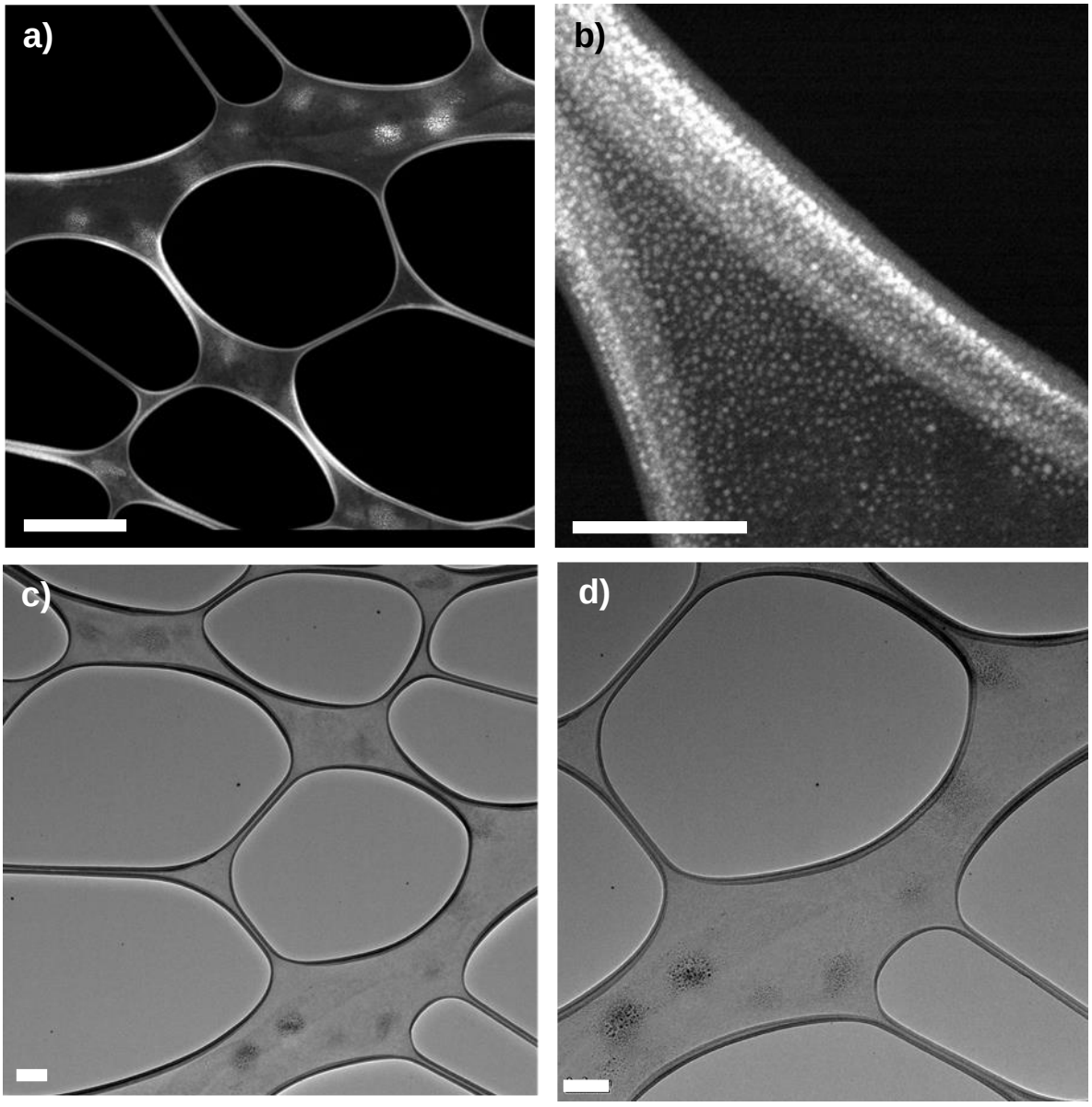

Figure 2.4.3: TEM/STEM images of **1**/PPP/$CHCl_3$ samples that were drop-casted on carbon-coated TEM grids. **a)**, **b)** STEM mode. **c)**, **d)** TEM mode Scale bars equal: **a)** 1 μm, **b)**-**d)** 200 nm.

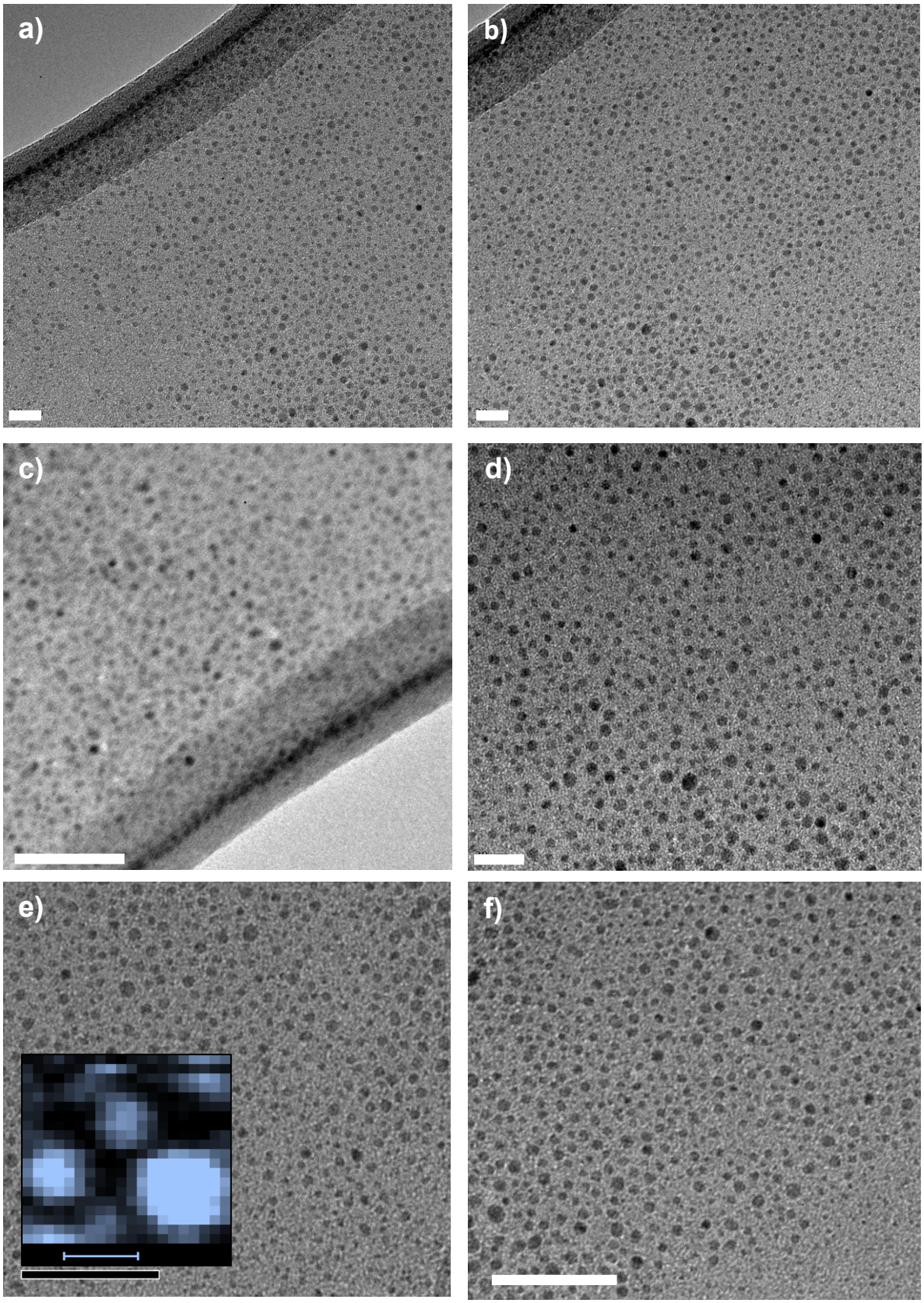

Figure 2.4.4: TEM images of **1**/PPP/$CHCl_3$ samples that were drop-casted on carbon-coated TEM grids. Scale bars equal: **a)**, **b)** & **d)** 20 nm, **c)**, **e)** & **f)** 50 nm. **e) Inset**; EDX mapping of the element Cu, scale bar equals 20 nm.

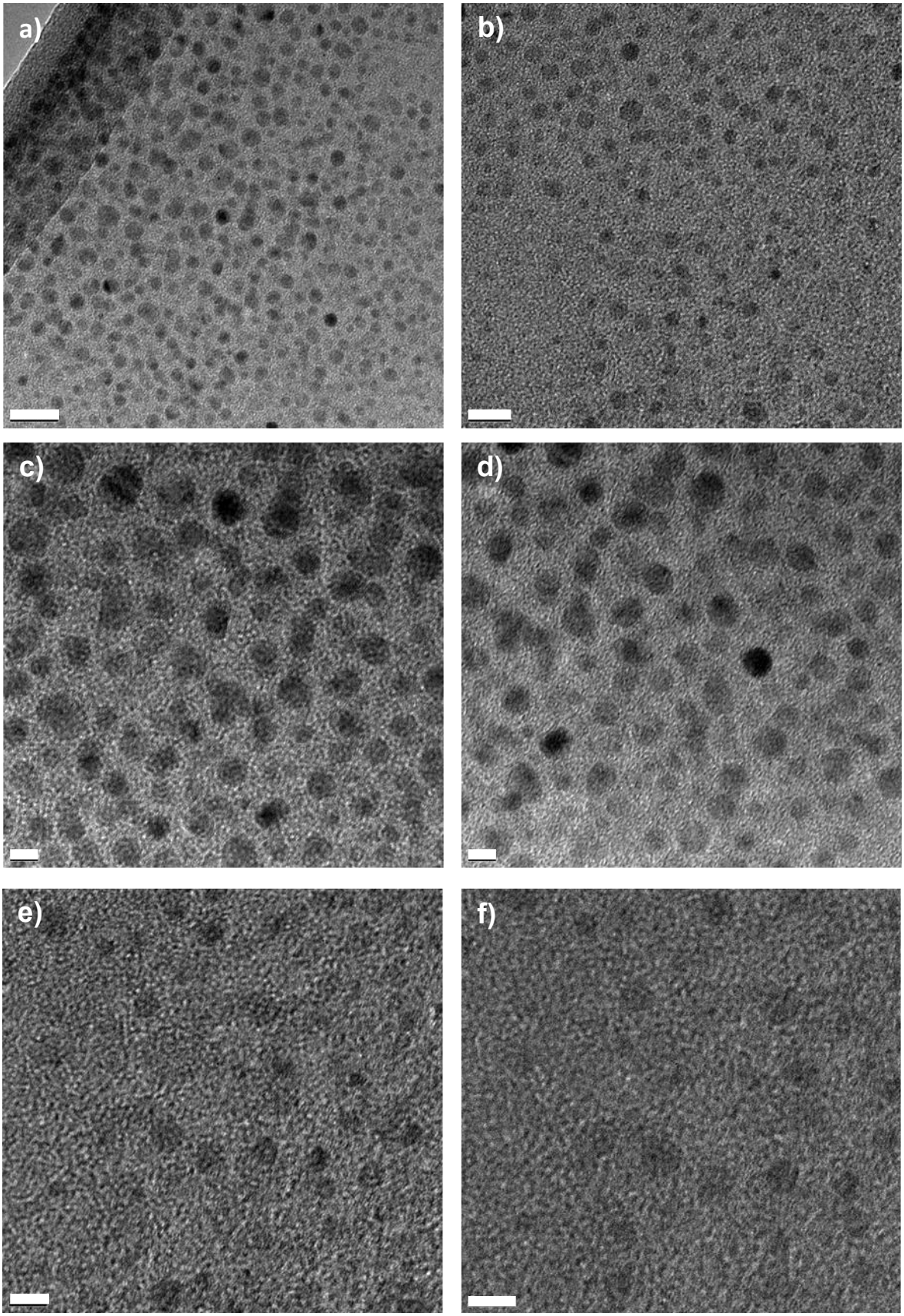

Figure 2.4.5: High resolution TEM images of **1**/PPP/$CHCl_3$ samples that were drop-casted on carbon-coated TEM grids. Scale bars equal **a)** 20 nm, **b)** 10 nm, **c)** - **f)** 5 nm.

Associated size distributions from TEM micrographs were measured (**Figure 2.4.6**). They show the homogeneous nature of the deposition with 80% of the particles from the solution appearing to be between 4 and 5.99 nm in diameter and all the remaining particles within the adjoining defined size categories (see **Figure 2.4.6,** below). This suggests that molecular species of the cages are experimentally visible.

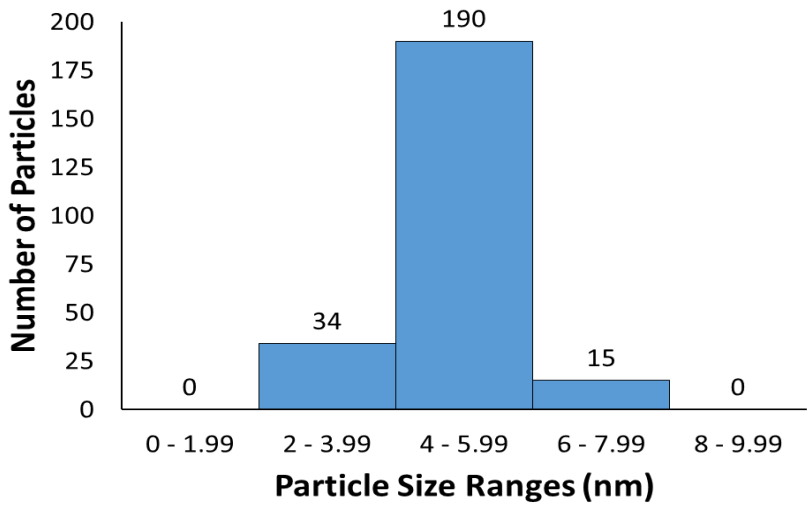

Figure 2.4.6: Particle-size distribution (measured from **Figure 2.4.4, d)**).

Atomic force microscopy (AFM) studies were conducted and are in-line with the electron microscopy experiments. For these AFM studies crystals of **1** (0.1 mg) were dissolved using PPP (0.05 mL) in $CHCl_3$ (1 mL) and drop-casted onto Highly Ordered Pyrolytic Graphite (HOPG). The sample was left to dry in air and then imaged with AFM analysis using tapping mode (**Figure 2.4.7**). Many particles can be identified on the HOPG samples; the AFM study confirms particle heights varying from 4 to 7 nm.

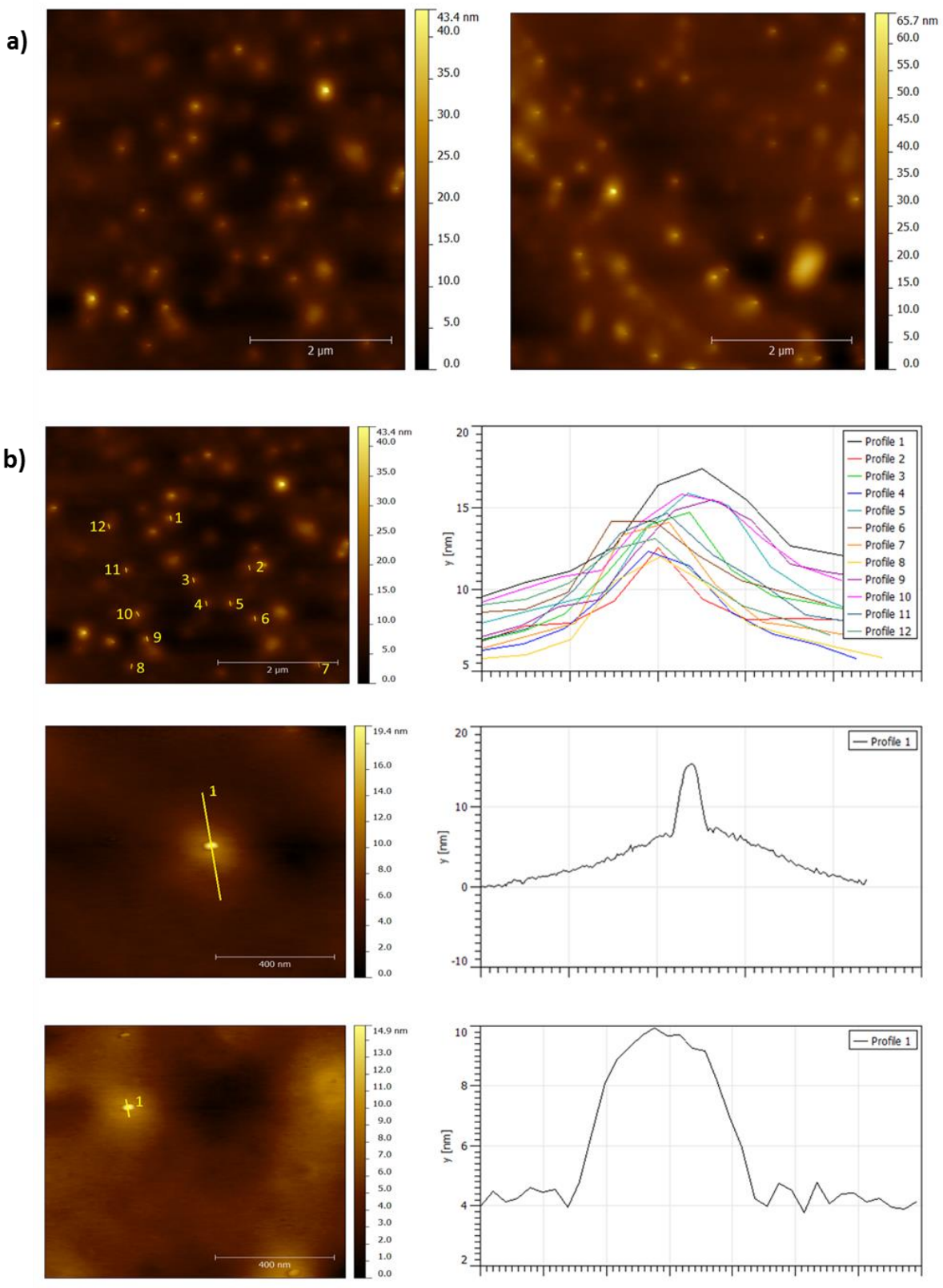

Figure 2.4.7: AFM Studies**. a)** AFM overview images, **b)** AFM/height analysis of individual particles of **1**/PPP/$CHCl_3$ solution drop-casted on HOPG.

2.5 Possible binding sites and uptake studies using **1**

Among the most intriguing developments in the field of supramolecular chemistry are examples that show how molecular cages can provide avenues to synthetic macromolecules with enzyme-type characteristics,[28–31] demonstrating how hollow local binding environments influence the transition states and ultimately performances of catalytic transformations. However, as new research strands are emerging and target guests are becoming more complex, achievements are hampered by a limited availability of capsules with large-diameter inner cavities whose dimensions, pore openings, surface properties and ligand characteristics allow the uptake and release of desired species at appropriate diffusion rates.[32–36]

A significant feature of {Cu_2}-based MOFs results from the lability of the terminal coordination solvent molecules of the SBUs which can facilitate guest binding. Particularly, symmetric structures with linearly arranged {Cu_2} SBUs can provide 'molecular traps' for suitably sized molecules whose donor atoms facilitate the bridging between the two active coordination sites of adjacent SBUs.[26,27,48] In this context, the observed symmetric arrangement of the six {Cu_2} units whose labile solvent molecules locate linearly opposite to each other and whose molecular axes point towards a single focal point is expected to be ideal to facilitate guest binding. The slightly tetragonally distorted octahedral inner arrangements in **1A** are characterized by {Cu–Cu} distances of 16.7, 15.9 and 15.6 Å, and 16.6, 16.4 and 15.4 Å of opposite located {Cu_2} units. Further binding sites are provided by {Cu_2} units of the outer shell whose labile solvent sites point to the inside of the molecular entities. Noteworthy are the 'super-paddlewheel' units in **1A** which have previously been employed to trap suitably sized guests (for example, CO_2 gas molecules, pyrazine or pyridine derivatives) between opposite located {Cu_2} units.[26,27,48] The observed Cu–Cu distances in these sub-units in **1A** vary between *ca.* 9.1 and 9.2 Å. The cages represent highly augmented species with exceptionally large void spaces and nanoscopic openings as visualised by the space-filling representations (**Figure 2.3.5**).

Based on the crystal data, the largest pore/window openings in **1** involving the outer square and triangular faces are represented by max. cross-sectional distances of *ca*. 9.8 Å (C-C atom distance between opposite phenyl rings) and 6.8 Å (C-C atom distance between adjacent phenyl rings), respectively. In **1A** the four square openings allow two orthogonal channels to extend through the entire diameter of the cage. This structural feature of **1A** provides facile access to the central cavity and is expected to promote uptake or release of guest molecules at high diffusion rates. One should note that where $\{Cu_2\}$ units locate below the centre of the square faces, four smaller windows provide accessibility to the inner sphere. In addition, triangular faces, afford accessible windows to the binding sites associated with the sub-cages or 'molecular traps' that make up **1**. Possible interactions between the solubilised cages and secondary small, functionalising molecules that can potentially interact with the cages were evaluated in preliminary steady-state and time-resolved fluorescence experiments using a fluorescent yellow coloured chromophore known as 7-amino-4-methylcoumarin (AMC) (**Figure 2.5.1**).

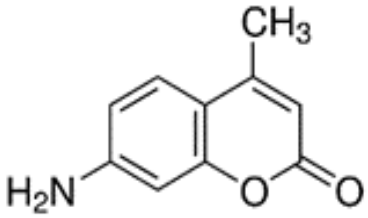

Figure 2.5.1: Molecular structure of 7-amino-4-methylcoumarin (AMC).

2.5.1 Uptake studies using crystals of **1**

Crystals of **1** when dispersed in an AMC/$CHCl_3$ solution (*ca.* 5 x 10^{-9} M) appear to adsorb 7-amino-4-methylcoumarin (AMC). The solid material of **1** undergoes a colour change from blue to a dark blue/green colour suggesting that absorption of the yellow coloured AMC takes place (**Figure 2.5.1**, **a)**). The fluorescence of the AMC/$CHCl_3$ solution with dispersed crystals of **1** was recorded over time. The solutions give rise to a fluorescence emission centred at 398 nm when excited at 338 nm. The fluorescence intensity of the solution is shown to decrease, suggesting that the concentration of AMC in solution is decreasing whilst being absorbed into crystals of **1**.

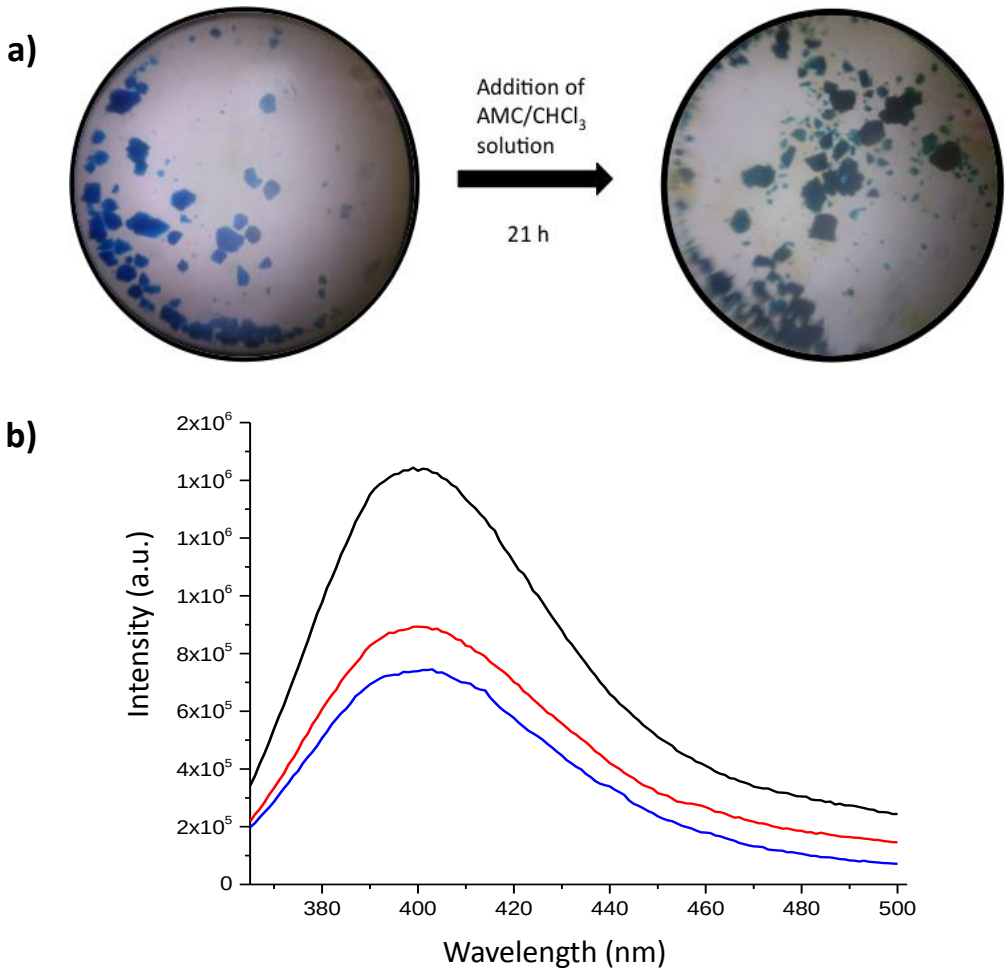

Figure 2.5.2: a) Images of crystals of **1** that were dispersed in a solution of AMC in $CHCl_3$ (*ca.* 5 x 10^{-9} M) highlighting the observed colour change. **b)** Fluorescence spectra when a few individual crystals of **1** were added to the solution of AMC in $CHCl_3$ (*ca.* 5 x 10^{-9} M). **Black line**: AMC/$CHCl_3$ solution. **Red line: 1** soaked in AMC/$CHCl_3$ solution for 30 minutes. **Blue line: 1** soaked in AMC/$CHCl_3$ solution for 20 hours.

2.5.2 Uptake studies using dissolved molecules of **1**/PPP

The dissolution of **1** can be monitored using UV-vis absorbance spectroscopy whereby signals that arise from π-π*and n–π* transitions of the **L1** ligand can be traced (**Figure 2.5.3**, **a)**). Upon dissolving individual crystals of **1** using 4-(3-phenylpropyl)pyridine (PPP) in $CHCl_3$, weak bands emerge at 286 and 307 nm next to a strong signal whose absorbance maximum is reached below 275 nm that predominantly arises from the excess of PPP in solution. An AMC solution in $CHCl_3$ shows a maximum absorbance at 338 nm. Excitation spectra were measured for solutions of AMC, **1**/PPP/AMC and **1**/PPP (**Figure 2.5.3, b)**). Light of different wavelengths is used to excite each solution and the relative fluorescence intensity of those solutions were recorded. Both the AMC and **1**/PPP/AMC solutions show fluorsecence maxima when excited with a wavelength centred at 338 nm. The **1**/PPP solution shows weak fluorescence when excited with a wavelength centred at 304 nm (**Figure 2.5.3**, **a) inset**). Based on the absorbance and excitation spectra, an excitation wavelength of 338 nm was applied. It is observed that the fluorescence emission maximum of AMC/$CHCl_3$ solutions is efficiently quenched when aliquots of **1**/PPP are added, leaving the lower intensity emission bands at 369 and 384 nm which originate from **1** (**Figure 2.5.3**, **c)**). This strong fluorescence quenching effect indicates that the fluorophore molecules bind to **1**/PPP resulting in superimposable fluorescence spectra at an AMC/cage mole ratio of ca. 30:1 (**Figure 2.4.4**). Addition of PPP dissolved in $CHCl_3$ to a solution of AMC in $CHCl_3$ shows negligible quenching of AMC fluorescence. The interactions between AMC and the cage molecules and the kinetics of this intermolecular quenching process were evaluated by Stern–Volmer analyses (**Figure 2.5.3**, **d)**). The I_0/I versus [**1**] plot is characteristic for static quenching and the high $K_{Stern-Volmer}$ constant (**Figure 2.5.3**, **d) inset**) is indicative of strong binding between potential host and guest molecules. Corresponding fluorescence lifetime measurements involving additions of **1**/PPP to an AMC solution in $CHCl_3$ give typical mono-exponential decays in the nanosecond range (**Figure 2.5.4**). The lifetime observed for a solution of AMC in $CHCl_3$ was 6.01 ns while for solutions of **1**/PPP and **1**/PPP/AMC in $CHCl_3$ it was observed to be 2.87 and 2.90 ns, respectively. The observed lifetimes do not depend on the relative quencher/fluorophore ratio, which further supports the static interactions between host and guest molecules in the ground state. In addition, while it is clear that fluorescence from AMC is quenched by interactions with **1**, the

fluorescence from **1** which likely derives from the **L1** ligand is unaffected by the possible interaction with AMC.

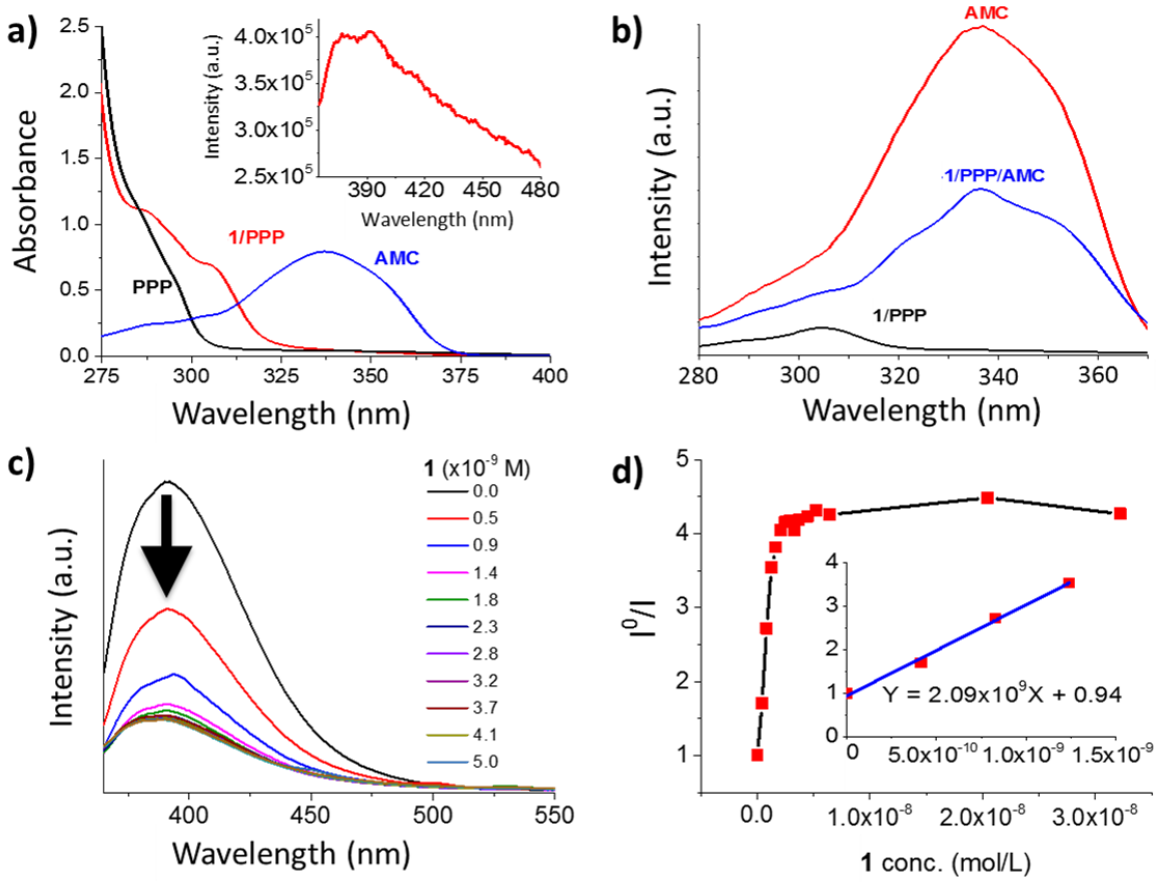

Figure 2.5.3: a) UV-vis absorbance spectra. **Black line:** PPP in $CHCl_3$ ([PPP] = 1×10^{-5} M). **Red line: 1**/PPP in $CHCl_3$ ([**1**] = 2×10^{-5} M, [PPP] = 7.5×10^{-4} M). **Blue line:** 7-amino-4-methylcoumarin (AMC) in $CHCl_3$ ([AMC] = 1×10^{-5} M). **a) inset**; Fluorescence spectrum of **1**/PPP in $CHCl_3$ ([**1**] = 2×10^{-6} M, [PPP] = 7.5×10^{-5} M, λ_{ex} = 338 nm). **b)** Excitation spectra. **Red line:** AMC in $CHCl_3$ (1×10^{-7} M, λ_{em} = 391 nm). **Blue line: 1**/PPP/AMC in $CHCl_3$ ([**1**] = 8×10^{-8} M, [PPP] = 3×10^{-6} M, [AMC] = 4×10^{-7} M, λ_{em} = 391 nm). **Black line: 1**/PPP ([**1**] = 2×10^{-7} M, [PPP] = 7.5×10^{-6} M, λ_{em} = 387 nm). **c)** Fluorescence titrations characterizing the host–guest interactions between a $CHCl_3$ solution of 7-amino-4-methylcoumarin (AMC) ([AMC] = 1×10^{-7} M, λ_{em} = 391 nm; λ_{ex} = 338 nm) and a solution of **1**/PPP/$CHCl_3$. Fluorescence quenching when aliquots of a **1**/PPP solution in $CHCl_3$ ([**1**] = 2×10^{-7} M, [PPP] = 7.5×10^{-6} M) are added to an AMC solution in $CHCl_3$ (1×10^{-7} M). **d)** Stern–Volmer plots (λ_{em} = 391 nm; λ_{ex} = 338 nm) that are characteristic for static quenching and indicating binding (**inset**) between **1** and AMC.

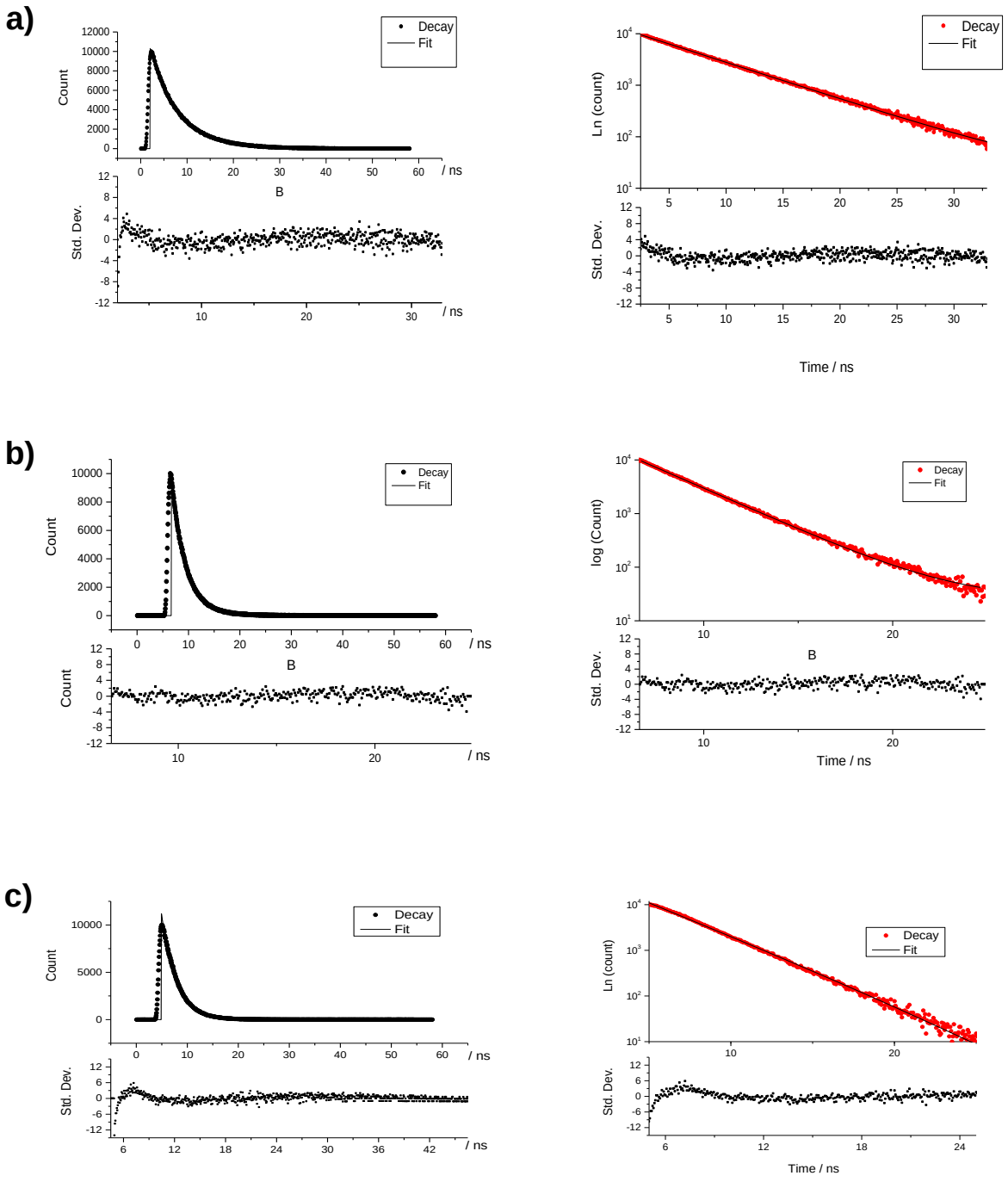

Figure 2.5.4: Photophysical Studies. **a)** Lifetime measurement of AMC in $CHCl_3$ (1 x 10^{-7} M, λ_{ex} = 338 nm, λ_{em} = 391 nm). τ = 6.01 ns (mono-exponential fit). **b)** Lifetime measurement of **1**/PPP in $CHCl_3$ ([**1**] = 2 x 10^{-7} M, [PPP] = 7.5 x 10^{-6} M, λ_{ex} = 338 nm, λ_{em} = 391 nm). τ = 2.90 ns (mono-exponential fit). **c)** Lifetime measurement of **1**/PPP/AMC in $CHCl_3$ ([**1**] = 7 x 10^{-9} M, [PPP] = 7.5 x 10^{-6} M, [AMC] = 1 x 10^{-7} M, λ_{ex} = 338 nm, λ_{em} = 391 nm). τ = 2.87 ns (mono-exponential fit).

Consecutive STEM analyses of the resulting **1**/PPP/AMC/$CHCl_3$ solutions that were drop-casted on grids give rise to mono-dispersed species (similar to those of previously discussed in **Figures 3.4.4 – 3.4.6**) suggesting that the molecular cages (**1**/PPP) maintain their integrity upon AMC interaction (**Figure 2.5.5**).

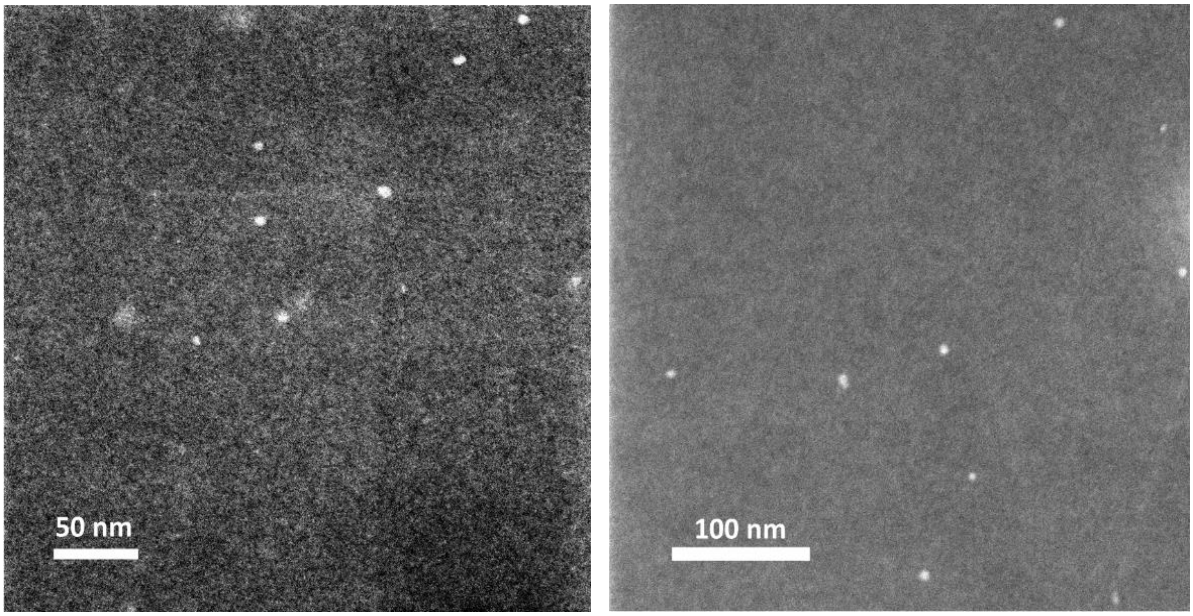

Figure 2.5.5: Scanning transmission electron microscopy (STEM) images of **1**/PPP/AMC/$CHCl_3$ ([**1**] = 8 x 10^{-8} M, [PPP] = 3 x 10^{-6} M, [AMC] = 4 x 10^{-9} M) samples that were drop-casted on carbon-coated TEM grids (binding study involving the addition of **1**/PPP to an AMC/$CHCl_3$ solution); acceleration voltage of 300 kV. Low-concentrated samples that approximately match those used in the photophysical studies.

2.6 Conclusion and future work

A synthetic approach to spherical coordination cages whose cross-sectional diameters are among the largest of crystallographically characterised synthetic, hollow supramolecular species is reported. The tri-functional organic ligand **H_3L1** promotes the formation of cage-type molecules of **1** that can be solubilised and potentially functionalised through coordinative interactions at the labile coordination sites of the {Cu_2} SBUs. The coordination cages may be regarded as endohedral supramolecular cages that are composed of multiple smaller sub-cages providing numerous binding sites. The molecular species are composed of defined, various-sized cavities, containing different pore/channel openings and their topological features are comparable to those of 'paddlewheel'-based MOFs with A_3X_4 composition.

Correspondingly to endohedral Pd(II)/Pt(II)-based coordination cages,[37–41] the structural complexity distinguishes these supramolecular Keplerates from large diameter, single-shell MOPs and provides a new perspective to supramolecular host–guest approaches. Particularly noteworthy are the oppositely located labile coordination sites of the {Cu_2} units that can facilitate guest binding and which are known to act as molecular traps.[26] Initial photophysical studies suggest that these sites, together with the intricate molecular structures give rise to guest-binding. Electron microscopy studies indicate that the nanoscopic species are accessible on a single-molecule level.

The structural characteristics of **1** are expected to provide possibilities for facile functionalisation at the periphery, for complex separations and for catalytic transformations utilising the different cavities of the sub-cages. Future research will investigate these aspects. Further, we will investigate the host–guest interactions/structures in more detail and focus on resolving, discrete atom conformations in the central cavity of the cages.

2.7 References

1 T. R. Cook, Y.-R. Zheng and P. J. Stang, *Chem. Rev.*, 2013, **113**, 734–777.

2 H. Furukawa, K. E. Cordova, M. O'Keeffe and O. M. Yaghi, *Science*, 2013, **341**, 1230444.

3 J. J. Perry IV, J. A. Perman and M. J. Zaworotko, *Chem. Soc. Rev.*, 2009, **38**, 1400.

4 V. Guillerm, D. Kim, J. F. Eubank, R. Luebke, X. Liu, K. Adil, M. S. Lah and M. Eddaoudi, *Chem. Soc. Rev.*, 2014, **43**, 6141–6172.

5 M. Yoshizawa, J. K. Klosterman and M. Fujita, *Angew. Chem. Int. Ed.*, 2009, **48**, 3418–3438.

6 M. D. Pluth, R. G. Bergman and K. N. Raymond, *Acc. Chem. Res.*, 2009, **42**, 1650–1659.

7 S. Zarra, D. M. Wood, D. a Roberts and J. R. Nitschke, *Chem. Soc. Rev.*, 2014, **44**, 419–432.

8 X. Hang, B. Liu, X. Zhu, S. Wang, H. Han, W. Liao, Y. Liu and C. Hu, *J. Am. Chem. Soc.*, 2016, **138**, 2969–2972.

9 S. Leininger, B. Olenyuk and P. J. Stang, *Chem. Rev.*, 2000, **100**, 853–908.

10 D. J. Tranchemontagne, Z. Ni, M. O'Keeffe and O. M. Yaghi, *Angew. Chem. Int. Ed.*, 2008, **47**, 5136–5147.

11 S. J. Dalgarno, N. P. Power and J. L. Atwood, *Coord. Chem. Rev.*, 2008, **252**, 825–841.

12 J.-R. Li and H.-C. Zhou, *Nat. Chem.*, 2010, **2**, 893–898.

13 J. Bai, *Science*, 2003, **300**, 781–783.

14 J. M. Breen and W. Schmitt, *Angew. Chem. Int. Ed.*, 2008, **47**, 6904–6908.

15 X.-S. Wang, M. Chrzanowski, W.-Y. Gao, L. Wojtas, Y.-S. Chen, M. J. Zaworotko and S. Ma, *Chem. Sci.*, 2012, **3**, 2823–2827.

16 M. D. Ward and P. R. Raithby, *Chem. Soc. Rev.*, 2013, 1619–1636.

17 W. Cullen, M. C. Misuraca, C. A. Hunter, N. H. Williams and M. D. Ward, *Nat. Chem.*, 2016, **8**, 231–236.

18 Q.-Q. Wang, S. Gonell, S. H. A. M. Leenders, M. Dürr, I. Ivanović-Burmazović and J. N. H. Reek, *Nat. Chem.*, 2016, **8**, 225–230.

19 C. García-Simón, M. Garcia-Borràs, L. Gómez, T. Parella, S. Osuna, J. Juanhuix, I. Imaz, D. Maspoch, M. Costas and X. Ribas, *Nat. Commun.*, 2014, **5**, 5557.

20 K. Wu, K. Li, Y.-J. Hou, M. Pan, L.-Y. Zhang, L. Chen and C.-Y. Su, *Nat. Commun.*, 2016, **7**, 10487.

21 B. Therrien, *Top. Curr. Chem.*, 2012, **319**, 35–55.

22 J. Wang, C. He, P. Wu, J. Wang and C. Duan, *J. Am. Chem. Soc.*, 2011, **133**, 12402–12405.

23 X. Yan, T. R. Cook, P. Wang, F. Huang and P. J. Stang, *Nat. Chem.*, 2015, **7**, 342–348.

24 T. K. Ronson, S. Zarra, S. P. Black and J. R. Nitschke, *Chem. Commun.*, 2013, **49**, 2476–90.

25 O. M. Yaghi, M. O'Keeffe, N. W. Ockwig, H. K. Chae, M. Eddaoudi and J. Kim, *Nature*, 2003, **423**, 705–714.

26 J.-R. Li, J. Yu, W. Lu, L.-B. Sun, J. Sculley, P. B. Balbuena and H.-C. Zhou, *Nat. Commun.*, 2013, **4**, 1538.

27 V. Brega, M. Zeller, Y. He, H. Peter Lu and J. K. Klosterman, *Chem. Commun.*, 2015, **51**, 5077–5080.

28 C. J. Hastings, D. Fiedler, R. G. Bergman and K. N. Raymond, *J. Am. Chem. Soc.*, 2008, **130**, 10977–10983.

29 M. J. Wiester, P. A. Ulmann and C. A. Mirkin, *Angew. Chem. Int. Ed.*, 2011, **50**, 114–137.

30 Y.-T. Lai, E. Reading, G. L. Hura, K.-L. Tsai, A. Laganowsky, F. J. Asturias, J. A. Tainer, C. V. Robinson and T. O. Yeates, *Nat. Chem.*, 2014, **6**, 1065–1071.

31 D. M. Kaphan, M. D. Levin, R. G. Bergman, K. N. Raymond and F. D. Toste, *Science*, 2015, **350**, 1235–1238.

32 B. Olenyuk, J. a Whiteford, a Fechtenkötter and P. J. Stang, *Nature*, 1999, **398**, 796–799.

33 S. Sato, J. Iida, K. Suzuki, M. Kawano, T. Ozeki and M. Fujita, *Science*, 2006, **313**, 1270–1273.

34 Q.-F. Sun, J. Iwasa, D. Ogawa, Y. Ishido, S. Sato, T. Ozeki, Y. Sei, K. Yamaguchi and M. Fujita, *Science*, 2010, **328**, 1144–1147.

35 N. Giri, M. G. Del Pópolo, G. Melaugh, R. L. Greenaway, K. Rätzke, T. Koschine, L. Pison, M. F. C. Gomes, A. I. Cooper and S. L. James, *Nature*, 2015, **527**, 216–220.

36 D. Fujita, Y. Ueda, S. Sato, H. Yokoyama, N. Mizuno, T. Kumasaka and M. Fujita, *Chem*, 2016, **1**, 91–101.

37 Q.-F. Sun, T. Murase, S. Sato and M. Fujita, *Angew. Chem. Int. Ed.*, 2011, **50**, 10318–10321.

38 B. Sun, M. Wang, Z. Lou, M. Huang, C. Xu, X. Li, L.-J. Chen, Y. Yu, G. L. Davis, B. Xu, H.-B. Yang and X. Li, *J. Am. Chem. Soc.*, 2015, **137**, 1556–1564.

39 I. A. Bhat, D. Samanta and P. S. Mukherjee, *J. Am. Chem. Soc.*, 2015, **137**, 9497–9502.

40 Q.-F. Sun, S. Sato and M. Fujita, *Nat. Chem.*, 2012, **4**, 330–333.

41 M. Han, D. M. Engelhard and G. H. Clever, *Chem. Soc. Rev.*, 2014, **43**, 1848–1860.

42 R. K. Castellano and J. Rebek, *J. Am. Chem. Soc.*, 1998, **120**, 3657–3663.

43 K. Sonogashira, *J. Organomet. Chem.*, 2002, **653**, 46–49.

44 K. Sonogashira, Y. Tohda and N. Hagihara, *Tetrahedron Lett.*, 1975, **16**, 4467–4470.

45 A. C. Legon and D. J. Millen, *Chem. Soc. Rev.*, 1987, **16**, 467.

46 C. A. Hunter and J. K. M. Sanders, *J. Am. Chem. Soc.*, 1990, **112**, 5525–5534.

47 K. Byrne, M. Zubair, N. Zhu, X. P. Zhou, D. S. Fox, H. Zhang, B. Twamley, M. J. Lennox, T. Düren and W. Schmitt, *Nat. Commun.*, 2017, **8**, 1–9.

48 N. Zhu, M. J. Lennox, G. Tobin, L. Goodman, T. Düren and W. Schmitt, *Chem. - A Eur. J.*, 2014, **20**, 3595–3599.

49 S. Sarkar, S. Q. N. Shah, H. Bögge, A. X. Trautwein, M. Schmidtmann, B. Hauptfleisch, A. Müller, P. Kögerler, V. Schünemann and S. Sarkar, *Angew. Chem. Int. Ed.*, 2002, **38**, 3238–3241.

50 S. S. Y. Chui, S. M. F. Lo, J. P. H. Charmant, a G. Orpen and I. D. Williams, *Science*, 1999, **283**, 1148–1150.

51 B. Chen, M. Eddaoudi, S. T. Hyde, M. O'Keeffe and O. M. Yaghi, *Science*, 2001, **291**, 1021–1023.

52 W. Lu, D. Yuan, A. Yakovenko and H.-C. Zhou, *Chem. Commun.*, 2011, **47**, 4968.

53 A. F. Wells, *Acta Cryst. A*, 1986, **42**, 133–134.

54 H. Furukawa, J. Kim, K. E. Plass and O. M. Yaghi, *J. Am. Chem. Soc.*, 2006, **128**, 8398–8399.

55 J.-R. Li, D. J. Timmons and H.-C. Zhou, *J. Am. Chem. Soc.*, 2009, **131**, 6368–6369.

56 L. Zhang, C. I. Onet, R. Clérac, M. Rouzières, B. Marzec, M. Boese, M. Venkatesan and W. Schmitt, *Chem. Commun.*, 2013, **49**, 7400–7402.

57 V. Otero, D. Sanches, C. Montagner, M. Vilarigues, L. Carlyle, J. A. Lopes and M. J. Melo, *J. Raman Spectrosc.*, 2014, **45**, 1197–1206.

58 B. H. Stuart, *Infrared Spectroscopy: Fundamentals and Applications*, John Wiley & Sons, Ltd, 2005.

59 K. Nakamoto, *Infrared and Raman Spectra of Inorganic and Coordination Compounds*, John Wiley & Sons, Ltd, 6th edn., 2008.

60 G. B. Deacon and R. J. Phillips, *Coord. Chem. Rev.*, 1980, **33**, 227–250.

61 A. Gupta, S. Chempath, M. J. Sanborn, L. A. Clark and R. Q. Snurr, *Mol. Simul.*, 2003, **29**, 29–46.

62 S. L. Mayo, B. D. Olafson and W. A. Goddard, *J. Phys. Chem.*, 1990, **94**, 8897–8909.

63 A. K. Rappe, C. J. Casewit, K. S. Colwell, W. A. Goddard and W. M. Skiff, *J. Am. Chem. Soc.*, 1992, **114**, 10024–10035.

64 J. J. Potoff and J. I. Siepmann, *AIChE J.*, 2001, **47**, 1676–1682.

65 K. S. Walton and R. Q. Snurr, *J. Am. Chem. Soc.*, 2007, **129**, 8552–8556.

66 P. L. Llewellyn, F. Rodriquez-Reinoso, J. Rouqerol and N. Seaton, *Characterization of porous solids VII: proceedings of the 7th international symposium on the characterization of porous solids*, Elsevier, 2006.

67 L. D. Gelb and K. E. Gubbins, *Langmuir*, 1998, **14**, 2097–2111.

68 L. Sarkisov and A. Harrison, *Mol. Simul.*, 2011, **37**, 1248–1257.

69 R. C. Reid, T. K. Sherwood and R. E. Street, *The Properties of Gases and Liquids*, McGraw-Hill, 1987.

Chapter 3

A durable MOF for water oxidation catalysis

3 A durable MOF for water oxidation catalysis

3.1 Introduction

In this chapter a porous and highly stable metal-organic framework (MOF) is presented and its use as a water oxidation catalyst is explored. The ligand 4,4',4''-(benzene-1,3,5-triyltris(ethyne-2,1-diyl)tribenzoic acid (**H_3L2**), was initially chosen as it has previously been used within the research group to synthesise a range of MOFs containing Zn(II), Cu(II), and lanthanide ions.[1–4]

A structurally stable MOF with the formula $Me_2NH_2[Co_5(\mathbf{L2})_3(\mu_3\text{-}OH)_2(H_2O)_2(DMF)_2]$ (**2**) containing pentanuclear SBUs, was synthesised. The $\{Co_5\}$ SBU contains four solvent molecules in accessible binding sites on Co(II) ions and thus, the compound was considered to be used in water oxidation catalysis.[5,6] Water oxidation catalysis was envisioned considering that other cobalt(II)-containing MOFs have previously been used for this application.[7–10] Cobalt is an earth abundant metal and cobalt(II)-containing polyoxometalates as well as cobalt oxides have been shown to provide relatively cheap catalysts for water oxidation with good activity.[11–15]

The structure of **2,** its characterisation including gas sorption studies are discussed, followed by electrochemical and photochemical water oxidation studies, as well as MOF electrosynthesis experiments and water oxidation with the resulting MOF films.

3.2 Synthesis and characterisation of 4,4',4''-(benzene-1,3,5-triyltris (ethyne-2,1-diyl))tribenzoic acid, (**H_3L2**)

The ligand discussed in this chapter 4,4',4''-(benzene-1,3,5-triyltris(ethyne-2,1-diyl))tribenzoic acid, (**H_3L2**) was synthesised using a modified literature procedure (**Scheme 3.2.1**).[16] The first step involves the synthesis of 1,3,5-tris((trimethylsilyl)ethynyl)benzene using a Sonogashira coupling reaction.[17] For this purpose, 1,3,5-tribromobenzene was dissolved with ethynyltrimethylsilane in TEA. $[Pd^{II}(PPh_3)_2Cl_2]$ and $Cu^{I}I$ catalysts were added and the mixture was heated to 80°C for 16 hours under N_2 atmosphere. The solvent was removed under vacuum, the crude product dissolved in DCM and washed 3 times with a saturated NH_3 aqueous solution. A silica column was eluted with hexane yielding pure 1,3,5-tris((trimethylsilyl)ethynyl)benzene. Step two concerns the removal of the silyl groups. This was achieved by dissolving the 1,3,5-tris((trimethylsilyl)ethynyl)benzene in CH_2Cl_2, add and mixing it at 35°C for 4 hours with a concentrated K_2CO_3-MeOH solution. The K_2CO_3 was neutralised using a 1M HCl solution. The solvent was removed under vacuum and the crude product was purified using a silica column with a CH_2Cl_2 eluent yielding pure 1,3,5-triethynylbenzene. In step three a second Sonogashira coupling reaction was carried out to combine 1,3,5-triethynylbenzene and methyl 4-iodobenzoate by refluxing the reaction mixture at 80°C for 24 hours in a THF : TEA mixture (1 : 1 by volume). This was purified by washing the crude compound as in step one and then eluting using a silica column with a hexane : THF mixture as eluent (1 : 2 by volume) to yield pure trimethyl 4,4',4''-(benzene-1,3,5-triyltris(ethyne-2,1-diyl))tribenzoate. The final step involves a base catalysed de-esterification to remove the methyl groups and form the carboxylic acids. This was done using excess LiOH in a solvent mixture of THF : H_2O (1 : 1 by volume) and was carried out over 3 hours at room temperature. The THF was removed under vacuum leaving a solution in H_2O. The reaction mixture was acidified using a 1 M HCl solution precipitating crude product. This was washed with deionised H_2O, dried under vacuum and then purified using column chromatography with a THF mobile phase yielding pure 4,4',4''-(benzene-1,3,5-triyltris(ethyne-2,1-diyl)tribenzoic acid, **H_3L2**.

A combination of mass spectrometry and ^{1}H-NMR, ^{13}C-NMR, FT-IR and Raman spectroscopy experiments confirmed the formation of **H_3L2**. Characteristically, ^{1}H-NMR experiments in deuterated dimethyl sulfoxide give rise a singlet signal at 7.89 ppm with an integration of three protons corresponding to H-atoms located on the central phenyl ring

of the organic ligand. Two doublet signals found at 8.01 and 7.72 ppm, both of which integrate to six protons can be attributed to the twelve H-atoms on the remaining phenyl rings (**Figure 3.2.1**).

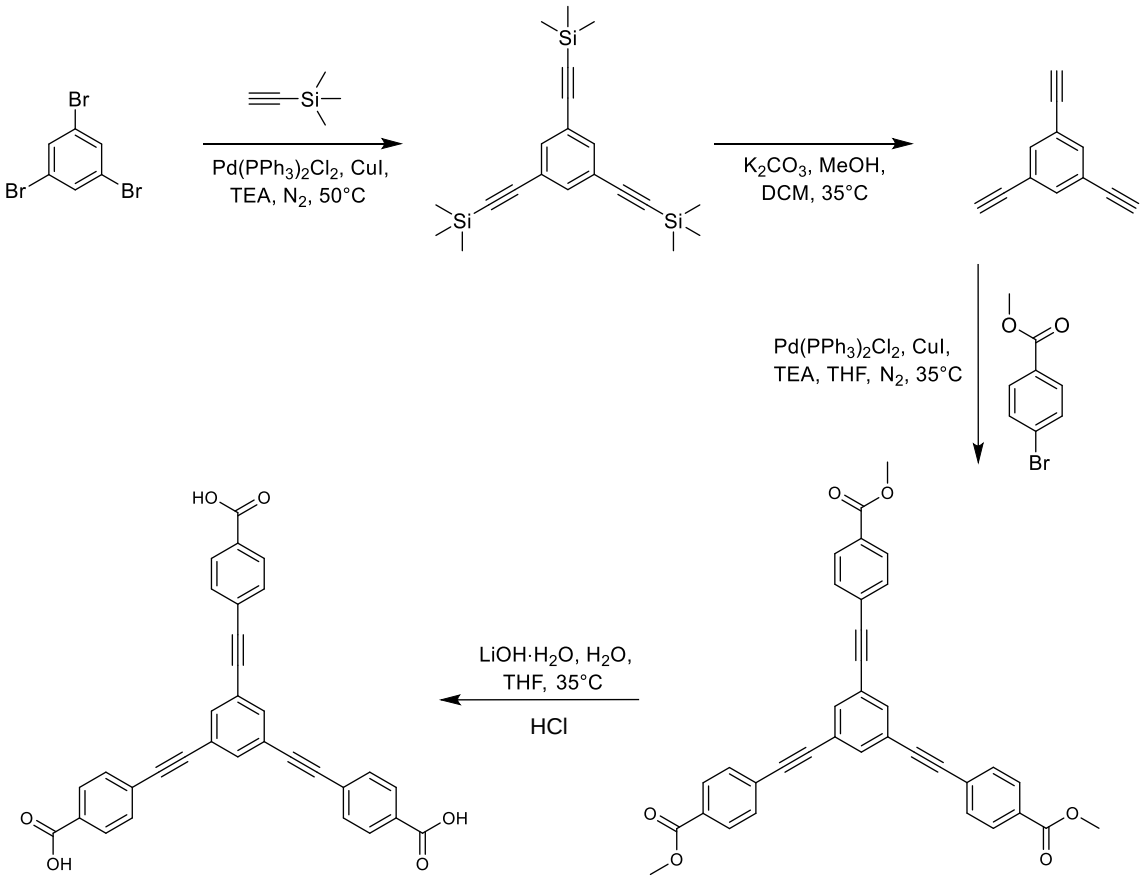

Scheme 3.2.1: Synthetic procedure used for the synthesis of **H_3L2**.

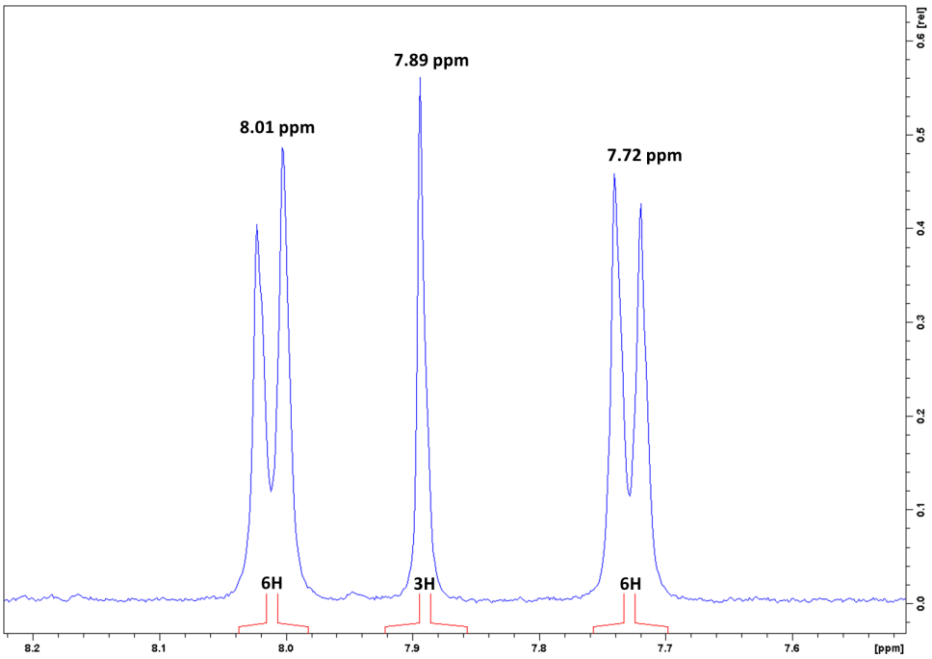

Figure 3.2.1: ^{1}H-NMR spectrum of **H_3L2** in DMSO-d_6.

3.3 $Me_2NH_2[Co_5(\mathbf{L2})_3(\mu_3\text{-}OH)_2(H_2O)_2(DMF)_2]$ (**2**)

3.3.1 Synthesis and structural characterisation of $Me_2NH_2[Co_5(\mathbf{L2})_3(\mu_3\text{-}OH)_2(H_2O)_2(DMF)_2]$ (**2**)

The self-assembly of **2** was observed when **H_3L2** and $Co(NO_3)_2{\cdot}6H_2O$ (1 : 2 molar ratio) were heated in DMF at 90°C for 48 hours. Phase-pure purple single crystals of **2** formed in the reaction mixture and were used for single crystal X-ray analysis. A yield of *ca.* 43% was obtained. **2** crystallises in the monoclinic space group *C*2/*c*. The compound has the molecular formula $Me_2NH_2[Co_5(\mathbf{L2})_3(\mu_3\text{-}OH)_2(H_2O)_2(DMF)_2]$.

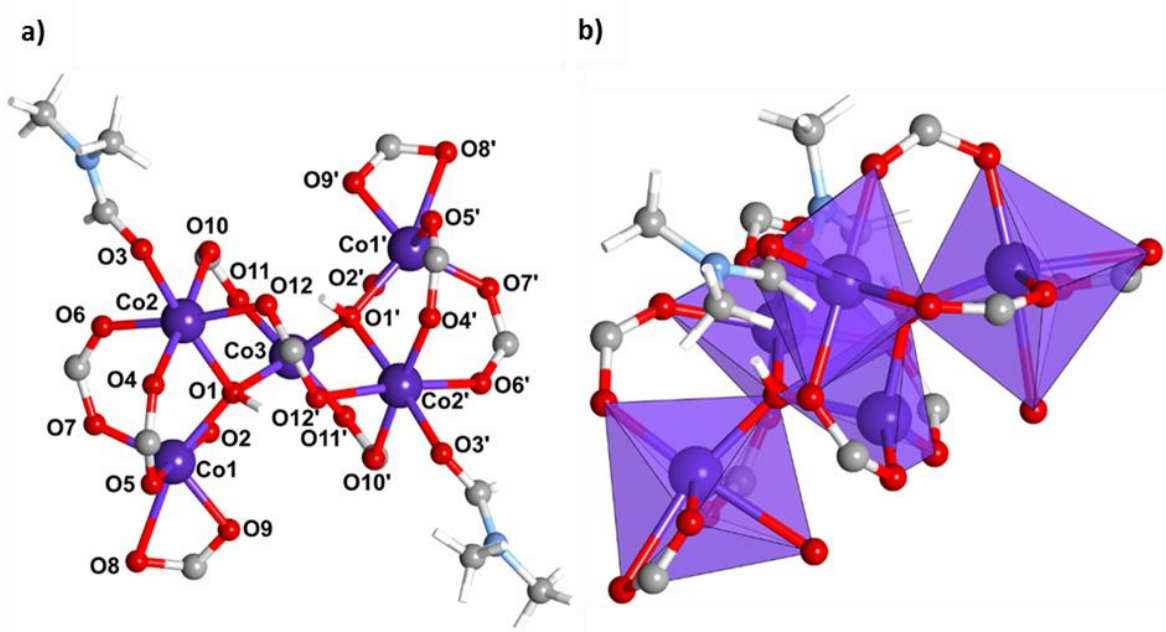

Figure 3.3.1: a) View down the crystallographic *b*-axis showing the $\{Co_5\}$ SBU with two μ_3-bridging OH^- groups, nine coordinated **L2** carboxylate ligand moieties, two DMF molecules and two H_2O molecules. **b)** View of the SBU down the [111]-direction using a transparent polyhedral representation to highlight the coordination environment of the four octahedrally coordinated Co(II) atoms and one tetrahedrally surrounded Co(II) atom (Co(3)). Colour key: Co purple, O red, C grey, N pale blue, H white.

2 contains a non-planar, pentanuclear {Co_5} SBU which is characterized by C2 rotational symmetry (**Figure 3.3.1**). The unit can be visualized as composed of two, symmetry-related, vertex-sharing, {μ_3-OH}-centered triangular Co(II) arrangements.

Altogether, the pentanuclear unit in **2** is stabilised by nine carboxylate moieties that derive from nine deprotonated **H_3L2** ligands which impart stability to the SBU. All carboxylate functionalities facilitate bidentate bridging modes, with the exception of two carboxylate moieties which contain weakly bound Co(1)-O(8)/O(8') bonding components (**Table 3.3.2**). The remaining coordination sites of the Co(II) centres are provided by the two μ_3-OH^- ligands, two coordinating monodentate DMF molecules and two weakly coordinating H_2O molecules (Co(1)-O(2)). The observed geometrical parameters and corresponding bond valence sum (BVS) analysis (**Table 3.3.3**) confirms that all Co ions adopt +2 oxidation states. Thus, this SBU relates to the corresponding MOFs containing pentanuclear Zn(II) complexes.[1] Correspondingly, each {Co_5} SBU carries an overall charge of -1 which is likely compensated for by disordered dimethyl ammonium counter ions ($Me_2NH_2^+$) which often form due to the hydrolysis of DMF upon heating.[18]

The asymmetric unit of **2** is represented by a single {μ_3-OH^-}-centered triangular Co(II) arrangement. It contains three crystallographically independent Co(II) ions, a μ_3-OH^- ligand, one coordinating DMF molecule and one coordinating H_2O molecule as well as one complete organic **L2** ligand and one half **L2** ligand. The environment around Co(1) is best described as distorted octahedral. The angles between *trans* located oxygen atoms surrounding Co(1) deviate widely from the ideal angle of 180° to give values of 133.7°, 156.2° and 174.7°. Co(2) also adopts an octahedral coordination geometry giving rise to angles between *trans* located oxygen atoms varying between 173.14° and 176.62°. The Co(3) atom adopts a distorted tetrahedral geometry that is characterised by angles varying between 95.03° and 120.3°, thus deviating from the ideal tetrahedral angle of 109.5°.

To further evaluate the coordination environments of the three structurally independent cobalt atoms in **2**, the program *SHAPEv2.5* was used. The software analyses the coordination environment surrounding each metal ion and evaluates the level of distortion from ideal angles of defined shapes. It is based on the algorithm defined by Pinsky and Avnir for the calculation of continuous shape measures and on definitions of minimal distortion paths as well as generalised interconversion coordinates.[19–21]

A value of 0 indicates a perfect fit to a particular shape while larger numbers highlight a greater level of distortion away from the ideal values (**Table 3.3.1**). This analysis supports the structural description whereby the binding environments of Co(1) and Co(2) were found to be best described as distorted octahedra whilst the coordination sphere of Co(3) can be assigned as distorted tetrahedral.

Table 3.3.1: SHAPEv2.1 evaluations of the coordination around each cobalt atom in **2**. The lowest number indicates the closest fit to the idealised geometry.

Structure [ML_6]	Hexagon	Pentagonal pyramid	Octahedron	Trigonal prism	Johnson pentagonal pyramid J2
Symmetry	D_{6h}	C_{5v}	O_h	D_{3h}	C_{5v}
Co(1)	30.954	18.133	4.479	11.118	21.487
Co(2)	31.622	28.261	0.277	15.352	31.677
Structure [ML_4]	Square	Tetrahedron	Seesaw or sawhorse (cis-divacant octahedral)		Axially vacant trigonal bipyramidal
Symmetry	D_{4h}	T_d	C_{2v}		C_{3v}
Co(3)	27.351	0.938	7.852		3.028

The Co-OH bond distances in **2** vary between 1.981(3) Å and 2.088(3) Å. The carboxylate Co-O bond distances vary between 1.939(3) Å and 2.162(3) Å, except for the Co(1)-O(8) bond distance of 2.446(7) Å. This bond is longer than most Co(II) carboxylate bonds but may still be regarded within the scope of weak Co(II)-O interactions. The coordinated DMF molecules give rise to a Co(2)-O(3) distance of 2.090(3) Å and the coordinated H_2O molecule results in a Co(1)-O(2) distance of 2.482(9) Å. The latter long bond distance can partially be explained by evaluating at the thermal ellipsoids in the crystal structure of **2**. The electron density of the oxygen atom of the coordination H_2O molecule is extremely dispersed, indicating that molecules are disordered in-between the Co(1) and Co(3) atom positions. There are also large thermal ellipsoids associated with O(8) and O(9) atoms of the carboxylate moiety. These atoms show a displacement of the atom over various positions contributing to the relatively long Co(1)-O(8) distance of 2.446(7) Å which is characteristic for weak carboxylate Co-O interactions.

Table 3.3.2: Selected bond distances and angles of coordination environments found in **2**.

Atoms	Distance [Å]	Atoms	Angle [°]
Co(1)-O(1)	**1.981(3)**	O(1)-Co(1)-O(8)	**156.20**
Co(1)-O(2)	**2.482(9)**	O(2)-Co(1)-O(5)	**174.7(2)**
Co(1)-O(5)	**2.019(3)**	O(7)-Co(1)-O(9)	**133.7(3)**
Co(1)-O(7)	**1.979(3)**	O(1)-Co(1)-O(5)	**98.76(13)**
Co(1)-O(8)	**2.446(7)**	O(1)-Co(1)-O(2)	**76.7(2)**
Co(1)-O(9)	**1.982(5)**	O(1)-Co(1)-O(7)	**107.75(14)**
		O(1)-Co(1)-O(9)	**102.2(2)**
Co(2)-O(1)	**2.088(3)**		
Co(2)-O(3)	**2.090(3)**	O(1)-Co(2)-O(3)	**173.14(11)**
Co(2)-O(4)	**2.075(3)**	O(4)-Co(2)-O(10)	**176.62(12)**
Co(2)-O(6)	**2.084(3)**	O(6)-Co(2)-O(12)	**174.30(12)**
Co(2)-O(10)	**2.128(3)**	O(1)-Co(2)-O(4)	**89.55(12)**
Co(2)-O(12)	**2.162(3)**	O(1)-Co(2)-O(6)	**97.00(11)**
		O(1)-Co(2)-O(10)	**93.64(13)**
Co(3)-O(1)	**2.012(3)**	O(1)-Co(2)-O(12)	**87.00(11)**
Co(3)-O(11)	**1.939(3)**		
		O(1)-Co(3)-O(11)	**103.29(13)**
		O(1)-Co(3)-O(11')	**116.26(14)**
		O(1)-Co(3)-O(1')	**95.03(17)**
		O(11)-Co(3)-O(11')	**120.3(2)**

Table 3.3.3: Bond valence sum (BVS) analysis of Co ions in **2**.

	R_0	β	Oxidation State
Co(1)	1.6920	0.37	2.035
Co(2)	1.6920	0.37	1.974
Co(3)	1.6920	0.37	2.006

From a topological point of view, it is interesting to note, that the equilateral triangular symmetry of the organic **L2**$^{3-}$ linker translates to the structure of the *in-situ* formed pentanuclear SBU. Hence, although the SBU formally represents a 9-connecting node, the stabilising organic ligands can be grouped into 3×3 sets whose struts point in three distinct directions of space and enclose *ca.* 120° angles. This binding geometry that is distinctively promoted by the shape and nature of the organic ligand, results in a 3D MOF structure with 'honeycomb' topology as portrayed when viewing down the crystallographic *c*-axis (**Figure 3.3.2**, **a)** & **c)**).

The peripheral phenyl rings on the **L2**$^{3-}$ linkers contribute to the overall stability of the framework by providing attractive edge to face interactions between the positively polarised CH moieties at the edge of phenyl rings to the electron-rich π-systems on adjacent phenyl rings as highlighted by green circles in **Figure 3.3.2**. The distances between interacting phenyl rings vary between *ca.* 3.1 to 3.5 Å when measuring from the centre of the hydrogen atom on one phenyl ring to the centroid of the interacting phenyl ring (edge to face interactions) which are typical distances for these types of interactions.[22,23]

The 3D structure of **2** is further characterised by two symmetry-equivalent interwoven nets. This twofold interpenetration is facilitated by parallel displacement π–π interactions between pairs of the central aromatic **L2**$^{3-}$ phenyl ring moieties (centroid–centroid distance of *ca.* 3.2 Å) aiding stability to the overall structure of the compound. Despite this dual interwoven nature, the structure of **2** is characterised by cylindrically pore openings that extend along the crystallographic *c*-axis with diameters varying between 8.2 and 17.0 Å when measuring hydrogen-hydrogen distances and 7.8 Å when measuring the oxygen-oxygen distances from the bound solvent molecules on either side of the pore opening (**Figure 3.3.3**).

The void space within the structure of **2** as calculated using the RASPA Software package accounts for 48.6% of the unit cell volume.[24] This space is filled by disordered solvent molecules and counter ions. Two types of cylindrical channels/pores can be seen in the crystal structure of **2** (**Figure 3.3.4**). Channels extending parallel to the crystallographic *c*-axis are *ca*. 6.2 Å in diameter. Smaller pores extend in the [101]-direction and appear to have openings which are *ca*. 5.7 Å in diameter.

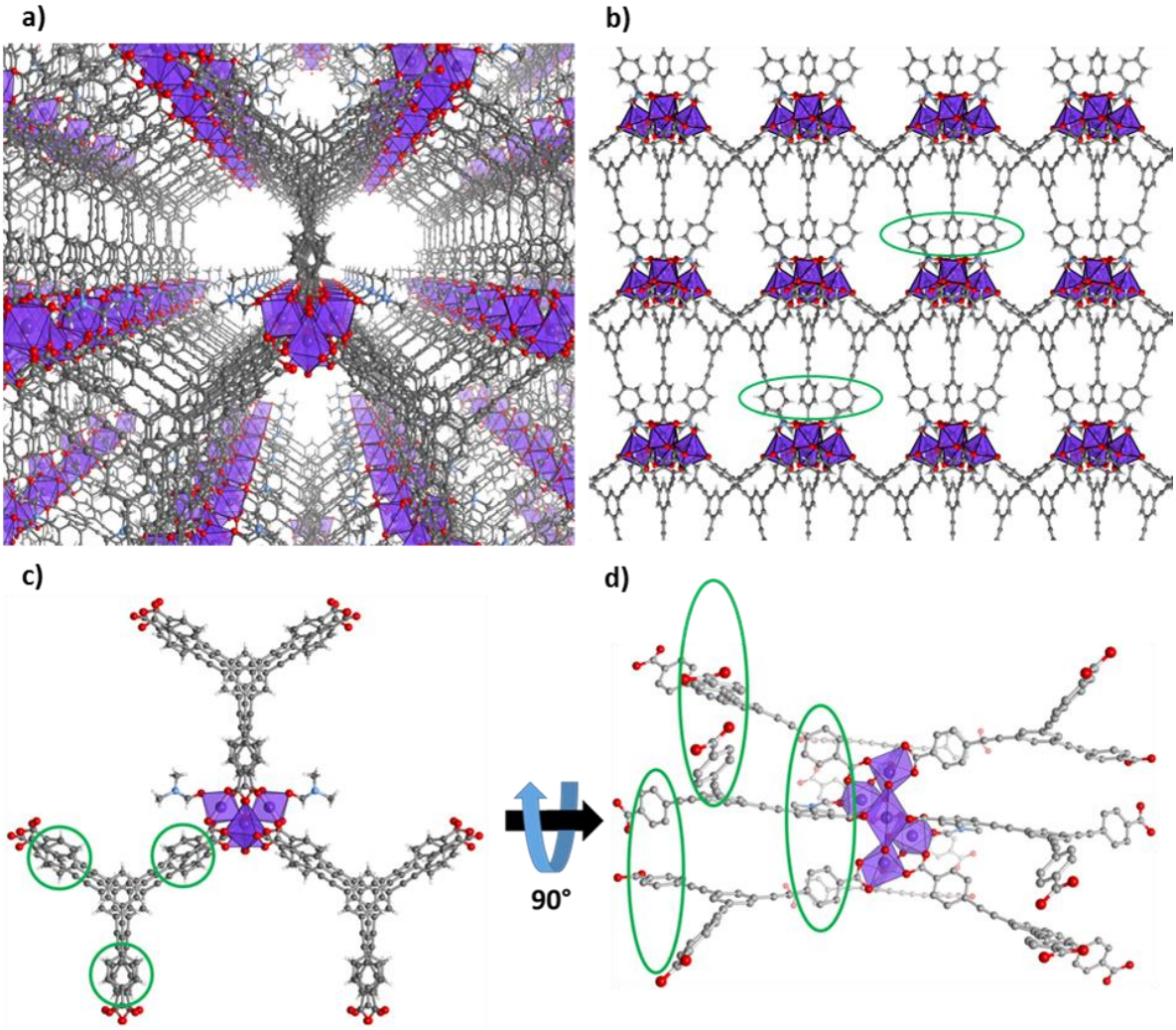

Figure 3.3.2: a), **b)** Single net representations of **2**. **a)** Perspective view down the crystallographic *c*-axis. **b)** View down the crystallographic *a*-axis with edge to face interactions highlighted by green circles. **c)**, **d)**, The $\{Co_5\}$ SBU with the nine $\mathbf{L2}^{3-}$ ligands attached with areas of edge to face interactions highlighted by green circles. Hydrogen atoms are excluded for clarity. **c)** Viewed in the direction of the crystallographic *c*-axis, **d)** Viewed in the direction of the crystallographic *b*-axis. Colour key: Co purple, O red, C grey, N pale blue, H white.

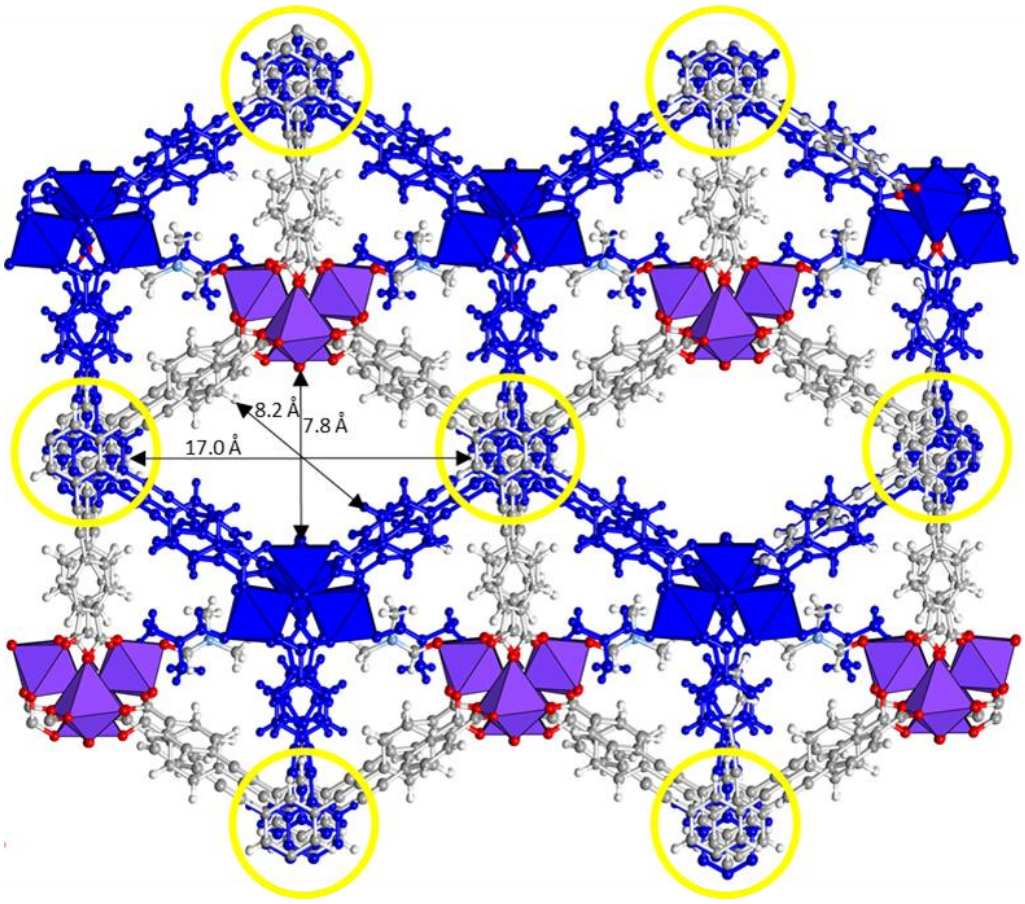

Figure 3.3.3: Ball and stick representation of **2** with one net highlighted in blue. Viewing down the crystallographic *c*-axis. Areas which contain parallel displacement π-π interactions between different nets are highlighted by yellow circles. Distances measured from atom centre to atom centre are shown. Colour key: Co purple, O red, N pale blue, C grey, H white.

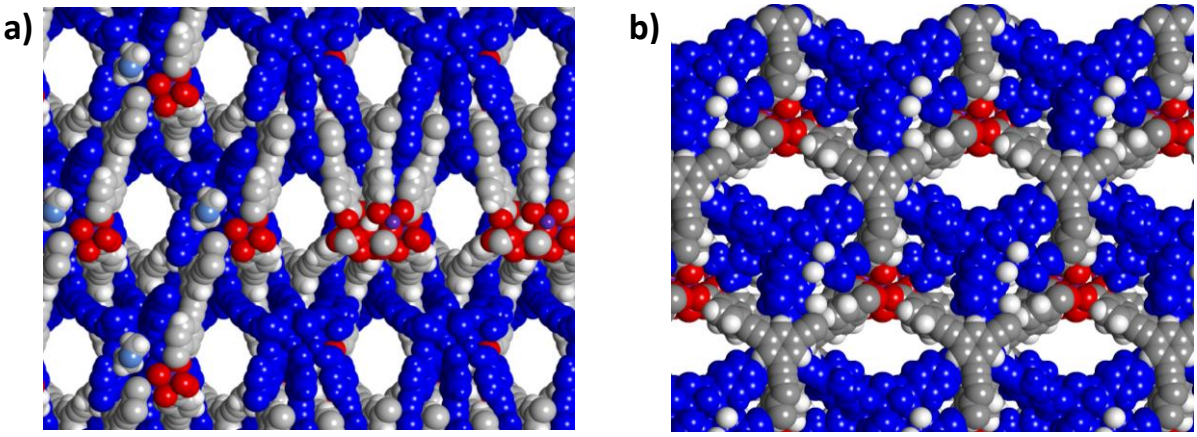

Figure 3.3.4: a), b) Space-filling representations of **2** with one net highlighted in blue. **a)** Viewing down the *101*-direction. **b)** Viewing down the *c*-axis. Colour key: Co purple, O red, N pale blue, C grey, H white.

Table 3.3.3: Crystallographic details for compound **2**.

Identification code	**2**
Empirical formula	$C_{105}H_{63}Co_5N_2O_{24}$
Formula weight	2031.22
Temperature/K	120(2)
Crystal system	Monoclinic
Space group	*C*2/*c*
a	25.154(5) Å
b	36.948(7) Å
c	19.512(4) Å
α	90.00°
β	123.47°
γ	90.00°
Volume	15126(5) $Å^3$
Z	4
Density (calculated)	0.892 g/cm^3
Absorption coefficient (μ)	0.585 mm^{-1}
F(000)	4136.0
Crystal size	0.5 × 0.4 × 0.3 mm^3
Radiation	MoKα (λ = 0.71073)
Theta range for data collection	1.10 to 26.02°
Index ranges	-30 ≤ h ≤ 31, -44 ≤ k ≤ 22, -25 ≤ l ≤ 24
Reflections collected	37414
Independent reflections	15154 [R_{int} = 0.0516]
Completeness to theta = 25.68°	100%
Refinement method	Full-matrix least-squares on F^2
Data/restraints/parameters	15154/11/625
Goodness-of-fit on F^2	0.942
Final R indexes [I>=2σ(I)]	R_1 = 0.0543, wR_2 = 0.1433
Final R indexes [all data]	R_1 = 0.0851, wR_2 = 0.1514
Largest diff. peak/hole	0.665/-0.659 e $Å^{-3}$

3.3.2 Physicochemical characterisation of **2**

3.3.2.1 X-ray powder diffraction

For X-ray powder diffraction experiments crystals of **2** were ground into powder form and a PXRD pattern was recorded on an APEX II DUO X-ray diffractometer to characterise the phase-purity of the synthesised bulk material. The PXRD pattern was measured in a capillary at 220 K to obtain low-angle reflections and to avoid loss of crystallinity associated with solvent evaporation from the sample (**Figure 3.3.5**). The experimental pattern and a simulated PXRD pattern (based on the single crystal X-ray diffraction data) match closely confirming the phase-purity of the synthesised material. Three major signals are visible in the measured pattern between $2\theta = 4$ and 10^{o}. The low-angle signal is broad and centred at $2\theta = 4.92°$. This signal appears to be resolved into two signals at 4.82° and 5.26° in the simulated pattern. The signals in the measured pattern at 7.05° and 8.48° match closely with the reflections in the simulated pattern.

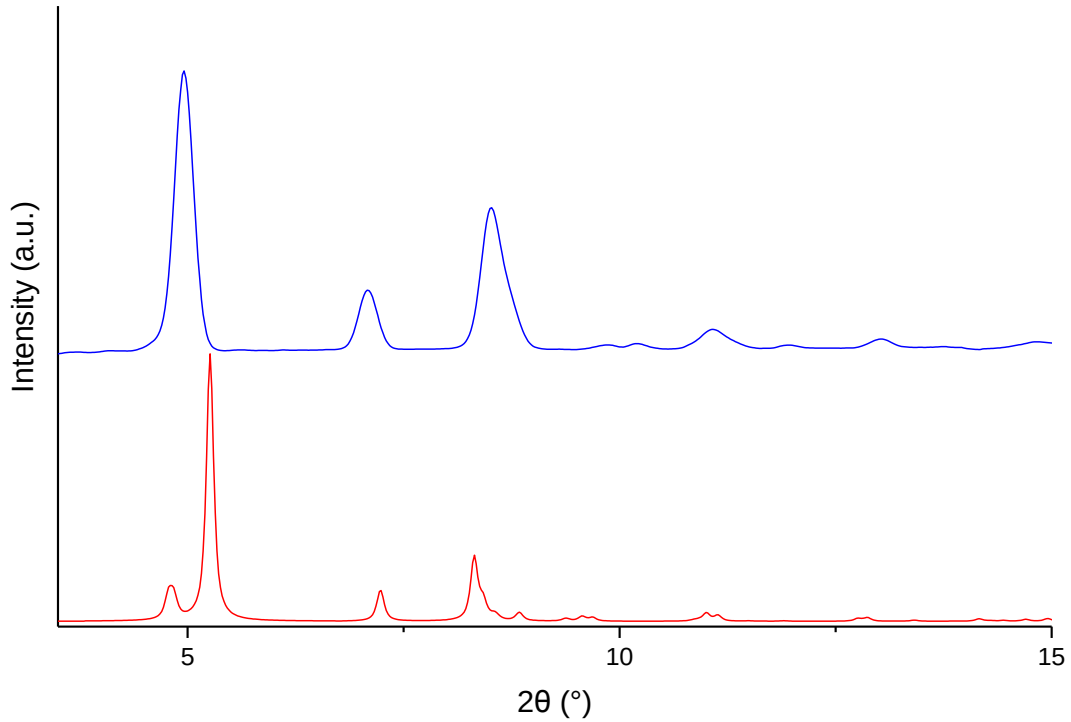

Figure 3.3.5: PXRD patterns of **2**. Calculated from the single crystal data (red) and measured crystals (blue).

3.3.2.2 Raman and FT-IR spectroscopy

Raman and FT-IR spectroscopic methods were used to characterise crystals of **2** and a powdered sample of **H_3L2**. The Raman spectrum of **2** is dominated by stretches that derive from **L2**, further confirming the presence of the ligand in the MOF (**Figure 3.3.6**). The signals at 991 cm^{-1} in the spectrum of **2** and at 993 cm^{-1} in the spectrum of **H_3L2**, derive from CH_2 rocking vibrations. Bands in the spectrum of **2** at 1125, 1139 and 1169 cm^{-1} derive from C-C single bond vibrations. Two corresponding bands can be identified in the spectrum of **H_3L2** at 1127 and 1169 cm^{-1}. In the spectrum of **2,** the most intense signals derives from the aromatic C=C bond vibrations and appear at 1582 and 1605 cm^{-1}. In the spectrum of **H_3L2** related bands can be identified at 1585 and 1610 cm^{-1}, respectively. Another prominent signal is found at 2212 cm^{-1} and derives from the alkyne C≡C vibration in the spectrum of **2**. The corresponding signal appears slightly shifted to 2217 cm^{-1} in the spectrum of **H_3L2**.[25,26] These strong Raman signals assigned to the alkyne C≡C vibrations are barely visible in the FT-IR of **H_3L2** and not seen in the FT-IR of **2** further confirming the assignment as being correct as this type of vibrations are known to be particularly weak in FT-IR spectroscopy.[26]

The FT-IR spectrum of **2** also reveals signals which primarily derive from the organic ligand **L2** (**Figure 3.3.7**). A weak band at 2928 cm^{-1} in the spectrum of **2** corresponds to C-H stretches predominantly deriving from DMF molecules. Thus, this stretch is not visible in the spectrum of **H_3L2** which reveals a broad signal between 3300 and 2500 cm^{-1} deriving from the O-H stretching within H-bonds found in carboxylic acids. A barely visible signal at 2209 cm^{-1} in the spectrum of **H_3L2** derives from the symmetric C≡C stretching vibration (the corresponding stretch is identifiable in the Raman spectrum). At 1605 and 1582 cm^{-1} in **H_3L2** and 1603 and 1582 cm^{-1} in **2,** C=C bond vibrations of aromatic moieties are observed (corresponding to equivalent stretches in the Raman spectrum). The spectrum of **H_3L2** confirms the presence of carboxylic acid groups, with the C=O, C-O and O-H in/out of plane stretches appearing at 1723, 1235, 1419 and 930 cm^{-1} respectively. In the spectrum of **2** asymmetric carboxylate COO^- and symmetric stretches occur at 1546 and 1403 cm^{-1} respectively ($\Delta_{asy\text{-}sym}$ = 143 cm^{-1}).[25,27–29]

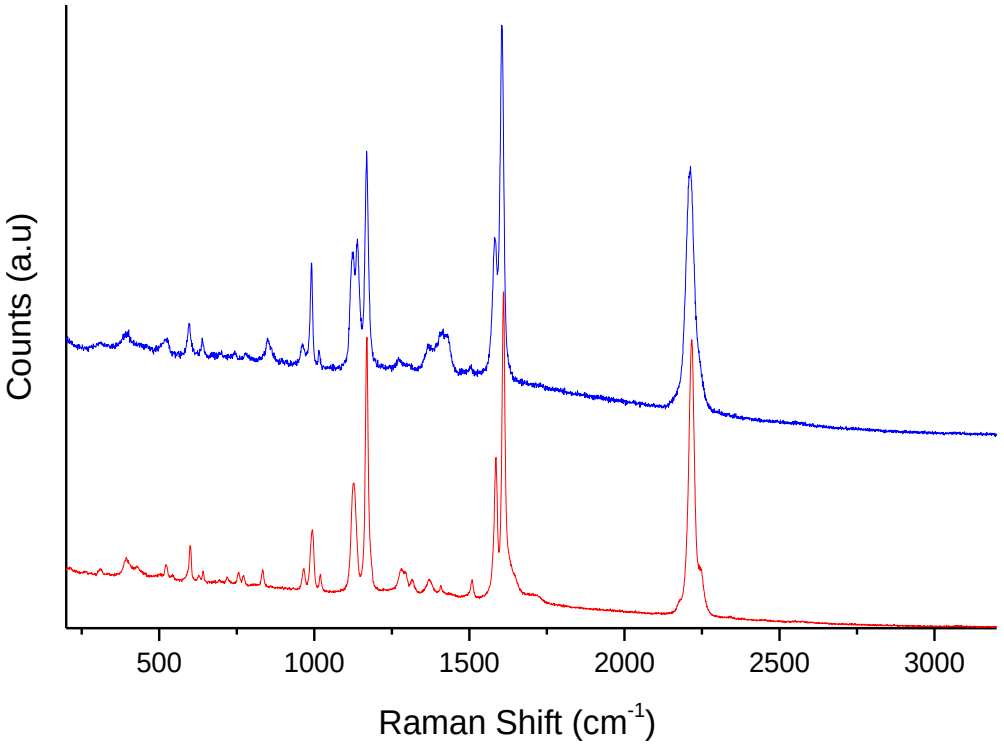

Figure 3.3.6: Raman spectra of crystals of **2** (blue) and **H_3L2** (red).

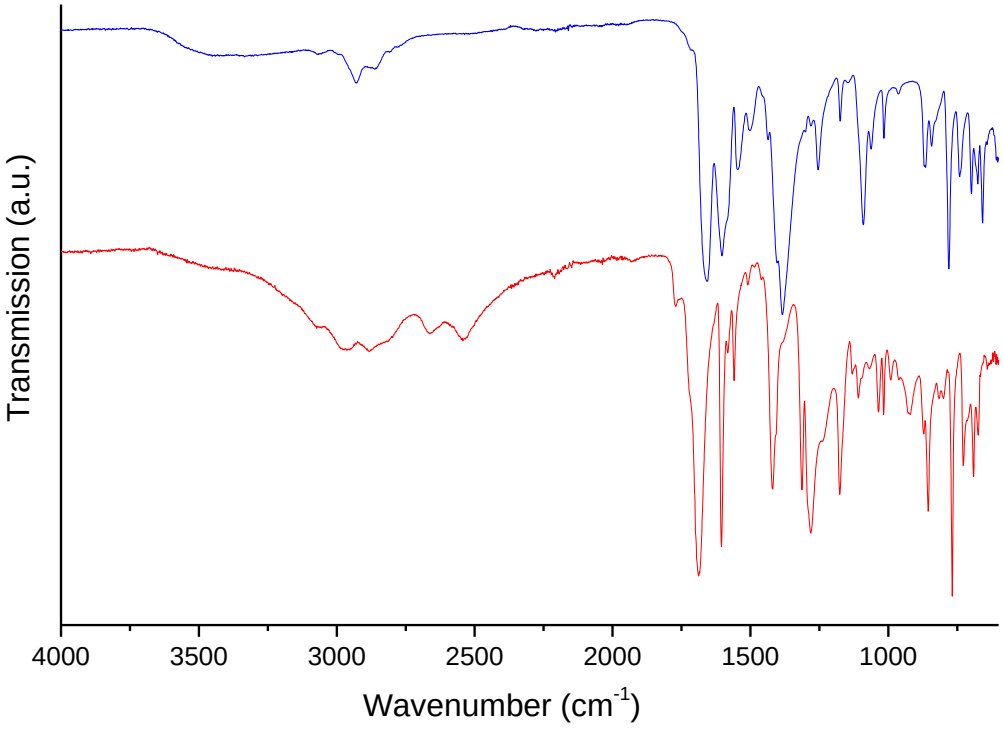

Figure 3.3.7: FT-IR spectra of **2** (blue) and **H_3L2** (red).

3.3.2.3 Scanning electron microscopy and energy dispersive X-ray spectroscopy

Crystals of **2** in DMF were drop casted onto an aluminium stub mount, dried in air for 24 hours. These were then examined using scanning electron microscopy (SEM) and energy-dispersive X-ray (EDX) spectroscopy (**Figure 3.3.8**). The obtained Co/C atomic ratio was 1 : 18, is in reasonable agreement with the expected value of 1 : 21 for **2** corresponding to the molecular formula $Me_2NH_2[Co_5(\mathbf{L2})_3(\mu_3\text{-}OH)_2(H_2O)_2(DMF)_2] = Co_5C_{107}H_{67}O_{24}N_3$.

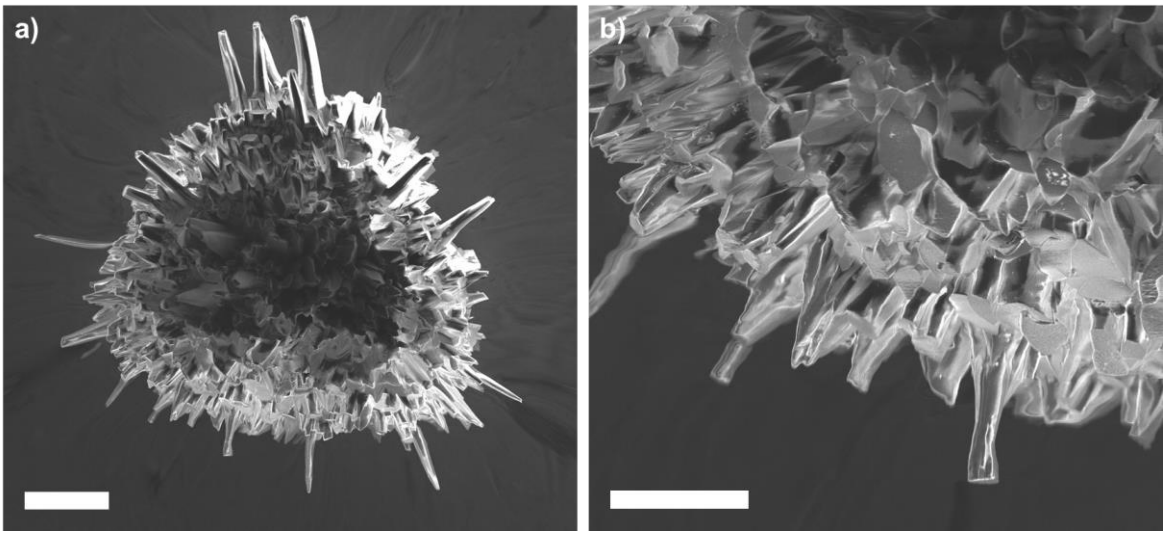

Figure 3.3.8: SEM images showing a cluster of crystals composed of **2**. Scale bars: **a)** 0.2 mm, **b)** 0.1 mm.

3.3.3 Thermogravimetric and gas sorption characterisation of **2**

3.3.3.1 Thermogravimetric analysis

Thermogravimetric analysis (TGA) of **2** was performed in an N_2 atmosphere at a heating rate of 3°C per minute (**Figure 3.3.9**). It reveals an initial weight loss of *ca.* 47% between 25 and 90°C which can be attributed to the loss of H_2O and DMF solvent molecules in the pores which are represented by a calculated void space of 48.6% of the unit cell volume. Another thermogravimetric step of *ca.* 18.5% is observed between 90 to 200°C which derives most likely from the removal of more strongly bound solvent molecules including coordination solvent molecules and ammonium counter-ions. There is a further weight loss of *ca.* 26.5% between 380 and 470°C that results from the decomposition of the organic ligand.

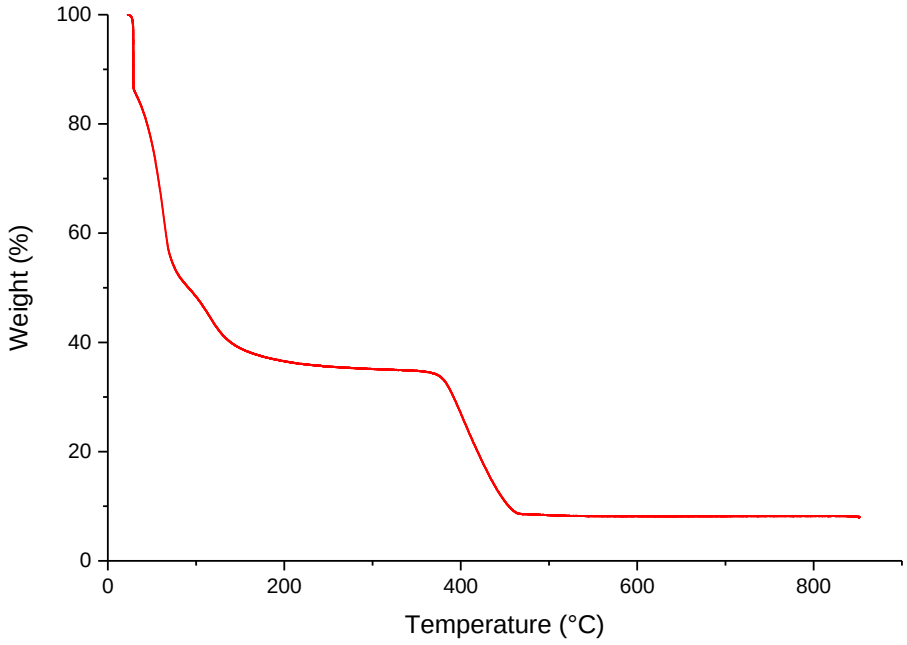

Figure 3.3.9: TGA of compound **2** carried out in an N_2 atmosphere at a heating rate of 3°C per minute.

3.3.3.2 Gas sorption experiments

It is expected that **2** would give rise to a large surface area based on similar structures found in the literature.[30,31] Prior to conducting gas sorption experiments on **2** it was necessary to exchange the constitutional solvent molecules in the structure of **2**. Crystals of **2** were soaked in DMF for three days, refreshing the used DMF with fresh DMF once per day to remove unreacted materials that could potentially be within the pores of **2**. The DMF was then exchanged with $CHCl_3$ for three days, refreshing the solution once per day. The crystals were transferred into a quartz measurement cell and the sample was activated by heating under vacuum at 100°C for 24 hours. The N_2 gas sorption shows a reversible type-I isotherm at 77 K with a steep uptake at low partial pressures (**Figure 3.3.10**). A maximum uptake of 497 cm^3/g at 740 Torr, which corresponds to an uptake of 621 mg/g, was achieved.

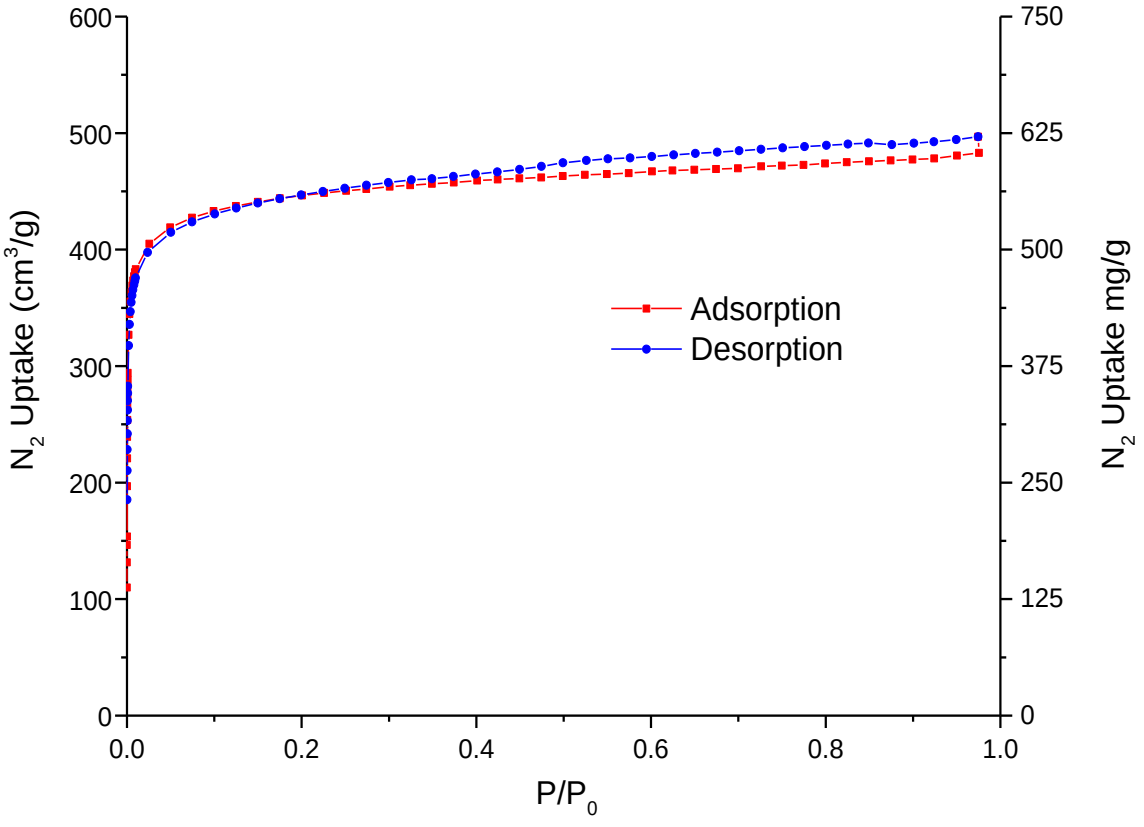

Figure 3.3.10: N_2 sorption isotherm of **2** measured at 77 K.

The BET surface area derived from this isotherm gives a value of 1755 m^2/g (**Figure 3.3.11** and **Table 3.3.4**). The points chosen for the BET calculation were selected according to the Rouquerol criteria.[32]

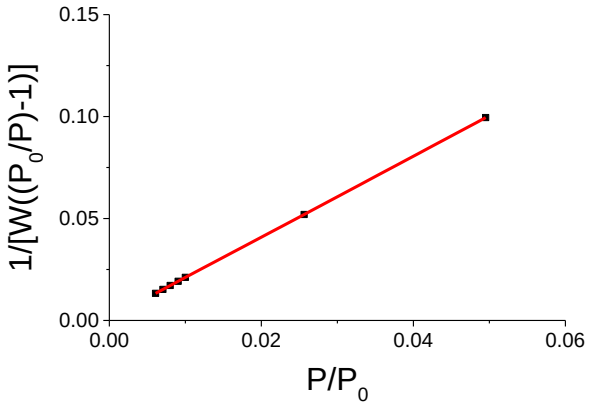

Figure 3.3.11: Plot of the linear region used to obtain the BET surface area of **2**.

Table 3.3.4: Table of BET values obtained from the BET Plot (**Figure 3.3.11**).

Slope	1.984
Intercept	1.230×10^{-3}
r (correlation coefficient)	0.999999
C constant	1613.460
BET Surface Area	1755 m^2/g

The H_2 gas sorption shows a reversible isotherm at 77 K (**Figure 3.3.12**) with an uptake of 211 cm^3/g at 756 Torr which corresponds to an uptake of 1.84 wt%. When compared to literature values, the wt% uptake corresponds closely with that of several known MOFs with comparable surface areas.[33] The CO_2 gas uptake isotherms were obtained at 278 K, 288 K and 298 K. The isotherm at 278 K shows an uptake of 65 cm^3/g at 755 Torr (**Figure 3.3.13**).

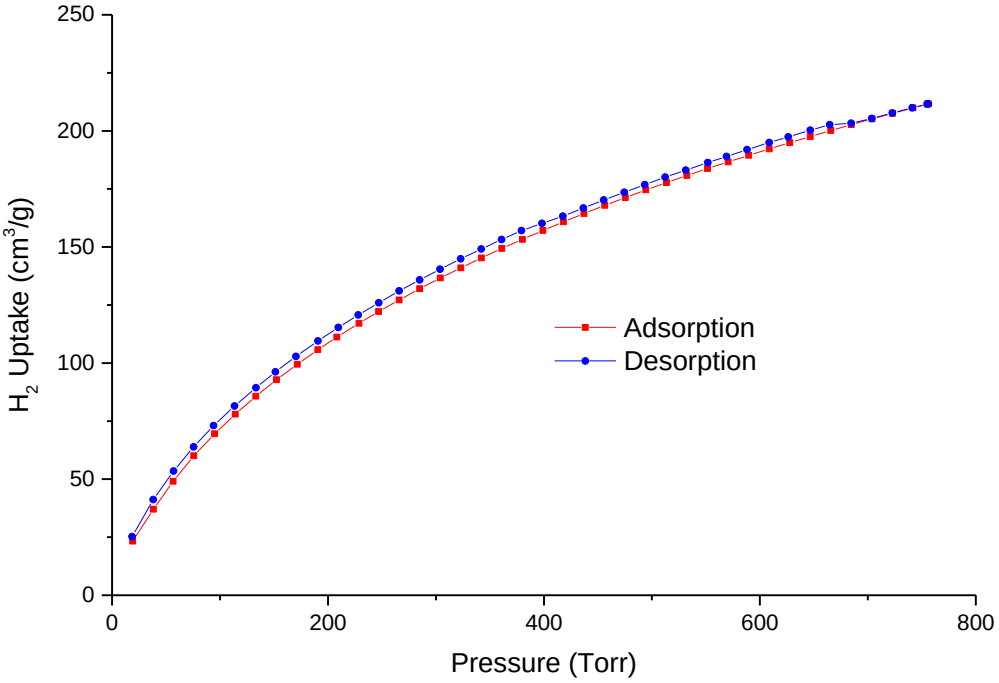

Figure 3.3.12: H_2 sorption isotherm of **2** measured at 77 K.

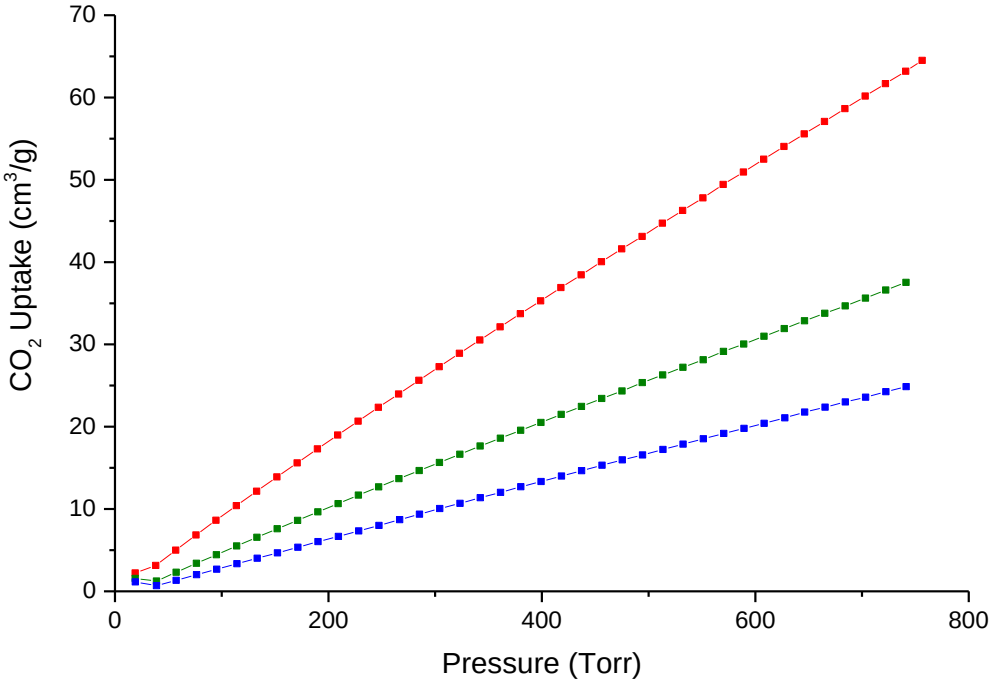

Figure 3.3.13: CO_2 adsorption isotherms of **2** measured at a range of temperatures. 278 K (red), 288 K (green) and 298 K (blue).

3.4 Use of **2** as water oxidation catalyst

The structural and hydrolytic robustness of the pentanuclear unit of **2** derives from the coordination behaviour of the carboxylate ligands whilst the 3D structure of the MOF is further supported by strong, prevailing stabilizing π-π interactions.

The polynuclear nature of the SBU, which allows oxidation/electron-equivalents to be distributed over several sites as well as the feature that the SBUs in the structure each contain two accessible, coordinated solvent molecules that penetrate into the void channels from identical binding sites, prompted us to use the structure for catalysis experiments – in particularly oxygen evolution reaction (OER) experiments. It is further interesting to note, the location of these weakly bound solvent molecules, that sit between two Co(II) centres, 2.483 Å from Co(2) and 2.681 Å from Co(3).

This proximity could potentially facilitate several different OER mechanisms involving one or two Co(II) centres. These include water nucleophilic attack (WNA) as well as bimolecular mechanisms involving two closely situated water molecules bound to adjacent Co(II) centres (especially considering that the distance between the two Co(II) centres is relatively short at 3.529 Å). Thus rendering this highly porous MOF particularly suitable for OER investigations.[34]

The π-π interactions throughout the interpenetrated MOF along with the conjugated nature of the **L2** ligand, are both expected to lead to satisfactory electronic conductivity which should aid its activity as an electrocatalyst.[35]

In addition, the carboxylate moiety that is found *cis* to the weakly bound solvent molecules and that is characterised by a relatively long Co(1)-O(8) bond length of 2.446 Å, may decrease the required potential for water oxidation as it could potentially stabilise reaction intermediates such as CO-OH and Co-OOH through hydrogen bonding interactions.[36,37] It may also increase the kinetics of the reaction, increasing the O_2 production rate by acting as a proton shuttle.[38,39]

3.4.1 Cyclic voltammetry using **2**/CP

Crystals of **2** were dried under vacuum, ground into a fine powder and blended with commercial carbon paste (CP, a blend of carbon black and an organic oil binder). Conductive solutions of KNO_3 (1 M) and KPi buffer (50 mM, pH 7.2) in H_2O were used for all electrochemical experiments at 20°C.

Cyclic voltammetry (CV) experiments were performed using a 10% by weight **2**/CP blend which were used to fill an electrode with a surface area of 0.071 cm^2 (**Figure 3.4.1**). This electrode was used in combination with a Pt-mesh counter-electrode and an Ag/AgCl (3 M) reference electrode to complete the three-electrode configuration. A scan rate of 100 mV/sec was used for experiments. One observes initial increases in current densities starting from 1.15 V (vs. NHE) which is attributed to the oxidation of Co(II) species to Co(III) species and this continues till 1.30 V (vs. NHE) whereupon there is a large increase in current density which is attributed to the oxidation of the coordinated H_2O molecules.[40]

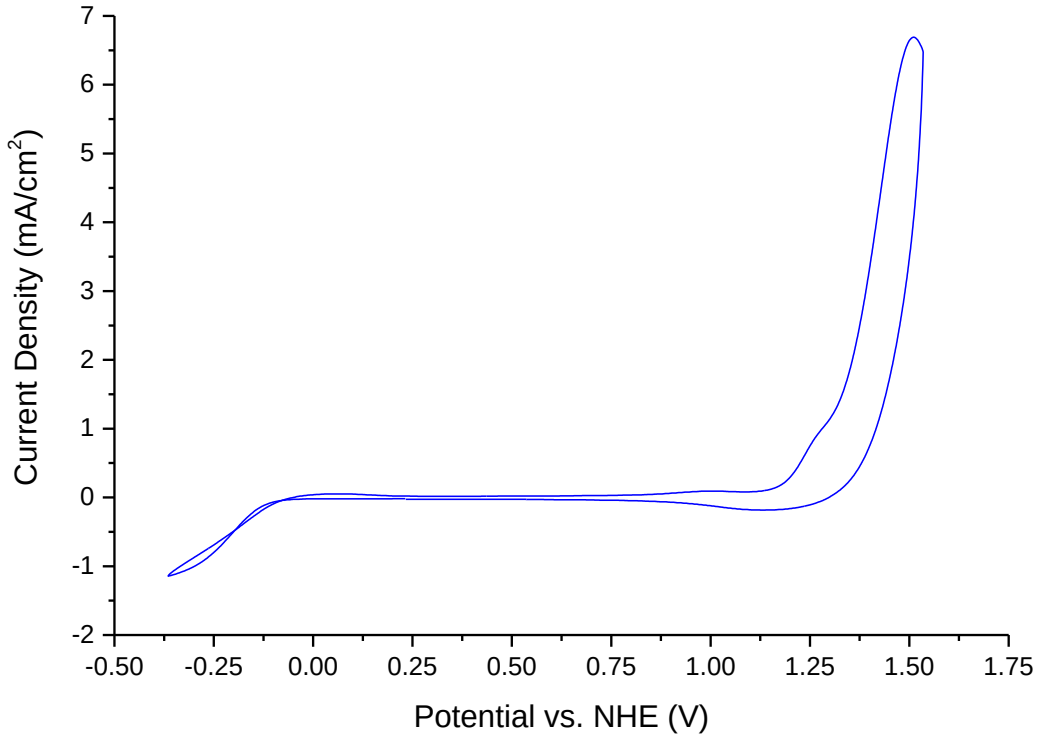

Figure 3.4.1: Cyclic voltammetry (CV) experiment using a 10 wt% **2**/CP electrode. Scan rate 100 mV/sec.

3.4.2 Linear sweep voltammetry studies

Crystals of **2** were dried under vacuum, ground into a fine powder and blended with commercial carbon paste (CP, a blend of carbon black and an organic oil binder). Conductive solutions of KNO_3 (1 M) and KPi buffer (50 mM, pH 7.2) in H_2O were used for all electrochemical experiments at 20°C. For linear sweep voltammetry (LSV) experiments (**Figure 3.4.2**), **2**/CP blends were used to fill a rotating disk electrode (RDE) with a surface area of 0.071 cm^2. This electrode was used in combination with a Pt-mesh counter-electrode and an Ag/AgCl (3 M) reference electrode to complete the three-electrode configuration. A range of **2**/CP ratios were tested from 5% to 40% (by weight) and with a RDE rotation rate of 1600 rpm and a scan rate of 1 mV/sec for all LSV experiments. It was found that at higher catalyst loadings, the paste became brittle and were inclined to crack and break. Therefore, it was decided to restrict the maximum catalyst loadings to 40 wt%.

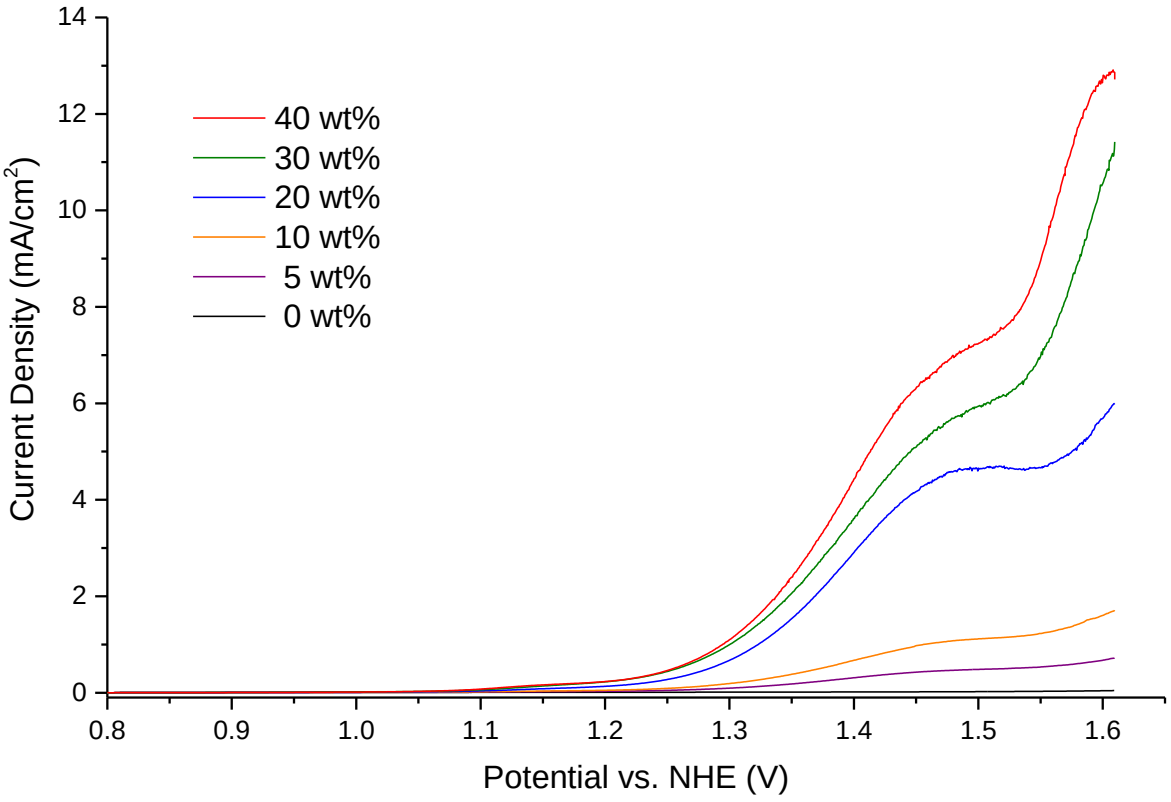

Figure 3.4.2: Comparative electrochemical behaviour for different catalyst loadings in CP at a RDE rotation rate of 1600 rpm and a scan rate of 1 mV/sec. Legend: Weight percentages of **2** in CP electrodes for each LSV experiment.

When compared to the flat increase in current density when only using CP, the **2**/CP blends show significant increases in current density indicating catalytic responses deriving from H_2O oxidation. For all blends, one observes similar patterns to those observed in the CV experiments (**Figure 3.4.1**). There are initial increases in current densities starting from *ca.* 0.25 V of overpotential which is attributed to the oxidation of Co^{II} species to Co^{III} species.[40] From *ca.* 0.4 V we see a significant increase in current density which is attributed to the oxidation of the coordinated H_2O molecules.[40] The rate of increase in current density briefly decreases for all blends between 0.60 and 0.75 V and can may derive from mass transfer limitations. Onset potentials (**Figure 3.4.3** and **Table 3.4.1**) were estimated from the intersection points between the tangent lines of the Faradaic (current density > 0.2 mA/cm^2) and non-Faradaic (current density < 0.01 mA/cm^2) currents. Based on these analyses, the 30% to 40% blends reveal the lowest onset overpotentials.

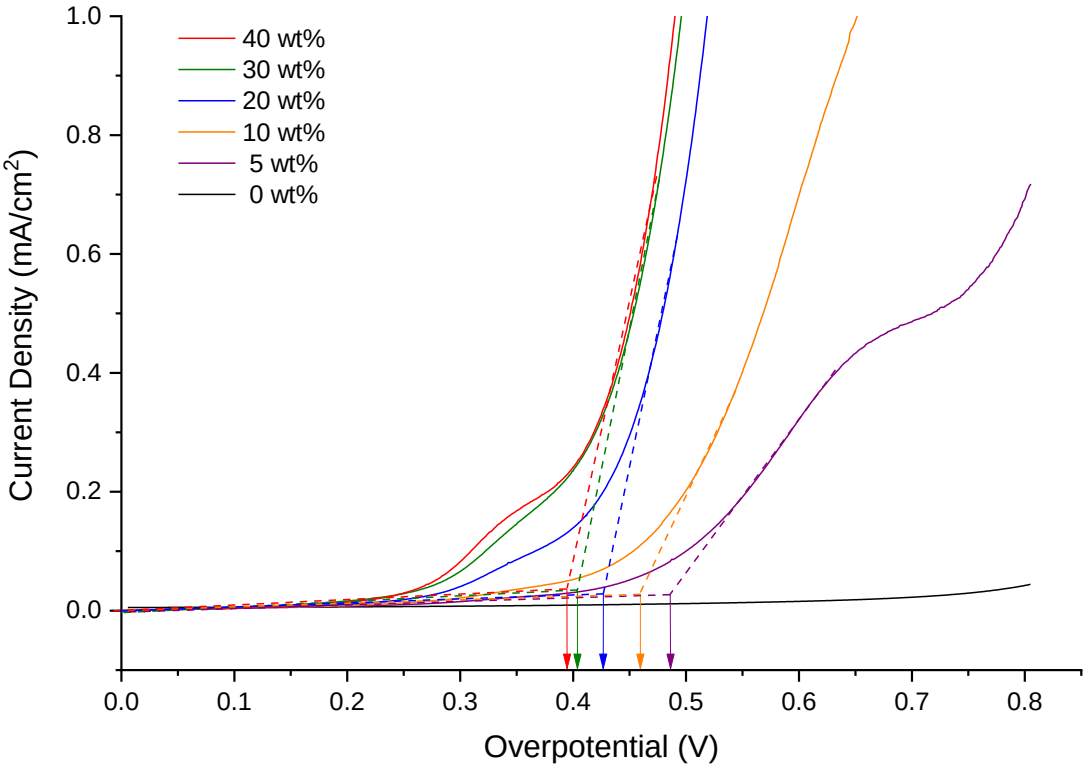

Figure 3.4.3: Comparative electrochemical behaviour for different catalyst loadings in CP at a RDE rotation rate of 1600 rpm and a scan rate of 1 mV/sec showing onset overpotentials. Legend: Weight percentages of **2** in CP electrodes for each LSV experiment.

Table 3.4.1: Comparison of onset overpotentials obtained from LSV data for a range of **2**/CP electrodes.

Catalyst %	Onset overpotential (V)
40	0.394
30	0.403
20	0.426
10	0.459
5	0.486

The different blends give rise to onset overpotentials varying from 0.486 V (5 wt% of **2**) to 0.394 V (40 wt% of **2**). This increase is consistent, with the increasing catalyst loadings within the CP blends. When compared to the pure CP electrode (control experiment), one observes a considerable increase in current density even using electrodes containing a 5 wt% catalyst loading. The results confirm that the catalytic activity derives from **2** and shows that there is a negligible contribution to the increase in current density from the CP.

3.4.3 Tafel plots

Tafel plots for **2**/CP blends were derived from the LSV experiments. The plots were examined using overpotential values in the 0.4 - 0.6 V range were H_2O oxidation is observed (**Figure 3.4.4**) and Tafel slopes were obtained for each blend (**Table 3.4.2**). The Tafel slope depends on the rate-determining step of the electrochemical process and a lower slope corresponds to a more rapid increase in the current density following the onset of water oxidation.[41] The slopes that were obtained, range from 133 to 176 mV/dec. Ideally we would expect lower Tafel slopes than those obtained but this may be related to the insulating nature of the material (relative to other materials) as well as limited diffusion within the MOF. It should be mentioned that it is actually difficult to compare results from different literature studies due to the various different experimental methods used. The most meaningful comparison to make is by comparing the Tafel slopes to other cobalt-based MOFs that reveal electrocatalytic OER activity at pH 7. MOFs, abbreviated as Fe_3-Co_2 MOF, MOF-74-Co and ZIF-67 have been shown to have

Tafel slopes of 134, 129 and 125 mV/dec, which are all very similar to the determined Tafel slopes of **2**.[42]

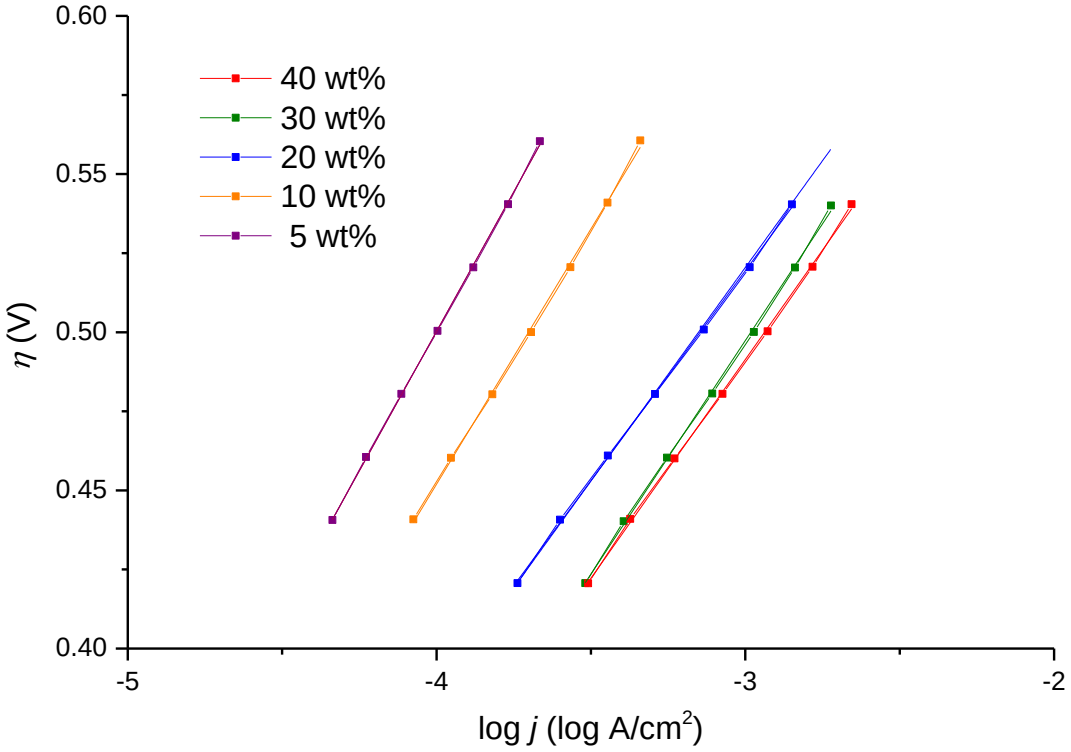

Figure 3.4.4: Tafel region for different **2**/CP electrodes using various catalyst loadings; 5% (purple), 10% (orange), 20% (blue), 30% (green), 40% (red).

Table 3.4.2: Summary of Tafel slopes obtained for each **2**/CP electrode.

% of **2** in CP electrode by weight	Slope (mV/dec)
5%	176
10%	161
20%	133
30%	148
40%	138

3.4.4 Post-catalytic solution characterisation

After the LSV experiments were completed, the individual aqueous solutions used with each **2**/CP blend, were tested for possible cobalt(II) leaching and the presence of other catalytically active species that derive from **2**. For this purpose, the **2**/CP electrodes were replaced with conventional untreated glassy carbon RDE and the LSV experiments were repeated using the post-catalytic reaction solutions (**Figure 3.4.5**). Negligible activity was observed. In fact, the experiments of glassy carbon electrodes in post-catalytic reaction solutions did no differ significantly to experiments in which freshly prepared buffered solutions were employed. Thus, only significant degradation of **2** through leaching was not detectable.

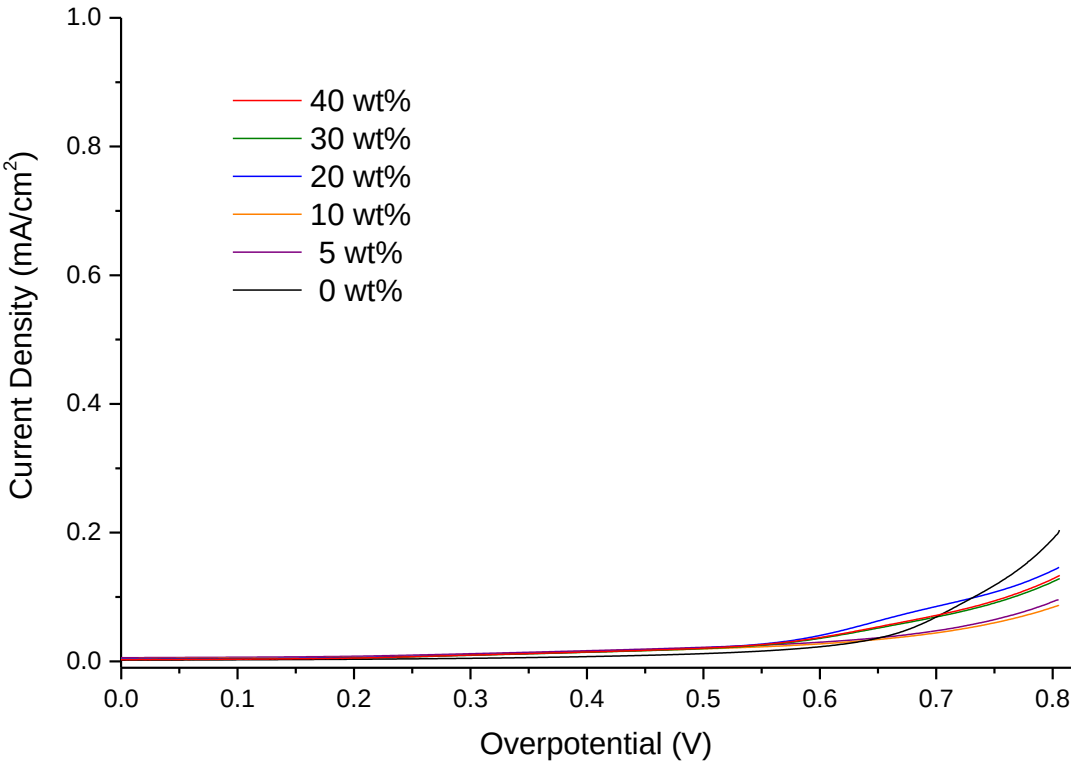

Figure 3.4.5: LSV experiments involving glassy carbon electrodes and post-catalytic reaction solutions (derived from LSV experiments using CP/**2** electrodes at various catalyst loadings). RDE rotation rate of 1600 rpm and a scan rate of 1 mV/sec. Legend: Weight percentages of **2** in CP electrodes for each LSV experiment.

3.4.5 Bulk H_2O electrolysis using **2**/CP electrodes

Chronopotentiometry at a constant current density was conducted employing 20 wt% **2**/CP electrodes to evaluate the stability of **2**. The experiments were carried out for 24 hours using a **2**/CP working electrode, a Pt mesh counter electrode and an Ag/AgCl reference electrode at a set current density of 1 mA/cm^2. A solution of KNO_3 (1 M) and KPi buffer (50 mM, pH 7.2) in H_2O was used at 20°C (**Figure 3.4.6**). This bulk electrolysis experiment demonstrates that the **2**/CP electrode is stable for a time period of over 24 hours at the applied current. The applied set-up gives rise to a potential of *ca.* 1.4 V vs. NHE. A small decrease in the potential is observed during the experimental time period possibly due to increased electronic conductivity of the sample or due to surface modification of the electrode increasing the available surface area.[43]

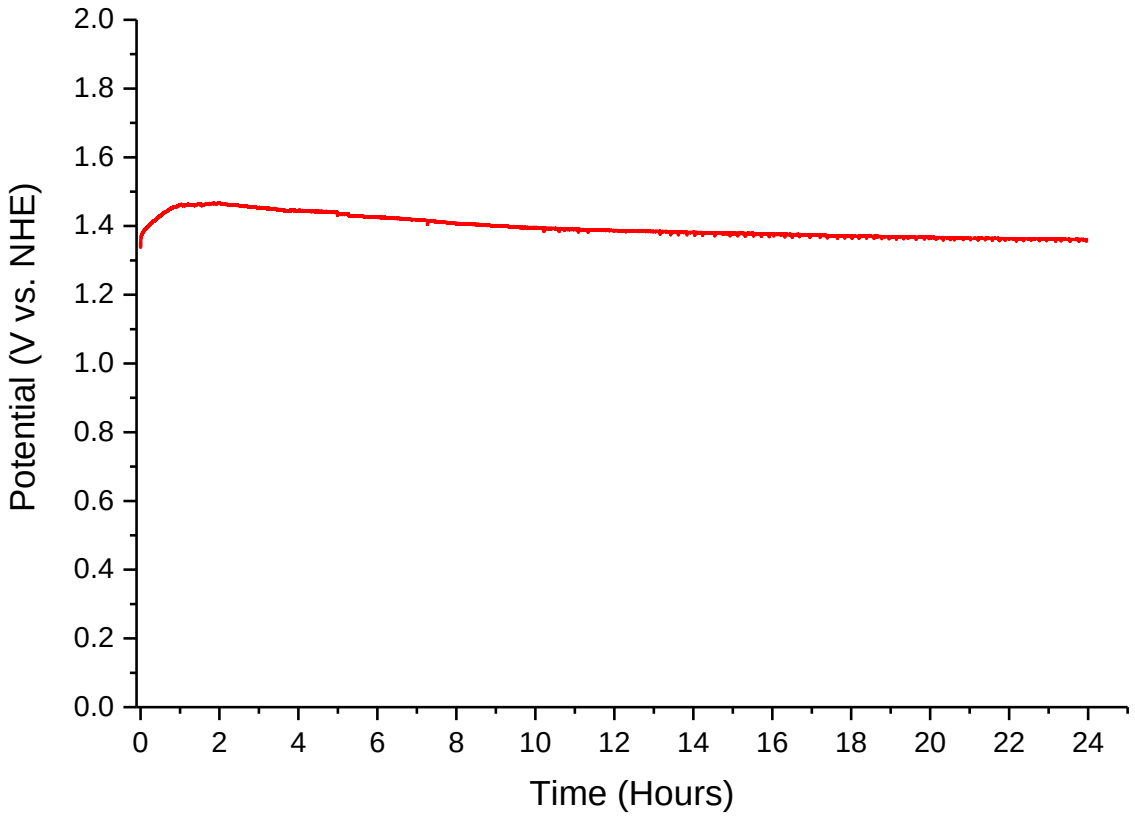

Figure 3.4.6: Chronopotentiometry using a 20 wt% **2**/CP electrode. Current density set at 1 mA/cm^2 at pH 7.2.

After the bulk electrolysis experiments, the surface of the **2**/CP blend (20%) electrode was analysed. Under an optical microscope fragments of **2** could be clearly identified whereby the characteristic purple colour of the original crystals was maintained. These crystals at the electrode surface were analysed using Raman spectroscopy (**Figure 3.4.7**). The resulting spectrum is identical to the spectrum of freshly prepared, pristine crystals of **2**. No detectable quantities of cobalt oxides (CoO_x), for instance Co_3O_4, were detectable by Raman spectroscopy. The analyses suggest that **2** retained its structural integrity during the chronopotentiometry over a time period of 24 hours.

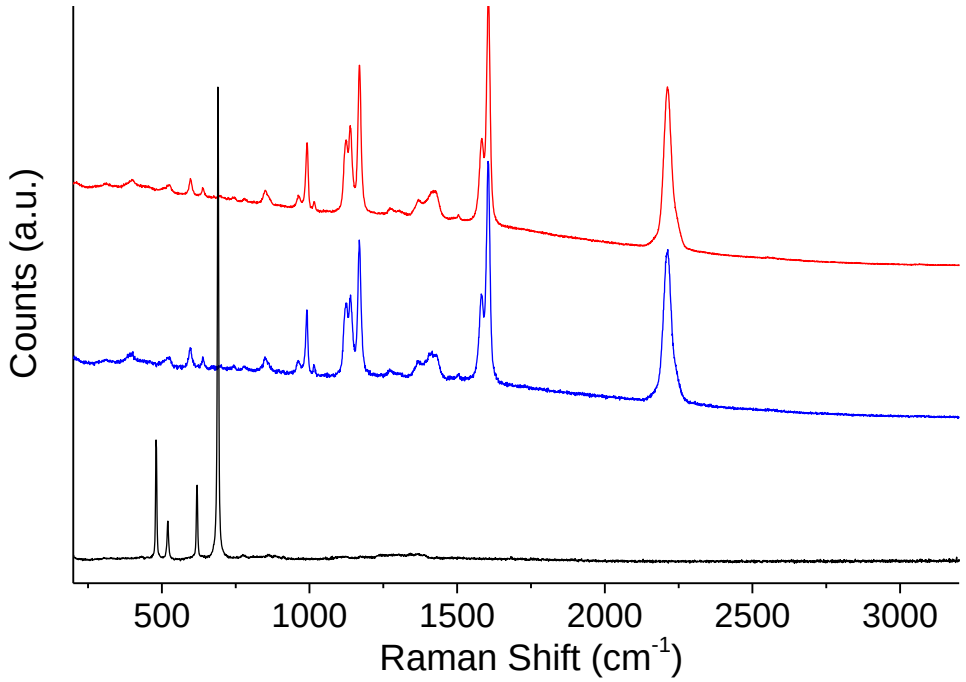

Figure 3.4.7: Raman spectrum of **2**, before (blue) and after (red) the bulk electrolysis experiments.

3.4.6 Photo-induced water oxidation catalysis

To further investigate the catalytic activity of **2** and to quantify the production of O_2, photo-induced water oxidation experiments were performed. $[Ru(bpy)_2(deeb)]Cl_2$ (4 mg) was used as a photosensitiser with $Na_2S_2O_8$ as a sacrificial oxidant (6 mg) in aqueous phosphate buffer solutions (10 mM in deionised H_2O, 10 mL, pH 7).[44] Dry powders of **2** were added to the solutions and the vials were covered with aluminium foil to avoid an early reaction if exposed to light. The mixtures were sonicated for 15 minutes and then stirred continuously during the entire experiment. The reaction mixtures were purged with N_2 gas to remove dissolved O_2 prior to illumination. An LED light source (465 nm, 10 mW/cm^2 at the centre of the vial) was used to illuminate the reaction vials. Various catalyst quantities ranging from 0.016 to 0.062 mg, were tested under the outlined experimental conditions whilst the evolved O_2 quantities were directly measured using a Clark electrode (**Figure 3.4.8**). When compared to the experiment without any catalyst present, one notes that **2** is clearly an OER catalyst greatly increasing the observed O_2 production.

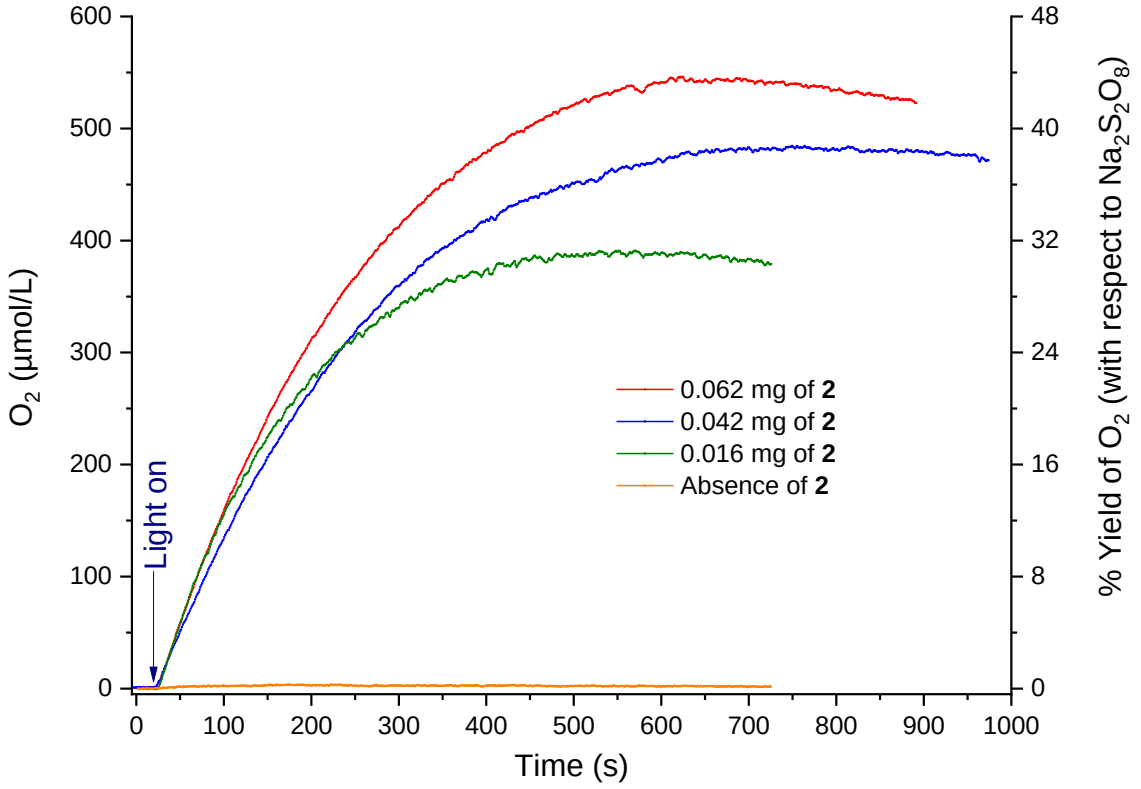

Figure 3.4.8: Photo-induced water OER using various quantities of **2** as a heterogeneous catalyst**.** Catalyst loadings: 0.062 mg (red), 0.042 mg (blue), 0.016 mg (green), control experiment in the absence of **2** (orange).

The achieved O_2 quantities, yields, TONs and TOFs are summarised in **Table 3.4.3**. Maximum O_2 yields vary from 390 (31.2% chemical yield) to 545 µmol/L (43.6% chemical yield) with increasing catalyst loadings from 0.016 mg to 0.062 mg respectively.

Turnover numbers (TONs) and turnover frequencies (TOFs) were calculated from the experimental data. The TONs vary from 89 to 248 whilst TOFs of 0.368 s^{-1} to 1.482 s^{-1} were achieved. Lower catalyst loadings resulted in the highest TONs and TOFs.

Comparing these results with other MOFs that were previously used as photo-induced OER catalysts, it appears that **2** is exceptionally active under the detailed experimental conditions. However, it should be mentioned that it is difficult to accurately compare literature studies as there are various different parameters which influence the outcome of the individual experiments (pH value; light intensity; relative reactant concentrations, nature of the photosensitisers). Other reported MOFs that were used as OER catalysts under similar testing protocols, appear to be less active than **2**. Co-ZIF-67 achieves a maximum TOF of 0.035 s^{-1},[10] while a set of iridium-doped MOFs published by Wenbin Lin achieve a maximum TOF of only 0.00133 s^{-1}.[45] MIL-101(Fe) and MIL-101(Fe)-NH show TOFs of 0.10 and 0.048 s^{-1} and TONs of 27.30 and 15.74 respectively.[46]

Table 3.4.3: Max. O_2 quantities, O_2 chemical yields, TONs and TOFs from the photocatalytic OER experiments calculated from each plot in **Figure 3.4.8**.

Sample Mass (mg)	Max. O_2 (µmol/L)	Chemical yield (%)	TON	TOF (s^{-1})
0.062	545	43.6%	89	0.368
0.042	480	38.4%	116	0.399
0.016	390	31.2%	248	1.482
No catalyst	4	0.3%	N/A	N/A

The addition of extra quantities of $Na_2S_2O_8$ (6 mg) after each experimental run was used to test the continued activity of **2** (**Figure 3.4.9**). **2** was shown to maintain reasonable activity, however potentially due to the increasing ionic strength of the solution, the max. evolved O_2 quantity dropped from 545 µmol O_2 to approximately 95 µmol O_2 after the 4th run. In addition, it is known that the Ru/polypyridyl photosensitisers rapidly decompose under the photocatalytic reaction conditions.[47]

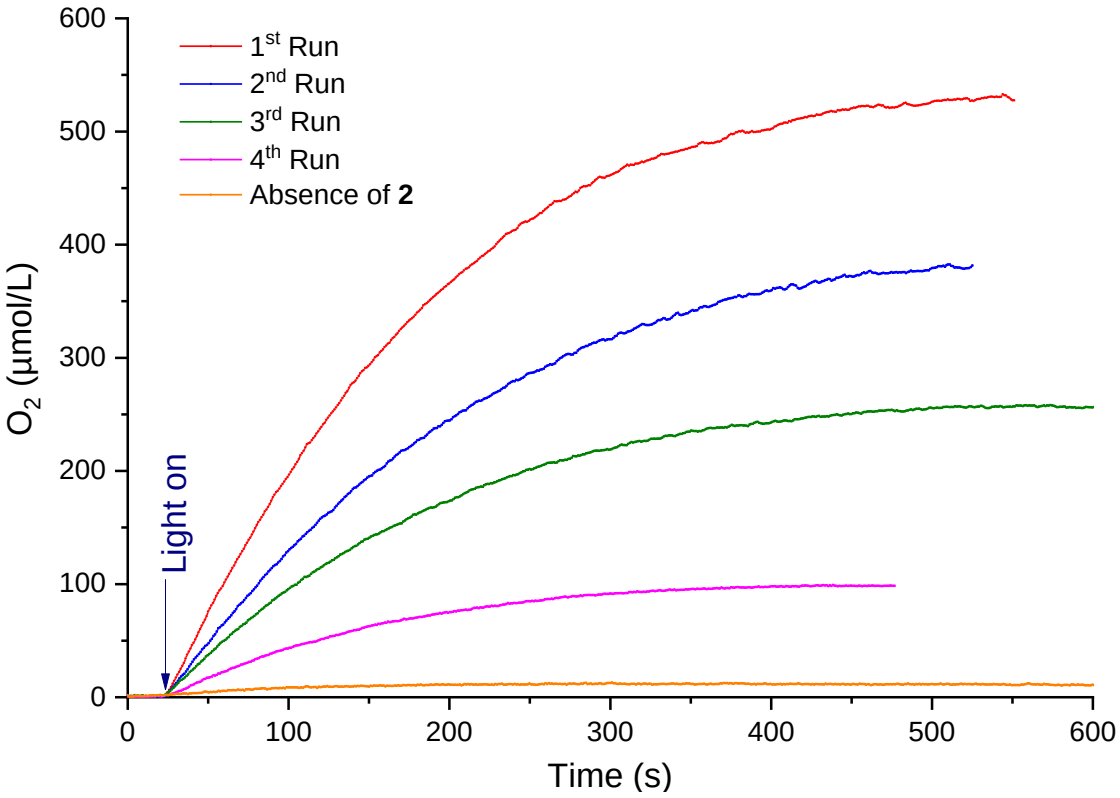

Figure 3.4.9: Photo-induced activity of **2** upon addition of additional quantities of $Na_2S_2O_8$ (6 mg) after each experimental run. Experimental conditions as previously described using 0.062 mg of **2**, 4 mg of $[Ru(bpy)_2(deeb)]Cl_2$ and 6 mg $Na_2S_2O_8$ added after each consecutive run.

3.5 Electrosynthesis of a material that structurally closely relates to **2**.

3.5.1 Electrochemical synthesis and electrode deposition

The electrochemical formation of **2** and its deposition on electrode surfaces was investigated. It was found that thin film coatings of **2** or a material that structurally closely relates to **2**, form on conductive fluorine doped tin oxide (FTO) coated glass electrodes. Coatings were deposited on 1 x 2 cm FTO-coated glass slides from solutions composed of $Co(NO_3)_2 \cdot 6H_2O$ (69 mg, 0.236 mmol) and **H_3L2** (73 mg, 0.143 mmol) dissolved in a deaerated 0.1 M solution of $(NBu_4)PF_6$ in DMF : H_2O (100 : 1, 15 mL). The FTO working electrode, Pt-wire counter electrode and an Ag/Ag(cryptand)$^+$ reference electrode[48] were immersed in the solution and a potential was applied. It was noticed that relatively even films can form at voltages between -1.1 and -1.9 V vs. Ag/Ag(cryptand)$^+$. However, voltages greater than -1.6 V gave the films a brownish colour. A potential of -1.5 V was found give smooth, even coatings with the same purple colour of crystals of **2** (**Figure 3.5.1**). The film coated FTO electrodes were removed from the reaction solution and washed with DMF (5 mL) and $CHCl_3$ (5 mL) and dried in air. The importance of water and nitrates during cathodic electrodeposition has previously been reported.[48,49] Both components have been shown to be extremely important either to facilitate the deprotonation of carboxylic acids and to avoid the formation of H_2 bubbles on the electrodes during the deposition (as nitrates are selectively reduced compared with H_2O).[48] It was decided to investigate the role of NO_3^- ions and perhaps use it to improve the quality of the electrodeposited films. It was found that the smoothness of the films and the attachment of the crystallites/particles to the FTO substrate surface could be enhanced by the addition of a small quantities of $NaNO_3$ (30 mg, 23.5 mM) to the solution.

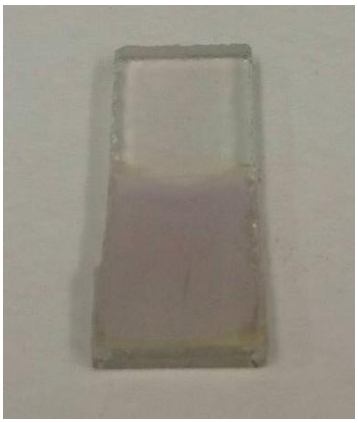

Figure 3.5.1: Film of **2** deposited at -1.5 V vs. Ag/Ag(cryptand)$^+$ after a deposition time of 5 minutes using an H_2O/DMF a reaction solution containing $NaNO_3$.

When depositing **2** on the surface of an FTO coated electrode, typically the current density decreases from an initial maximum before reaching a stable current density of ca. 0.2 mA/cm^3. The number of charges passing through the FTO electrode decreases from its initial rate reaching a constant rate indicating that a steady rate of deposition is achieved. A typical deposition plot is shown in **Figure 3.5.2**.

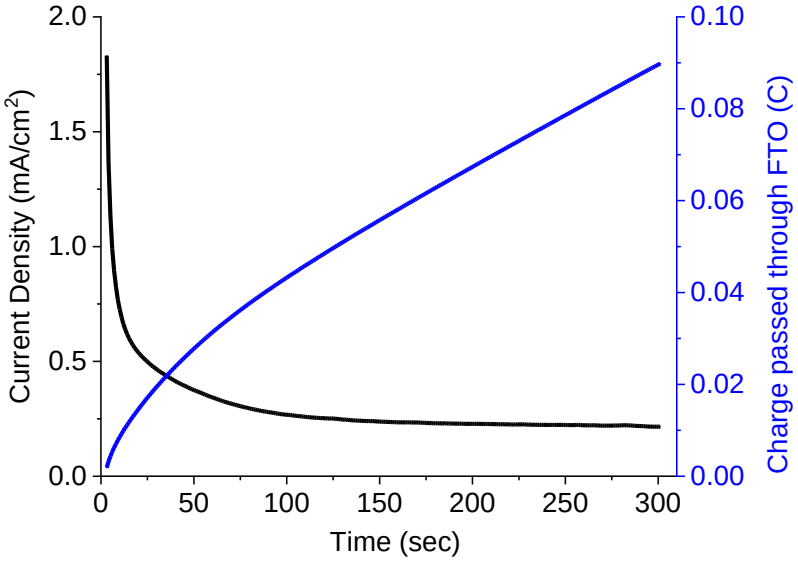

Figure 3.5.2: Typical electrodeposition plot for films of **2** (deposited at -1.5 V vs. Ag/Ag(cryptand)$^+$ for 5 minutes With $NaNO_3$).

3.5.2 Scanning electron microscopy characterisation FTO electrode materials

Films were electrochemically deposited as previously outlined over a time period of 5 minutes and imaged using electron microscopy techniques. Scanning electron microscopy (SEM) images of film coatings that were prepared in the absence and in the presence of nitrate ions show clear differences. Without addition of $NaNO_3$, the coatings appear uneven forming 'hollow pillars' (**Figure 3.5.3**). The diameters of the individual 'hollow pillar' structures deposited range between *ca.* 2 µm to 10 µm. Individual deposits are homogeneously distributed over the electron surface. Their cylindrical hollow morphology suggests that the materials deposit in the presence of gas bubbles on the surface. The addition of $NaNO_3$ to the aqueous solutions causes the growth of finer, evenly dispersed particles on the electrode surface (**Figure 3.5.4**). The particle sizes appear to be less than *ca.* 20 nm. Individual particles are attached to the electrode surface and appear to grow in connection to other individual particles forming aggregates.

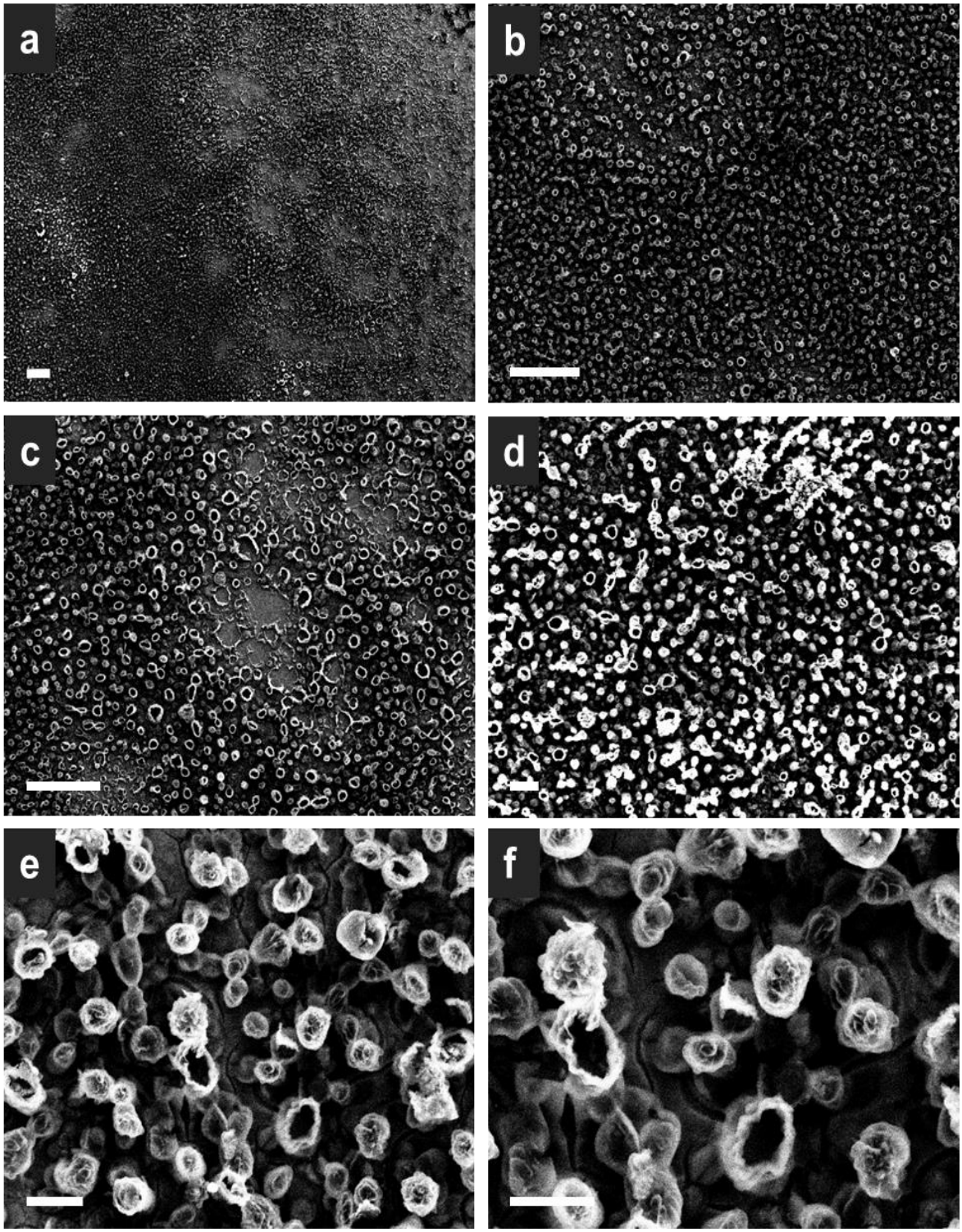

Figure 3.5.3: SEM images of FTO electro-deposited materials; the electrodeposition was carried out at -1.5 V vs. Ag/Ag(cryptand)$^{+}$ for a time period of 5 minutes in the absence of $NaNO_3$. Scale bars: **a)** 100 µm, **b)** 100 µm, **c)** 100 µm, **d)** 20 µm, **e)** 10 µm and **f)** 10 µm.

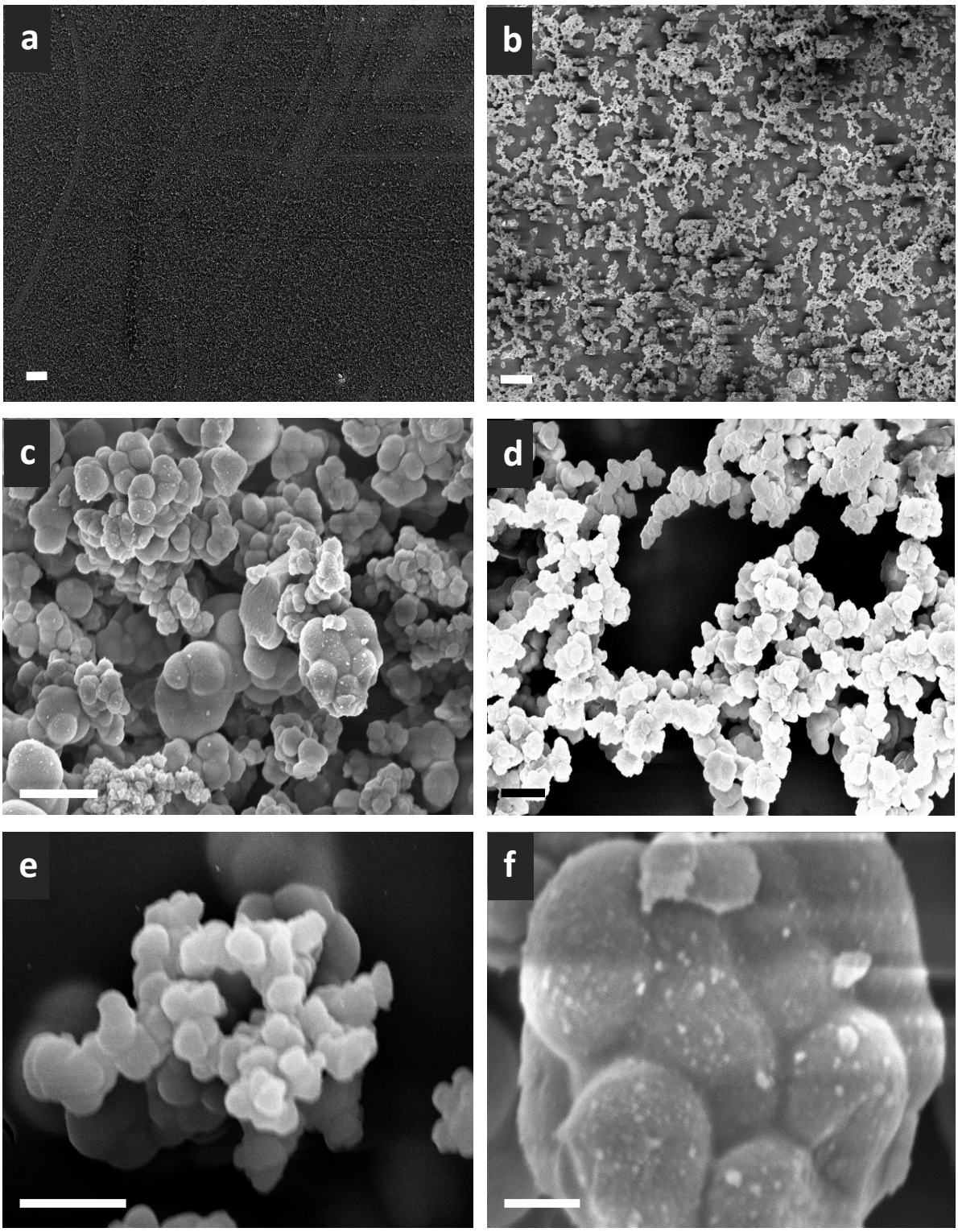

Figure 3.5.4: SEM images of FTO electrode-deposited materials; the electrodeposition was carried out at -1.5 V vs. Ag/Ag(cryptand)$^{+}$ for a time period of 5 minutes in the presence of $NaNO_3$. Scale bars: **a)** 100 µm, **b)** 10 µm, **c)** 1 µm, **d)** 1 µm, **e)** 1 µm and **f)** 200 nm.

3.5.3 Energy dispersive X-ray spectroscopy of FTO electrode-deposited materials

To characterise the relative composition of the deposited materials, the prepared FTO-electrodes were dried in air for 24 hours and analysed using energy-dispersive X-ray (EDX) spectroscopy at 20 kV (**Table 3.5.1**). At these experimental conditions the analysis technique is known to have a sample penetration depth of *ca*. 1 µm.[50] The relative atomic Co : C ratio was expected to be 1 : 21.4, based on the molecular formula of **2**, $Me_2NH_2[Co_5(\mathbf{L2})_3(\mu_3\text{-}OH)_2(H_2O)_2(DMF)_2]$ = $Co_5C_{74}H_{58}O_{24}N_3$. Since a cathodic, reducing potential was applied for the electrodeposition, it was important to investigate if metallic cobalt was deposited on the electrodes. However, ratios of 1 : 23.1 (in the absence of $NaNO_3$ in the deposition solution) and 1 : 26.2 (in the presence of $NaNO_3$ in the deposition solution) were obtained, thus closely corresponding to the expected values for **2**. A slightly higher C content may arise from constitutional DMF molecules lactated in the channels of the material and that were possibly not removed under the vacuum conditions of the electron microscope.

Table 3.5.1: Energy dispersive X-ray spectroscopy analysis of the electrodeposited materials on FTO electrodes (relative atomic Co : C ratio). Reported values are average values which were each derived from three separate measurements.

	Co	**C**
Corresponding to $Co_5C_{74}H_{58}O_{24}N_3$	1	21
Obtained relative atomic ratio (without $NaNO_3$)	1	23
Obtained relative atomic ratio (with $NaNO_3$)	1	26

3.5.4 Powder X-ray diffraction of thin films

For powder X-ray analyses, the electrosynthesised materials that were grown in the presence of $NaNO_3$ were removed from the FTO electrodes and placed in a capillary. However, the analyses were hampered by a rapid desolvation of the crystals and the materials, when dried crystals loose crystallinity partially transforming into an amorphous material. The process can be visualised by comparison of X-ray powder patterns of freshly prepared crystals and the deposited materials (**Figure 3.5.5**). The broad signals of the electrodeposited materials, however, still correlate with the main diffraction peaks of the crystalline compound. The broadness may additionally arise from the small particle sizes.

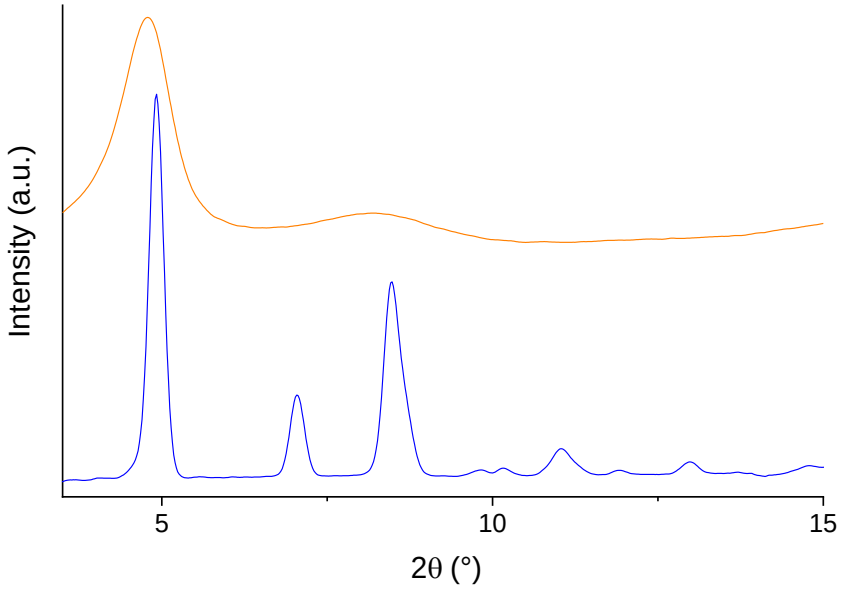

Figure 3.5.5: PXRD patterns of solvothermally synthesised crystals of **2** (blue) and dried electrosynthesised material (orange).

3.5.5 Raman and FT-IR spectroscopy of thin films

The surfaces of the electrodeposited films that were grown in the presence of $NaNO_3$ were examined using Raman spectroscopy and compared with the Raman spectrum of crystalline **2**. The spectra closely match suggesting that the deposited species structurally closely related to **2**. (**Figure 3.5.6**). The electrodeposited materials were removed from the FTO electrode and examined using FT-IR spectroscopy. Similarly to the Raman analysis, the IR spectrum of the deposited material is essentially identical to that of the crystalline bulk material of **2** (**Figure 3.5.7**).

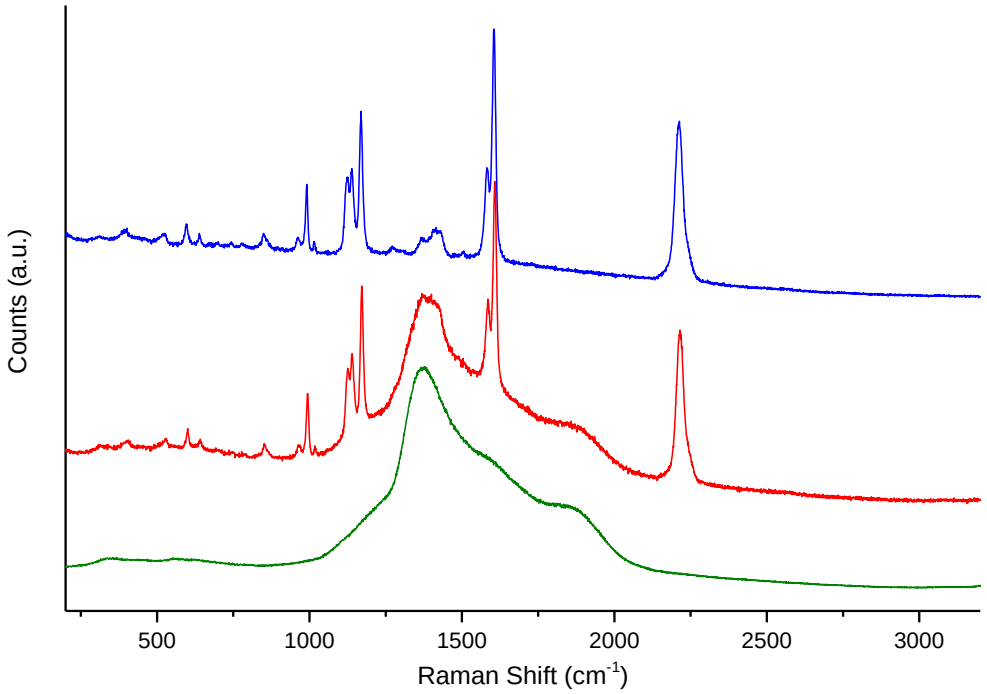

Figure 3.5.6: Raman spectra of crystals of **2** (blue), film grown on FTO (red), blank FTO (green).

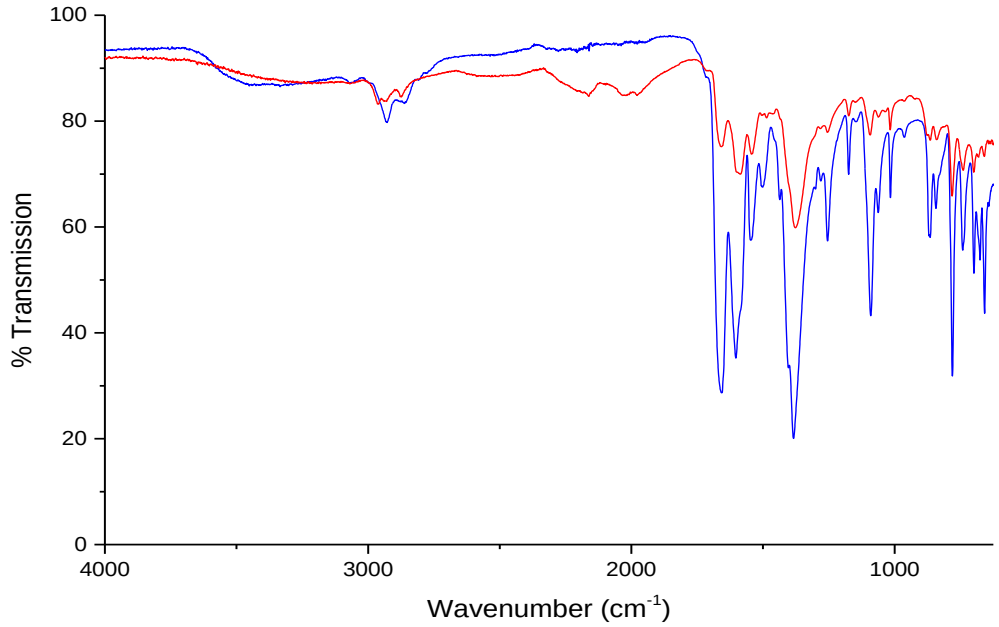

Figure 3.5.7: FT-IR spectra of crystals of **2** (blue) and deposits grown on FTO (red).

Considering the results of the EDX, X-ray diffraction, Raman and IR spectroscopy analyses, one can conclude that **2** and the electrochemically deposited materials on FTO-type electrodes (**2**/FTO) are essentially identical in composition or at least structurally closely related.

3.6 Water oxidation using **2**/FTO

3.6.1 Cyclic voltammetry using **2**/FTO electrodes

Cyclic voltammetry (CV) experiments were performed using 1 cm^2 **2**/FTO coatings on 1 x 2 cm^2 FTO glass slides (**Figure 3.6.1**). A conductive aqueous solution of KNO_3 (1 M) and KPi buffer (50 mM, pH 7.2) in H_2O was used at 20°C. The **2**/FTO electrode was used in the previously outlined three-electrode configuration. Strong catalytic waves characteristic for water oxidation are observed achieving 1 mA/cm^2 at 1.29 V (vs. NHE) and 5 mA/cm^2 at 1.45 V (vs. NHE) during cycle 1. Decreasing current densities with each consecutive CV cycle are observed whereby the rate of decrease reduced with each cycle reaching stable operation conditions after *ca*. 25 cycles. This effect can be explained by the decreasing available surface area of the electrode which is in contact with the solution due to the build-up of O_2 bubbles (**Figure 3.6.2**). When the bubbles were removed from the surface of the electrode and it was reused in CV experiments, a performance and current densities close to the original sample were again achievable (however some catalyst had clearly been detached from the FTO surface by the bubbles of O_2).

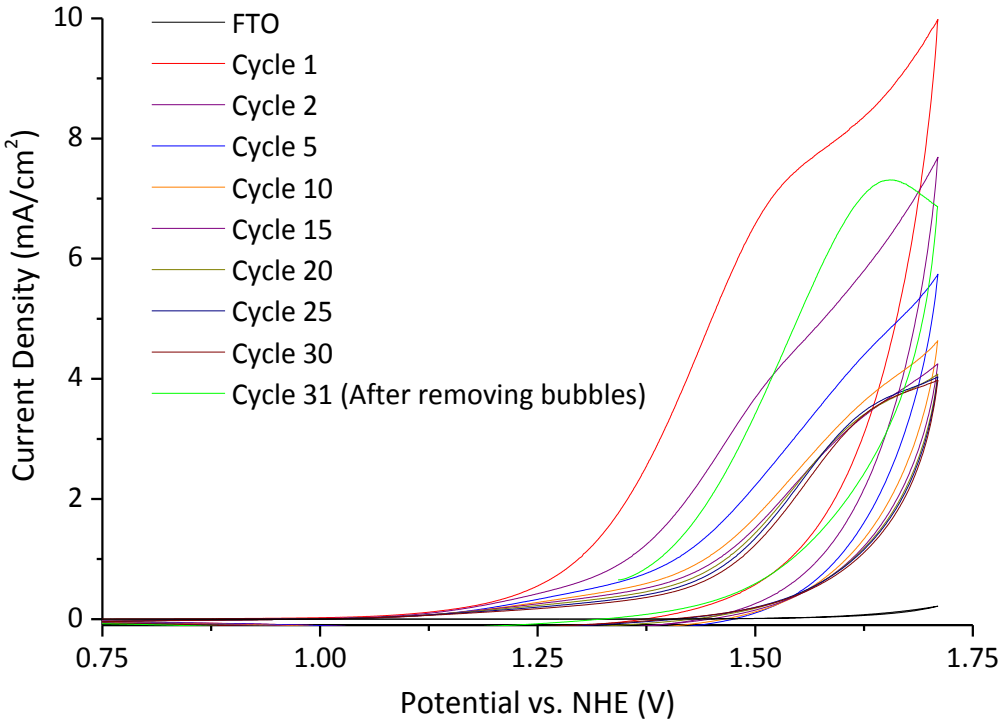

Figure 3.6.1: CV plot using **2**/FTO electrode electrodes showing multiple cycles in comparison to CV cycle of a blank FTO electrode (control experiment); applied potentials 0.75 to 1.7 V vs. NHE at a scan rate of 100 mV/sec.

Figure 3.6.2: 2/FTO electrodes covered by O_2 bubbles during CV experiments.

3.6.2 Linear sweep voltammetry and steady state electrolysis of thin films

Linear sweep voltammetry (LSV), steady state (SS) electrolysis experiments as well as Tafel plots were conducted to evaluate the water oxidation potentials of the **2**/FTO electrodes (**Figure 3.6.3**). **2**/FTO electrodes were used as the working electrode. This electrode was used in combination with a Pt-mesh counter-electrode and an Ag/AgCl (3 M) reference electrode to complete the three-electrode configuration. A scan rate of 1 mV/sec was used. As before, aqueous solutions of KNO_3 (1M) and KPi buffer (50mM, pH 7.2) were used at 20°C. **2**/FTO electrodes were used in LSV experiments before and after bulk electrolysis (which was done at an applied potential of +1.2 V vs. Ag/AgCl for 15 hours). For SS experiments an initial potential of +0.7 V was applied, increasing in increments of +0.05 V. Initially it took seconds to stabilise but this increased to *ca.* 15 minutes when a potential of 1.4 V vs. NHE was used. The resulting current was allowed to stabilise before each incremental potential increase and the current and potential were recorded. This approach allowed LSV and SS experiments to be compared.

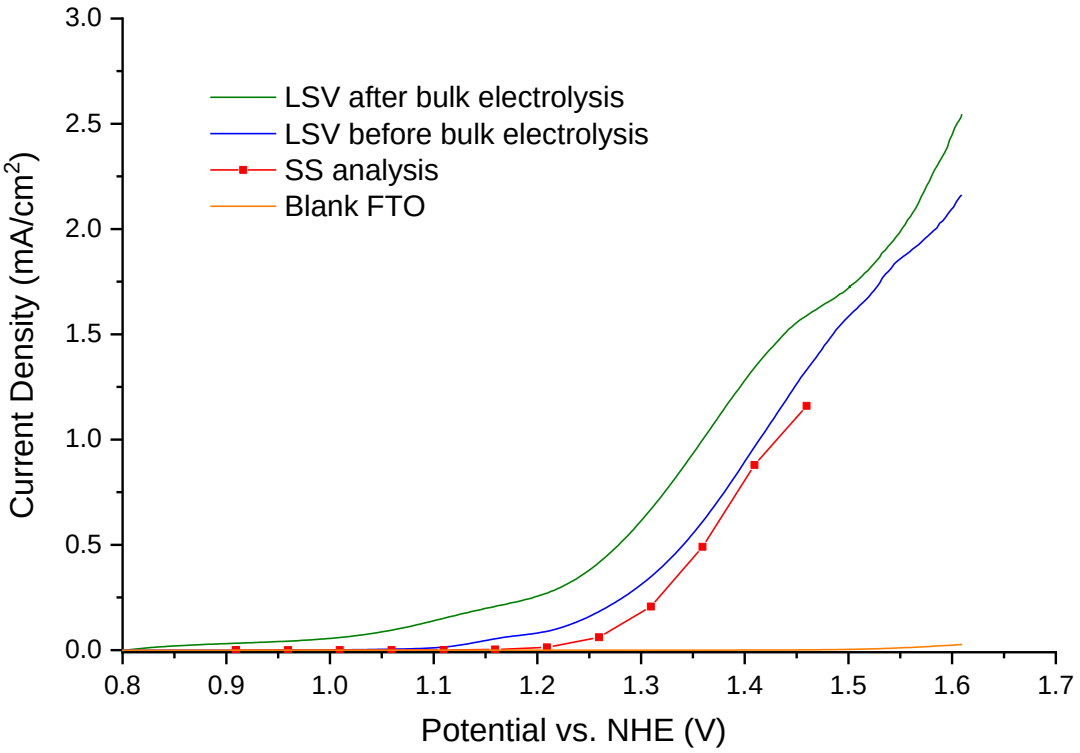

Figure 3.6.3: Comparative electrochemical behaviour for **2**/FTO electrodes with a blank FTO electrode.

When compared to the flat increase in current density when only using a blank FTO, **2**/FTO electrodes show significant increases in current density indicating catalytic OER responses. In all experiments one observes initial increases in current densities starting from an overpotential of *ca.* 0.25 V is attributed to the oxidation of Co^{II} species to Co^{III} species.[40] From *ca.* 0.4 V of overpotential one observes a significant increase in current density which is attributed to the oxidation of the coordinated H_2O molecules.[40] A similar effect trend was observed for the CP blends of crystalline **2** (**Figure 3.4.2**).

Onset overpotentials (**Figure 3.6.4** and **Table 3.6.1**) were estimated from the intersection points between the tangent lines of the Faradaic (current density > 0.2 mA/cm^2) and non-Faradaic (current density < 0.01 mA/cm^2) currents.

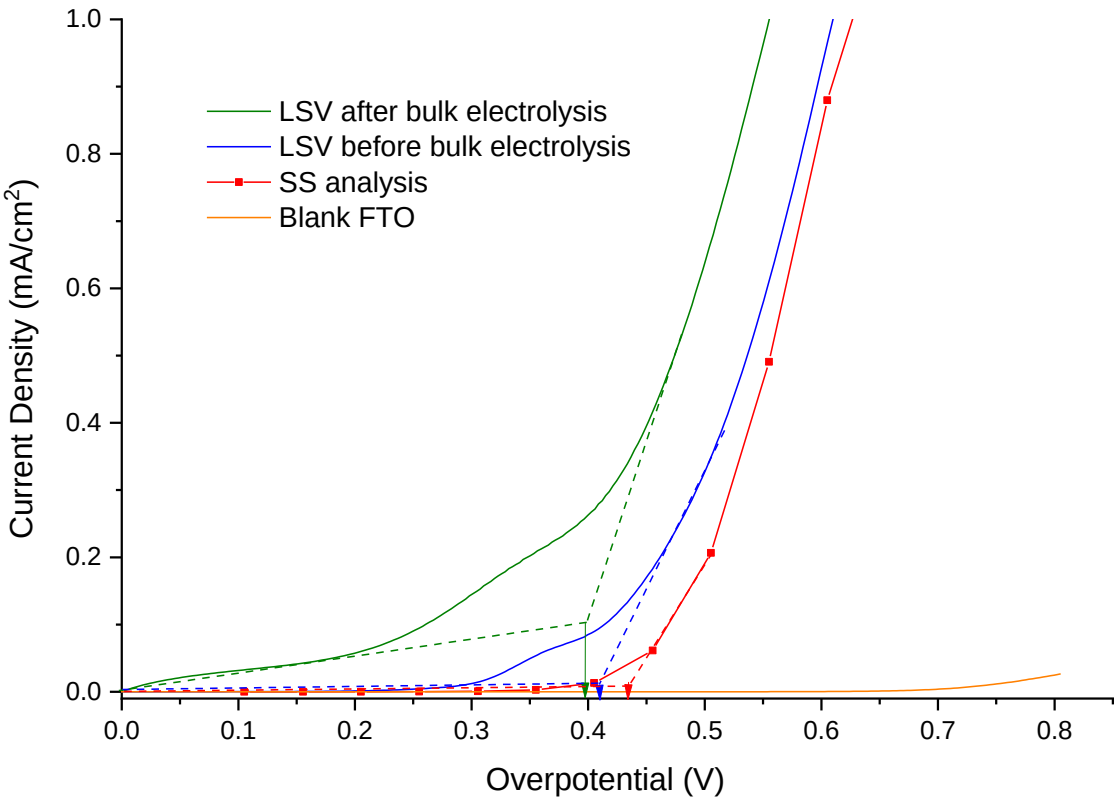

Figure 3.6.4: Comparative electrochemical behaviour **2**/FTO electrodes with a blank FTO electrode.

Table 3.6.1: Comparison of onset potentials obtained from LSV and SS data for **2**/FTO electrodes.

Catalytic Experiment	Onset overpotential
LSV after bulk electrolysis	0.397
LSV before bulk electrolysis	0.410
SS analysis	0.433

The analysis using **2**/FTO electrodes before and after bulk electrolysis and using two different experimental methods, highlight the close correspondence between onset overpotentials from LSV experiments before bulk electrolysis (0.410 V) and SS analysis (0.433 V). Indeed, the potentials are expected to be the similar, whereby variations may also arise from discrepancies between different **2**/FTO electrodes, capacitance effects and mass transport effects. The LSV after bulk electrolysis shows a lower onset overpotential of 0.397 V which we attribute to an increase in the conductivity of the coating or defect formation (**Table 3.6.1**) and which is consistent with the changes observed in **2**/CP electrodes (**Figure 3.4.5**).[43] These increases and slight variations of the onset overpotential may also derive form slight structural variations within the MOF-type materials. However, the determined OER activity characteristics of **2**/FTO electrodes and determined onset overpotentials compare very well with those **2**/CP electrodes which give rise to onset overpotentials ranging from 0.394 V (40 wt% blend) to 0.486 (5 wt% blend) (**Table 3.4.3**). This close match further suggests that the OER active material on the **2**/FTO electrodes is identical or at least closely structurally related to **2** in CP blends.

3.6.3 Tafel plots

Tafel plots for **2**/FTO electrodes were derived from both the SS and LSV experiments. The plots were examined using overpotential values in the 0.40 - 0.61 V range were H_2O oxidation is observed (**Figure 3.6.5**) and Tafel slopes were obtained for each electrode (**Table 3.6.2**). The slopes that were obtained, range from 157 to 213 mV/dec. These slopes are higher than those which were previously obtained for the **2**/CP blends which range from 133 to 176 mV/dec. Ideally we would expect lower Tafel slopes which are closer to those of the **2**/CP electrodes than those obtained but this provides further evidence of the insulating nature of the material (relative to other materials and to CP) as well as limited diffusion within the MOF.

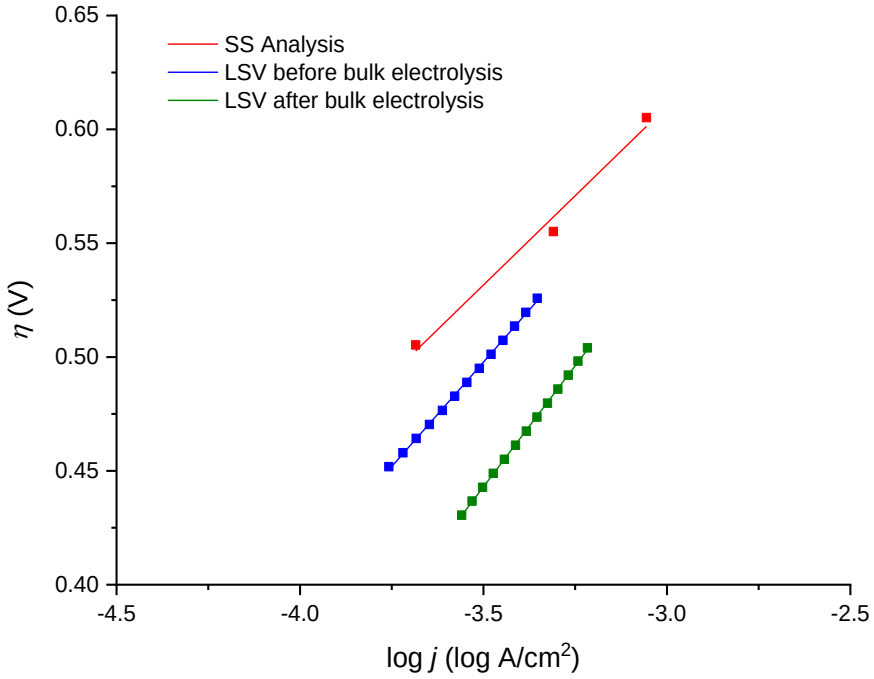

Figure 3.6.5: Tafel region for different **2**/FTO electrodes. SS Analysis (red), LSV before bulk electrolysis (blue), LSV after bulk electrolysis (green).

Table 3.6.2: Summary of Tafel slopes obtained for each **2**/FTO electrode.

2/FTO electrode	Slope (mV/dec)
SS Analysis	157
LSV before bulk electrolysis	183
LSV after bulk electrolysis	213

3.6.4 Bulk electrolysis of **2**/FTO electrodes

Chronoamperometry was used to evaluate the stability of the electrodeposited materials (**Figure 3.6.6**). The bulk electrolysis experiments were carried out over 15 hours using a conductive solution of KNO_3 (1 M) and a KPi buffer (50 mM, pH 7.2) in H_2O at 20°C. The **2**/FTO electrodes were used as the working electrode in the presence of a Pt counter electrode and an Ag/AgCl reference electrode. A potential of +1.2 V vs. Ag/AgCl (equivalent to +1.41 V vs. NHE) was applied. The setup gives rise to an initial current density of *ca.* 0.61 mA/cm^2 which slightly increases to *ca.* 0.71 mA/cm^2 during the time period of the experiment. The experiment highlights the stability of the **2**/FTO electrodes under working conditions. A small increase of the conductivity may arise form slight structural modifications of the catalyst including defect formations.[43]

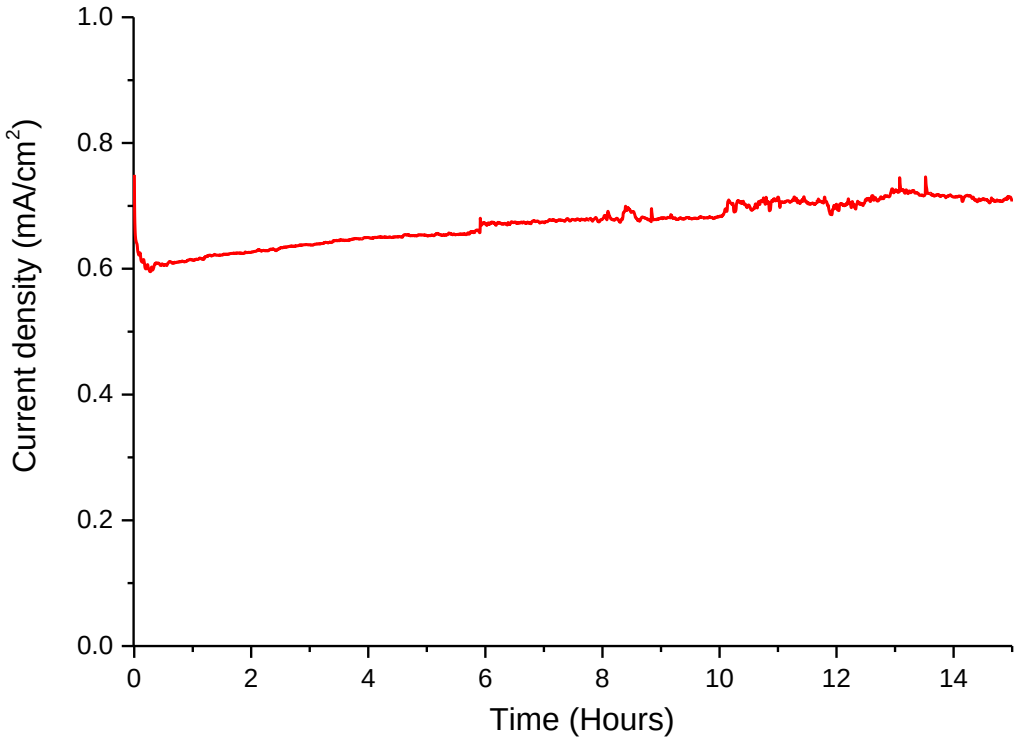

Figure 3.6.6: Chronoamperometry at pH 7.2 using **2**/FTO electrodes. Potential set at +1.2 V (vs Ag/AgCl).

The surface of the **2**/FTO electrodes were analysed using Raman spectroscopy after the bulk electrolysis experiment (+1.2 V vs. Ag/AgCl for 15 hours) (**Figure 3.5.14**). Visually, the electrodes did not change appearance during the experiment. A comparison of the Raman spectrum of a **2**/FTO electrode after the experiment with that of a freshly prepared pristine **2**/FTO electrode suggest that the deposited material remained unchanged. Furthermore, potential CoOx decomposition products, i.e. Co_3O_4 could not be detected. This analysis supports the hypothesis that the MOF-type catalyst remained intact during the bulk electrolysis experiments.

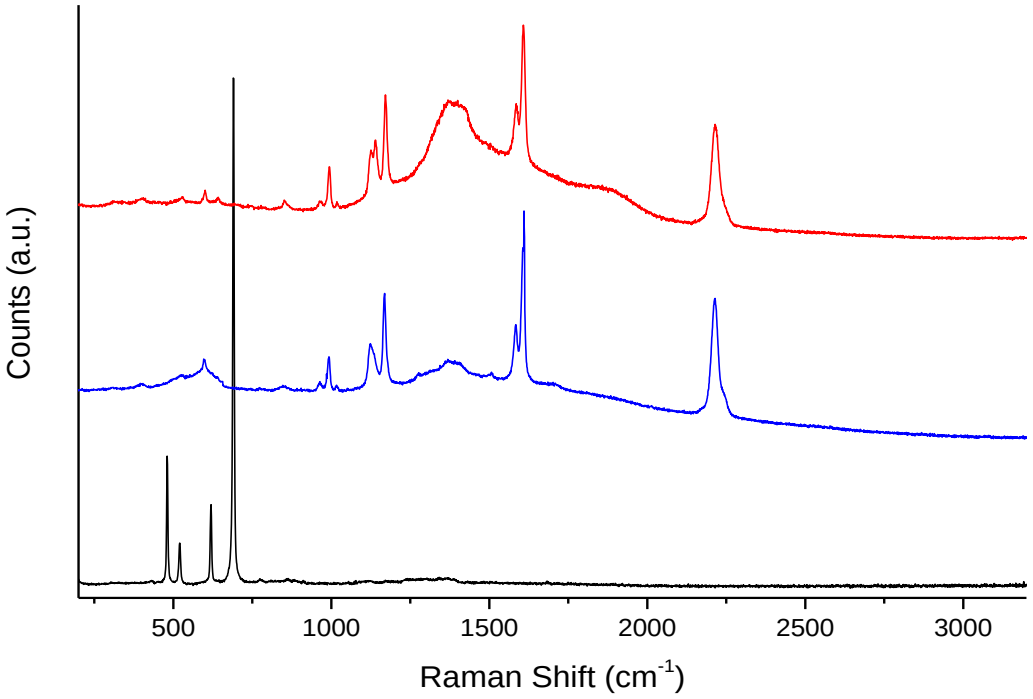

Figure 3.6.7: Raman spectra of **2**/FTO electrodes before (blue) and after bulk electrolysis (red). Raman spectrum of Co_3O_4 shown for comparisons (black).

3.6.5 X-ray photoelectron spectroscopy

X-ray photoelectron spectroscopy (XPS) was used to characterise freshly synthesised crystals of **2**, crystals of **2** that were kept dispersed in deionised H_2O for 18 months and **2**/FTO electrodes before, and after bulk electrolysis (+1.2 V vs. Ag/AgCl at pH 7.2 for 15 hours). These samples were then compared with reference samples of Co(II) acetate and Co_3O_4. XPS survey scans of these materials are similar and show the presence of all expected elements in **2** (**Figure 3.5.15**). The XPS data of freshly synthesised crystals of **2** matches closely with that of crystals which were kept in deionised H_2O for prolonged periods to time, substantiating the hydrolytic stability of **2** in water (**Figure 3.5.16**). This stability is noteworthy, as many carboxylate stabilised MOFs readily hydrolyse in the presence of H_2O.[51,52] Spectra of Co(II) acetate, freshly synthesised crystals of **2** and **2**/FTO electrodes before electrolysis reveal the same Co-derived signal confirming that all samples contain Co^{2+} ions in similar environments (**Figure 3.5.17**). The Co $2p_{1/2}$ and Co $2p_{3/2}$ signals along with their satellite features can be clearly resolved.[53,54] The XPS spectrum of Co_3O_4 is identical to reported literature data.[55,56] XPS spectra of **2**/FTO electrodes before and after bulk electrolysis experiments, are also very similar, thus highlighting the stability of the deposited compound under electrocatalytic OER conditions (**Figure 3.5.18**).[55] The Co $2p_{3/2}$ signal and its satellite feature are visible at 782 and 785 eV in both samples. Only very minor characteristic changes were observed in relation to the Co $2p_{1/2}$ satellite signals. The Co $2p_{1/2}$ signal and its satellite feature are found at 797 and 802 eV, respectively in the spectra of the **2**/FTO electrodes. After bulk electrolysis, a slightly reduced relative intensity of the $2p_{3/2}$ satellite signal is apparent. However, Co_3O_4 shows a single well-resolved signal for the $2p_{1/2}$ orbital at 795 eV with no distinguishable satellite feature and a strong characteristic $2p_{3/2}$ signal at 779 eV revealing an extremely weak satellite feature at 789 eV. Thus the formation of Co_3O_4 under the applied OER conditions can be excluded. The formation of minor, undetectable quantities of other CoOx species which are below the detection limit cannot absolutely be excluded. However, it is noteworthy that slightly reduced relative intensities of the $2p_{3/2}$ satellite signals have been observed for other molecular Co(II) OER catalysts.[57]

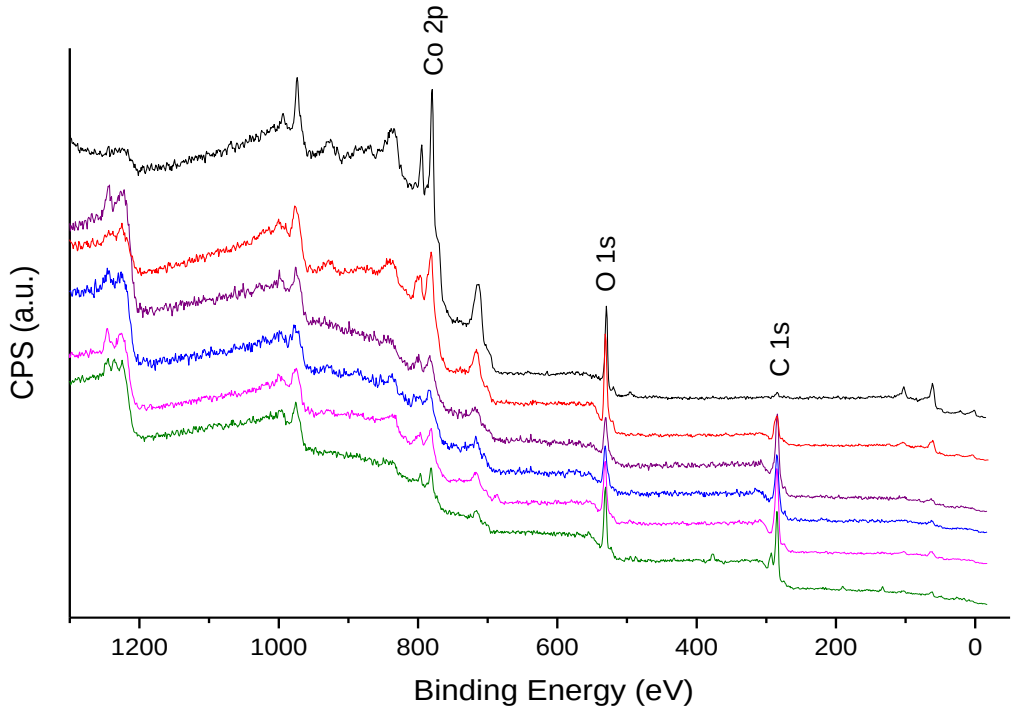

Figure 3.6.8: XPS overview spectra. Co_3O_4 (black), cobalt(II) acetate (red), Freshly synthesised crystals of **2** (purple), crystals of **2** kept in deionised water for 18 months (blue), pristine **2**/FTO electrodes (pink) and **2**/FTO electrodes after bulk electrolysis (green, +1.2 V vs. Ag/AgCl; pH 7.2; 15 hours).

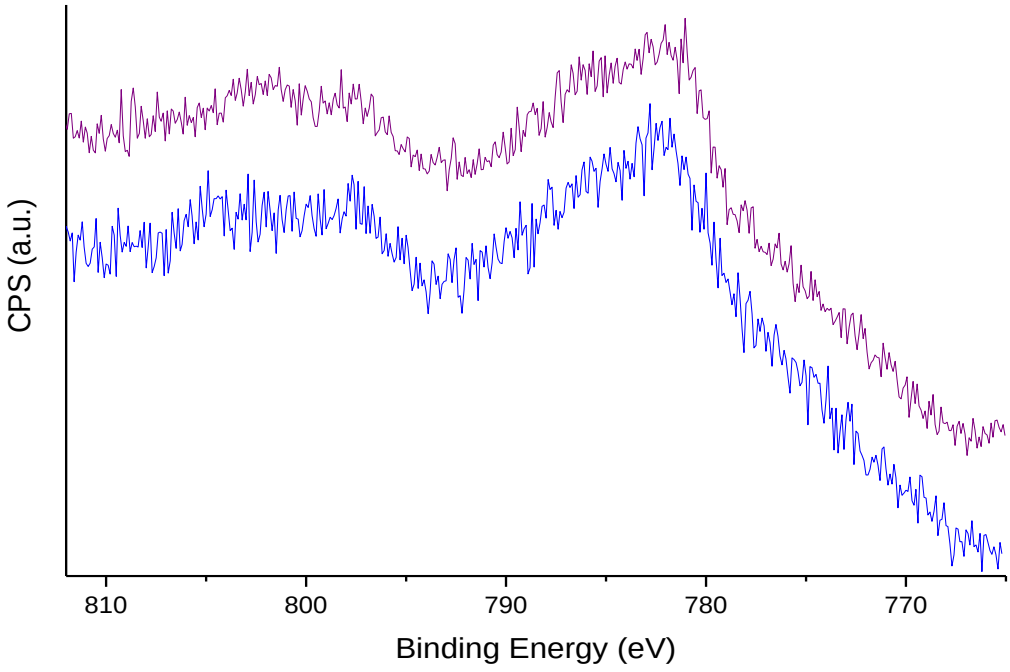

Figure 3.6.9: XPS spectra highlighting the Co(II)-derived signals. Freshly synthesised crystals of **2** (purple) and crystals of **2** that were kept in deionised H_2O for 18 months (blue).

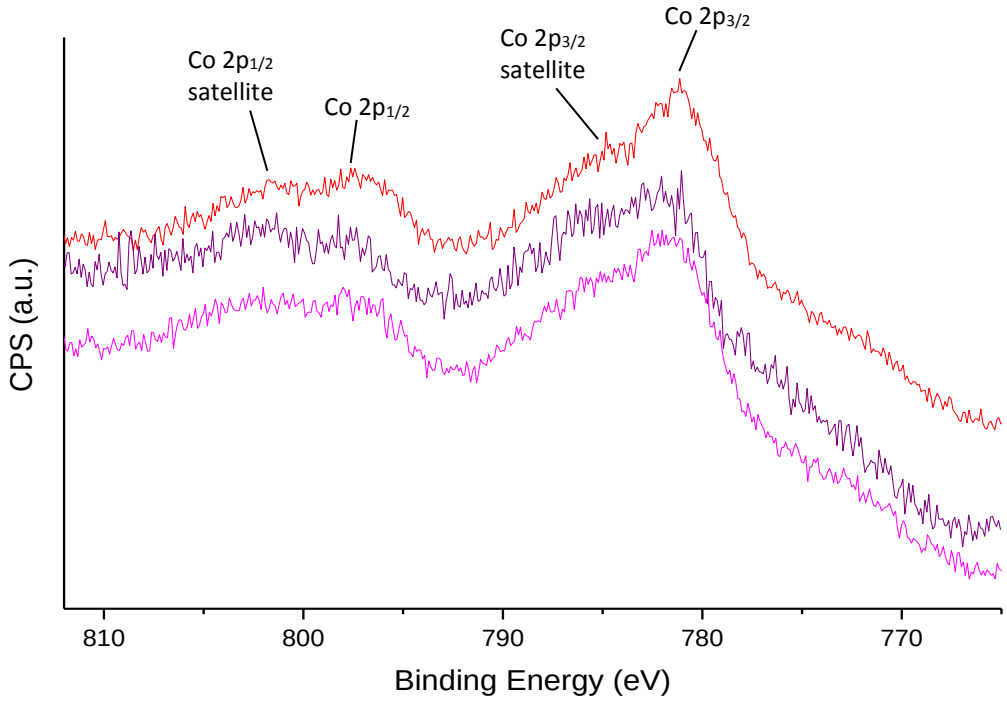

Figure 3.6.10: Comparison and assignment of XPS spectra focusing on the Co(II)-derived signals. Cobalt(II) acetate (red), freshly synthesised crystals of **2** (purple) and **2**/FTO (pink).

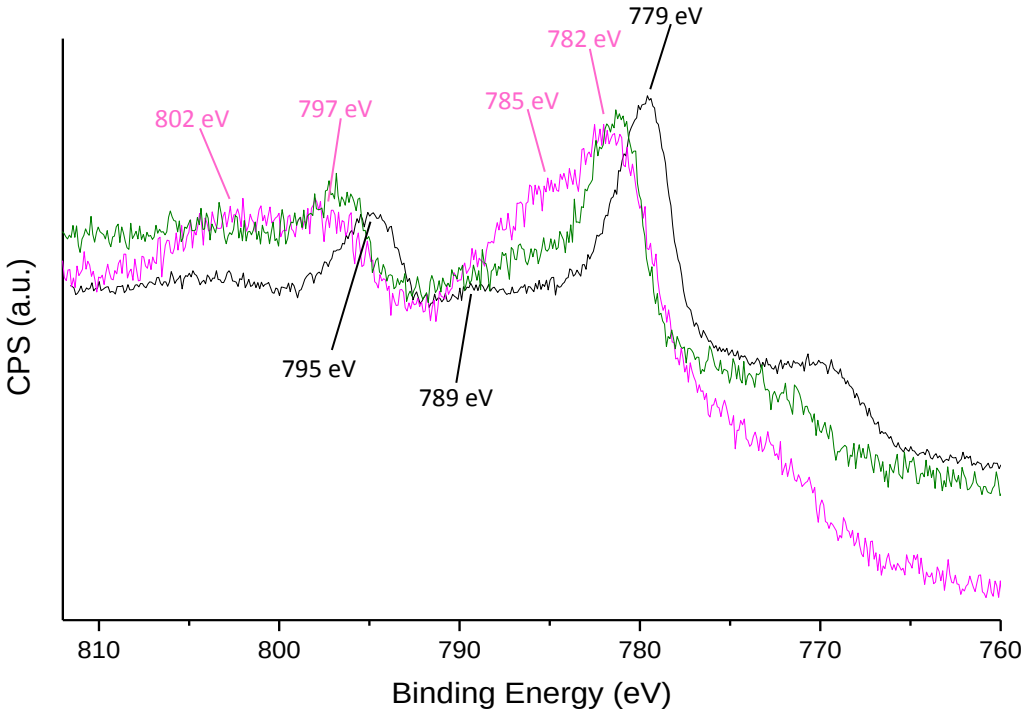

Figure 3.6.11: Comparison of XPS spectra focusing on the Co(II)-derived signals. Co_3O_4 (black), **2**/FTO before bulk electrolysis (pink) and **2**/FTO after bulk electrolysis (green; +1.2 V vs. Ag/AgCl; pH 7.2 for 15 hours).

3.7 Conclusion

A novel MOF, composed of pentanuclear cobalt(II) hydroxo-clusters, $Me_2NH_2[Co_5(\mathbf{L2})_3(\mu_3\text{-}OH)_2(H_2O)_2(DMF)_2]$ (**2**), was synthesised and was structurally characterised. The pentanuclear SBU is stabilised by nine carboxylates that derive from nine **L2** ligands that link the nodes into a honeycomb-type network. The MOF is twofold interpenetrated whereby π-π stacking interactions between different organic ligand phenyl rings add stability to the overall framework. The constitutional and structural attributes of the compounds were studied using a variety of analytical techniques including X-ray diffraction, Raman and IR spectroscopy and thermogravimetric analysis. The thermal stability allows constitutional solvent molecules (accessible void volume of 48.6%) to be removed whilst the framework stays intact.

The activated MOF is characterised by significant N_2 gas uptake, yielding a reversible type-I isotherm with a BET surface area of 1755 m^2/g. Particularly noteworthy is also the hydrolytic stability of the MOF in water, retaining its integrity for more than 18 months when dispersed in water. **2** catalyses the oxidation of water under photo-induced and electrocatalytic conditions. The OER experiments were carried out at pH 7.2 a condition under which few OER catalysts containing earth-abundant metals perform at satisfactory activity. Under photo-induced catalytic conditions relatively high turnover frequencies of 1.482 s^{-1} can be achieved. The compound reveals good electrocatalytic OER activity when used in carbon paste blends (**2**/CP) as electrodes. The **2**/CP electrodes give rise to activity reaching an onset overpotential of 0.394 V, 1 mA/cm^2 at an overpotential of 0.489 V (1.292 V vs. NHE) and 10 mA/cm^2 at an overpotential of 0.755 V (1.562 V vs. NHE). Tafel slopes of 133 – 176 mV/dec were obtained for the **2**/CP electrodes.

Interestingly, the MOF or a closely structurally related compound can be synthesised under electrochemical conditions and deposited on FTO-coated glass electrodes (**2**/FTO). Various analytical methods suggest a close structural and constitutional relationship between solvothermally synthesised **2** and electrochemically synthesised materials (**2**/FTO). **2**/FTO electrodes were also used for the electrocatalytic OER experiments revealing good performance and remarkably high stability under working conditions (bulk electrolysis experiments can be conducted for several weeks). The **2**/FTO electrodes facilitate onset overpotentials of 0.410 V which increases to 0.397 V after bulk

electrolysis. The current density reaches 1 mA/cm^2 at an overpotential of ca. 0.562 V (1.414 V vs. NHE, for the 2/FTO electrode after bulk electrolysis). Tafel slopes of 157 – 213 mV/dec were obtained for the **2**/FTO electrodes.

Post-catalytic characterisations highlight the high stability of the MOF during OER conditions. The MOF remains the predominant compound in the carbon paste and on the surface of the FTO electrodes. Cobalt oxides could not directly be identified, however the formation of undetectable quantities in the porous framework structure cannot be completely ruled out.

3.8 References

1 N. Zhu, G. Tobin and W. Schmitt, *Chem. Commun.*, 2012, **48**, 3638–3640.

2 N. Zhu, M. J. Lennox, T. Düren and W. Schmitt, *Chem. Commun.*, 2014, **50**, 4207–4210.

3 N. Zhu, D. Sensharma, P. Wix, M. J. Lennox, T. Düren, W.-Y. Wong and W. Schmitt, *Eur. J. Inorg. Chem.*, 2016, 1939–1943.

4 G. Tobin, S. Comby, N. Zhu, R. Clérac, T. Gunnlaugsson and W. Schmitt, *Chem. Commun.*, 2015, **51**, 13313–13316.

5 J. Concepcion and J. Jurss, *J. Am. Chem. Soc.*, 2008, **130**, 16462–16463.

6 G. Duca, *Homogeneous Catalysis with Metal Complexes: Fundamentals and Applications*, Springer, 2012.

7 E. A. Flügel, V. W. H. Lau, H. Schlomberg, R. Glaum and B. V. Lotsch, *Chem. - A Eur. J.*, 2016, **22**, 3676–3680.

8 J. Jiang, L. Huang, X. Liu and L. Ai, *ACS Appl. Mater. Interfaces*, 2017, **9**, 7193–7201.

9 S. Wang, Y. Hou, S. Lin and X. Wang, *Nanoscale*, 2014, **6**, 9930–9934.

10 Q. Xu, H. Li, F. Yue, L. Chi and J. Wang, *New J. Chem.*, 2016, **40**, 3032–3035.

11 M. Blasco-Ahicart, J. Soriano-López, J. J. Carbó, J. M. Poblet and J. R. Galan-Mascaros, *Nat. Chem.*, 2018, **10**, 24–30.

12 Q. Yin, J. M. Tan, C. Besson, Y. V Geletii, D. G. Musaev, A. E. Kuznetsov, Z. Luo, K. I. Hardcastle and C. L. Hill, *Science*, 2010, **328**, 342–345.

13 X. B. Han, Z. M. Zhang, T. Zhang, Y. G. Li, W. Lin, W. You, Z. M. Su and E. B. Wang, *J. Am. Chem. Soc.*, 2014, **136**, 5359–5366.

14 I. Roger, M. A. Shipman and M. D. Symes, *Nat. Rev. Chem.*, 2017, **1**, 1–13.

15 X. Deng and H. Tüysüz, *ACS Catal.*, 2014, **4**, 3701–3714.

16 K. Sonogashira, *J. Organomet. Chem.*, 2002, **653**, 46–49.

17 K. Sonogashira, Y. Tohda and N. Hagihara, *Tetrahedron Lett.*, 1975, **16**, 4467–4470.

18 X. R. Hao, X. L. Wang, Z. M. Su, K. Z. Shao, Y. H. Zhao, Y. Q. Lan and Y. M. Fu, *Dalton Trans.*, 2009, 8562–8566.

19 M. Pinsky and D. Avnir, *Inorg. Chem.*, 1998, **37**, 5575–5582.

20 D. Casanova, J. Cirera, M. Llunell, P. Alemany, D. Avnir and S. Alvarez, *J. Am. Chem. Soc.*, 2004, **126**, 1755–1763.

21 J. Cirera, E. Ruiz and S. Alvarez, *Chem. - A Eur. J.*, 2006, **12**, 3162–3167.

22 C. A. Hunter and J. K. M. Sanders, *J. Am. Chem. Soc.*, 1990, **112**, 5525–5534.

23 M. O. Sinnokrot and C. D. Sherrill, *J. Phys. Chem. A*, 2004, **108**, 10200–10207.

24 D. Dubbeldam, S. Calero, D. E. Ellis and R. Q. Snurr, *Mol. Simul.*, 2016, **42**, 81–101.

25 V. Otero, D. Sanches, C. Montagner, M. Vilarigues, L. Carlyle, J. A. Lopes and M. J. Melo, *J. Raman Spectrosc.*, 2014, **45**, 1197–1206.

26 E. Smith and G. Dent, *Modern Raman Spectroscopy - A Practical Approach*, John Wiley & Sons, Ltd, Chichester, UK, 2005.

27 B. H. Stuart, *Infrared Spectroscopy: Fundamentals and Applications*, John Wiley & Sons, Ltd, 2005.

28 K. Nakamoto, *Infrared and Raman Spectra of Inorganic and Coordination Compounds*, John Wiley & Sons, Ltd, 6th Edn., 2008.

29 G. B. Deacon and R. J. Phillips, *Coord. Chem. Rev.*, 1980, **33**, 227–250.

30 S. Lowell, J. E. Shields, M. A. Thomas and M. Thommes, *Characterization of porous solids and powders: surface area, pore size and density*, Kluwer Academic Publishers, 2004.

31 A. J. Howarth, A. W. Peters, N. A. Vermeulen, T. C. Wang, J. T. Hupp and O. K. Farha, *Chem. Mater.*, 2017, **29**, 26–39.

32 J. Rouquerol, P. Llewellyn and F. Rouquerol, in *Studies in surface science and catalysis*, Elsevier, 2007, vol. 160, 49–56.

33 H. W. Langmi, J. Ren, B. North, M. Mathe and D. Bessarabov, *Electrochim. Acta*, 2014, **128**, 368–392.

34 M. Schilling and S. Luber, *Front. Chem.*, 2018, **6**, 1–21.

35 L. Sun, M. G. Campbell and M. Dincă, *Angew. Chem. Int. Ed.*, 2016, **55**, 3566–3579.

36 R. Matheu, M. Z. Ertem, J. Benet-Buchholz, E. Coronado, V. S. Batista, X. Sala and A. Llobet, *J. Am. Chem. Soc.*, 2015, **137**, 10786–10795.

37 M. Craig, G. Coulter, E. Dolan, J. Soriano-lópez, W. Schmitt and M. García-Melchor, *ChemRxiv*, 2019, 7963592.

38 M. Lafrance and K. Fagnou, *J. Am. Chem. Soc.*, 2006, **128**, 16496–16497.

39 Y. Surendranath, M. W. Kanan and D. G. Nocera, *J. Am. Chem. Soc.*, 2010, **132**, 16501–16509.

40 J. Soriano-López, D. G. Musaev, C. L. Hill, J. R. Galán-Mascarós, J. J. Carbó and J. M. Poblet, *J. Catal.*, 2017, **350**, 56–63.

41 A. J. Bard and L. R. Faulkner, *Electrochemical methods, fundamentals and applications*, John Wiley & Sons, Inc, 2nd Edn., 2001.

42 J. Q. Shen, P. Q. Liao, D. D. Zhou, C. T. He, J. X. Wu, W. X. Zhang, J. P. Zhang and X. M. Chen, *J. Am. Chem. Soc.*, 2017, **139**, 1778–1781.

43 H. Zhang and R. Lv, *J. Mater.*, 2018, **4**, 95–107.

44 E. V. J. and B. Å. Markus D. Kärkäs, Tanja M. Laine, in *Applied Photosynthesis*, Intech open, 2016, 189–219.

45 C. Wang, Z. Xie, K. E. Dekrafft and W. Lin, *J. Am. Chem. Soc.*, 2011, **133**, 13445–13454.

46 L. Chi, Q. Xu, X. Liang, J. Wang and X. Su, *Small*, 2016, **12**, 1351–1358.

47 B. Limburg, E. Bouwman and S. Bonnet, *ACS Catal.*, 2016, **6**, 5273–5284.

48 M. Li and M. Dincă, *J. Am. Chem. Soc.*, 2011, **133**, 12926–12929.

49 M. Li and M. Dincă, *Chem. Mater.*, 2015, **27**, 3203–3206.

50 A. Wassilkowska, A. Czaplicka-Kotas, M. Zielina and A. Bielski, *Tech. Trans. Chem.*, 2014, **18**, 133–148.

51 H. Furukawa, F. Gándara, Y.-B. Zhang, J. Jiang, W. L. Queen, M. R. Hudson and O. M. Yaghi, *J. Am. Chem. Soc.*, 2014, **136**, 4369–4381.

52 J. J. Low, A. I. Benin, P. Jakubczak, J. F. Abrahamian, S. A. Faheem and R. R. Willis, *J. Am. Chem. Soc.*, 2009, **131**, 15834–15842.

53 C. Yu, Y. Wang, J. Zhang, X. Shu, J. Cui, Y. Qin, H. Zheng, J. Liu, Y. Zhang and Y. Wu, *New J. Chem.*, 2016, **40**, 6881–6889.

54 J. F. Moulder, W. F. Stickle, P. E. Sobol and K. D. Bomben, *Handbook of X-ray Photoelectron Spectroscopy*, Physical Electronics, Inc., 1995.

55 S. C. Petitto, E. M. Marsh, G. A. Carson and M. A. Langell, *J. Mol. Catal. A Chem.*, 2008, **281**, 49–58.

56 S. C. Petitto and M. A. Langell, *J. Vac. Sci. Technol. A Vacuum, Surfaces, Film.*, 2004, **22**, 1690–1696.

57 J. Soriano-López, F. Song, G. R. Patzke and J. R. Galan-Mascaros, *Front. Chem.*, 2018, **6**, 1–8.

Chapter 4

A series of isoreticular MOF structures with mixed-metal SBUs

4 A series of isoreticular MOF structures with mixed-metal SBUs

4.1 Introduction

From alloys[1,2] to mixed-metal clusters, the synergistic effects of different combinations of metals in materials are well documented.[3,4] A range of different strategies to introduce mixtures of multiple metal types into MOFs have been applied, including; (i) The introduction of metal centres in linker molecules,[5,6] (ii) The modification of SBUs to include multiple metal types, either by using multiple metals in MOF reaction mixtures or through post-synthetic modifications,[7–9] (iii) The incorporation of metal-nanoparticles or complexes inside the cavity of the MOF.[10–12]

This chapter will focus exclusively on the modification of SBUs in MOFs to include multiple metal types by using combinations of metals in the synthetic reaction mixtures. This approach has previously yielded up to 10 different metals in the same MOF, MOF-74 that is characterised by a tubular pore structure and a 1-periodic secondary building unit (a rod shaped SBU), however the authors documented a random distribution of metal ions and did not resolve exact metal positions within the SBU.[13] MOFs containing two or more metal ions within the same SBU are rare, because their attempted synthesis often yields mixed MOF phases instead of phase-pure mixed-metal MOFs.[14] In addition certain metal ions can be especially difficult to distinguish from each other using conventional X-ray diffraction techniques. High quality crystals and powerful synchrotron X-ray sources, as well as complementary techniques are often required to accurately assign metal ions to their respective positions in the SBU, but this can only be useful if the metal ions within the SBU are arranged in an ordered manner. Most reports of mixed-metal MOFs assume that there is a random distribution of the various metal types and focus the publication on the altered properties of the resulting materials.[7–9] Publications with site-specific incorporation of metal centres are less common and they usually use step-wise synthetic approaches to introduce metals into specific positions in SBUs.[15–17]

Previously, our group published a Zn-based MOF $[Zn_3(\mathbf{L2})_2(DMF)_2]$ containing linear trinuclear $\{Zn_3\}$ SBUs.[18] We note that there are two sites on the $\{Zn_3\}$ SBU in this MOF containing coordinated solvent molecules which could present an opportunity to utilise this structure for catalysis applications, i.e. water oxidation applications if the Zn(II) ions could be replaced with more catalytically active metal ions. In addition, the structure contains

large channels filled with solvent molecules extending through the MOF crystals in all three crystallographic directions. This may provide accessibility to most SBUs in the structure. Therefore the synthesis of MOFs based on the $[Zn_3(\mathbf{L2})_2(DMF)_2]$ structure using mixtures of earth abundant metal ions known to show catalytic activity was attempted.[19]

Three structurally related novel mixed-metal MOFs were synthesised using mixtures of Mn^{2+} and Co^{2+} (compound **3**) and Zn^{2+} and Co^{2+} (compounds **4** and **5**) ions. A combination of conventional X-ray diffraction analysis, EDX spectroscopy, XPS analysis, UV-vis absorption spectroscopy and computational analysis to accurately resolve the relative positions of metal ions within the SBUs was carried out. In addition, provisional catalytic studies were carried out to evaluate possible water oxidation activity of the newly synthesised compounds.

4.2 Ligand Synthesis

The ligand **H_3L2** was used for the synthesis of compounds **3**, **4** and **5** in this chapter. Its synthesis is described in **Section 3.2** of the previous chapter.

4.3 $[MnCo_2(\mathbf{L2})_2(H_2O)_2]$ (**3**)

4.3.1 Synthesis and structural characterisation of $[MnCo_2(\mathbf{L2})_2(H_2O)_2]$ (**3**)

The self-assembly of **3** was observed when **H_3L2**, $MnCl_2{\cdot}2H_2O$ and $Co(NO_3)_2{\cdot}6H_2O$ (1:1:2 mole ratio) were heated in DMF at 90°C for 72 hours. Phase-pure bright blue crystals of **3** were formed in the reaction mixture and were used for single crystal X-ray diffraction analysis. A yield of 36% was obtained. **3** crystallises in the tetragonal space group $P4_322$. The compound has the molecular formula $[MnCo_2(\mathbf{L2})_2(H_2O)_2]$.

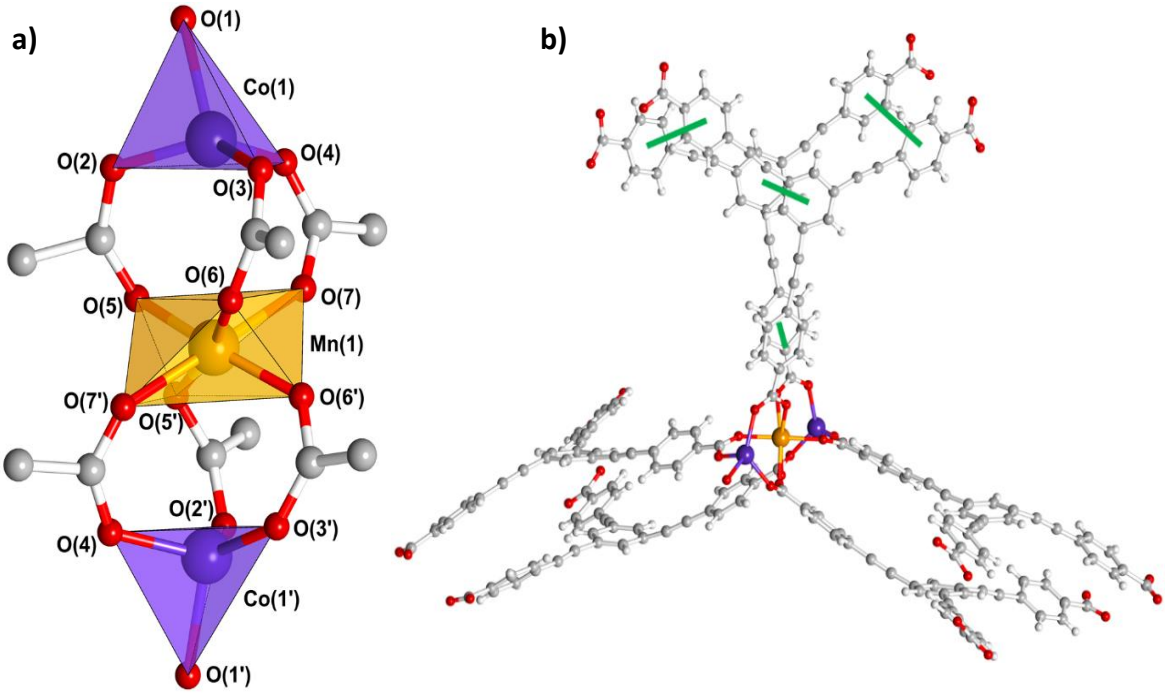

Figure 4.3.1: a) View of the $\{Mn_1Co_2\}$ SBU of **3** along the *[1 1 1]*-direction with coordinated bridging carboxylate groups from six $\mathbf{L2}^{3-}$ ligands and two coordinated H_2O molecules (O(1)/O(1')). Transparent polyhedral representations are used to highlight the coordination environments of the metal ions. Atoms of interest are labelled. **b)** View of the SBU with six $\mathbf{L2}^{3-}$ ligands attached; view in the *[-1 0 0]*-direction. Green lines are used to highlight π-π interactions between phenyl rings in adjacent ligands. Colour key: Co (purple), Mn (orange), O (red), C (grey), H (white).

The asymmetric unit of **3** is represented by a central Mn(II) ion, a peripheral Co(II) ion, a coordinating water molecule as well as one complete coordinating **L2**$^{3-}$ ligand. A third Co(II) ion is generated through symmetry operations forming the hourglass shaped {Mn_1Co_2} trinuclear cluster with a Co(1)-Mn(1)-Co(1') angle of 174.33° and a Co(1)-Co(1') distance of 7.06 Å when measuring from the centre of each ion (**Figure 4.3.1 a)**). This trinuclear cluster in **3** is stabilised by a total of six carboxylate moieties that derive from six deprotonated **H_3L2** ligands which impart stability to the SBU. All carboxylate functionalities facilitate bidentate bridging modes. The centrally located Mn(1) atom is connected to each peripheral Co(II) centre through three bridging carboxylate groups from **L2**$^{3-}$ ligands. This results in a 6-coordinate octahedral Mn(1) centre and 4-coordinate tetrahedral Co(1)/Co(1') centres which acquire the remaining O-donors from coordinated solvent molecules. These coordinated solvent molecules appear crystallographically as O-atoms and are resolved as H_2O molecules but could potentially also derive from disordered DMF molecules. The carboxylate Mn(1)-O bond distances vary between 2.160(13) Å and 2.231(12) Å while the carboxylate Co-O bond distances are slightly shorter varying between 1.955(8) Å and 2.180(10) Å. The Co-OH_2 bond distance is 2.188(17) Å.

Surrounding Mn(1), the angles between *trans* located O-atoms deviate modestly from an ideal angle of 180° to 169.78(4)° and 179.18(4)°. If O(6) and O(5') are considered to be in the axial sites surrounding Mn(1), then the remaining O-atoms (O(6'), O(5), O(7) and O(7')) are in the equatorial plane. In an ideal octahedral geometry, an angle of 90° is expected between *cis* located oxygen atoms surrounding the Mn(1) octahedral metal centre. However, the O(6)-Mn(1)-(O5') axis is tilted towards the symmetry equivalent O(6')-Mn(1)-O(5) axis within the equatorial plane resulting in reduced O(6)-Mn(1)-O(6') and O(5')-Mn(1)-O(5) angles of 63.16(6)° and 49.36(6)°, respectively. This tilting towards the equatorial plane results in a highly distorted, 'flattened' octahedral coordination environment (**Figure 4.3.2**, **a)**).

The H_2O derived O(1) atom is bent towards one of its neighbouring faces of the Co(1)-based tetrahedron. The binding geometry is characterised by O(1)-Co(1)-O(2) and O(1)-Co(1)-O(4) angles of 86.0(6) and 99.0(5)°, respectively, thus deviating significantly from an ideal tetrahedral angle of 109.5°. Concomitantly, the O(1)-Co(1)-O(3) angle is widened to 125.1(5)°. The location of the O(1) atom further promotes the non-linearity of

the SBU to give a O(1)-Mn(1)-Co(1') angle of 159.67°. The base of the tetrahedron that characterises the coordination environment of Co(1) is formed by the donor atoms O(2), O(3) and O(4). Their atoms position are raised up towards the O(1) atom, resulting in angles of 104.6(3)°, 114.6(5)° and 125.0(5)° which also deviate from the ideal tetrahedral angle (**Figure 4.3.2, b)**).

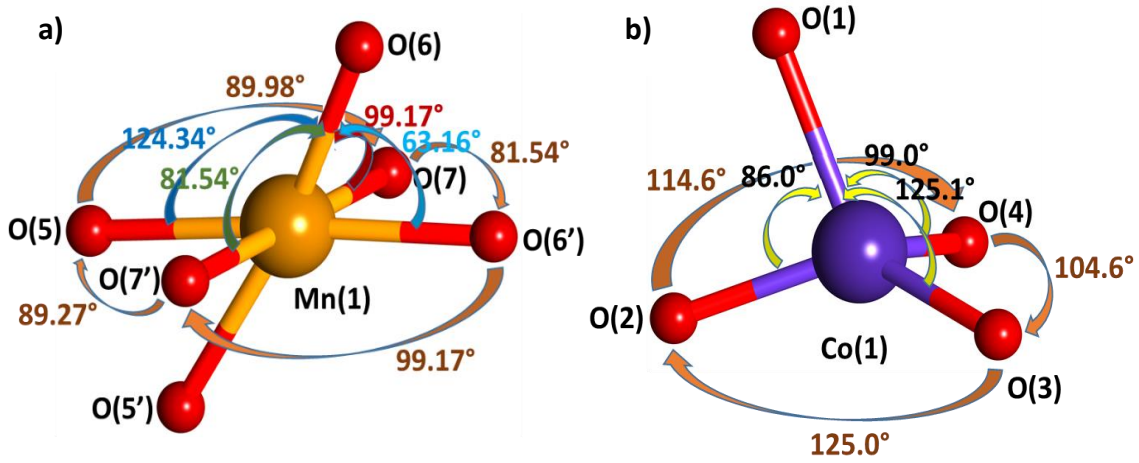

Figure 4.3.2: Coordination environment of the symmetry-independent metal ions in **3** showing selected angles between coordinated O-atoms. **a)** The Mn(1) coordination environment. **b)** The Co(1) coordination environment (Which is identical to the symmetry equivalent Co(1')). O(1) derives from a coordinated H_2O molecule, while O(2) to O(7) derive from coordinated **L2**$^{3-}$ ligands. Colour key: Mn (orange), Co (purple), O (red).

The {Mn_1Co_2} SBU formally represents a 6-connecting node whereby it is linked *via* six **L2**$^{3-}$ ligands to six neighbouring SBUs. The **L2**$^{3-}$ ligands can be grouped into 2 × 3 sets whose struts point in three distinct directions of space and enclose *ca.* 120° angles (**Figure 4.3.1 b)**). Parallel displacement π-π interactions between phenyl rings in each strut possibly add to the stability of the overall 3D structure. The distances between the centre of one interacting phenyl ring to the centre of a neighbouring phenyl ring varies between *ca.* 4.0 Å and *ca.* 4.5 Å which are typical values for weakly interacting aromatic moities.[20,21] It is further noteworthy that the assignment of an ordered structure, in which the Mn(II) ions are octahedrally coordinated and the Co(II) centres adopt tetrahedral binding environments, lead to improved quality values during the structural refinement of the X-ray data.

Table 4.3.1: Selected bond distances and angles of the coordination environments in **3**.

Atoms	Distance [Å]	Atoms	Angle [°]
Mn(1)-O(5)	**2.231(12)**	O(5)-Mn(1)-O(6')	**169.78(4)**
Mn(1)-O(6)	**2.160(13)**	O(7)-Mn(1)-O(7')	**179.18(4)**
Mn(1)-O(7)	**2.221(8)**	O(5)-Mn(1)-O(5')	**49.36(6)**
		O(5)-Mn(1)-O(6)	**124.34(4)**
Co(1)-O(1)	**2.188(17)**	O(5)-Mn(1)-O(7)	**89.98(4)**
Co(1)-O(2)	**1.976(16)**	O(5)-Mn(1)-O(7')	**89.27(4)**
Co(1)-O(3)	**2.180(10)**	O(6)-Mn(1)-O(6')	**63.16(6)**
Co(1)-O(4)	**1.955(8)**	O(6)-Mn(1)-O(7)	**99.17(4)**
		O(6)-Mn(1)-O(7')	**81.54(4)**
		O(1)-Co(1)-O(2)	**86.0(6)**
		O(1)-Co(1)-O(3)	**125.1(5)**
		O(1)-Co(1)-O(4)	**99.0(5)**
		O(2)-Co(1)-O(3)	**125.0(5)**
		O(2)-Co(1)-O(4)	**114.6(5)**
		O(3)-Co(1)-O(4)	**104.6(3)**

The $\{Mn_1Co_2\}$ SBUs in **3** are located along a 4_3-screw axis which extend in the direction of the crystallographic *c*-axis and results in the formation of helical chain moieties (**Figure 4.3.3**). $\mathbf{L2^{3-}}$ ligands further interlink such helical assemblies through their carboxylate groups whereby all $\mathbf{L2^{3-}}$ ligands bind to two different helical chains only.

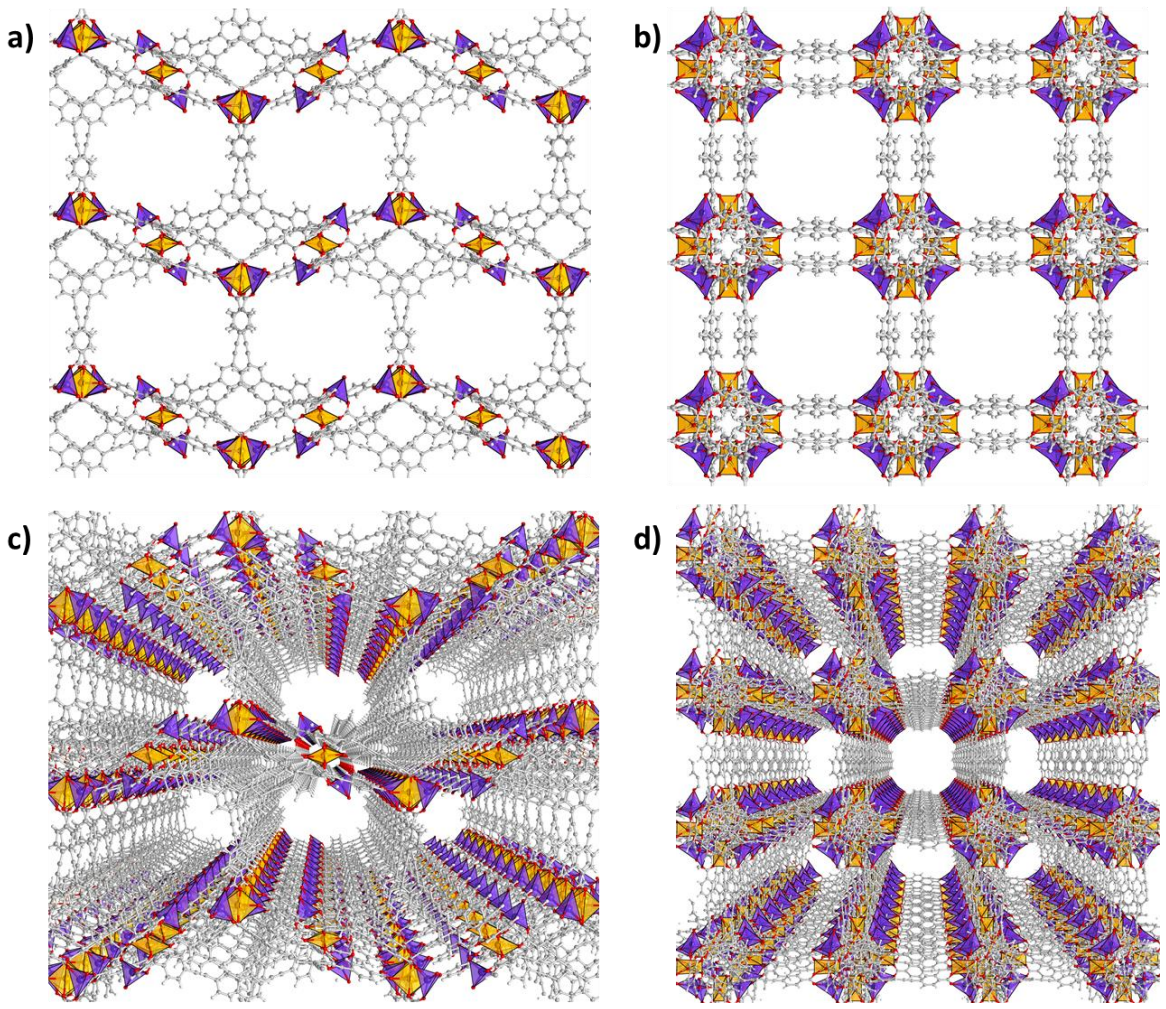

Figure 4.3.3: Ball-and-stick representations with cobalt and manganese atoms shown as polyhedra. **a)**, **c)** View down the crystallographic *b*-axis. **b)**, **d)** View down the crystallographic *c*-axis. Colour key: Co purple, Mn (orange), O (red), C (grey), H (white).

The structure of **3** is two-fold interpenetrated and consists of two symmetry equivalent chiral interwoven nets (**Figure 4.3.4**). This interweaving likely adds to the stability of the MOF without significantly affecting the pore/channel sizes in the framework.[18] **3** forms an open framework structure with voids/channels accessible from all three crystallographic directions. T-shaped π-π interactions between the phenyl groups in different nets are observed leading to interatomic distances of *ca.* 4.7 Å between the centres of each interacting phenyl ring. Such distances are characteristic for interwoven MOF structures and typical for weak π-π interactions or related dispersion forces.[21]

Desolvated crystals of **3** were found to have a density of 0.477 g/cm^3. The void space was calculated using the RASPA[22] software package and it was found to occupy 72.91% of the cell volume of the crystal structure. Van der Waals space filling models show that **3** has large accessible pores that extend in all three crystallographic directions (**Figure 4.3.4**). Cylindrical pores are observed along the crystallographic *c*-axis and are characterised by diameters of *ca.* 11.6 Å. Larger rectangular shaped pores, that are observed along both the crystallographic *a* and *b*-axes have cross-sectional dimensions of *ca.* 15.4 Å x 10.1 Å.

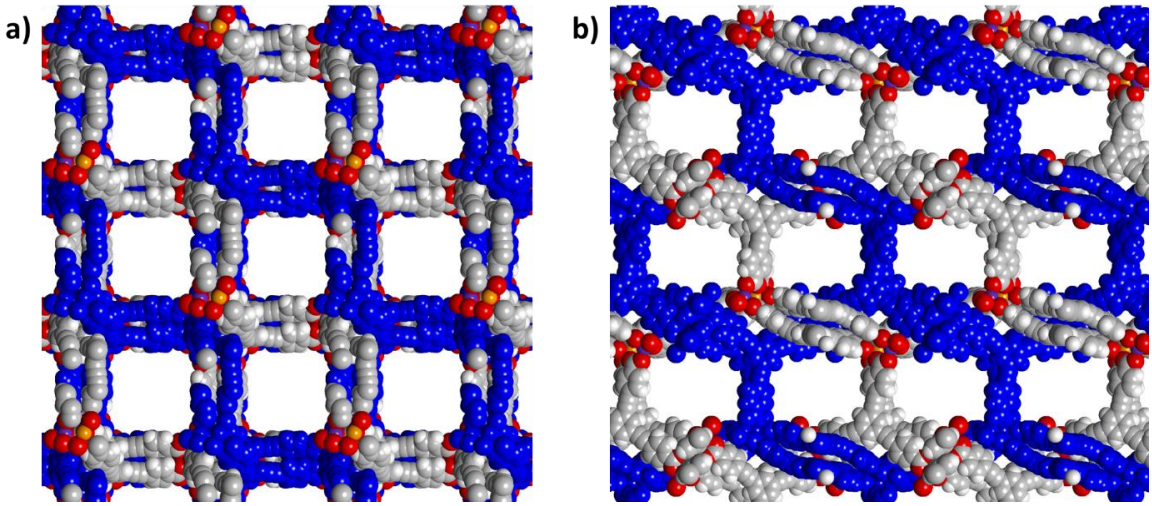

Figure 4.3.4: Space filling representations of **3** showing both interpenetrated nets with one net highlighted in blue, **a)** view down the crystallographic *c-axis*, **b)** view down the crystallographic *b-axis*. Colour key: Co (purple), Mn (orange), O (red), C (grey), H (white).

Table 4.3.2: Crystal data and X-ray refinement details for **3**.

Identification code	**3**
Empirical formula	$C_{66}H_{34}Co_2Mn_1O_{14}$
Formula weight	1223.72 g mol^{-1}
Temperature	215(2) K
Wavelength	1.54178 Å
Crystal system	Tetragonal
Space group	*P* 4_3 2 2
Unit cell dimensions	a = 20.950(6) Å
	b = 20.950(6) Å
	c = 38.736(9) Å
	α = 90°
	β = 90°
	γ = 90°
Volume	17001(11) $Å^3$
Z	4
Density (calculated)	0.478 Mg/m^3
Absorption coefficient	2.297 mm^{-1}
F(000)	2484
Crystal size	0.25 x 0.2 x 0.2 mm^3
Theta range for data collection	2.109 to 50.702°
Index ranges	-20 ≤ h ≤ 20, -21 ≤ k ≤ 19, -38 ≤ l ≤ 38
Reflections collected	83019
Independent reflections	8944 [R_{int} = 0.0858]
Completeness to theta = 50.702°	99.6 %
Absorption correction	Semi-empirical from equivalents
Max. and min. transmission	0.7500 and 0.5738
Refinement method	Full-matrix least-squares on F^2
Data / restraints / parameters	8944 / 64 / 128
Goodness-of-fit on F^2	0.902
Final R indices [I>=2σ(I)]	R1 = 0.0980, wR2 = 0.2532
Final R indices (all data)	R1 = 0.1740, wR2 = 0.2898
Absolute structure parameter	0.185(17)
Largest diff. peak and hole	0.439 and -0.194 e.$Å^{-3}$
Flack parameter	0.185(17)

4.3.2 Physicochemical characterisation of **3**

4.3.2.1 X-ray powder diffraction

For X-ray powder diffraction experiments, crystals of **3** were ground into a powder and a PXRD pattern was recorded to characterise the phase purity of the synthesised bulk material. The PXRD pattern was measured in a capillary at 220 K to obtain low angle peaks and to avoid loss of crystallinity associated with solvent evaporation from the sample (**Figure 4.3.5**). The experimental pattern and a simulated PXRD pattern (based on the single crystal X-ray diffraction data) match closely confirming the crystalline phase-purity of the synthesised material. Two major signals are visible in the measured pattern below $2\theta = 5°$. The most intense of these signals is found at a 2θ angle of 4.4° and appears in the simulated pattern at 4.3°. The second signal is found at an angle of 4.9° and is observed in the simulated pattern at 4.8°. Additional signals at $2\theta > 5°$ can be seen in both patterns. The signals at 6.22° and 6.58° match closely with the reflections in the simulated pattern.

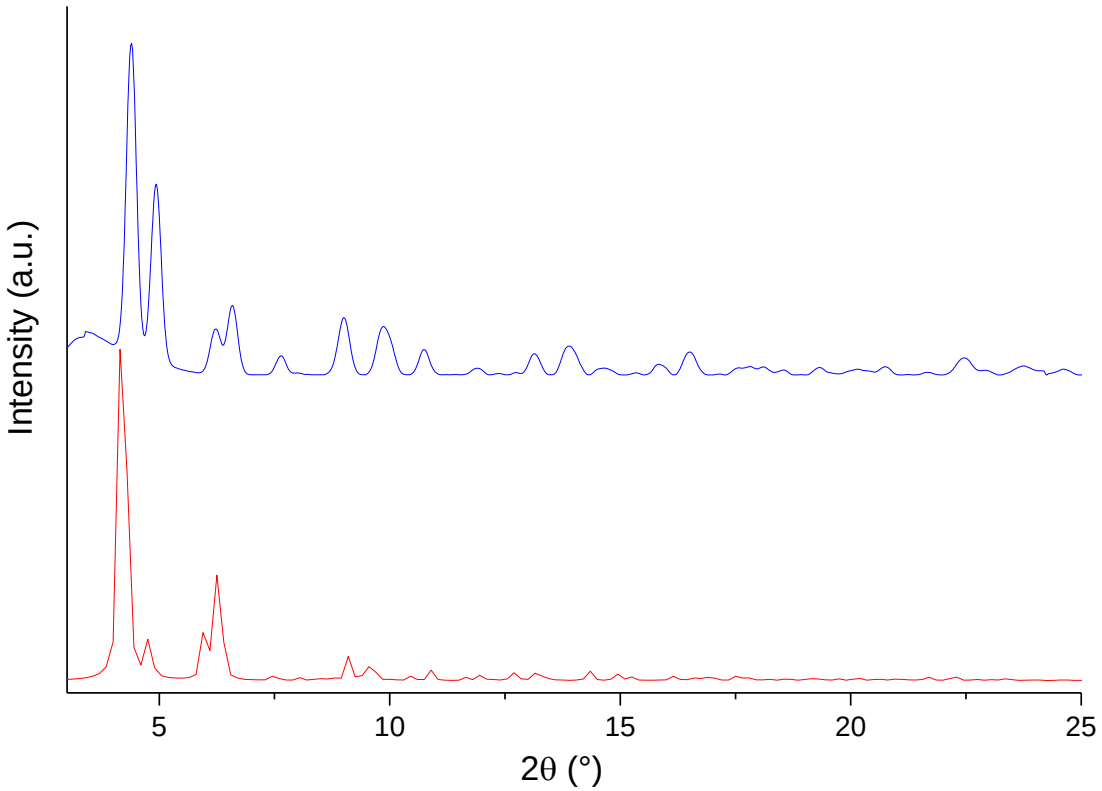

Figure 4.3.5: PXRD patterns of **3**. Measured crystals (blue) and calculated from the single crystal data (red).

4.3.2.2 Raman and FT-IR spectroscopy

Raman and FT-IR spectroscopic methods were used to characterise crystals of **3** and a powdered sample of **H_3L2**. The Raman spectrum of **3** is dominated by stretches that derive from **$L2^{3-}$**, further confirming the presence of the ligand in the MOF (**Figure 4.3.6**). The signals, at 989 cm^{-1} in the spectrum of **3** and 993 cm^{-1} in **H_2L2**, derive from CH_2 rocking vibrations. Bands in the spectrum of **3** at 1122, 1140 and 1169 cm^{-1} derive from C-C single bond vibrations. Two corresponding bands can be identified in the spectrum of **H_3L2** at 1127 and 1169 cm^{-1}. In the spectrum of **3,** the most intense signals derive from the aromatic C=C bond vibrations and appear at 1584 and 1605 cm^{-1}. In the spectrum of **H_3L2** related bands can be identified at 1585 and 1610 cm^{-1}, respectively. Another prominent signal is found at 2214 cm^{-1} and derives from the alkyne C≡C vibration in the spectrum of **3**. The corresponding signal appears slightly shifted to 2217 cm^{-1} in the spectrum of **H_3L2**.[23,24] These strong Raman signals assigned to the alkyne C≡C vibrations are barely visible in the FT-IR spectrum of **H_3L2** and not seen in the FT-IR spectrum of **3**, further confirming the assignment as being correct as these types of vibrations are known to appear particularly intense in the Raman spectra but weak in the FT-IR spectra.[24]

The FT-IR spectrum of **3** also reveals signals which primarily derive from the organic ligand **$L2^{3-}$** (**Figure 4.3.7**). A distinctive band at 2962 cm^{-1} in the spectrum of **3** corresponds to C-H stretches predominantly deriving from DMF molecules located in the pores of a freshly prepared sample. At 1605 and 1582 cm^{-1} in **H_3L2** and 1603 and 1579 cm^{-1} in **3,** C=C bond vibrations of aromatic moieties are observed (corresponding to equivalent stretches in the Raman spectrum). The spectrum of **H_3L2** confirms the presence of carboxylic acid groups, with the C=O, C-O and O-H in/out of plane stretches appearing at 1723, 1235, 1419 and 930 cm^{-1} respectively. In the spectrum of **3** asymmetric carboxylate COO^- and symmetric stretches occur at 1534 and 1402 cm^{-1} respectively ($\Delta_{asy\text{-}sym}$ = 132 cm^{-1}).[23,25–27]

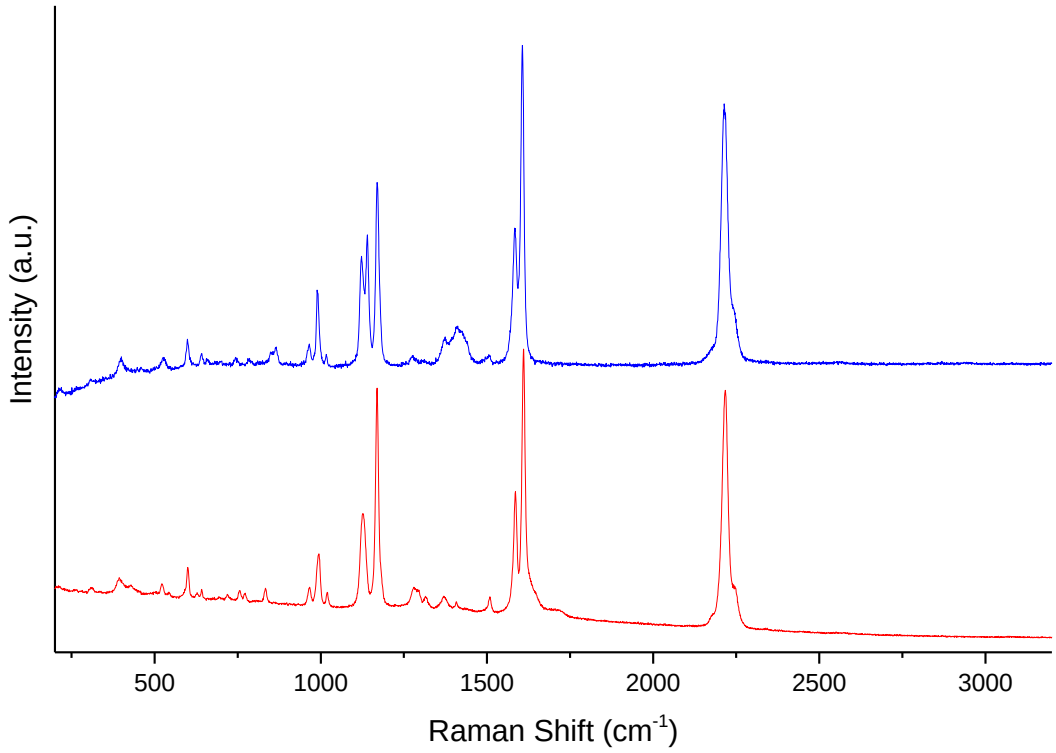

Figure 4.3.6: Raman spectra of crystals of **3** (blue) and **H_3L2** (red).

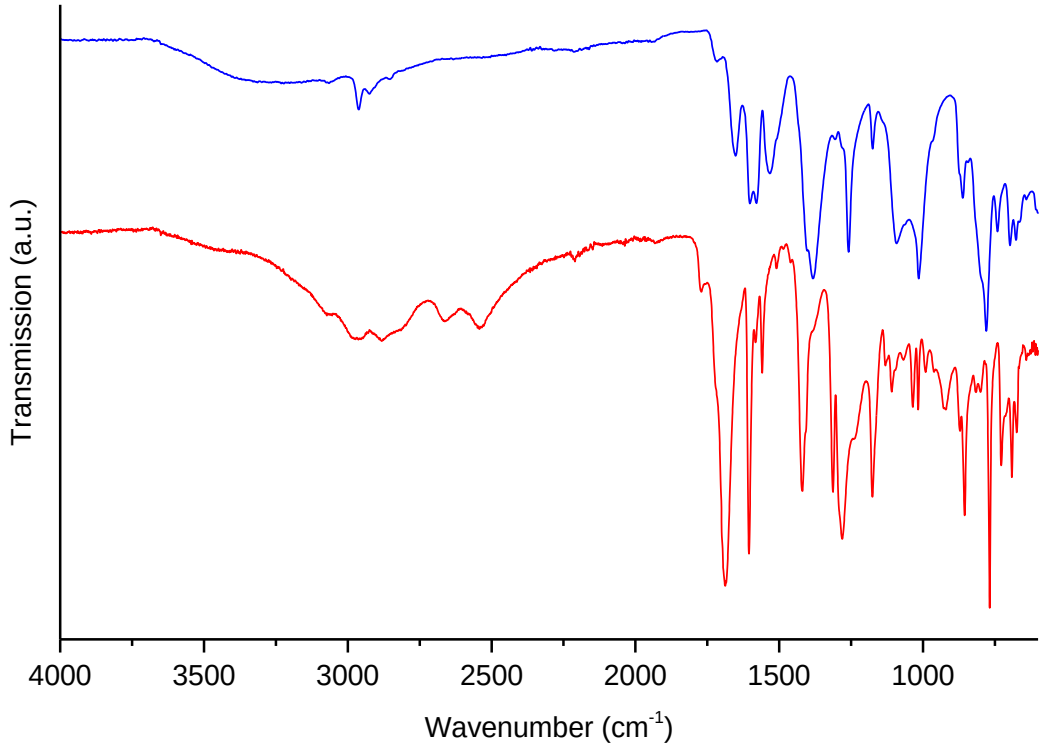

Figure 4.3.7: FT-IR spectra of **3** (blue) and **H_3L2** (red).

4.3.3 Characterisation of metal ion distributions within the SBU of **3**

Due to the crystallographic similarities between Co^{2+} and Mn^{2+} metal ions, additional analysis methods were required to assign the metal ion distributions within the SBU of **3**.

4.3.3.1 Energy-dispersive X-ray spectroscopy

Crystals of **3** in DMF were placed onto a carbon tab, dried in air for 24 hours and analysed using Energy-Dispersive X-ray spectroscopy (EDX) (**Figure 4.3.8**). The relative atomic percentages of the constituent elements were evaluated (**Table 4.3.3**). The results point to a Mn:Co composition of 1.2%:2.2% in **3**. This corresponds closely to the 1:2 Mn:Co ratio of metal ions that was used during the synthesis of **3**. This is consistent and within the analytical accuracy of the EDX method.

Table 4.3.3: EDX spectroscopy showing the relative atomic percentages in **3**.

Elements	C	O	Mn	Co
Calculated atomic %	75.8	19.0	1.1	2.1
Found atomic %	74.9	21.6	1.2	2.2

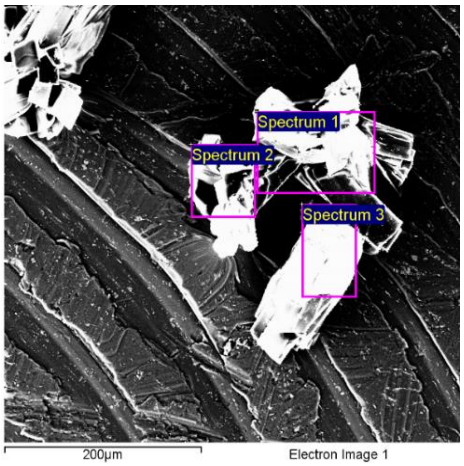

Figure 4.3.8: SEM picture showing crystals of **3** with regions taken for EDX analysis highlighted in pink coloured boxes.

4.3.3.2 Solid state UV-vis-NIR spectroscopy

Freshly synthesised crystals of **3** were ground in DMF, following solvent exchange using $CHCl_3$. A suspension of crystals of **3** in $CHCl_3$ was then drop-casted onto a quartz slide. The quartz slide was left to dry in air leaving a coating of the crystals. The sample was then covered with a second quartz slide and this was used for the spectroscopic studies which were carried out in the spectral range between 300 to 800 nm (**Figure 4.3.9**). For comparative purposes, absorbance spectra were recorded using $Mn(CH_3CO_2)_2$, $Co(CH_3CO_2)_2$ and **H_3L2** solutions in DMF. Strong signals of **3** were observed in the UV range of the electromagnetic spectrum below *ca.* 400 nm which can be attributed to π-π* and n–π* transitions that derive from the **$L2^{3-}$** ligand and metal-ligand charge transfer (MLCT) transitions. A band is observed centred at *ca.* 483 nm which is followed by prominent broad band in the region between *ca.* 520 to 660 nm. The latter can be attributed to d-d transitions of Co^{2+} ions and results in crystals with intense blue colour (**Figure 4.3.9, inset**). It partly overlaps with the band observed for $Co(CH_3CO_2)_2$ in DMF.

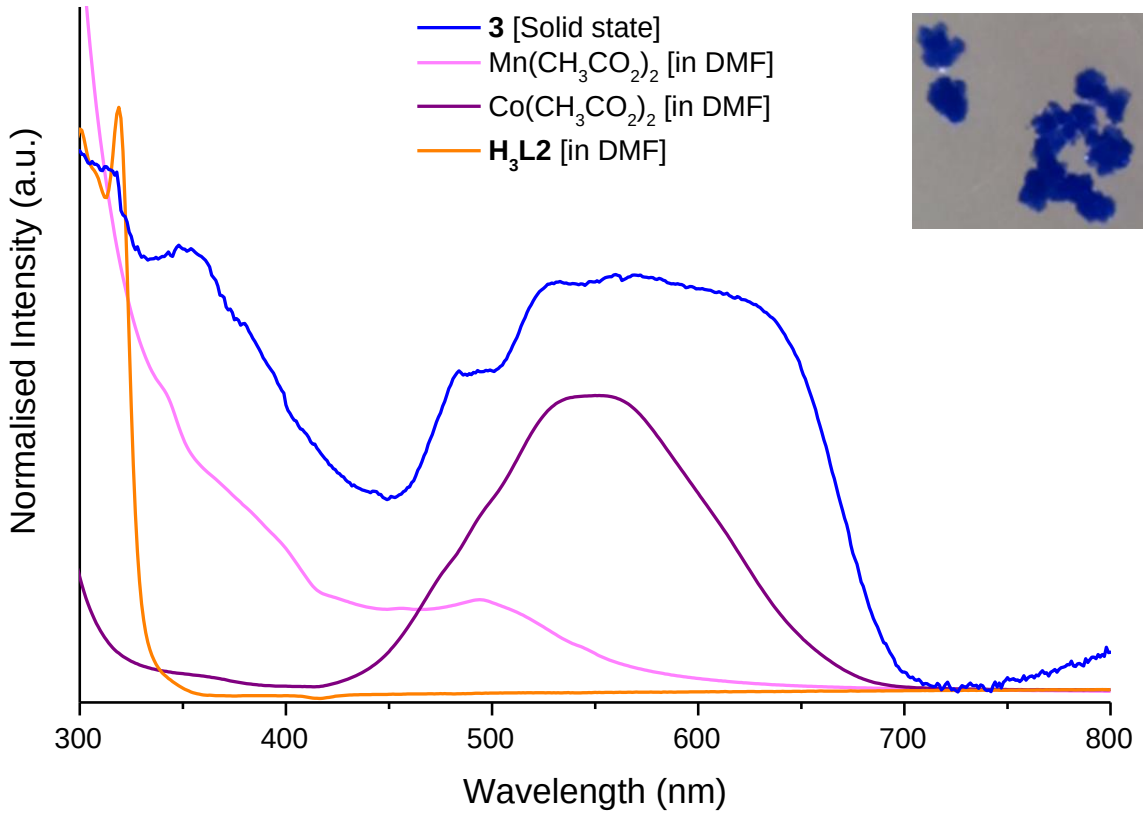

Figure 4.3.9: Solid state and solution UV-vis-NIR spectroscopy. ***Inset:*** Visible light microscope images of crystals of **3**.

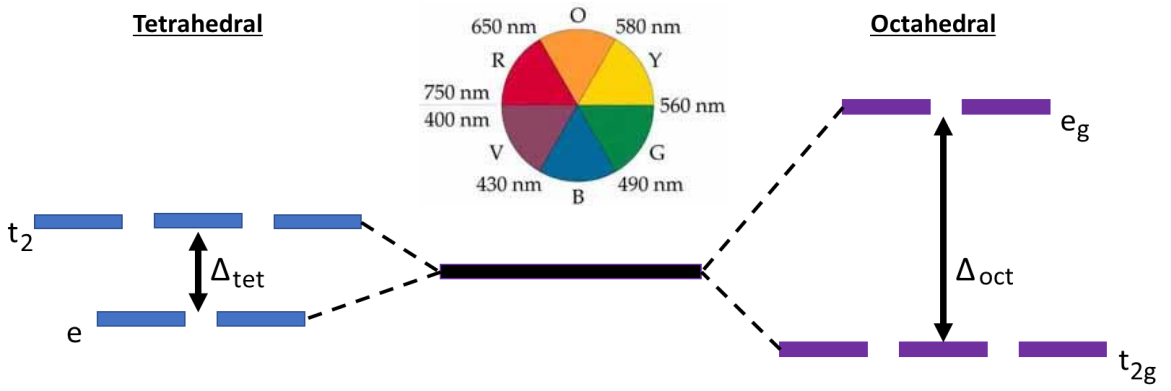

Figure 4.3.10: Representation of orbital splitting in tetrahedral and octahedral metal complexes. ***Inset:*** The colour wheel (when a metal complex appears a certain colour, it is absorbing light wavelengths primarily at the opposite side of the colour wheel).

The Δ_{Oct} energy gap between d-orbitals is larger than the Δ_{Tet} energy gap (**Figure 4.3.10**). According to the Laporte selection rule these d-d transitions are forbidden in centrosymmetric coordination environments such as octahedral complexes meaning they often have faint colours and lower extinction coefficients. This rule does not apply to non-centrosymmetric environments such as tetrahedral complexes which often give rise to intense colours and significantly higher extinction coefficients.[28,29]

The Mn^{2+} ions contribute slightly to the visible colour of **3**. The d-d transitions in Mn^{2+} ions are generally known to result in low intensity band with low extinction coefficients. They can be observed in $Mn(CH_3CO_2)_2$ at *ca.* 494 nm and possibly in **3** centred at *ca.* 483 nm. These transitions are Laporte forbidden due to the centro-symmetry of the octahedral coordination environment. Other compounds with octahedrally coordinated Mn^{2+} ions may appear pale pink/orange in colour (e.g. $Mn(CH_3CO_2)_2{\cdot}4H_2O$).[28,30]

The Co^{2+} ions most likely contribute to the intense blue colour of **3**. The tetrahedral Co^{2+} coordination positions give rise to non-Laporte forbidden transitions. These d-d transitions are observed in the spectrum of **3** as a broad band between ca. 520 to 660 nm. Tetrahedral Co(II) coordination compounds are often purple (anhydrous $Co(CH_3CO_2)_2$) or blue ($[CoCl_4]^{2-}$) in colour.[28] Compounds with octahedrally coordinated Co(II)ions usually

appear red to purple in colour; they appear pale in colour due to their Laporte forbidden transitions (e.g. $Co(CH_3CO_2)_2 \cdot 4H_2O$).[28,30,31]

Diffuse reflectance measurements were performed on crystals of **3** and the results were processed using the remission function[32] to allow for comparison with literature data (**Figure 4.3.11**). The experimental results were compared with spectra of the Zn(II)/carboxylate-based MOF, MOF-5, in which either tetrahedrally or octahedrally coordinated Co(II) ions were incorporated through doping (see reference 17). The results demonstrate that the spectrum of **3** closely corresponds to that of MOF-5 containing tetrahedrally coordinated Co(II) ions, thus confirming the structural assignment of **3**. In addition, the most prominent peak at *ca.* 495 nm in the spectrum of MOF-5 containing octahedrally coordinated Co(II) ions, is not observed in the spectrum of **3**, suggesting that the central octahedral site is not occupied by Co^{2+} ions.

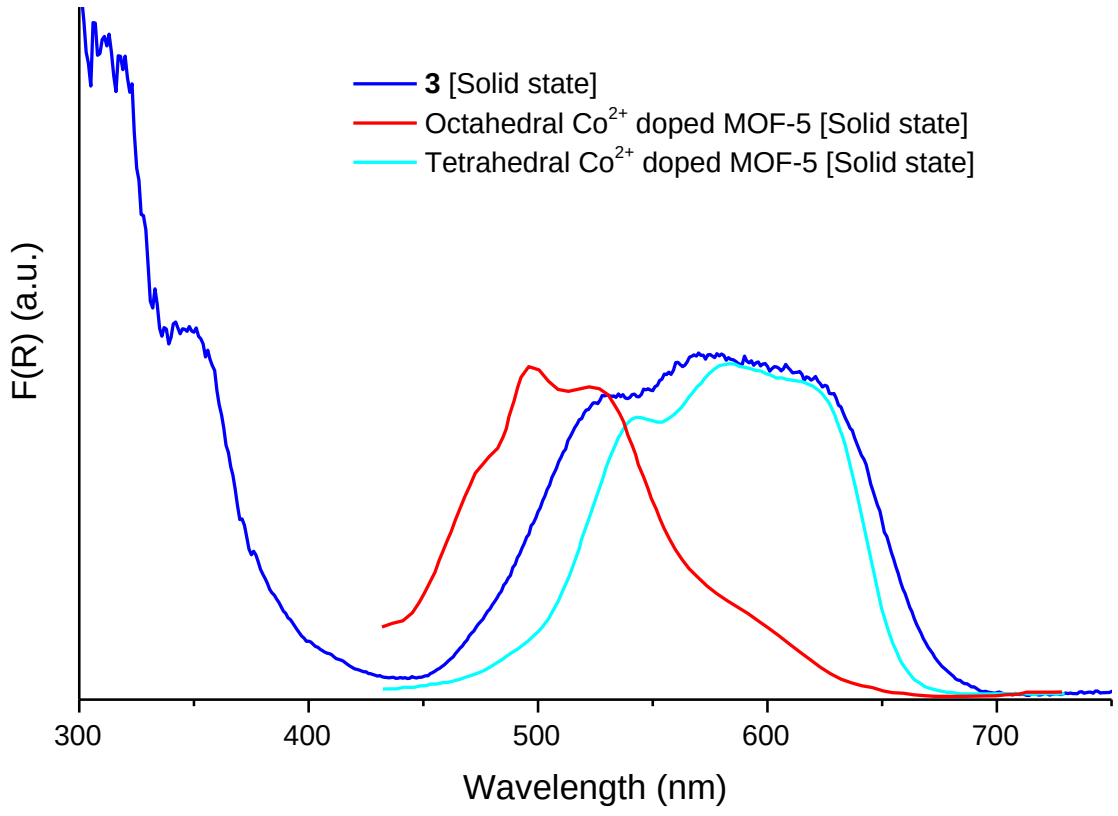

Figure 4.3.11: Solid state diffuse reflectance spectroscopy of crystals of **3** (converted using the remission function).[32] Spectra of Co(II) doped MOF-5 samples are used for comparative purposes and were taken from reference 17.

4.3.3.3 X-ray photoelectron spectroscopy

X-ray photoelectron spectroscopy (XPS) was used to characterise freshly synthesised crystals of **3**. This sample was then compared to reference samples of anhydrous Co(II) acetate and Mn(II) acetate containing Co(II) centres in tetrahedral and Mn(II) ions in octahedral coordination environments, respectively. XPS survey scans of **3** show that it contains Co, Mn, O and C (**Figure 4.3.12**). The spectrum of **3** shows similar Co and Mn derived signals as those observed for Co(II) acetate and Mn(II) acetate, respectively. This confirms that **3** contains Co^{2+} and Mn^{2+} ions in similar binding environments to those in the Co(II) and Mn(II) acetate reference samples. The Co $2p_{1/2}$ and Co $2p_{3/2}$ signals along with their satellite features can be clearly resolved (**Figure 4.3.13**).[33,34] In addition, the Mn $2p_{1/2}$ and Mn $2p_{3/2}$ signals are also visible (**Figure 4.3.14**).[35]

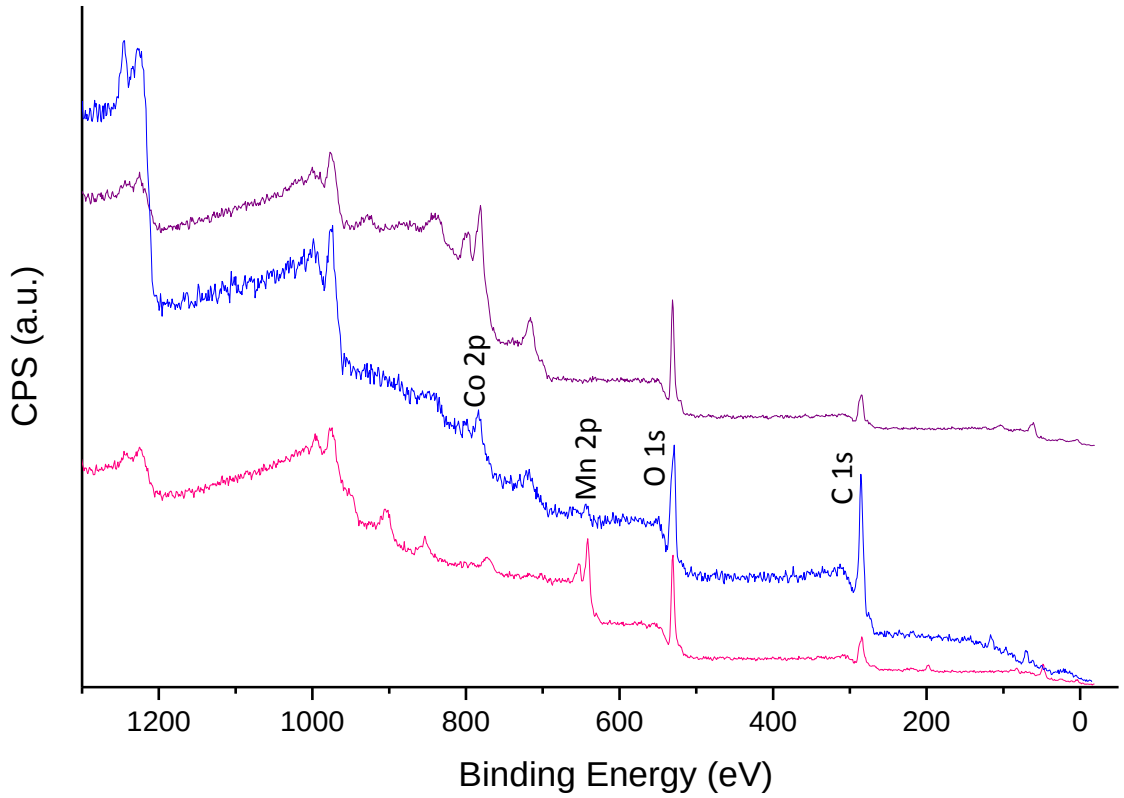

Figure 4.3.12: XPS survey spectra. Freshly synthesised crystals of **3** (blue), Co(II) acetate (purple) and Mn(II) acetate (pink).

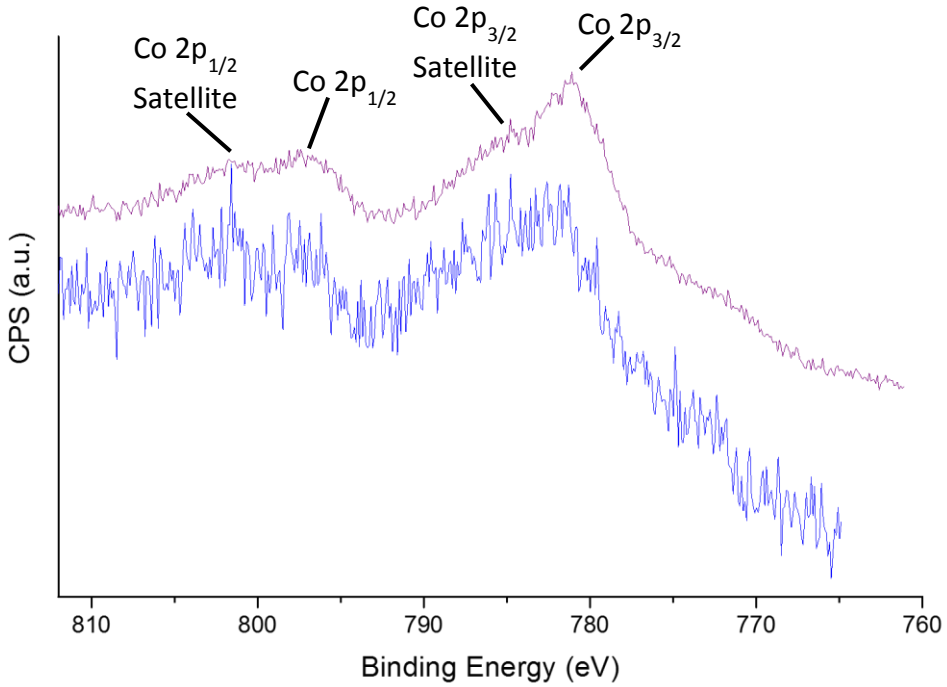

Figure 4.3.13: XPS spectra highlighting the Co(II)-derived signals. Anhydrous Co(II) acetate (purple) and freshly synthesised crystals of **3** (blue).

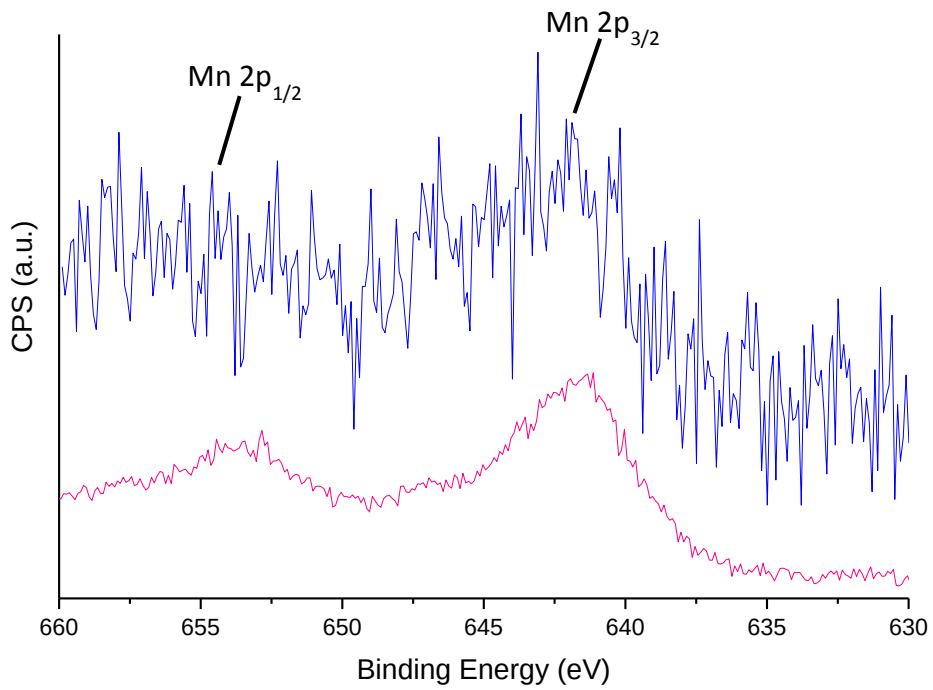

Figure 4.3.14: XPS spectra highlighting the Mn(II)-derived signals. Freshly synthesised crystals of **3** (blue) and Mn(II) acetate (pink).

The Pauling electronegavity of Mn and Co are suitably different to allow the XPS signals of coordinated carboxylate O-atoms to be shifted relative to each other and viewed as two distinct peaks in the XPS spectrum (Pauling electronegavity: Mn = 1.55, Co = 1.88) (**Figure 4.3.15**). Peak fittings were applied and the area under each signal was integrated and compared, giving a ratio of *ca.* 48%:52%). Considering the EDX data which suggested a Mn:Co ratio of *ca.* 1:2, the metal ion positions can be reasonably resolved in the SBU. The outer tetrahedral metal positions of the SBU are each coordinated by four oxygen donor atoms, three of which derive from carboxylates from coordinated **L2**$^{3-}$ ligands and one of which derives from coordinated solvent molecules. The latter my even be removed under the high vacuum conditions of the XPS system. The central octahedral metal position on the SBU is coordinated by six oxygens, all of which derive from carboxylates from coordinated **L2**$^{3-}$ ligands. The combination X-ray diffraction, computational data, optical spectroscopy and EDX data points to a structural assignment where the Mn^{2+} ions are located in the central octahedral positions and both the Co^{2+} ions are located in the outer tetrahedral positions. This would mean that six oxygen atoms are coordinated to Mn^{2+} ions and four or less oxygen atoms are coordinated to each Co^{2+} ion, resulting in a {Mn-O}:{Co-O} ratio that is expected to vary between 6:8 - 6:6. A statistical distribution of the two metal ions over the atom positions of the SBU could not give integrational values close to a 1:1 distribution. Thus, the XPS data supports the structural assignment.

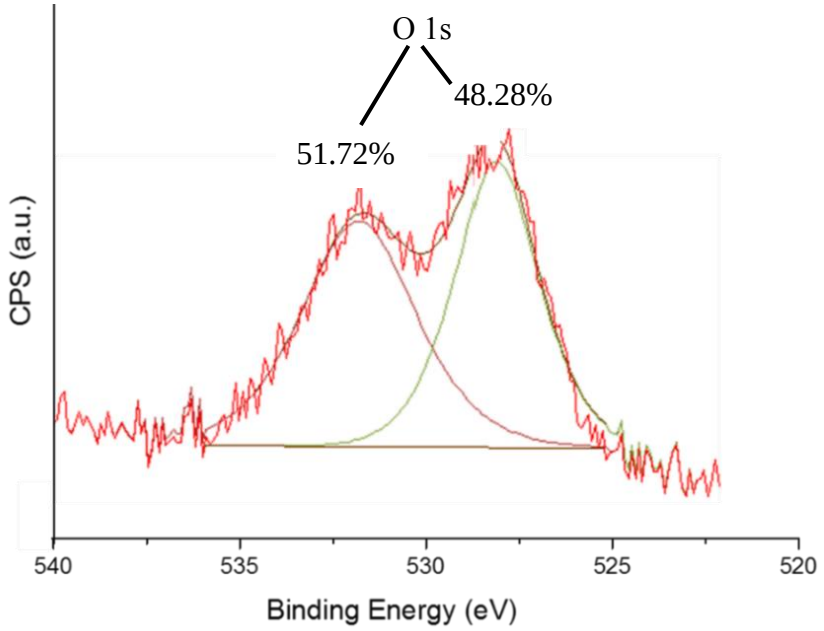

Figure 4.3.15: XPS spectra highlighting the O-derived signals in freshly synthesised crystals of **3**; peak fittings shown as solid lines.

4.3.3.4 Computational modelling

Computational modelling was performed using a simplified model chosen to explore possible $\{Mn_1Co_2\}$ SBU configurations and to assess the stabilities of different metal ion configurations within the trinuclear moiety, see **Section 6.1** for experimental details.

The stability of the SBU was found to be higher when the central octahedral site is occupied by a Mn^{2+} ion rather than a Co^{2+} ion. The computed electronic energy of **3** was found to be *ca.* 11 kJ/mol lower when the Mn^{2+} ion is located in the central octahedral position compared to a structural isomer in which this position is occupied by a Co^{2+} ion (**Table 4.3.4**).

The $\{M_3\}$ SBU structure is predicted to be close to linear when a Mn^{2+} ion is located in the central octahedral position of the SBU giving a Co-Mn-Co angle of *ca.* 178°. However, when the Mn^{2+} ion is in one of the peripheral tetrahedral positions of the $\{M_3\}$ SBU then the Mn-Co-Co angle is predicted to be *ca.* 160°. The experimental crystallographic results determine a Co-Mn-Co angle of *ca.* 174°, further implying that the Mn^{2+} ion predominantly occupies the central octahedral position in the $\{M_3\}$ SBU.

Additionally, the metal-metal distances for both possible SBU configurations were calculated and compared with the experimental results that were derived from the X-ray crystal structure determination (**Table 4.3.5**). The experimental results closely match with the calculated results when the Mn^{2+} ion is preferentially located the central octahedral position further suggesting that the structurally assigned atom positions in the SBU are correct.

Table 4.3.4: Computed electronic energies for stabilisation energy calculations for the two possible metal ion configurations of the $\{Mn_1Co_2\}$ SBU in **3** (1 Hartree = 2625.50 KJ/mol). Abbreviations: oct = metal ion is situated in the central octahedral position of the SBU; tet = metal ion is situated in the peripheral tetrahedral position of the SBU.

	Multiplicity (no. of unpaired electrons +1)	Energy (Hartrees)	Energy (KJ/mol)
$Co_{(tet)}$-$Mn_{(oct)}$-$Co_{(tet)}$	12 (*high-spin*)	-3411.3753	-8956565
$Mn_{(tet)}$-$Co_{(oct)}$-$Co_{(tet)}$	12 (*high-spin*)	-3411.3713	-8956555

Table 4.3.5: Comparison of experimental and calculated metal ion to metal ion distances in the two possible metal ion configurations of the $\{Mn_1Co_2\}$ SBU in **3**. Abbreviations: oct = metal ion is situated in the central octahedral position of the SBU; tet = metal ion is situated in the peripheral tetrahedral position of the SBU.

Mn^{2+} ion in the central octahedral position (Distances in Å)		
Metal ion positions	Experimental	Calculated
$Mn_{(oct)}$-$Co_{(tet-1)}$	3.54	3.59
$Mn_{(oct)}$-$Co_{(tet-2)}$	3.54	3.61
$Co_{(tet-1)}$-$Co_{(tet-2)}$	7.07	7.20
Mn^{2+} ion in the peripheral tetrahedral position (Distances in Å)		
Metal ion positions	Experimental	Calculated
$Mn_{(tet)}$-$Co_{(oct)}$	3.54	3.26
$Co_{(oct)}$-$Co_{(tet)}$	3.54	3.50
$Mn_{(tet)}$-$Co_{(tet)}$	7.07	6.66

4.3.4 Thermogravimetric and gas sorption characterisation of **3**

4.3.4.1 Thermogravimetric analysis

Thermogravimetric analysis (TGA) of **3** was performed in an N_2 atmosphere at a heating rate of 3°C per minute (**Figure 4.3.16**). It reveals an initial weight loss of *ca.* 70% between 20 and 100°C which can be attributed to the loss of constitutional solvent molecules in the pores. The void volume was previously shown to occupy 72.91% of **3**, therefore it is likely that a large quantity of solvent could be contained in this space. This thermogravimetric step extends to *ca.* 200°C which most likely derives from the removal of more strongly bound solvent molecules such as coordination solvent molecules. There is a further weight loss of *ca.* 19% between 350 and 850°C assigned to the decomposition of the organic $\mathbf{L2}^{3-}$ ligand.

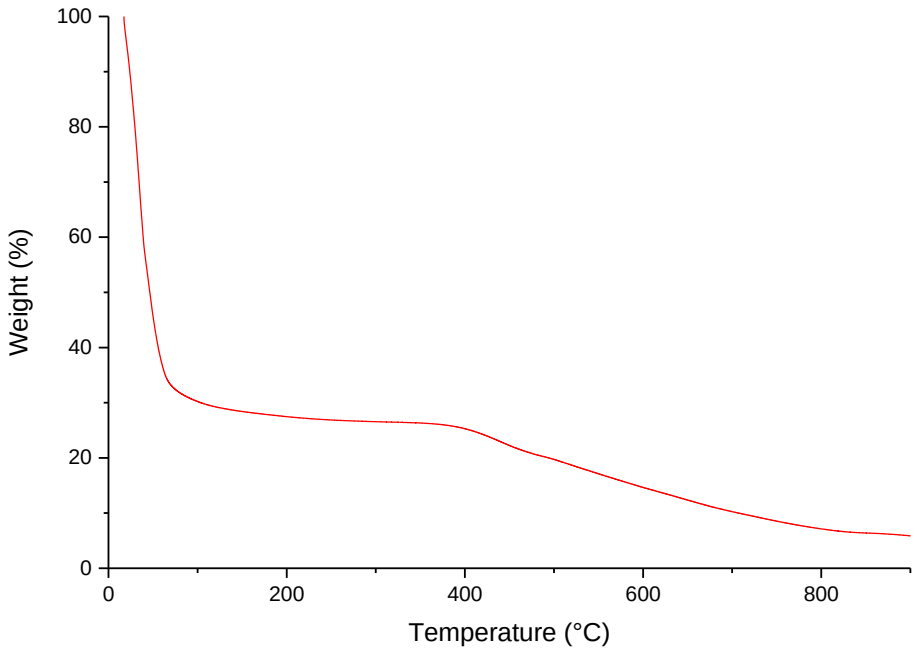

Figure 4.3.16: TGA of compound **3** carried out in an N_2 atmosphere at a heating rate of 3°C per minute.

4.3.4.2 Gas sorption and BET surface area determination experiments of **3**

Prior to conducting gas sorption experiments on **3** it was necessary to exchange the constitutional solvent molecules in the pores of **3**. Thus crystals that resulted from the reaction solution were dispersed in DMF for three days, refreshing the used DMF with fresh DMF once per day, to remove unreacted materials that could potentially be located within the pores of **3**. The DMF was then replaced by $CHCl_3$ and the crystals were then left in this solvent system for three days, refreshing the solution once per day. The crystals were then transferred into a quartz measurement cell and the sample was activated by heating under vacuum at 50°C for 1 hour. The N_2 gas sorption data recorded at 77 K, reveals a type-I isotherm that is characterised by a steep uptake at low partial pressures which corresponds to N_2 adsorption in the accessible micropores of **3**. This is followed by a progressive increase in in the uptake with increasing pressures likely due to surface adsorption on crystals or particles of **3** (**Figure 4.3.17**). A maximum uptake of 153 cm^3/g at 711 Torr was achieved, which corresponds to an uptake of 192 mg/g. The H_2 gas sorption at 77 K using the material reveals a reversible isotherm leading to an uptake of 87 cm^3/g at 756 Torr which corresponds to a H_2 uptake of 0.76 wt% (**Figure 4.3.20**). A CO_2 gas uptake isotherm was obtained at 278 K. It shows an uptake of 48 cm^3/g at 756 Torr (**Figure 4.3.21**).

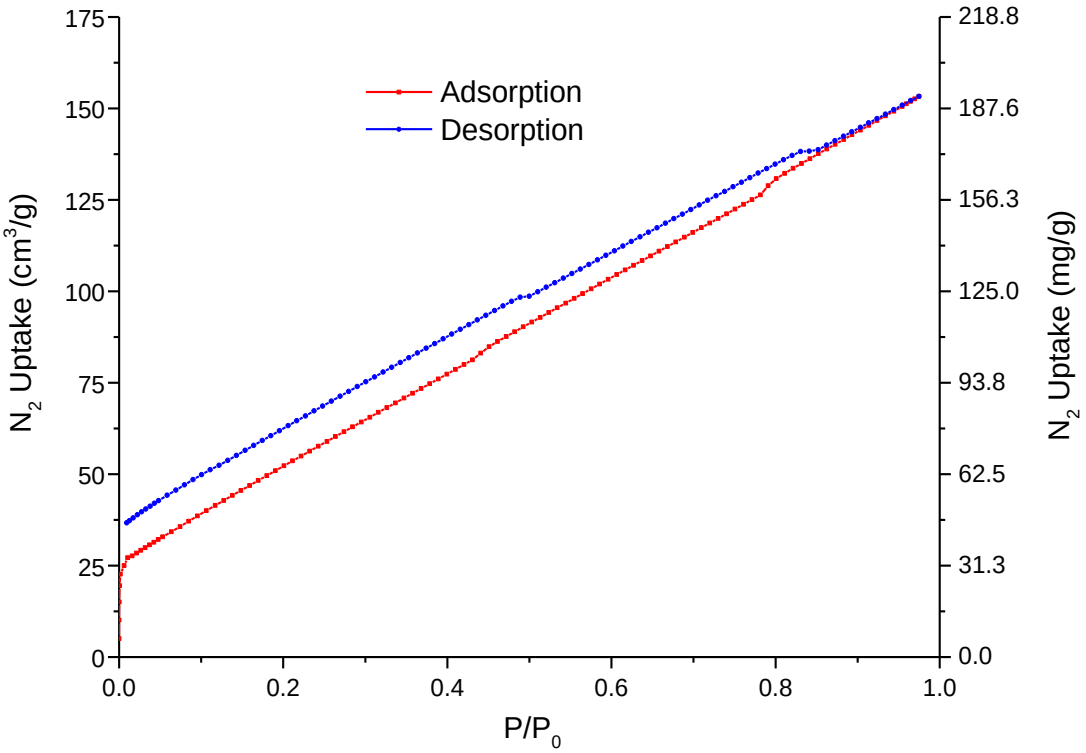

Figure 4.3.17: N_2 sorption isotherm of **3** measured at 77 K.

The BET surface area derived from the N_2 isotherm gives a value of 230 m^2/g (**Table 4.3.6**). The points chosen for the BET calculation were selected using the micropore BET assistant within the Quantachrome ASiQwin software package (**Figure 4.3.19**). The calculated theoretical surface area of **3** using RASPA software[22] was found to be 3211 m^2/g. This is significantly higher than the experimentally determined BET surface area indicating that the open-framework structure of **3** collapses during the degassing process despite the mild activation conditions.

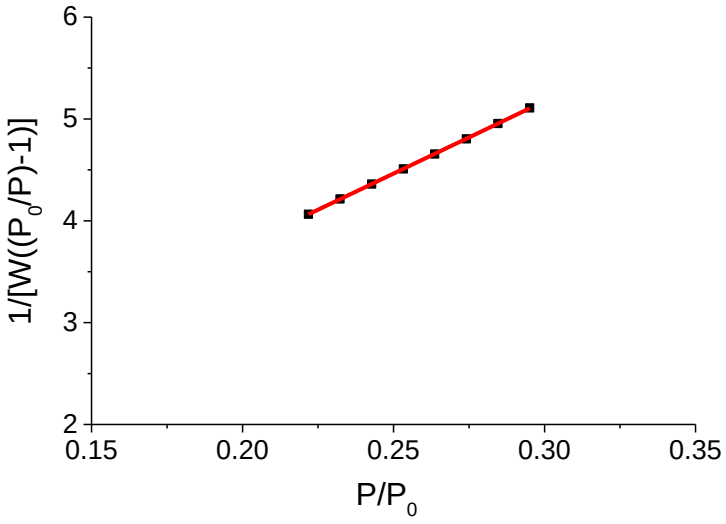

Figure 4.3.18: Plot of the linear region used to obtain the BET surface area of **3** derived from the N_2 gas sorption data.

Table 4.3.6: Table of values obtained from the BET Plot of **3**.

Slope	14.207
Intercept	9.121×10^{-1}
r (correlation coefficient)	0.999986
C constant	16.570
BET Surface Area	230 m^2/g

The pore size distribution of **3** was calculated from the N_2 isotherm data using the Quantachrome AsiQwin software NLDFT using the slit pore, NLDFT equilibrium mode model derived from N_2 at 77 K using carbon materials (**Figure 4.3.19**).[36] Pores were found to be centred at 12.3 and 14.1 Å. Pores with diameters beyond 16 Å appeared as broad pores which most likely derive from the N_2 surface adsorption between particles. Using the RASPA software package,[22] the pore sizes were calculated based on the crystal structure. Two predominant pore sizes were determined. A minor pore was found at a diameter centred at 12.2 Å and a major pore at a diameter centred at 13.7 Å (**Figure 4.3.19**). These correspond closely to the pores-sizes that derive from the experimental data. However, the comparative data also confirms that parts of open-framework structure collapses on activation, i.e. due to capillary forces that prevail during the desolvation.

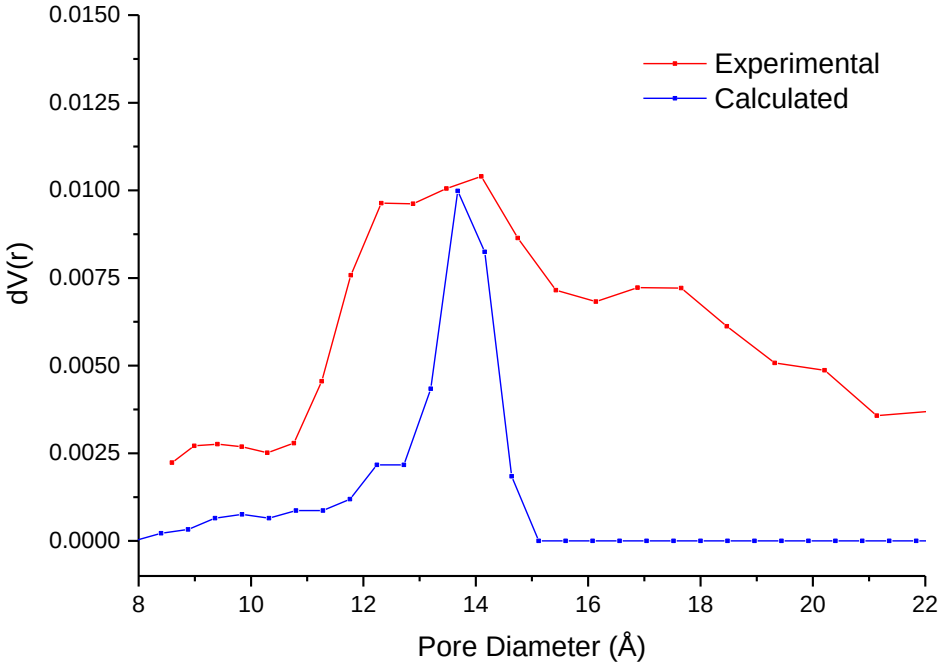

Figure 4.3.19: Pore size distribution plots of **3,** calculated from N_2 gas uptake data (red), calculated from single crystal data using RASPA software (blue).

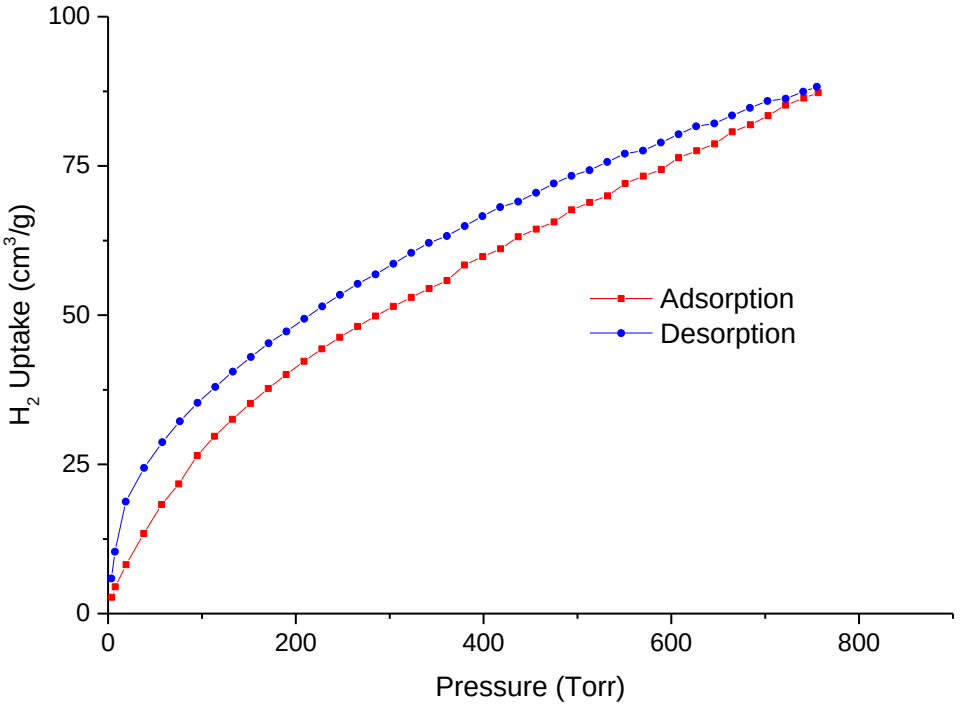

Figure 4.3.20: H_2 sorption isotherm of **3** measured at 77 K.

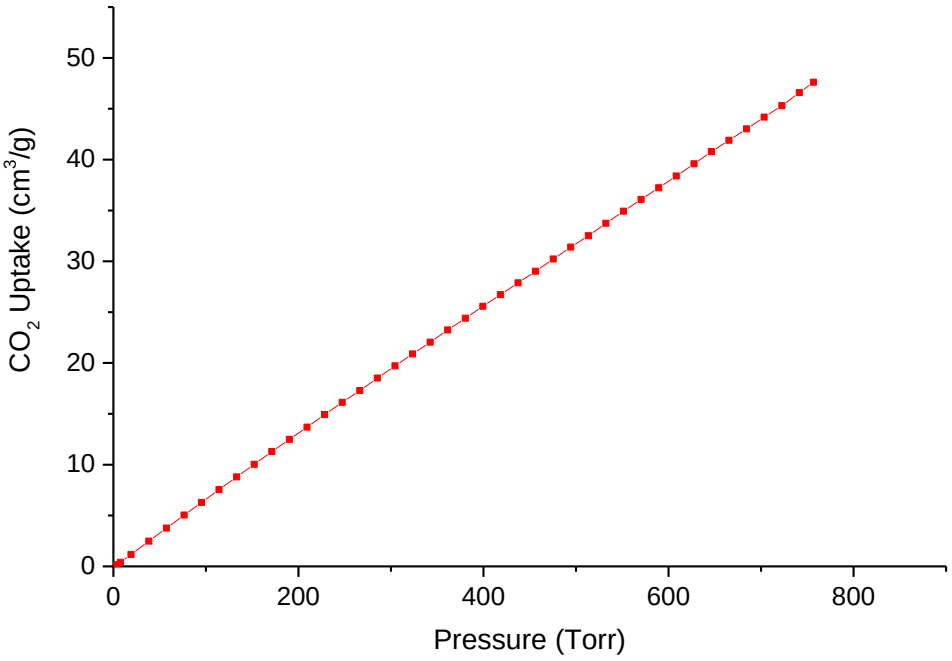

Figure 4.3.21: CO_2 isotherms of **3** measured at 278 K.

4.3.5 Photo-induced water oxidation catalysis

Due to the presence of Co^{2+} ions located at the peripheral, partially solvated tetrahedral sites in the $\{Mn_1Co_2\}$ SBU, **3** was expected to show water oxidation activity. To investigate the possible catalytic activity of **3**, preliminary photo-induced water oxidation experiments were performed. $[Ru(bpy)_3]Cl_2$ (1.875 mg) was used as a photosensitiser and was added with $Na_2S_2O_8$ (11.9 mg) as a sacrificial oxidant to aqueous phosphate buffered solutions (10 mM in deionised H_2O, 10 mL, pH 7).[37] Dry powders of **3** were added to the solutions and the vials were covered with aluminium foil to avoid an early reaction if exposed to light. The mixtures were sonicated for 15 minutes and then stirred continuously during the entire experiment. The reaction mixtures were purged with N_2 gas to remove dissolved O_2 prior to illumination. An LED light source (465 nm, 10 mW/cm^2 at the centre of the vial) was used to illuminate the reaction vials. Various quantities of **3** ranging from 0.1 to 0.3 mg, were tested for catalytic activity under the outlined experimental conditions whilst the evolved O_2 quantities were directly measured using a Clark electrode (**Figure 4.3.22**). When compared to the experiment without any catalyst present, one notes that the presence of **3** clearly results in an increase in the observed O_2 production indicating that it may act as a catalyst for the OER.

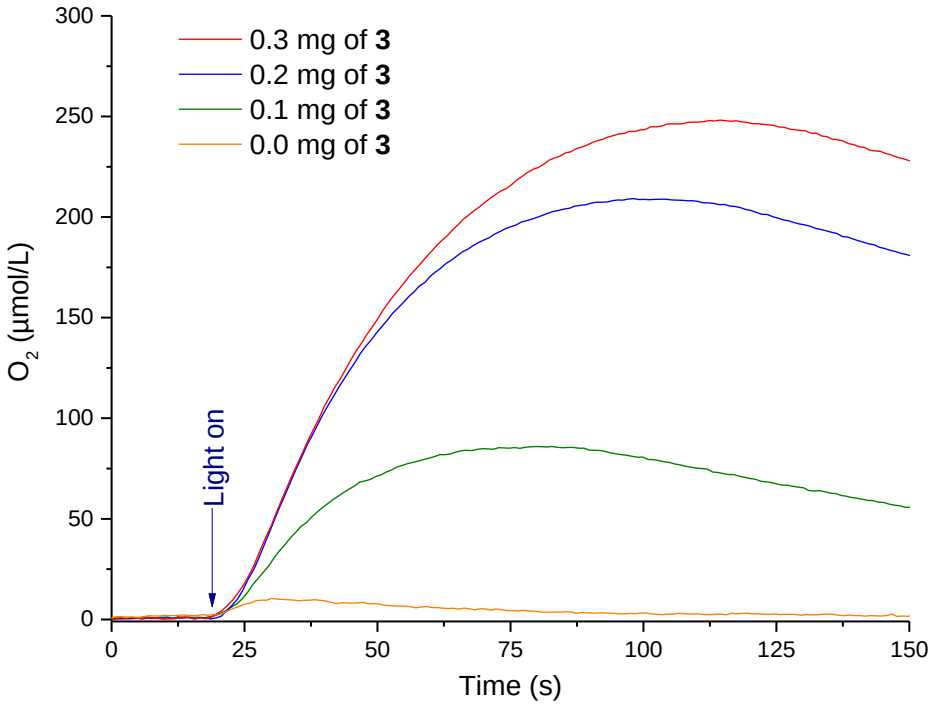

Figure 4.3.22: Photo-induced water OER using various quantities of **3** to test its potential as a heterogeneous catalyst**.** Control experiment in the absence of **3** (orange).

The achieved O_2 quantities, chemical yields (in relation to $Na_2S_2O_8$), turnover numbers (TONs) and turnover frequencies (TOFs) are summarised in **Table 4.3.7**. Maximum O_2 production varies from 86 µmol/L to 248 µmol/L with increasing catalyst loadings of 0.1 mg to 0.3 mg, respectively.

TONs and TOFs were calculated from the experimental data. The TONs vary from 5.1 to 6.4 whilst relatively high TOFs of 0.123 s^{-1} to 0.200 s^{-1} were achieved. The lowest 0.1 mg catalyst loading resulted in the highest TOF of 0.2 s^{-1} while the catalyst loading of 0.2 mg resulted in the best TON of 6.4. Leaching of Co(II) or Mn(II) ions into the reaction mixture was not observed and post-catalytic filtrates did not reveal activity. The results indicate that the OER activity primarily results from the Co(II) sites that provide accessible sites *via* the coordination water molecules. Further experiments and characterisation may be required to comment on the fate and stability of **3** during OER conditions.

Table 4.3.7: Max. O_2 quantities, O_2 chemical yields, TONs and TOFs from the photocatalytic OER experiments calculated from each plot in **Figure 4.3.22**.

Quantity of **3** added (mg)	Max. O_2 (µmol/L)	Chemical yield (%)	TON	TOF (s^{-1})
0.3	248	5.0	5.1	0.123
0.2	209	4.2	6.4	0.184
0.1	86	1.7	5.3	0.200
No catalyst	10	0.2	N/A	N/A

4.4 $[CoZn_2(\mathbf{L2})_2(DMF)_2]$ (**4**)

4.4.1 Synthesis and structural characterisation of $[CoZn_2(\mathbf{L2})_2(DMF)_2]$ (**4**)

The self-assembly of **4** was observed when **H_3L2**, $Zn(NO_3)_2{\cdot}6H_2O$ and $Co(NO_3)_2{\cdot}6H_2O$ (3:2:1 mole ratio) were heated in DMF at 90°C for 72 hours. Pale pink crystals of **4** were formed. These were washed with DMF. A yield of 32% was obtained. **4** is isostructural to **3** and crystallises in the tetragonal space group $P4_322$ with the molecular formula $[CoZn_2(\mathbf{L2})_2(DMF)_2]$.

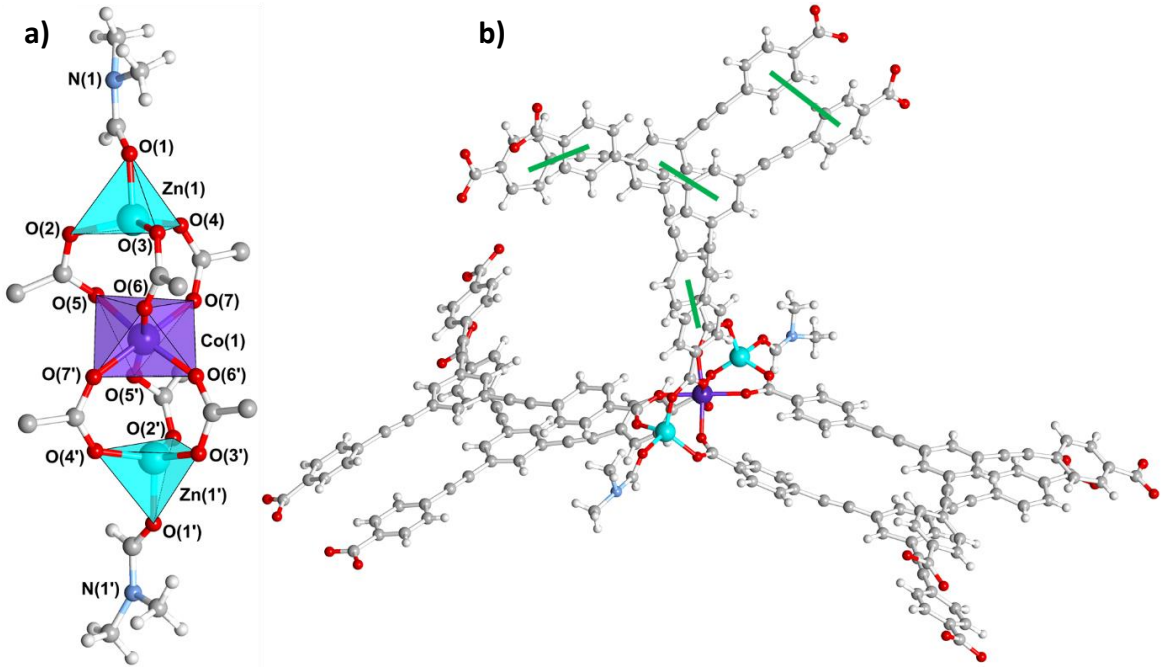

Figure 4.4.1: a) View of the $\{Co_1Zn_2\}$ SBU in **4** from the *[-1 3 -1]*-direction showing, coordinated carboxylate groups from the six $\mathbf{L2}^{3-}$ ligands and two DMF molecules. Transparent polyhedral representations are used to highlight the coordination environments of the metal ions. Atoms of interest are labelled. **b)** View of the $\{Co_1Zn_2\}$ SBU with six $\mathbf{L2}^{3-}$ ligands attached viewing along the *[2 1 0]*-direction. Green lines are used to highlight π-π interactions between phenyl rings in adjacent ligands. Colour key: Zn (cyan), Co (purple), O (red), N (pale blue), C (grey), H (white).

The asymmetric unit of **4** is represented by a central Co(II) ion, a peripheral Zn(II) ion, and one complete coordinating **L2**$^{3-}$ ligand. Also differently to **3**, the peripheral Zn(II) ion, has a coordinating DMF molecule attached, rather than a H_2O molecule. A second Zn(II) ion is generated through symmetry operations forming the 'hourglass' shaped $\{Co_1Zn_2\}$ trinuclear SBU with a Zn(1)-Co(1)-Zn(1') angle of 180° and a Zn(1)-Zn(1') distance of 7.07 Å when measuring from the centre of each ion (**Figure 4.4.1 a)**).

As for **3** the trinuclear cluster in **4** is stabilised by a total of six bidentate bridging carboxylate moieties that derive from six deprotonated **L2**$^{3-}$ ligands. Here, the carboxylate Co(1)-O bond distances vary between 1.981(8) Å and 2.067(7) Å while the carboxylate Zn-O bond distances are slightly shorter varying between 1.895(7) Å and 1.905(7) Å. The coordinating DMF molecules give rise to Zn(1)-O(1) bond distance of 1.925(8) Å.

Surrounding the central, octahedrally coordinated Co(1) centre, the angles between *trans* located O-atoms deviate modestly from the ideal angle of 180°, to give values of 171.6(2)° and 179.4(3)°. The angles between *cis* located O-atoms surrounding Co(1) vary from 83.6(3)° to 96.9(3)°. This results in an almost ideal octahedral coordination environment of Co(1).

The DMF derived O(1) atom locates close to the linear Zn(1)-Co(1)-Zn(1') axis resulting in a O(1)-Co(1)-O(1') angle of 177.3°. The base of the tetrahedron can be visualised as formed from O(2), O(3) and O(4). As in **3**, these are raised up towards the O(1) atom resulting in the angles between O(1) and the carboxylate O-atoms varying between 99.4° and 99.5°. The angles between the O(2), O(3) and O(4) atoms are 108.6(3)°, 116.0(3)° and 126.2(3)°) (**Figure 4.4.2**).

The 3D structure that results from the 6-connecting $\{Co_1Zn_2\}$ nodes are located along 4_3-screw axes that extend parallel crystallographic *c*-axis. The resulting structure is shown in **Figure 4.4.3**. As in **3**, displacement π-π interactions between phenyl rings in each strut stabilise the structure. Similarly to **3**, the distances between the centre of one interacting phenyl ring to the centre of the neighbouring phenyl ring varies between *ca.* 3.8 Å and *ca.* 4.4 Å, consistent with literature values.[20,21]

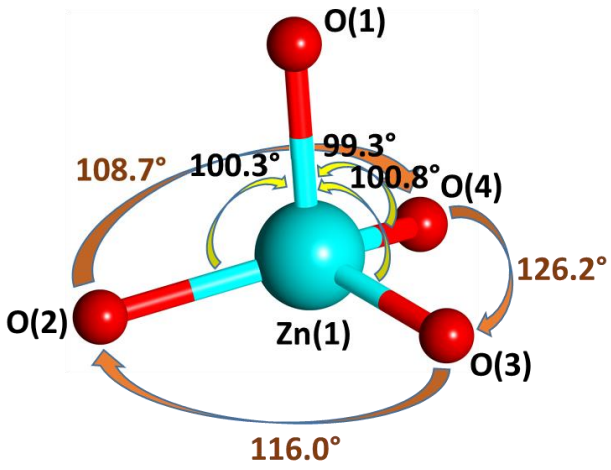

Figure 4.4.2: The coordination environment of the Zn(1) ion in **4**. O(1) derives from a coordinated DMF molecule, while O(2), O(3) and O(4) derive from coordinated **L2**$^{3-}$ ligands. Colour key: Zn (cyan), O (red).

Table 4.4.1: Selected bond distances and angles of coordination environments found in **4**.

Atoms	Distance [Å]	Atoms	Angle [°]
Co(1)-O(5)	**2.067(7)**	O(5)-Co(1)-O(6')	**171.6(2)**
Co(1)-O(6)	**1.981(8)**	O(7)-Co(1)-O(7')	**179.4(3)**
Co(1)-O(7)	**2.023(6)**	O(5)-Co(1)-O(5')	**83.6(3)**
		O(5)-Co(1)-O(6)	**95.2(3)**
Zn(1)-O(1)	**1.925(8)**	O(5)-Co(1)-O(7)	**88.2(2)**
Zn(1)-O(2)	**1.905(7)**	O(5)-Co(1)-O(7')	**91.4(2)**
Zn(1)-O(3)	**1.900(6)**	O(6)-Co(1)-O(6')	**88.2(2)**
Zn(1)-O(4)	**1.895(7)**	O(6)-Co(1)-O(7)	**96.9(3)**
		O(6)-Co(1)-O(7')	**83.6(3)**
		O(1)-Zn(1)-O(2)	**100.3(3)**
		O(1)-Zn(1)-O(3)	**100.8(3)**
		O(1)-Zn(1)-O(4)	**99.3(3)**
		O(2)-Zn(1)-O(3)	**116.0(3)**
		O(2)-Zn(1)-O(4)	**126.2(3)**
		O(3)-Zn(1)-O(4)	**108.7(3)**

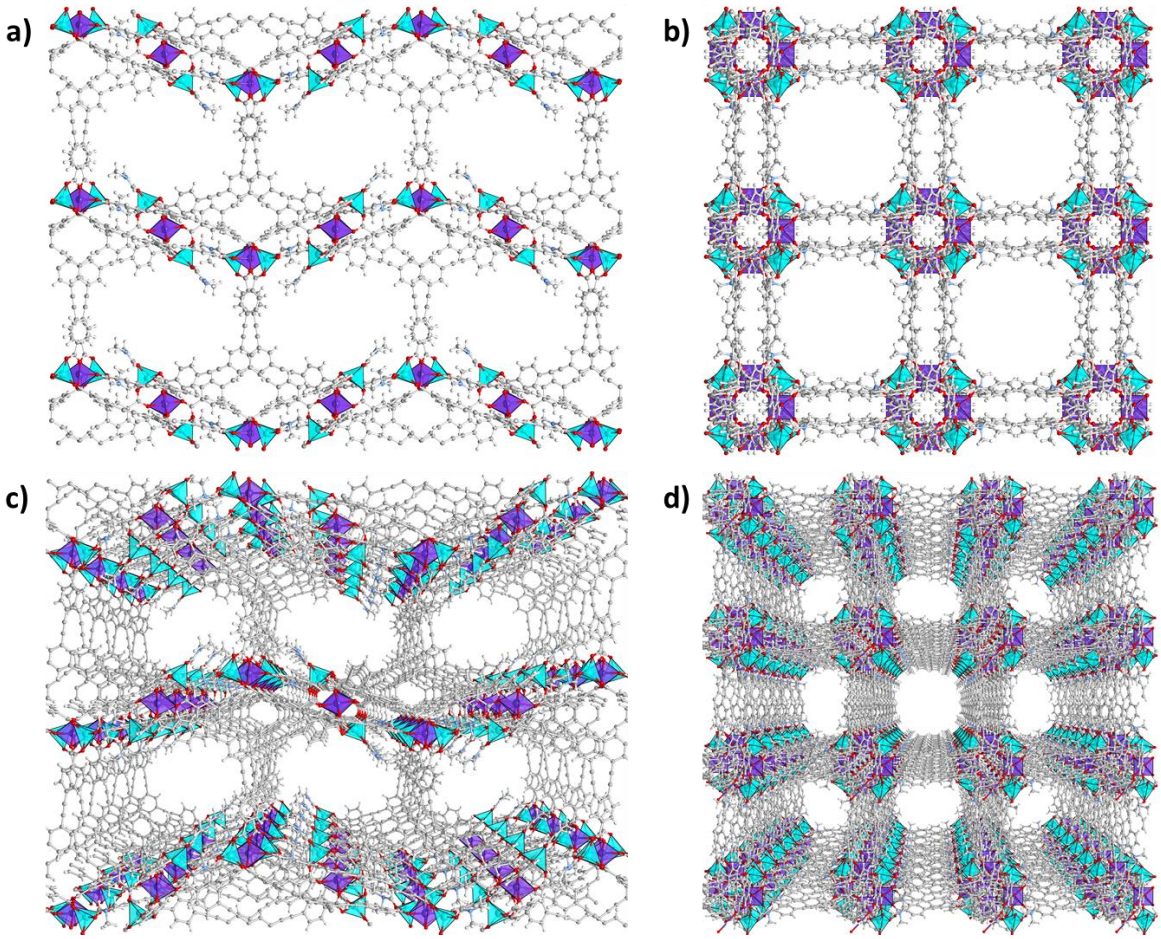

Figure 4.4.3: Ball-and-stick representations with cobalt and zinc atoms shown as polyhedral. **a), c)** View down the crystallographic b-axis. **b), d)** View down the crystallographic c-axis. Colour key: Zn (cyan), Co (purple), O (red), N (pale blue), C (grey), H (white).

As with **3**, **4** consists of two symmetry equivalent chiral interwoven nets (**Figure 4.4.4**) that interact *via* T-shaped π-π interactions between the phenyl moieties (distances of *ca.* 4.8 Å between the centre of each interacting phenyl ring).[21] The solvent accessible void space of the structure, as calculated using the RASPA software package,[22] of 70.2% of the unit cell volume, is slightly smaller that of **3**. This is most like due to the presence of coordinating DMF molecules (instead of water molecules) and the bond distances between Zn and O atoms which are observed to be shorter than those for Mn and O. Thus, the pores/channels in **4** are marginally smaller than in **3**.

Consistently, activated, desolvated crystals of **4** were found to have a slightly higher calculated density (0.549 g/cm^3) than crystals of **3** (0.478 g/cm^3). This is likely because Zn-atoms have larger molecular masses than Mn and Co atoms as well as the fact that the coordinated solvent was resolved as DMF in **4** and H_2O in **3**.

The cylindrical pores that are observed along the crystallographic *c*-axis have diameters of *ca.* 11.6 Å. Whilst the rectangular shaped pores that extend in the directions of the crystallographic *a* and *b-axes*, have cross-sections of *ca.* 15.4 Å x 9.9 Å (**Figure 4.4.4**).

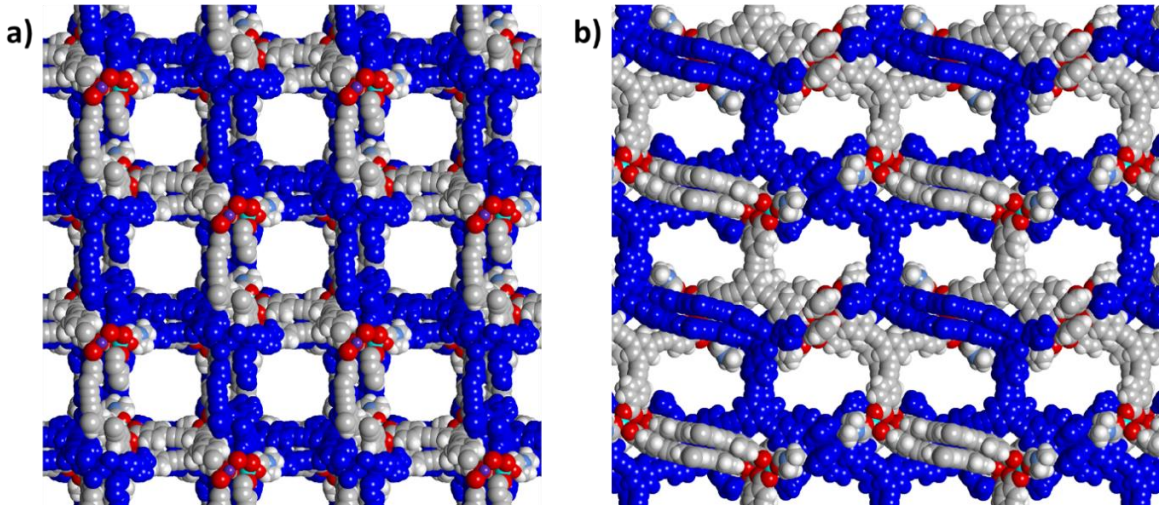

Figure 4.4.4: Space filling representations of **4** showing both interwoven nets with one net highlighted in blue, **a)** view down the crystallographic *c-axis*, **b)** view down the crystallographic *b-axis*. Colour key: Zn (cyan), Co (purple), O (red), N (pale blue), C (grey), H (white).

Table 4.4.2: Crystal data from the structural determination of **4**.

Identification code	**4**
Empirical formula	$C_{72}H_{44}CoZn_2N_2O_{14}$
Formula weight	1350.76 g mol^{-1}
Temperature	220(2) K
Wavelength	1.54178 Å
Crystal system	Tetragonal
Space group	*P* 4_3 2 2
Unit cell dimensions	a = 20.2897(4) Å
	b = 20.2897(4) Å
	c = 39.6783(10) Å
	α = 90°
	β = 90°
	γ = 90°
Volume	16334.4(8) $Å^3$
Z	4
Density (calculated)	0.549 Mg/m^3
Absorption coefficient	1.349 mm^{-1}
F(000)	2756
Crystal size	0.55 × 0.08 × 0.08 mm^3
Theta range for data collection	2.177 to 55.317°
Index ranges	-21 ≤ h ≤ 21, -21 ≤ k ≤ 21, -39 ≤ l ≤ 41
Reflections collected	109207
Independent reflections	10338 [R_{int} = 0.1600, R_{sigma} = 0.0905]
Completeness to theta = 55.317°	99 %
Absorption correction	Multi-Scan
Max. and min. transmission	0.236 and 0.751
Refinement method	XL refinement using least-squares minimisation
Data / restraints / parameters	10338 / 22 / 414
Goodness-of-fit on F^2	0.989
Final R indices [I>=2σ(I)]	R1 = 0.0744, wR2 = 0.1931
Final R indices (all data)	R1 = 0.1160, wR2 = 0.2272
Flack parameter	0.015(7)
Largest diff. peak and hole	0.40 and -0.39 e.$Å^{-3}$
Flack parameter	0.015(7)

4.4.2 Physicochemical characterisation of **4**

4.4.2.1 X-ray powder diffraction

The PXRD pattern of a powder of **4** was measured in a capillary in DMF at 220 K (**Figure 4.4.5**). The experimental pattern and a simulated PXRD pattern that was generated using the single crystal X-ray diffraction data, reveal corresponding signals confirming the phase-purity of the synthesised material. These patterns are almost identical to those obtained for crystals of **3**. The most intense signal is observed at 2θ = 4.4° and is resolved in the simulated pattern at 4.35°. Another characteristic signal is centred at 2θ = 4.95° and appears the simulated pattern at 4.88°. In addition, the signals at 6.22° and 6.59° match the reflections in the simulated pattern. Additional signals at 2θ >7° can be seen in both patterns.

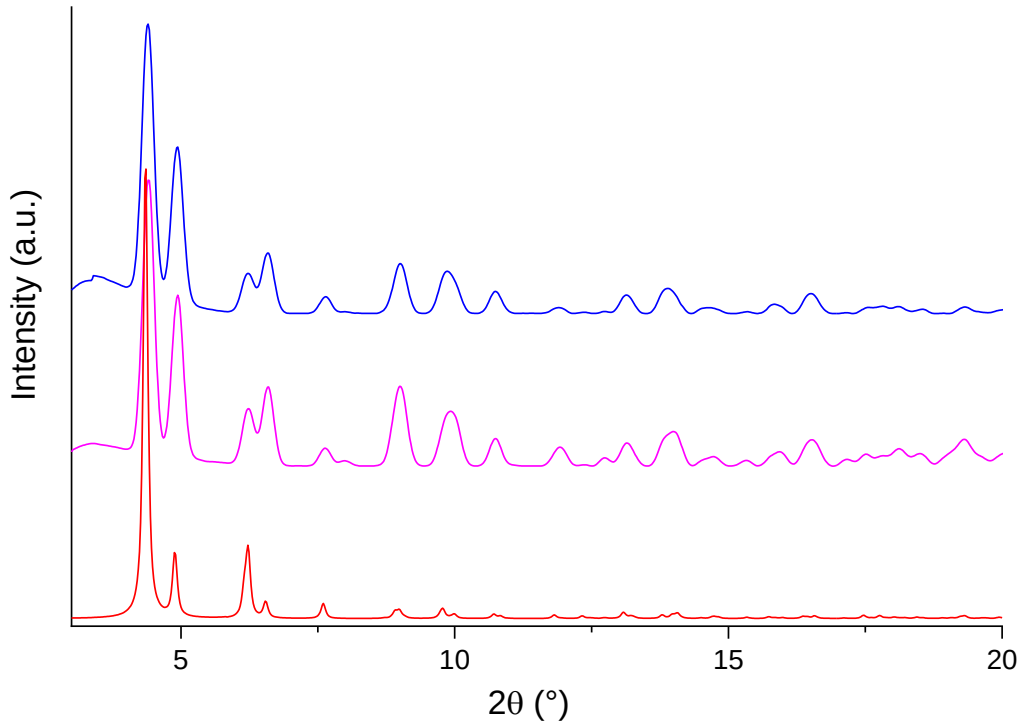

Figure 4.4.5: PXRD patterns. Measured crystals of **3** (blue), **4** (pink) and calculated from the single crystal data of **4** (red).

4.4.2.2 Raman and FT-IR spectroscopy

The Raman and FT-IR spectra of **4** are almost identical to the corresponding spectra of **3** and are predominantly characterised by bands that derive from the vibrations of the organic ligand. Characteristically, the asymmetric and symmetric stretches that derive from the carboxylate functionalities undergo shifts that are in-line with the observed binding behaviour with the MOF structure ($\Delta_{asy\text{-}sym}$ = 129 cm^{-1}). For assignment of the signals, see **Section 5.3.2.2**.

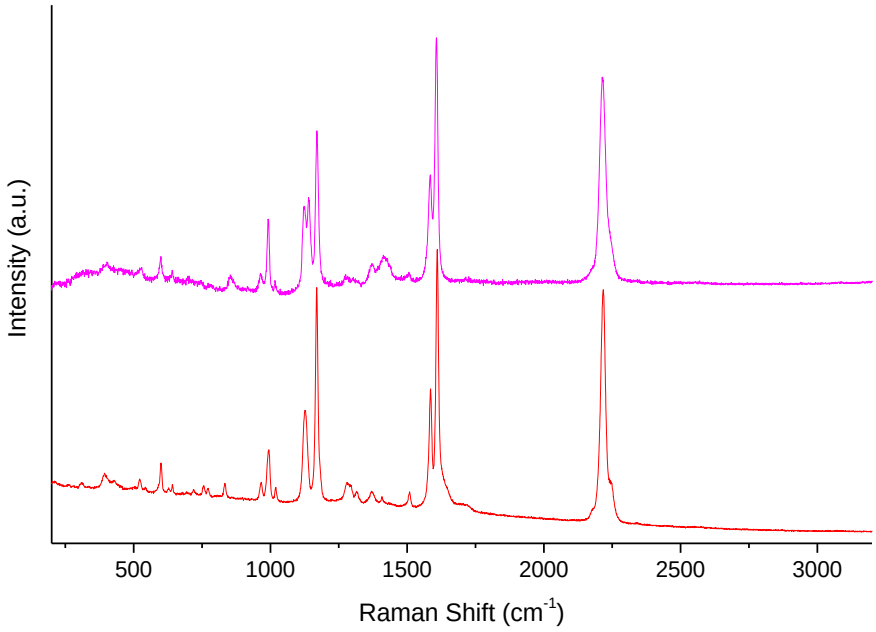

Figure 4.4.6: Raman spectra of crystals of **4** (pink) and **H_3L2** (red).

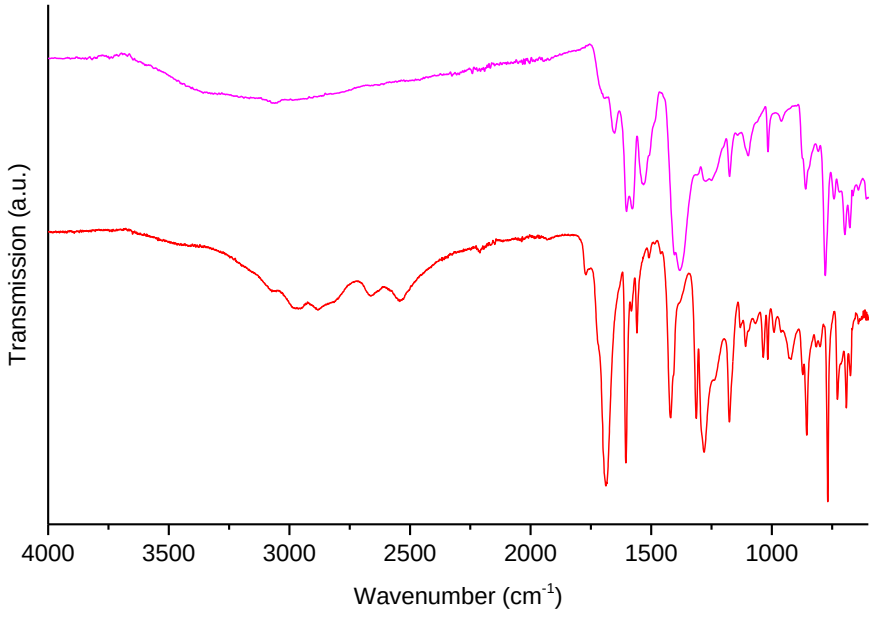

Figure 4.4.7: FT-IR spectra of **4** (pink) and **H_3L2** (red).

4.4.3 Characterisation of metal ion distributions in the SBU of **4**

Although the crystal structure refinement suggested the described ordered atom arrangement in **4**, due to the structural similarities between Co^{2+} and Zn^{2+} metal ions, additional analysis methods were required to determine the metal ion distributions within the SBU of **4**.

4.4.3.1 Energy-dispersive X-ray spectroscopy

For energy-dispersive X-ray spectroscopy (EDX) analysis, crystals of **4** in DMF were placed onto a carbon tab, dried in air for 24 hours and analysed (**Figure 4.4.8**). The relative atomic percentages of the constituent elements were determined (**Table 4.4.3**). The results point to a relative Zn:Co ratio in **4** that reaches to 2.1%:0.9%. This corresponds closely to the 2:1 Zn to Co ratio of metal ions that was used during the synthesis of **4**.

Table 4.4.3: EDX spectroscopy showing the relative atomic percentages in **4**.

Elements	C	O	Zn	Co
Calculated atomic %	74.4	19.4	2.2	1.1
Found atomic %	77.7	19.3	2.1	0.9

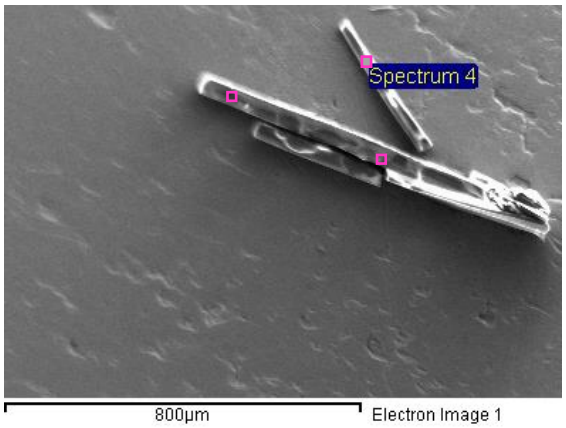

Figure 4.4.8: SEM image showing crystals of **4** with regions taken for EDX analysis highlighted in pink coloured boxes.

4.4.3.2 Solid state UV-Vis spectroscopy

For optical measurements, freshly synthesised crystals of **4** were ground in DMF and then dispersed in $CHCl_3$. A suspension of crystals of **4** in $CHCl_3$ was then drop-casted onto a quartz slide. The quartz slide was left to dry in air leaving a coating of the crystals. For analyses, the sample was covered with a second quartz slide and spectroscopic studies were carried out in the spectral range between *ca.* 300 to 800 nm on the sample of **4** (**Figure 4.4.9**). For comparative purposes absorbance spectroscopy was carried out on $Zn(CH_3CO_2)_2$, $Co(NO_3)_2$, $Co(CH_3CO_2)_2$ and **H_3L2** solutions in DMF. Strong bands are observed in the spectrum of **4** in the UV range of the electromagnetic spectrum below *ca.* 400 nm which can be attributed to π-π*and n–π* transitions in the **$L2^{3-}$** ligands as well as metal-ligand charge transfer (MLCT) transitions. A broad band is observed from *ca.* 490 to 600 nm and it is attributed to d-d transitions in Co^{2+} ions in **4**. This band partly overlaps with the corresponding d-d transition bands observed in both $Co(NO_3)_2{\cdot}6H_2O$ and $Co(CH_3CO_2)_2$.[30] The band in **4** was found to be shifted to shorter wavelengths in relation to the absorptance observed in **3**, indicating that the energy gap between d-d energy levels is increased in **4**. This results in crystals with pale pink colours (**Figure 4.4.9, inset**).

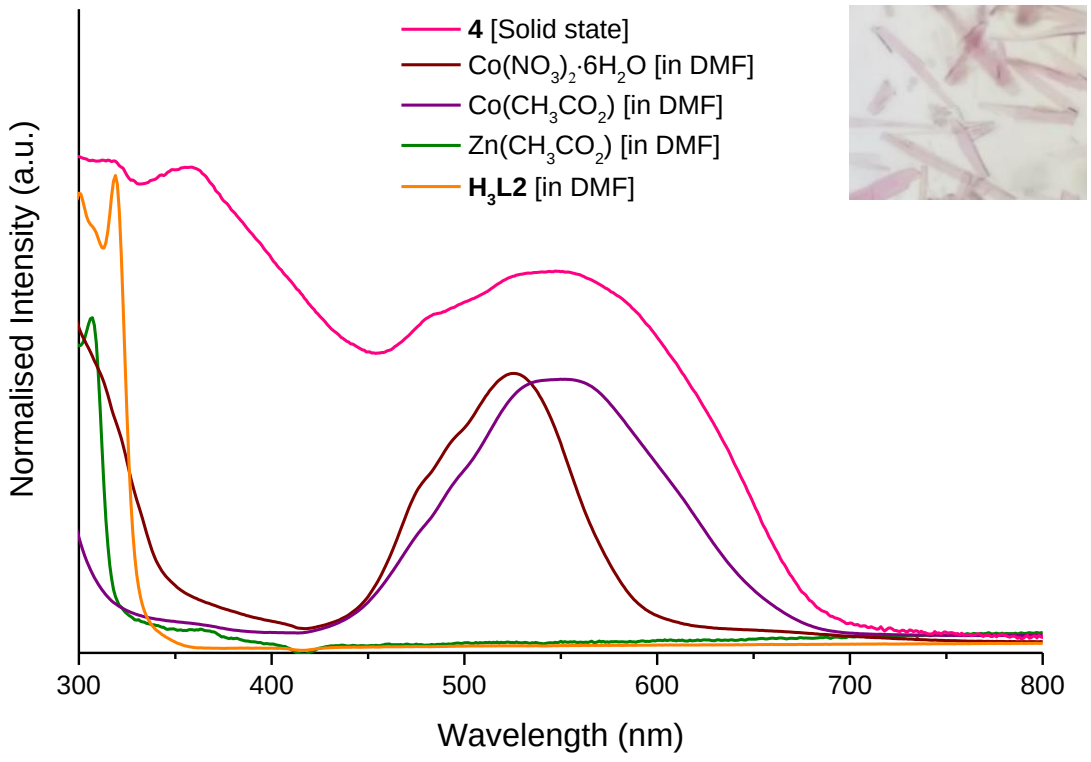

Figure 4.4.9: Solid-state and solution UV-Vis-NIR spectroscopy. ***Inset:*** Visible light microscope picture of crystals of **4**.

As previously discussed in **Section 4.3.3.2**, the UV-vis absorption of transition metal compounds and the resulting compound colour can give information about the coordination environments in which the metal ions are found in.

The d^{10} Zn^{2+} ions contribute little to the visible colour of **4** as both, t_{2g} and e_g* orbitals are fully occupied. Comparable compounds often appear as white in colour (e.g. $Zn(CH_3CO_2)_2$ and Zn_3(**L2**)$_2(DMF)_2$).[18]

The Co^{2+} ions significantly contribute to the visible pale pink colour of **4**. The octahedral coordination environment of the Co^{2+} ion gives rise to Laporte forbidden d-d transitions and weak bands with low extinction coefficients. These transitions are observed for **4** as a broad band that occurs between *ca.* 490 to 600 nm. Thus the resulting spectrum is consistent with that of other reported pale compounds containing Co(II) ions in octahedral environments (e.g. hydrated $Co(CH_3CO_2)_2{\cdot}4H_2O$) and distinctively different to species containing tetrahedrally coordinated Co(II) ions (e.g. anhydrous $Co(CH_3CO_2)_2$ or $[CoCl_4]^2$).[28,30,31]

As for **3**, diffuse reflectance measurements were performed using crystals of **4** and the spectra were converted using the remission function. This approach allowed comparison with literature data of the Zn-based MOF, MOF-5 containing either octahedrally or tetrahedrally coordinated Co(II) ions in the framework (**Figure 4.4.10**).[17] The results show that the spectrum of **4** closely corresponds to that of MOF-5 that contains Co(II) ions in octahedral coordination environments. In addition, there is almost no overlap with the bands of MOF-5 containing tetrahedrally coordinated Co(II) ions. Thus, the data of the optical measurements are consistent with the structural assignment of single-crystal X-ray diffraction studies.

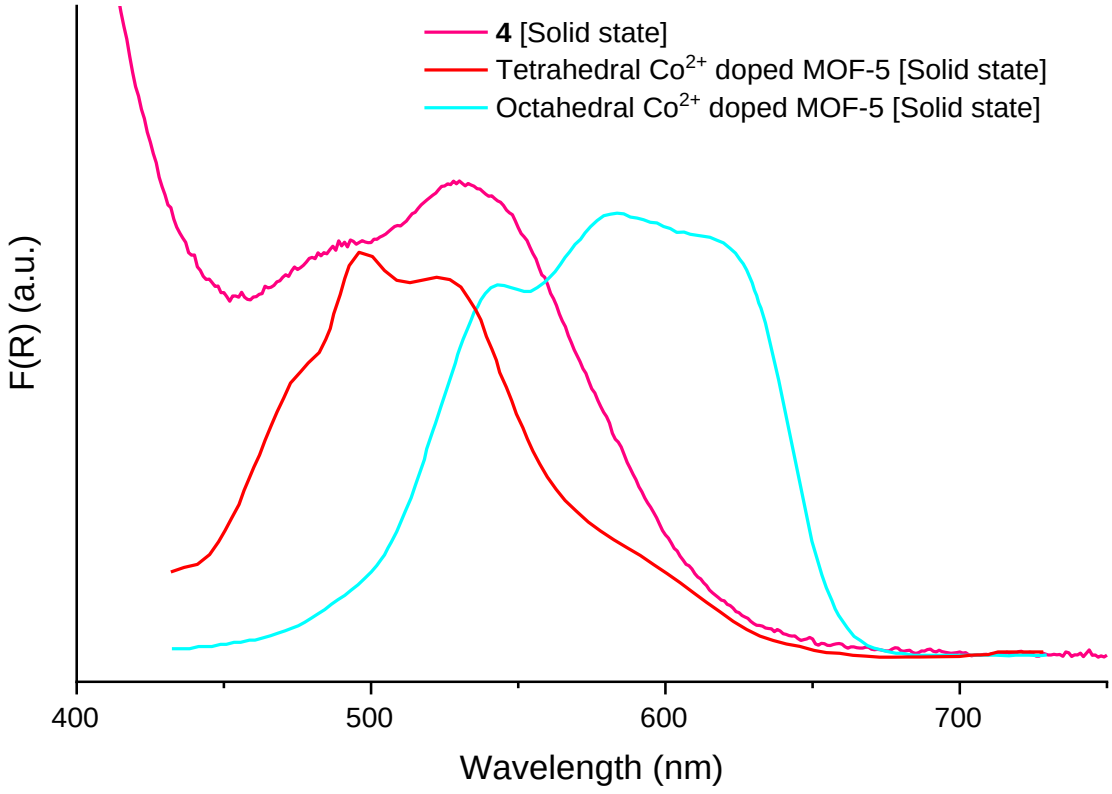

Figure 4.4.10: Solid-state diffuse reflectance spectroscopy of crystals of **4** (converted using the remission function). Spectra of Co(II) doped MOF-5 (data obtained from reference 17).

4.4.3.3 X-ray photoelectron spectroscopy

X-ray photoelectron spectroscopy (XPS) was used to characterise freshly synthesised crystals of **4** and to provide a comparison to the XPS data of **3**. This sample was then compared to reference samples of hydrated Co(II) acetate and anhydrous Zn(II) acetate that contain octahedrally coordinated Co(II) and tetrahedrally coordinated Zn(II) cetres, respectively. XPS survey scans show that **4** contains Co, Zn, O and C atoms (**Figure 4.4.11**). The spectrum of **4,** generally shows similar Co and Zn derived signals as Co(II) acetate and Zn(II) acetate, respectively.. The Co $2p_{1/2}$ and Co $2p_{3/2}$ signals and associated satellite are detectable in the spectrum as shown in **Figure 4.4.12**.[33,34] In addition, the Zn $2p_{3/2}$ signal is resolved at *ca.* 1022 eV (**Figure 4.4.13**).[38]

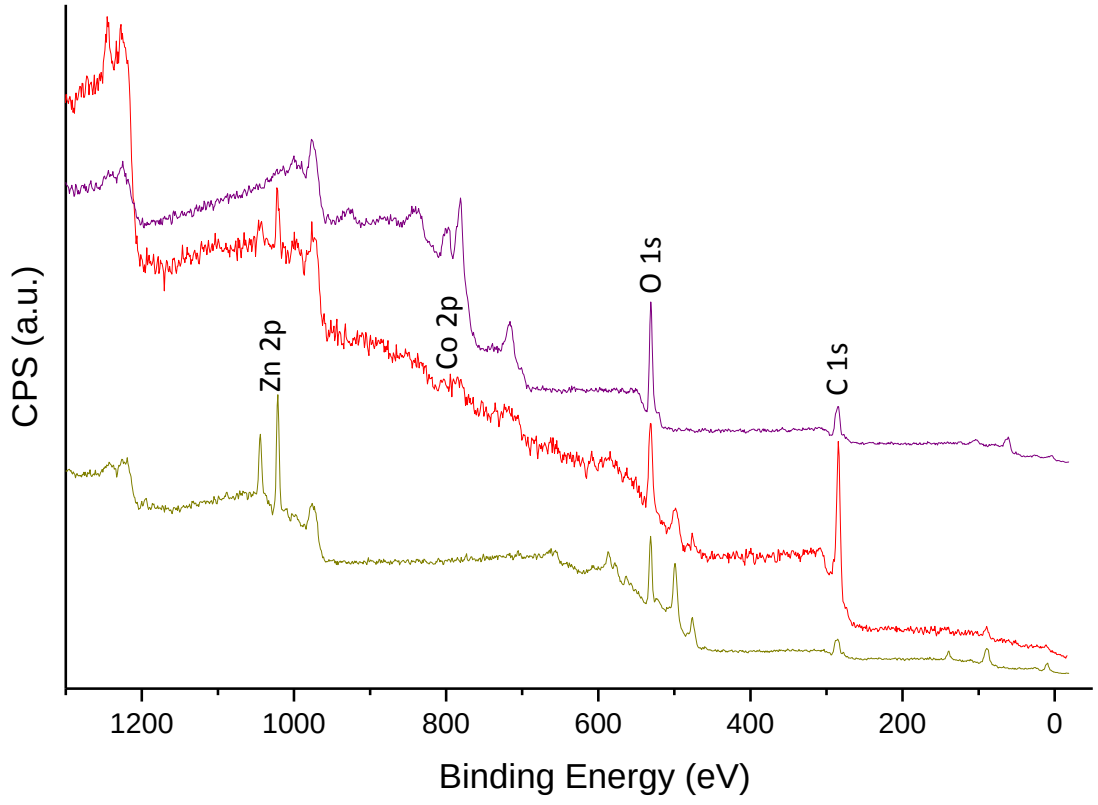

Figure 4.4.11: XPS survey spectra. Freshly synthesised crystals of **4** (red), Co(II) acetate (purple) and Zn(II) acetate (dark yellow).

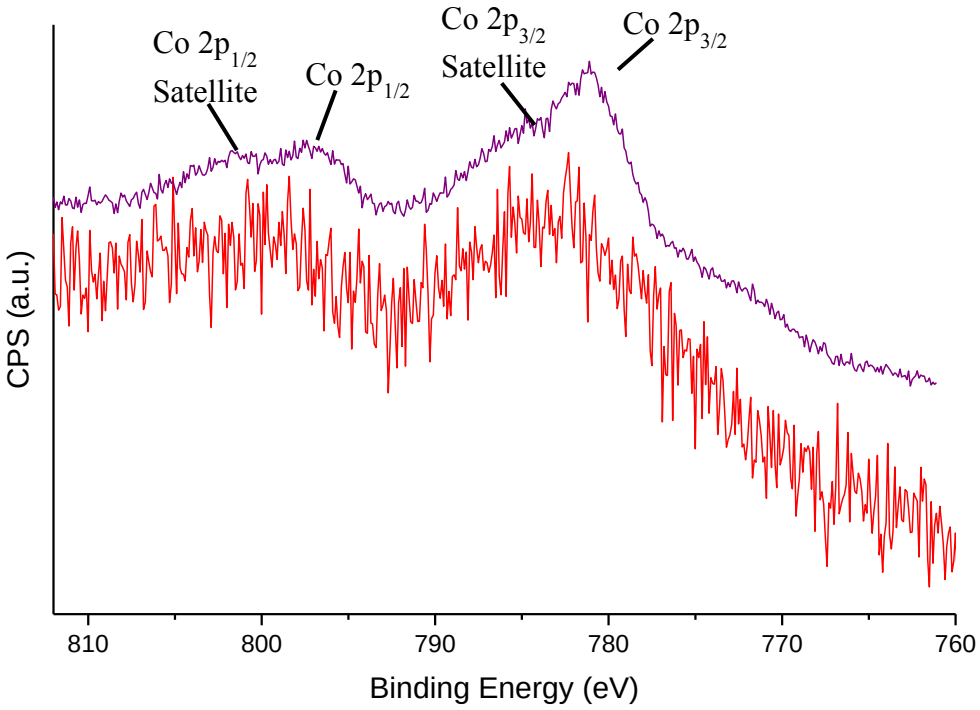

Figure 4.4.12: XPS spectra highlighting the Co(II)-derived signals. Co(II) acetate (purple) and freshly synthesised crystals of **4** (red).

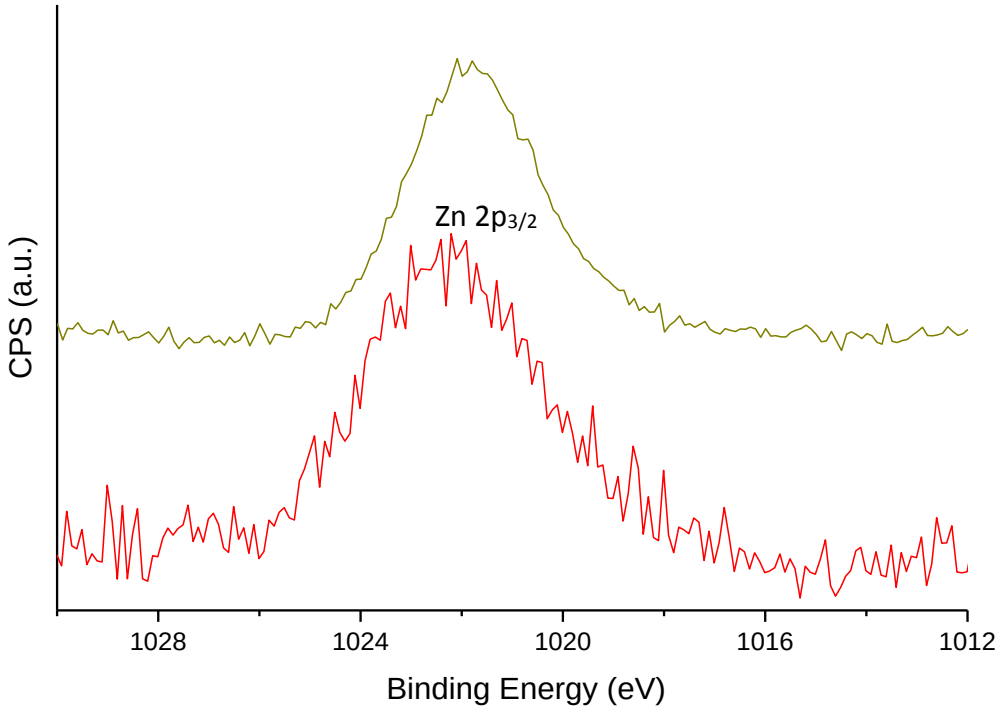

Figure 4.4.13: XPS spectra highlighting the Zn(II)-derived signals. Zn(II) acetate (dark yellow) and freshly synthesised crystals of **4** (red).

For **3,** it was possible to differentiate two distinct O1s signals of carboxylate O-atoms in the two distinct coordination environments of the metal ions. For, **4** this proved not to be the case due to the spectral resolution of the instrument. For **3** a broadened O1s signal is detected (**Figure 4.4.14**). The Pauling electronegativity differences between Zn and Co are smaller than the corresponding differences between Mn and Co (Pauling electronegativity: Mn = 1.55, Zn =1.65, Co = 1.88) Thus the O1s peak appears unresolved which could be overcome by using a detection system with greater sensitivity and by using electrons with lower pass energies to excite crystals of **4**.

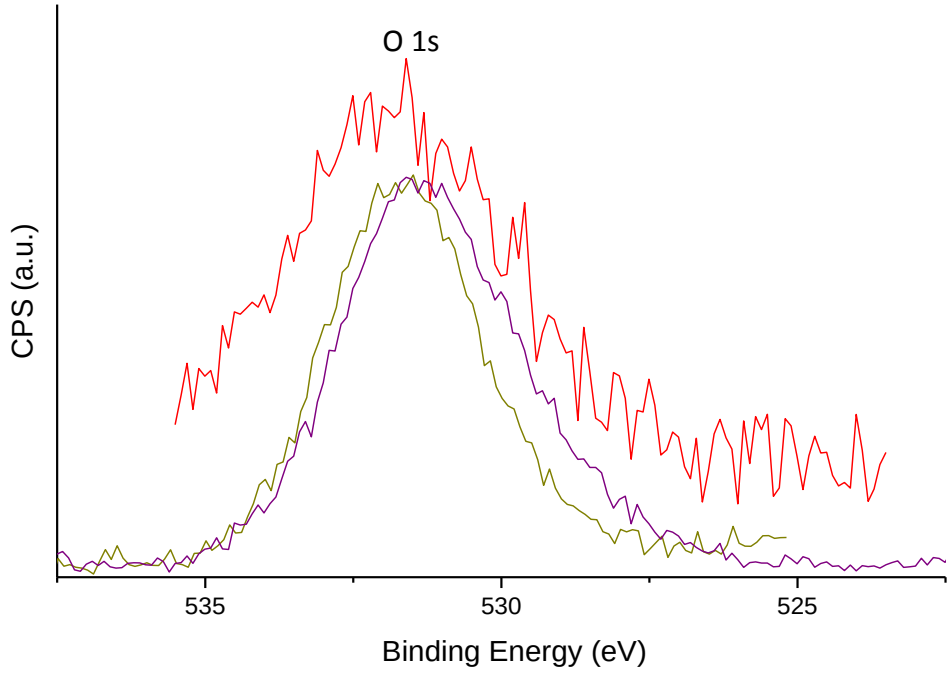

Figure 4.4.14: XPS spectra highlighting the O-derived signal in freshly synthesised crystals of **4** (red) with Zn(II) acetate (dark yellow) and Co(II) acetate (purple) shown as reference samples.

4.4.3.4 Computational modelling

Computational modelling also supports the structural assignment of the crystallographically ordered $\{Co_1Zn_2\}$ SBU, see **Section 6.1** for experimental details. The energetic stability of the SBU was found to be superior when the central octahedral coordinated position contained a Co^{2+} ion rather than a Zn^{2+} ion. The *high-spin* states of Co^{2+} were found to be more stable than the corresponding *low-spin* states. The computed electronic energy of **4** for Co^{2+} ions located in the central octahedral position was found to be *ca.* 17 kJ/mol lower (for the *high-spin* states) than when the Co^{2+} is located in the peripheral tetrahedral position (**Table 4.4.4**).

Furthermore, the $\{M_3\}$ SBU structure is predicted to be linear when a *high-spin* Co^{2+} ion is in the central octahedrally coordinated position. In a hypothetical *low-spin* configuration the structure is bent such resulting in a Zn-Co-Zn angle of *ca.* 165°. Similarly when the Co^{2+} ion is located in one of the peripheral tetrahedral positions of the $\{M_3\}$ SBU, then the Co-Zn-Zn angle is predicted to be *ca.* 157° (for both the *high-spin* and *low-spin* states). The experimental crystallographic results show a Zn-Co-Zn angle of *ca.* 180° further implying that a *high-spin* Co^{2+} ion occupies the central octahedral position in the $\{M_3\}$ SBU.

Additionally, the metal-metal distances for both possible SBU configurations were calculated and compared with the experimental results that derived from the crystal structure (**Table 4.4.5**). The experimental results match the theoretical results for both assumed configurations.

Table 4.4.4: Computed electronic energies for stabilisation energy calculations for the two possible metal ion configurations of the $\{Co_1Zn_2\}$ SBU in **4** (1 Hartree = 2625.50 KJ/mol). Abbreviations: oct = metal ion is situated in the central octahedral position of the SBU; tet = metal ion is situated in the peripheral tetrahedral position of the SBU.

	Multiplicity (no. of unpaired electrons +1)	Energy (Hartrees)	Energy (KJ/mol)
$Zn_{(tet)}$-$Co_{(oct)}$-$Zn_{(tet)}$	4 (*high-spin*)	-3615.3251	-9492036
	2 (*low-spin*)	-3615.2837	-9491927
$Co_{(tet)}$-$Zn_{(oct)}$-$Zn_{(tet)}$	4 (*high-spin*)	-3615.3187	-9492019
	2 (*low-spin*)	-3615.2747	-9491903

Table 4.4.5: Comparison of experimental and calculated metal-metal atom distances in the two possible configurations of the $\{Co_1Zn_2\}$ SBU in **4** with Co^{2+} in the high spin state. Abbreviations: oct = metal ion is situated in the central octahedral position of the SBU; tet = metal ion is situated in the peripheral tetrahedral position of the SBU.

Co^{2+} ion in the central octahedral position (distances in Å)		
Metal ion positions	Experimental	Calculated
$Co_{(oct)}$-$Zn_{(tet-1)}$	3.53	3.43
$Co_{(oct)}$-$Zn_{(tet-2)}$	3.53	3.46
$Zn_{(tet-1)}$-$Zn_{(tet-2)}$	7.07	6.89
Co^{2+} ion in the peripheral tetrahedral position (Distances in Å)		
Metal ion positions	Experimental	Calculated
$Co_{(tet)}$-$Zn_{(oct)}$	3.53	3.47
$Zn_{(oct)}$-$Zn_{(tet)}$	3.53	3.45
$Co_{(tet)}$-$Zn_{(tet)}$	7.07	6.80

4.4.4 Thermogravimetric and gas sorption characterisation of **4**

4.4.4.1 Thermogravimetric analysis

Thermogravimetric analysis (TGA) of **4** in an N_2 atmosphere at a heating rate of 3°C per minute. **Figure 4.4.15** reveals an initial weight loss of *ca.* 79% between 25 and 100°C which can be attributed to the loss of constitutional H_2O and DMF solvent molecules in the pores. The void volume was previously shown to occupy 70.5% of the unit cell volume of **4**, therefore it is likely that a large quantity of solvent could be present in this part of the structure. A small weight loss above 100°C results from the loss of coordination solvent molecules. The degradation of the organic ligand commences above *ca.* 350°C.

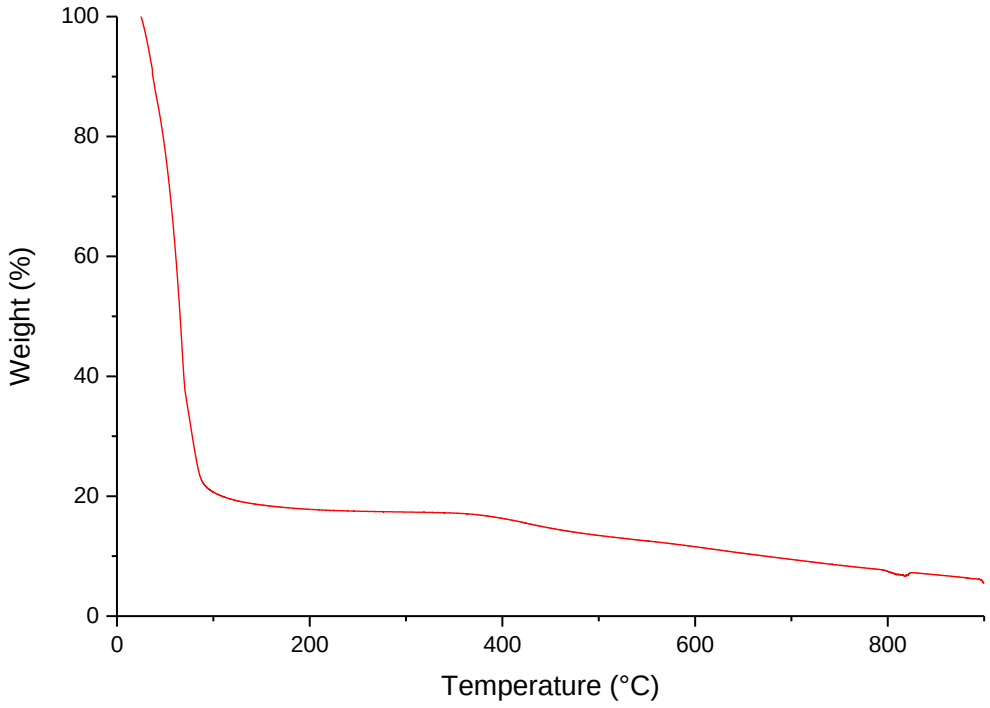

Figure 4.4.15: TGA of compound **4** carried out in an N_2 atmosphere at a heating rate of 3°C per minute.

4.4.4.2 Gas sorption and BET surface area determination experiments of **4**

Prior to conducting gas sorption experiments, a sample of **4** was solvent exchanged as described for **3** and transferred into a quartz measurement cell. Prior to the measurement the sample was activated by heating under vacuum at 50°C for 1 hour. The N_2 gas sorption data recorded at 77 K, is qualitatively similar to that of **3**. Revealing a type-I isotherm that is characterised by a steep uptake at low partial pressures followed by a progressive gas uptake increase due to surface adsorption (**Figure 4.4.16**). For this compound, a maximum uptake of 96 cm^3/g at 728 Torr, which corresponds to an uptake of 120 mg/g was observed.

The H_2 gas sorption data recorded at 77 K shows a reversible isotherm with an uptake of 70 cm^3/g at 757 Torr which corresponds to an uptake of 0.61 wt% (**Figure 4.4.19**). A CO_2 gas sorption isotherm was measured at 278 K. The material gives rise to a CO_2 uptake of 26 cm^3/g at 757 Torr (**Figure 4.4.20**).

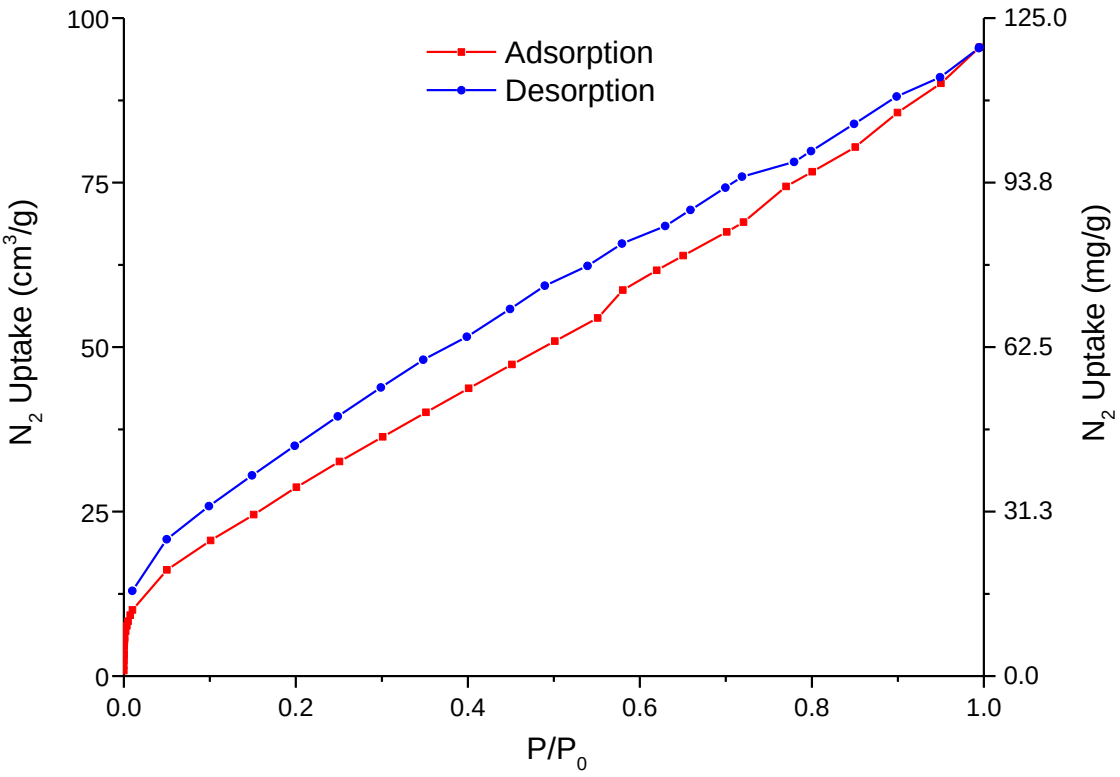

Figure 4.4.16: N_2 sorption isotherm of **4** measured at 77 K.

As for **3**, it appears that upon desolvation of the compound, the framework structure of **4** partially collapses. The BET surface area derived from the N_2 isotherm, gives a value of 109 m^2/g (**Table 4.4.6** and **Figure 4.4.17**) which differs significantly from that calculated using the RASPA software package.[22]

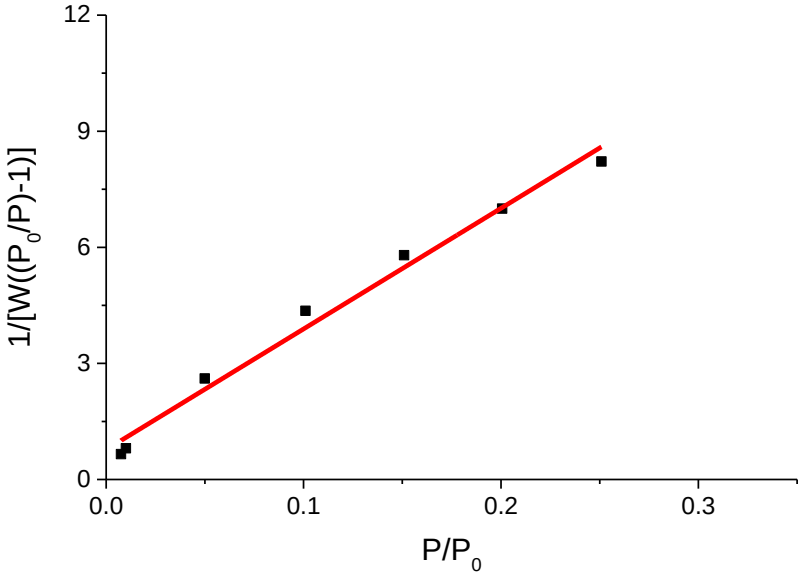

Figure 4.4.17: Plot of the linear region used to obtain the BET surface area of **4** derived from the N_2 gas sorption data.

Table 4.4.6: Table of values obtained from the BET Plot of **4**.

Slope	31.184
Intercept	7.720×10^{-1}
r (correlation coefficient)	0.993228
C constant	41.393
BET Surface Area	109 m^2/g

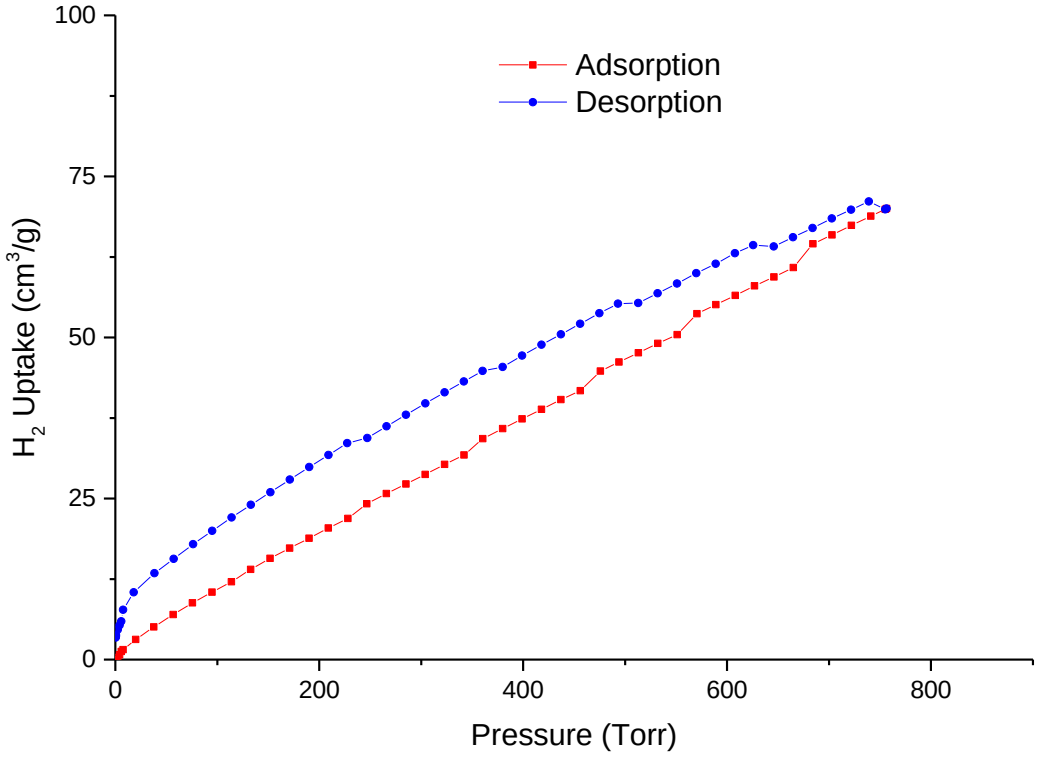

Figure 4.4.19: H_2 sorption isotherm of **4** measured at 77 K.

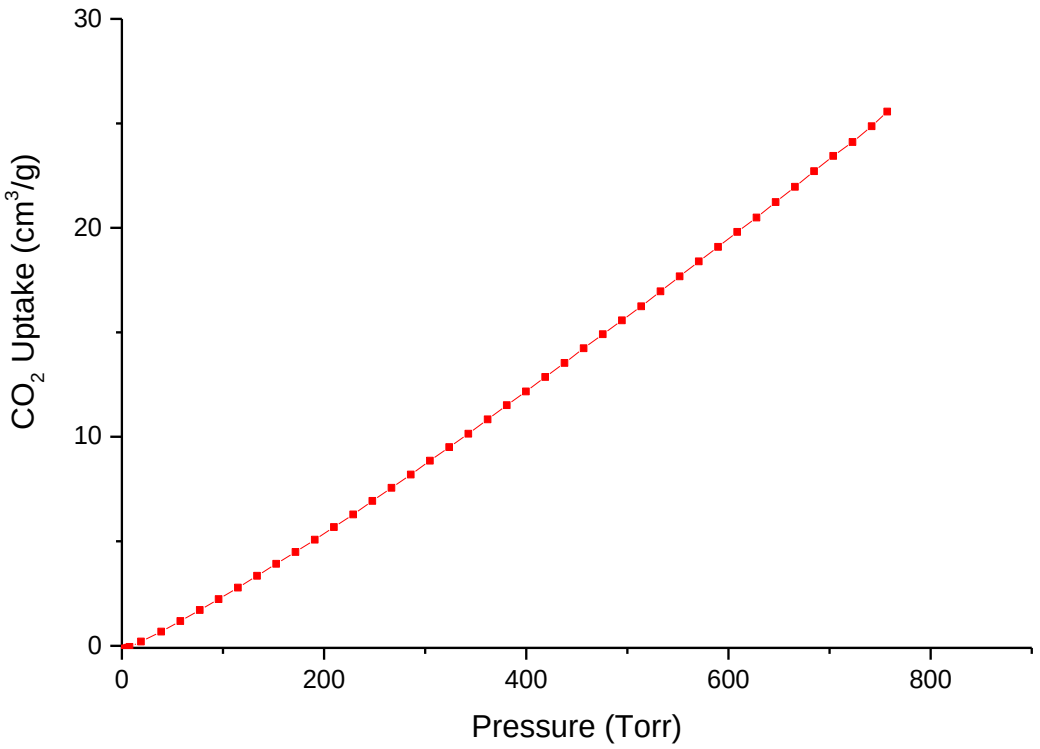

Figure 4.4.20: CO_2 isotherms of **4** measured at 278 K.

4.4.5 Photo-induced water oxidation catalysis

Due to the presence of Zn^{2+} ions located at the peripheral tetrahedral sites in the $\{Co_1Zn_2\}$ SBU, **4** was not expected to show significant water oxidation activity. To investigate the catalytic activity of **4** photo-induced water oxidation experiments were performed under conditions that were also used for experiments utilizing **3**.

Various quantities of **4** ranging from 0.1 to 0.3 mg, were tested for catalytic activity under the outlined experimental conditions (see **Section 5.3.5**) and using a Clark electrode (**Figure 4.4.21**). The experiments demonstrate that **4** promotes the formation of minor quantities of O_2 (in comparison to **3** and control experiments without any potential catalyst present).

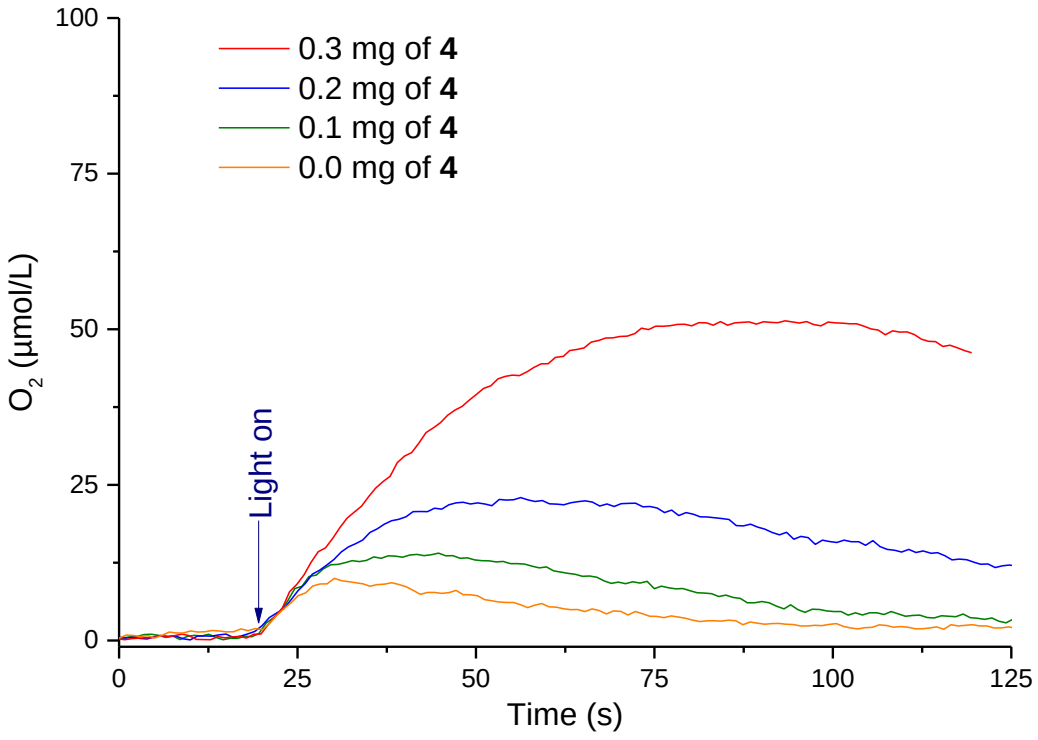

Figure 4.4.21: Photo-induced OER using various quantities of **4** to test its potential as a heterogeneous catalyst**.** Control experiment in the absence of **4** (orange).

The achieved O_2 quantities, chemical yields (in relation to $Na_2S_2O_8$), TONs and TOFs are summarised in **Table 4.4.7**. Maximum O_2 production varies from 14 to 51 µmol/L upon increasing the catalyst loading from 0.1 mg to 0.3 mg, respectively. TONs and TOFs were calculated from the experimental data. The TONs vary from 0.7 to 1.1 whilst TOFs of 0.032 s^{-1} to 0.058 s^{-1} were achieved.

Whilst the overall O_2 quantities in the presence of **4** appear to be relatively low during the photo-induced water oxidation experiments, the catalytic activity of **4** could originate from a range of factors.

Zinc oxides and complexes indeed can show water oxidation activity in photocatalytic and electro-catalytic systems.[39,40] The activity results from electron hole formation and high charge mobility. Photosensitisers may initiate this activity.[41,42] ZnO indeed, has emerged as an interesting catalytic material due to its low toxicity and high abundance. Thus, strategies are currently developed to overcome the intrinsic limitations of ZnO-based energy conversion devices.[43] However these mechanisms are unlikely to contribute substantially to activity in this compound. The residual catalytic activity of **4** may derive from partially hydrated Co^{2+} ions in the material. Defects in the structure such as missing or disordered ligands can result in a number of H_2O accessible coordination sites on Co^{2+} in **4**.[44,45] In addition, a small quantity of the Co^{2+} ions may be located in the peripheral tetrahedral sites.

Table 4.4.7: Max. O_2 quantities, O_2 chemical yields, TONs and TOFs from the photocatalytic OER experiments calculated from each plot in **Figure 4.4.22**.

Sample Mass (mg)	Max. O_2 (µmol/L)	Chemical yield (%)	TON	TOF (s^{-1})
0.3	51	1.03%	1.1	0.032
0.2	23	0.46%	0.7	0.033
0.1	14	0.28%	0.9	0.058
No catalyst	10	0.20%	N/A	N/A

4.5 $[ZnCo_2(\mathbf{L2})_2(DMF)_2]$ (**5**)

4.5.1 Synthesis and structural characterisation of $[ZnCo_2(\mathbf{L2})_2(DMF)_2]$ (**5**)

The self-assembly of **5** was observed when **H_3L2**, $Zn(NO_3)_2{\cdot}6H_2O$ and $Co(NO_3)_2{\cdot}6H_2O$ (3:1:2 ratio) were heated in DMF at 90°C for 72 hours. Orange crystals of **5** formed in the reaction mixture and were used for single crystal X-ray analysis. **5** was obtained as a trace product and appears to co-crystallise with $Me_2NH_2[Zn_5(\mathbf{L2})_3(\mu_3\text{-}OH)_2(DMF)_2]$ (see PXRD analysis).[18] **5** is isostructural to **3** and **4** and it crystallises in the tetragonal space group $P4_322$; the MOF is represented by the empirical formula $[ZnCo_2(\mathbf{L2})_2(DMF)_2]$.

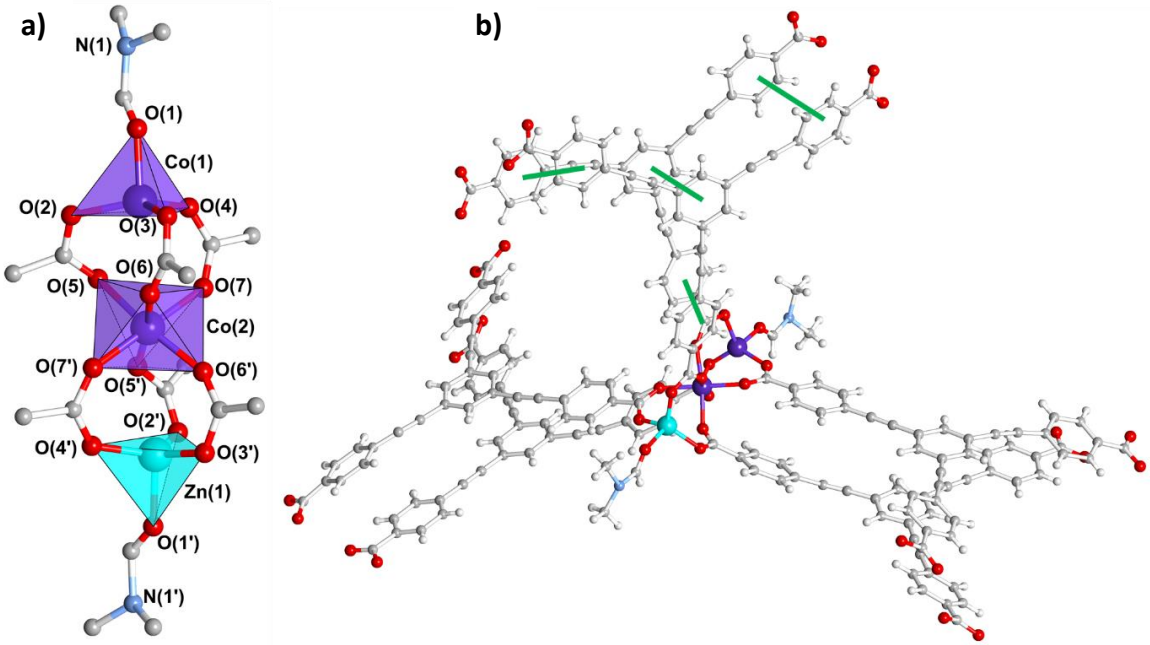

Figure 4.5.1: a) View of the $\{Zn_1Co_2\}$ SBU of **5** in the *[-1 3 -1]*-direction showing coordinated bridging carboxylate groups from six $\mathbf{L2}^{3-}$ ligands and two coordinated DMF molecules. Transparent polyhedral representations are used to highlight the coordination environments of the metal ions. Atoms of interest are labelled. **b)** View of the SBU with six $\mathbf{L2}^{3-}$ ligands attached; View in the *[2 1 0]*-direction. Green lines are used to highlight π-π interactions between phenyl rings in adjacent ligands. Colour key: Co (purple), Zn (cyan), O (red), N (pale blue), C (grey), H (white).

The asymmetric unit of **5** is represented by a central Co(II) ion, a peripheral ion which is refined as being 50% Co(II) : 50% Zn(II). One coordinating DMF molecule (which is partially resolved as a water molecule) as well as one complete coordinating **L2**$^{3-}$ ligand complete the asymmetric unit. A third Co(II)/Zn(II) atom position is generated through symmetry operations forming the hourglass shaped {Zn_1Co_2} trinuclear SBU with a Zn(1)-Co(2)-Co(1) angle of 180° and a Zn(1)-Co(1) distance of 7.06 Å when measuring from the centre of each ion (**Figure 4.5.1 a)**). The observed geometry is particularly similar to the SBU found in **4** albeit with a distinct ratio and arrangement of Zn(II) and Co(II) ions.

This trinuclear cluster in **5** is stabilised, as in the structures of both, **3** and **4**, by a total of six bridging bidentate carboxylate moieties that derive from six deprotonated **L2**$^{3-}$ ligands. Here, the carboxylate Co(2)-O bond distances vary between 2.025(7) Å and 2.073(5) Å while the carboxylate Co(1)/Zn(1)-O bond distances are slightly shorter varying between 1.913(5) Å and 1.952(6) Å. The coordinating DMF molecules give rise to a Co(1)/Zn(1)-O(1) bond distance of 2.009(6) Å. Surrounding the central, octahedrally coordinated Co(2) metal centre, the angles between *trans* located O-atoms deviate slightly from the ideal angle of 180°, to give angles varying from 172.5(2)° to 179.4(3)°. The angles between *cis* located O-atoms surrounding Co(2) vary from 83.5(2)° to 96.0(2)°. This results in an almost ideal octahedral coordination environment for Co(2).

Analogous to the construction observed in **4**, the DMF derived O(1) atom is located close to the linear Co(1)-Co(2)-Zn(1) axis resulting in a O(1)-Co(2)-O(1') angle of 177.14°. The base of the tetrahedron can be regarded as being formed from O(2), O(3) and O(4). These atom positions are raised up towards the O(1) atom resulting in the angles between O(1) and **L2**$^{3-}$ derived O-atoms varying between 99.4(3)° and 99.5(3)°. The angles between the O(2), O(3) and O(4) atoms are found to be between 110.2(3)° and 127.1(3)° (**Figure 4.5.2**). The 3D structure follows that in **3** and **4** whereby the 6-connecting {Zn_1Co_2} SBUs are observed along 4_3-screw axes which extends in the direction of the crystallographic *c*-axis (**Figure 4.5.3**). As in both **3** and **4**, displacement π-π interactions between phenyl rings in each strut add stability to the structure. The distances between the centre of one interacting phenyl ring to the centre of the overlapping phenyl moiety varies between *ca.* 3.8 Å and *ca.* 4.4 Å and are consistent with the interactions in **3, 4** and other literature examples.[20,21]

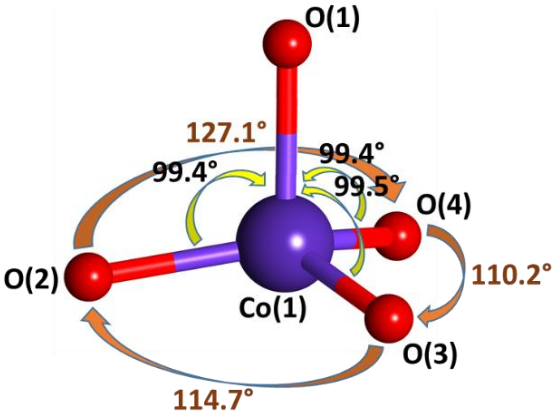

Figure 4.5.2: The Co(1) ion in **5** showing angles between coordinated O-atoms (which is identical to the symmetry equivalent Zn(1) coordination environment). O(1) derives from coordinated DMF molecules, while O(2), O(3) and O(4) derive from coordinated **L2**$^{3-}$ ligands. Colour key: Co (purple), O (red).

Table 4.5.1: Selected bond distances and angles of coordination environments found in **5**.

Atoms	Distance [Å]	Atoms	Angle [°]
Co(2)-O(5)	**2.061(6)**	O(5)- Co(2)-O(6')	**172.5(2)**
Co(2)-O(6)	**2.025(7)**	O(7)- Co(2)-O(7')	**179.4(3)**
Co(2)-O(7)	**2.073(5)**	O(5)- Co(2)-O(5')	**85.9(3)**
		O(5)- Co(2)-O(6)	**92.6(3)**
Co/Zn(1)-O(1)	**2.009(6)**	O(5)- Co(2)-O(7)	**89.1(2)**
Co/Zn(1)-O(2)	**1.951(6)**	O(5)- Co(2)-O(7')	**91.3(2)**
Co/Zn(1)-O(3)	**1.952(6)**	O(6)- Co(2)-O(6')	**89.8(4)**
Co/Zn(1)-O(4)	**1.913(5)**	O(6)- Co(2)-O(7)	**96.0(2)**
		O(6)-Co(2)-O(7')	**83.5(2)**
		O(1)-Co/Zn(1)-O(2)	**99.4(3)**
		O(1)-Co/Zn(1)-O(3)	**99.5(3)**
		O(1)-Co/Zn(1)-O(4)	**99.4(3)**
		O(2)-Co/Zn(1)-O(3)	**114.7(3)**
		O(2)-Co/Zn(1)-O(4)	**127.1(3)**
		O(3)-Co/Zn(1)-O(4)	**110.2(3)**

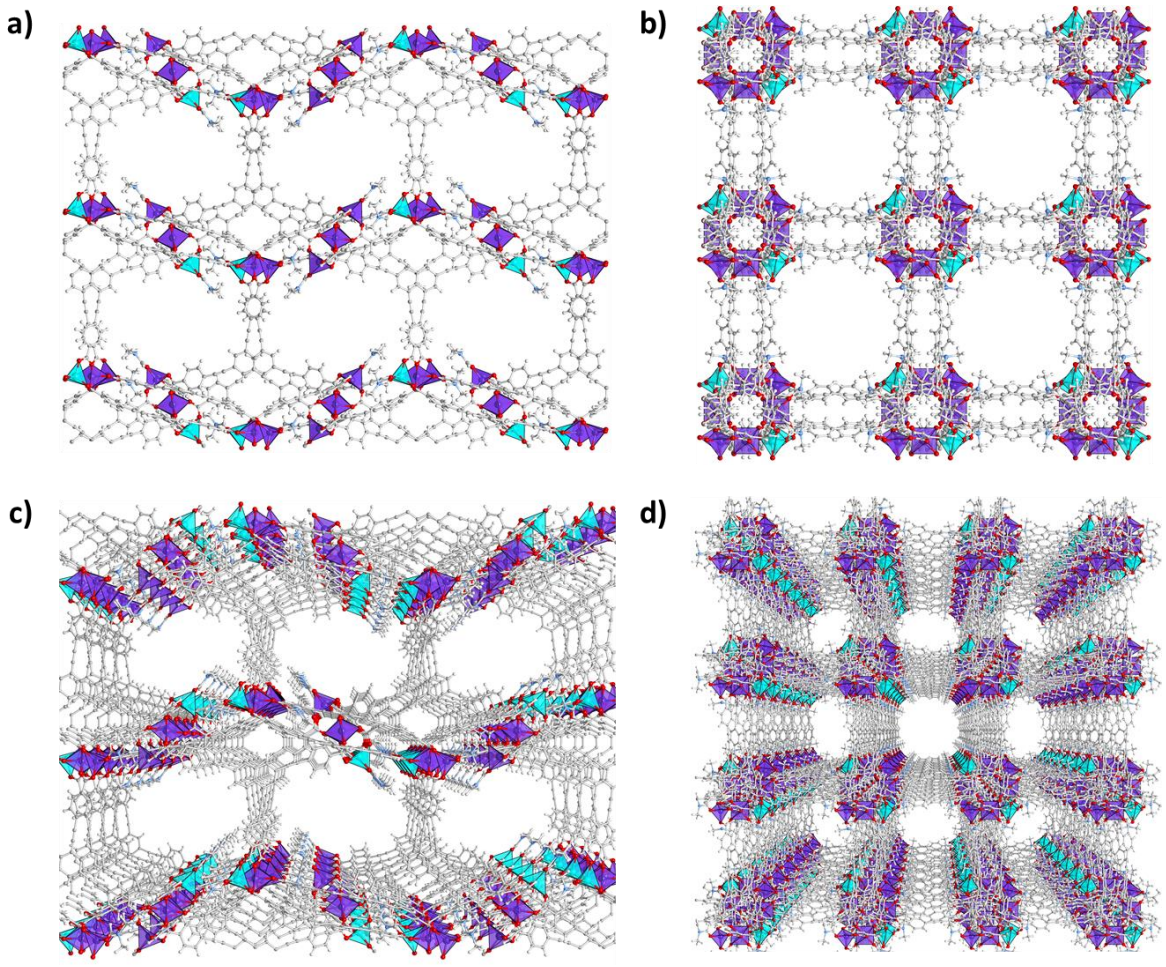

Figure 4.5.3: Ball and stick representations with cobalt and zinc atoms shown as coordination polyhedra. **a)**, **c)** View down the crystallographic *b*-axis. **b)**, **d)** View down the crystallographic *c*-axis. Colour key: Zn (cyan), Co (purple), O (red), N (pale blue), C (grey), H (white).

Like **3** and **4**, the structure of **5** consists of two symmetry equivalent chiral interwoven nets (**Figure 4.5.4**). As previously discussed for the other structures, T-shaped π-π interactions between phenyl groups in different nets are observed (distances of *ca.* 4.8 Å between the centre of each interacting phenyl ring).

Crystals of **5** were found to have a density of 0.545 g/cm^3 in the desolvated form. The void space was calculated using the RASPA software package[22] and it was found to occupy 69.3% of the crystal structure. Both of these values are almost identical to those of **4**. Van der Waals space filling models show that **5** has accessible pores in all three crystallographic directions (**Figure 4.5.4**). The cylindrical pores, observed along the crystallographic c-axis have diameters of *ca.* 11.6 Å. The larger rectangular shaped pores have cross-sectional dimensions of *ca.* 15.4 Å x 9.9 Å. For **5**, the theoretical surface area was calculated to be 2775 m^2/g.[22] Thus the data is consistent with that of **3** and **4**.

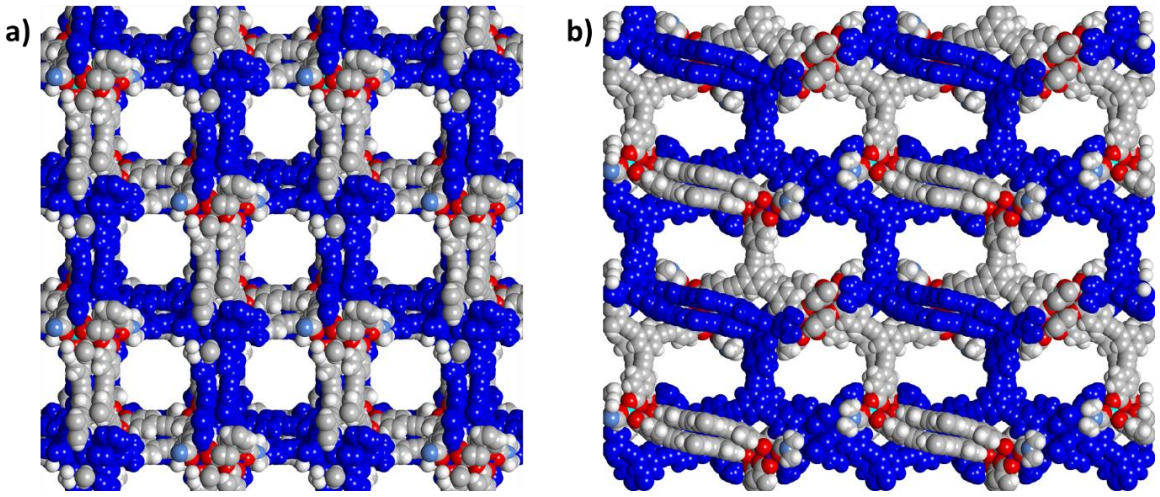

Figure 4.5.4: Space filling representations of **5** showing both interpenetrated nets with one net highlighted in blue, **a)** view in the direction of the crystallographic *c-axis*, **b)** view in the direction of the crystallographic *b-axis*. Colour key: Co (purple), Zn (cyan), O (red), N (pale blue), C (grey), H (white).

The crystal structure data for **5** is presented in **Table 4.5.2**. The structural assignment and outlined statistical disorder at the peripheral tetrahedral position led to the lowest quality values during the structure refinement.

Table 4.5.2: Crystal data from the structural determination of **5**.

Identification code	**5**
Empirical formula	$C_{68.86}H_{35.45}Co_2Zn_1N_{0.73}O_{14.14}$
Formula weight	1284.545
Temperature	215(2) K
Wavelength	1.54178 Å
Crystal system	Tetragonal
Space group	P 43 2 2
Unit cell dimensions	a = 20.2810(6) Å
	b = 20.2810(6) Å
	c = 39.6764(12) Å
	α = 90°
	β = 90°
	γ = 90°
Volume	16319.7(11) $Å^3$
Z	18
Density (calculated)	0.518 Mg/m^3
Absorption coefficient	1.952 mm^{-1}
F(000)	2581
Crystal size	0.43 x 0.08 x 0.08 mm^3
Theta range for data collection	2.447 to 50.619°
Index ranges	-20 ≤ h ≤ 13, -20 ≤ k ≤ 20, -39 ≤ l ≤ 39
Reflections collected	43744
Independent reflections	8618 [R_{int} = 0.0780]
Completeness to theta = 50.702°	99.9 %
Absorption correction	Semi-empirical from equivalents
Max. and min. transmission	0.7500 and 0.2201
Refinement method	Full-matrix least-squares on F^2
Data / restraints / parameters	8618 / 5 / 344
Goodness-of-fit on F^2	0.920
Final R indices [I>=2σ(I)]	R1 = 0.0493, wR2 = 0.1212
Final R indices (all data)	R1 = 0.0696, wR2 = 0.1290
Absolute structure parameter	0.056(8)
Largest diff. peak and hole	0.201 and -0.226 $e.Å^{-3}$
Flack parameter	0.056(8)

4.5.2 Physicochemical characterisation of **5**

4.5.2.1 X-ray powder diffraction

For X-ray powder diffraction experiments crystals of **3** were ground into a powder and a PXRD pattern was recorded to characterise the phase purity of the synthesised bulk material. The PXRD pattern was measured in a capillary at 220 K to avoid loss of crystallinity associated with solvent evaporation from the sample (**Figure 4.5.5**). The experimental and simulated PXRD patterns (based on the single crystal X-ray diffraction data) confirm that **5** represents the minor product within the bulk sample. Several lower intensity which derive from **5** can be resolved in the measured pattern. The diffraction pattern along with the orange colour of the crystals reveals that the dominant product is the related and previously reported compound $Me_2NH_2[Zn_5(\mathbf{L2})_3(\mu_3\text{-}OH)_2(DMF)_2]$.[18]

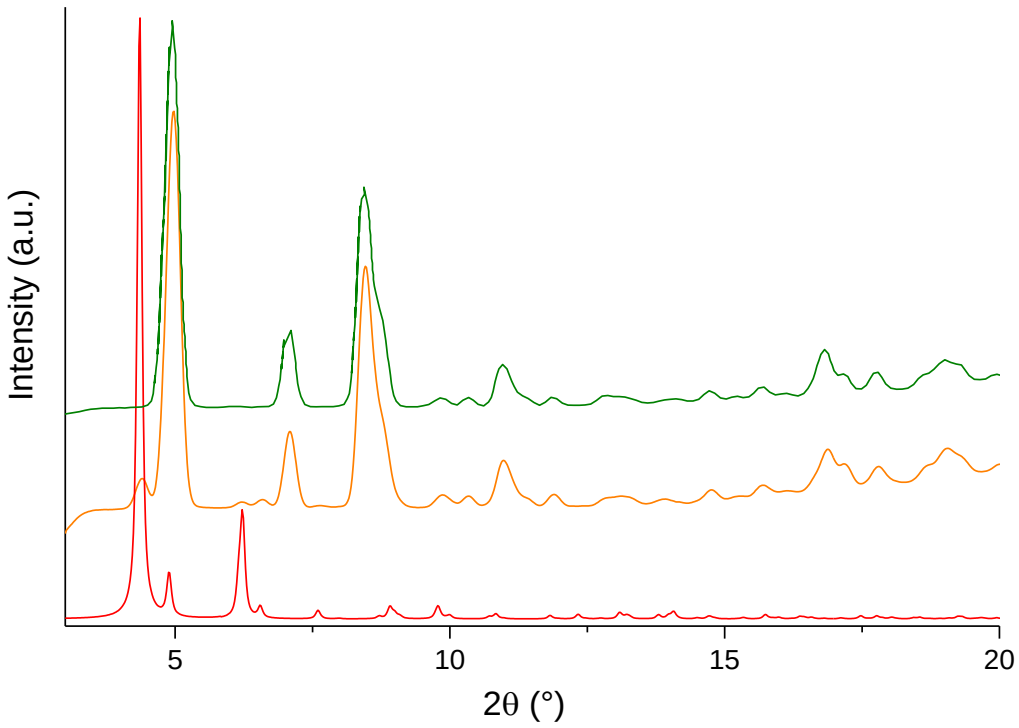

Figure 4.5.5: PXRD patterns. Measured crystals of **5** (orange), $Me_2NH_2[Zn_5(\mathbf{L2})_3(\mu_3\text{-}OH)_2(DMF)_2]$ (green) and calculated pattern from the single crystal data of **5** (red).

4.5.3 Characterisation of metal ion distributions in the SBU of **5**

4.5.3.1 Energy-dispersive X-ray spectroscopy

Selected crystals of **5** dispersed in DMF were placed onto a carbon tab, dried in air for 24 hours and analysed using energy-dispersive X-ray spectroscopy (EDX) (**Figure 4.5.6)**. The relative atomic percentages of the constituent elements were evaluated (**Table 4.5.3**). The results point to a relative Zn:Co ratio of *ca.* 1:2 present in **5**.

Table 4.5.3: EDX spectroscopy showing the relative atomic percentages in **5**.

Elements	C	O	Zn	Co
Calculated atomic %	74.2	22.5	1.1	2.3
Found atomic %	74.0	22.7	1.1	2.2

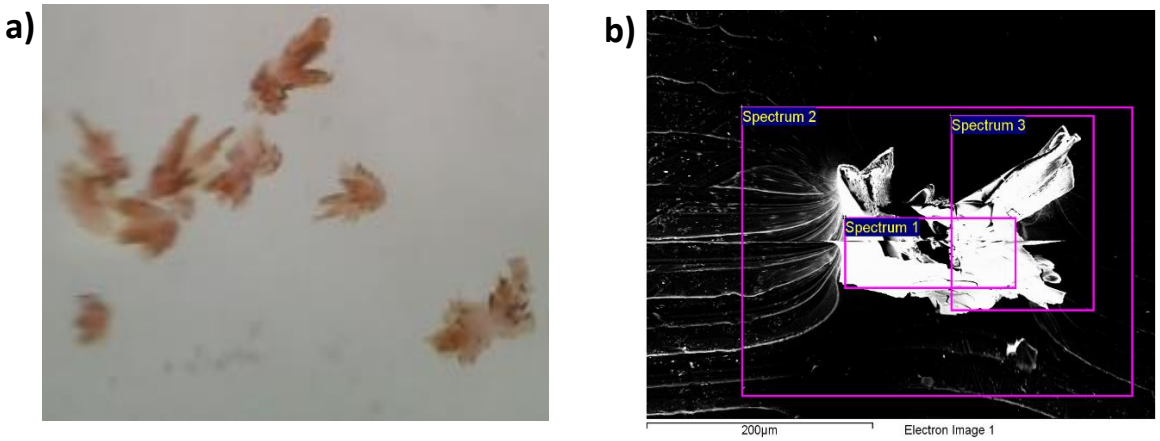

Figure 4.5.6: a) Visible light microscope pictures of crystals of **5**. **b)** SEM picture showing crystals of **5** with regions taken for EDX analysis highlighted in pink coloured boxes.

4.5.3.2 Computational modelling

Computational modelling was performed using a simplified model chosen to explore the possible $\{Zn_1Co_2\}$ SBU configurations and to assess the stabilities of the different metal ion configurations (see **Section 7.1** for experimental details). This modelling was then used as in **3** and **4** to aid the assignment of relative metal ion positions. The stability of the SBU was found to be superior when one of the two peripheral tetrahedral coordinated positions contained a Zn^{2+} ion rather than a both positions being occupied by Co^{2+} ions. The computed electronic energy of **5** for Zn^{2+} ions located in peripheral tetrahedral position was found to be *ca.* 31 kJ/mol lower compared to an assignment by which the Zn^{2+} ion is located in the central octahedral position (**Table 4.5.4**).

In addition, the $\{M_3\}$ SBU structure is predicted to be close to linear when the Zn^{2+} ion is in the central octahedral coordinated position of the SBU giving a Co-Zn-Co angle of *ca.* 176°. However, when the Zn^{2+} ion occupies one of the peripheral tetrahedral positions in the $\{M_3\}$ SBU, then the Zn-Co-Co angle is predicted to be *ca.* 176°. The experimental crystallographic results show a Co-Zn-Co angle of *ca.* 180°. Both angles are close to the experimental value further implying that either of metal ion arrangements in the SBU are possible.

Additionally, the metal-metal distances for both possible SBU configurations were calculated and compared with the experimental results from the X-ray crystal structure findings (**Table 4.5.5**). The experimental results match the theoretical results for both configurations.

Table 4.5.4: Computed electronic energies for stabilisation energy calculations for the two possible metal ion configurations of the $\{Zn_1Co_2\}$ SBU in **5** (1 Hartree = 2625.50 KJ/mol). Abbreviations; oct =metal ion is situated in the central octahedral position of the SBU; tet = metal ion is situated in the peripheral tetrahedral position of the SBU.

	Multiplicity (no. of unpaired electrons +1)	Energy (Hartrees)	Energy (KJ/mol)
$Co_{(tet)}$-$Zn_{(oct)}$-$Co_{(tet)}$	7 *(high spin)*	-3534.0507	-9278650
$Zn_{(tet)}$-$Co_{(oct)}$-$Co_{(tet)}$	7 *(high spin)*	-3534.0625	-9278681

Table 4.5.5: Comparison of experimental and calculated metal ion to metal ion distances in the two assigned metal ion configurations of the $\{Zn_1Co_2\}$ SBU in **5**. Abbreviations; oct = metal ion is situated in the central octahedral position of the SBU, tet = metal ion is situated in the peripheral tetrahedral position of the SBU.

Zn^{2+} ion in the central octahedral position (Distances in Å)		
Metal ion positions	Experimental	Calculated
Zn(oct)-Co(tet-1)	3.53	3.49
Zn(oct)-Co(tet-2)	3.53	3.52
Co(tet-1)-Co(tet-2)	7.06	7.01
Zn^{2+} ion in the peripheral tetrahedral position (Distances in Å)		
Metal ion positions	Experimental	Calculated
Zn(tet)-Co(oct)	3.53	3.49
Co(oct)-Co(tet)	3.53	3.52
Zn(tet)-Co(tet)	7.06	7.01

4.6 Conclusion

Three novel isoreticular MOFs composed of mixed metal SBUs, $[MnCo_2(\mathbf{L2})_2(H_2O)_2]$ (**3**), $[CoZn_2(\mathbf{L2})_2(DMF)_2]$ (**4**) and $[ZnCo_2(\mathbf{L2})_2(DMF)_2]$ (**5**) were successfully synthesised. The trinuclear unit in each structure is stabilised by six carboxylate functional groups which derive from six deprotonated $\mathbf{L2}^{3-}$ ligands. The SBUs in each MOF are interlinked by the $\mathbf{L2}^{3-}$ ligands into 4_3 helical chains which run along the crystallographic *c*-axes. These helical chains are further cross-linked via the $\mathbf{L2}^{3-}$ ligands resulting in 3D MOF structures. All three MOFs are twofold interwoven and are stabilised π-π stacking interactions between the phenyl rings in neighbouring $\mathbf{L2}^{3-}$ ligands.

The constitutional and structural attributes of these MOFs were studied using a variety of analytical techniques including X-ray diffraction, Raman and IR spectroscopy and thermogravimetric analysis. The assignment of the relative metal positions in each of the mixed-metal SBUs was substantiated using a range of complimentary techniques including X-ray diffraction, EDX spectroscopy, UV-vis-NIR spectroscopic studies, XPS, and computational modelling. The techniques strongly suggest that the metal arrangement in these coordination compounds is ordered and the positions are not statically occupied. In mixtures particular metal ions reveal a clear preference for the facilitated octahedral or tetrahedral coordination environments. It was found that the presence of Mn(II) ions in the reaction mixture pushes the reaction equilibrium towards the trinuclear SBU whilst the formation of other possible compounds is supressed.

Bulk powder X-ray diffraction was used to demonstrate the phase purity of **3** and **4**, while **5** forms in a reaction mixture with $Me_2NH_2[Zn_5(\mathbf{L2})_3(\mu_3\text{-}OH)_2(DMF)_2]$.[18] In addition, the X-ray diffraction studies confirm that the compounds preserve their crystallinity in the presence of DMF. Their phase purity allowed further investigation of the properties of **3** and **4**.

Gas sorption studies on compounds **3** and **4** demonstrate that both materials retain a degree of micro-porosity upon the removal of constitutional solvent molecules. However, substantially lower surface areas were measured, than one would expect considering the crystal structure and the theoretically calculated geometrical surface areas. This indicated that the framework rigidity of the compounds is limited and the structures have a tendency

to collapse due to prevailing capillary forces upon activation. Thus the structural attributes of 3-5 may be more suitable for solution based studies.

Preliminary studies using compounds **3** and **4** as components in photo-induced water oxidation in conjunction with $Ru(bpy)_2Cl_2$ as a photosensitisers, were conducted. The presence of each compound contributes to an increase in the level of oxygen production relative to when the MOFs are excluded from the reactions. This indicates that they may act as potential water oxidation catalysts. The significantly increased oxygen production when **3** (which contains terminal Co(II) ions in its SBU) is added to the reaction solution is particularly encouraging. The catalytic activity of the MOF is characterised by a maximum TON of 6.4 and a TOF of 0.200 s^{-1}. However, further experimental studies are required to further investigate the catalytic performance (e.g. electrocatalytic studies and characterisations) and the stability of the compounds.

4.7 References

1 M. Kikuchi, M. Takahahi and O. Okuno, *Dent. Mater. J.*, 2003, **22**, 328–342.

2 I. J. Polmear, *Mater. Sci. Technol.*, 1994, **10**, 1–16.

3 R. Raja, S. Hermans, D. S. Shephard, B. F. G. Johnson, R. Raja, G. Sankar, S. Bromley and J. M. Thomas, *Chem. Commun.*, 1999, 1571–1572.

4 J. M. Thomas, B. F. G. Johnson, R. Raja, G. Sankar and P. A. Midgley, *Acc. Chem. Res.*, 2003, **36**, 20–30.

5 S. M. Cohen, Z. Zhang and J. A. Boissonnault, *Inorg. Chem.*, 2016, **55**, 7281–7290.

6 S. M. J. Rogge, A. Bavykina, J. Hajek, H. Garcia, A. I. Olivos-Suarez, A. Sepúlveda-Escribano, A. Vimont, G. Clet, P. Bazin, F. Kapteijn, M. Daturi, E. V. Ramos-Fernandez, F. X. Llabrés i Xamena, V. Van Speybroeck and J. Gascon, *Chem. Soc. Rev.*, 2017, **46**, 3134–3184.

7 D. Sun, F. Sun, X. Deng and Z. Li, *Inorg. Chem.*, 2015, **54**, 8639–8643.

8 X. Song, M. Oh and M. S. Lah, *Inorg. Chem.*, 2013, **52**, 10869–10876.

9 K. P. Rao, M. Higuchi, J. Suryachandram and S. Kitagawa, *J. Am. Chem. Soc.*, 2018, **140**, 13786–13792.

10 H. Liu, L. Chang, C. Bai, L. Chen, R. Luque and Y. Li, *Angew. Chem. Int. Ed.*, 2016, **55**, 5019–5023.

11 Z.-M. Zhang, T. Zhang, C. Wang, Z. Lin, L.-S. Long and W. Lin, *J. Am. Chem. Soc.*, 2015, **137**, 3197–3200.

12 H. Noh, C.-W. Kung, T. Islamoglu, A. W. Peters, Y. Liao, P. Li, S. J. Garibay, X. Zhang, M. R. DeStefano, J. T. Hupp and O. K. Farha, *Chem. Mater.*, 2018, **30**, 2193–2197.

13 L. J. Wang, H. Deng, H. Furukawa, F. Gándara, K. E. Cordova, D. Peri and O. M. Yaghi, *Inorg. Chem.*, 2014, **53**, 5881–5883.

14 J. Bitzer and W. Kleist, *Chem. – A Eur. J.*, 2019, **25**, 1866–1882.

15 M. Bosch, S. Yuan, W. Rutledge and H.-C. Zhou, *Acc. Chem. Res.*, 2017, **50**, 857–865.

16 C. K. Brozek and M. Dincă, *Chem. Sci.*, 2012, **3**, 2110.

17 J. A. Botas, G. Calleja, M. Sánchez-Sánchez and M. G. Orcajo, *Langmuir*, 2010, **26**, 5300–5303.

18 N. Zhu, G. Tobin and W. Schmitt, *Chem. Commun.*, 2012, **48**, 3638–3640.

19 J. R. Galán-Mascarós, *ChemElectroChem*, 2015, **2**, 172–172.

20 C. A. Hunter and J. K. M. Sanders, *J. Am. Chem. Soc.*, 1990, **112**, 5525–5534.

21 M. O. Sinnokrot and C. D. Sherrill, *J. Phys. Chem. A*, 2004, **108**, 10200–10207.

22 D. Dubbeldam, S. Calero, D. E. Ellis and R. Q. Snurr, *Mol. Simul.*, 2016, **42**, 81–101.

23 V. Otero, D. Sanches, C. Montagner, M. Vilarigues, L. Carlyle, J. A. Lopes and M. J. Melo, *J. Raman Spectrosc.*, 2014, **45**, 1197–1206.

24 E. Smith and G. Dent, *Modern Raman Spectroscopy - A Practical Approach*, John Wiley & Sons, Ltd, 2005.

25 B. H. Stuart, *Infrared Spectroscopy: Fundamentals and Applications*, John Wiley & Sons, Ltd, 2005.

26 K. Nakamoto, *Infrared and Raman Spectra of Inorganic and Coordination Compounds*, John Wiley & Sons, Ltd, 6th Edn., 2008.

27 G. B. Deacon and R. J. Phillips, *Coord. Chem. Rev.*, 1980, **33**, 227–250.

28 D. C. Harris and M. D. Bertolucci, *Symmetry and Spectroscopy: An introduction to vibrational and electronic spectroscopy*, Oxford University Press, Inc., 1978.

29 F. A. Cotton, *Chemical Applications of Group Theory*, John Wiley & Sons, Inc, 3rd Edn., 1990.

30 R. T. Pflaum and A. I. Popov, *Anal. Chim. Acta*, 1955, **13**, 165–171.

31 F. L. Cooper, *Astrophys. J.*, 1910, **31**, 339.

32 E. L. Simmons, *Opt. Acta Int. J. Opt.*, 1972, **19**, 845–851.

33 C. Yu, Y. Wang, J. Zhang, X. Shu, J. Cui, Y. Qin, H. Zheng, J. Liu, Y. Zhang and Y. Wu, *New J. Chem.*, 2016, **40**, 6881–6889.

34 J. F. Moulder, W. F. Stickle, P. E. Sobol and K. D. Bomben, *Handbook of X-ray Photoelectron Spectroscopy*, Physical Electronics, Inc., 1995.

35 M. C. Biesinger, B. P. Payne, A. P. Grosvenor, L. W. M. Lau, A. R. Gerson and R. S. C. Smart, *Appl. Surf. Sci.*, 2011, **257**, 2717–2730.

36 G. Horvath and K. Kawazoe, *J. Chem. Eng. Japan*, 1983, **16**, 470–475.

37 E. V. J. and B. Å. Markus D. Kärkäs, Tanja M. Laine, in *Applied Photosynthesis*, Intech open, 2016, 189–219.

38 M. C. Biesinger, L. W. M. Lau, A. R. Gerson and R. S. C. Smart, *Appl. Surf. Sci.*, 2010, **257**, 887–898.

39 S. B. A. Hamid, S. J. Teh and C. W. Lai, *Catalysts*, 2017, **7**, 93.

40 P. R. Deshmukh, Y. Sohn and W. G. Shin, *J. Alloys Compd.*, 2017, **711**, 573–580.

41 B. Limburg, E. Bouwman and S. Bonnet, *ACS Catal.*, 2016, **6**, 5273–5284.

42 M. D. Kärkäs, T. M. Laine, E. V. Johnston and B. Akermark, in *Applied Photosynthesis - New Progress*, InTech, 2016, vol. 306, 129–132.

43 Y. Wang, L. Zhang, K. Cui, C. Xu, H. Li, H. Liu and J. Yu, *Nanoscale*, 2018, **10**, 3421–3428.

44 J. Ren, M. Ledwaba, N. M. Musyoka, H. W. Langmi, M. Mathe, S. Liao and W. Pang, *Coord. Chem. Rev.*, 2017, **349**, 169–197.

45 L. Liu, Z. Chen, J. Wang, D. Zhang, Y. Zhu, S. Ling, K.-W. Huang, Y. Belmabkhout, K. Adil, Y. Zhang, B. Slater, M. Eddaoudi and Y. Han, *Nat. Chem.*, 2019, **11**, 622–628.

Chapter 5

An extended tritopic carboxylate ligand for the generation of mesoporous MOFs

5 An extended tritopic carboxylate ligand for the generation of mesoporous MOFs

5.1 Introduction

Continuing on from the work discussed in chapters 4 and 5, it was decided to design and synthesise an extended ligand with a similar structure to **H_3L2** and to use this to synthesise novel MOFs. It was decided to continue using carboxylate functional groups due to their possibility of bidentate binding which allows them to act as bridges between metal atoms assisting in the generation of polynuclear SBUs.

The ligand 5,5'-((5'-(4-((4-carboxyphenyl)ethynyl)phenyl)-[1,1':3',1''-terphenyl]-4,4''-diyl)-bis(ethyne-2,1-diyl))benzoic acid, (**H_3L3**) was chosen for its extended tritopic nature and its rigidity (**Scheme 5.2.1**). It is characterised by distances of 14.5 Å from the centroid position in the central phenyl ring of the ligand to the outermost carboxylate oxygens, and a carboxylate oxygen-carboxylate oxygen distance of between 23.1 and 26.1 Å. According to the literature **H_3L3** was first used in work published in 2012 as a fluorophore for the selective detection of Cu^{2+} in aqueous media.[1] In 2015 another paper was published showing **H_3L3** in a series of "highly stable isoreticular lanthanide metal-organic frameworks".[2] These compounds were denoted as SUMOF-7IV and two MOFs containing **H_3L3** were synthesised with La(III) and Eu(III). The researchers were, however, unable to grow single crystals suitable for X-ray diffraction studies. In this chapter the synthesis and characterisation of a novel zinc based 3D framework synthesised using **H_3L3** will be outlined. The structure and its gas sorption properties will be discussed.

5.2 Synthesis and characterisation of 5,5'-((5'-(4-((4-carboxyphenyl) ethynyl)phenyl)-[1,1':3',1''-terphenyl]-4,4''-diyl)-bis(ethyne-2,1-diyl)) benzoic acid, (**H_3L3**)

The ligand discussed in this chapter 5,5'-((5'-(4-((4-carboxyphenyl)ethynyl)phenyl)-[1,1':3',1''-terphenyl]-4,4''-diyl)-bis(ethyne-2,1-diyl))benzoic acid, (**H_3L3**) was synthesised using a modified literature procedure (**Scheme 5.2.1**).[3] In step one a cyclisation reaction involving 4-bromoacetophenone was carried out.[4] For this purpose, the 4-bromoacetophenone was dissolved in ethanol at 0°C and $SiCl_4$ was added dropwise to the solution. The mixture was refluxed at 80°C for 24 hours (turning from red to yellow). After cooling to room temperature a saturated aqueous NH_4Cl solution was added to the mixture and stirred for 30 minutes. The precipitate was filtered off and washed with ethanol. The precipitate was washed with DCM and the pale yellow filtrate was collected. The filtrate was concentrated on a rotary evaporator, precipitating white crystals which were filtered off and washed with Ethanol and cold DCM yielding pure 1,3,5-tris(4-bromophenyl)benzene. Step two involves a Sonogashira coupling reaction.[5] 1,3,5-Tris(4-bromophenyl)benzene was dissolved with ethynyltrimethylsilane in a THF:TEA mixture. $Pd^{II}(PPh_3)_2Cl_2$ and CuI catalysts were added and the mixture was heated to 50°C for 16 hours under N_2. The solvent was removed under vacuum, the crude product dissolved in DCM and washed 3 times with an NH_3 aqueous solution. A silica column was run with DCM yielding pure 1,3,5-tris(4-(ethynyltrimethylsilane)phenyl)benzene. The third step concerns the removal of the silyl groups. This was done by dissolving the 1,3,5-tris(4-(ethynyltrimethylsilane)phenyl)benzene in DCM and mixing it at 35°C for 4 hours with a concentrated K_2CO_3-MeOH solution. The solvent was removed under vacuum and the crude product was purified using a silica column with a hexane:DCM (2:1) mobile phase yielding 1,3,5-tris(4-(ethynyl)phenyl)benzene. A second Sonogashira coupling reaction was carried out in step four and combined 1,3,5-tris(4-(ethynyl)phenyl)benzene with ethyl 4-iodobenzoate by refluxing the reaction mixture at 110°C for 5 days. This was purified by washing the crude compound as in step 2 and then running a silica column with hexane:THF (1:1) to yield pure Trimethyl-4,4',4''-(benzene-1,3,5-triyltris(ethyne-2,1-diyl))tribenzoate. The fifth and final step involves a base catalysed ester deprotection using excess LiOH. This was carried out over 3 hours at room temperature. The THF was removed under vacuum

leaving a solution in H_2O. The reaction mixture was acidified using a 1 M HCl solution precipitating 5,5'-((5'-(4-((4-carboxyphenyl)ethynyl)phenyl)-[1,1':3',1''-terphenyl]-4,4''-diyl)-bis(ethyne-2,1-diyl))benzoic acid, **H_3L3**. This was washed with deionised H_2O and cold THF to yield pure product.

A combination of ^{1}H-NMR, ^{13}C-NMR, mass spectrometry and FT-IR spectroscopy confirmed the formation of **H_3L3**. ^{1}H-NMR spectroscopy in deuterated dimethyl sulfoxide reveals a singlet signal at 8.06 ppm with an integration corresponding to 3 H-atoms in relation to those found on the central phenyl ring. Four doublet signals found at 8.03, 7.99, 7.73, 7.70 ppm all of which integrate to 6 H-atoms can be attributed to the 24 H-atoms in the remaining phenyl rings. The acidic carboxylate H-atoms were not identifiable due to fast exchange.

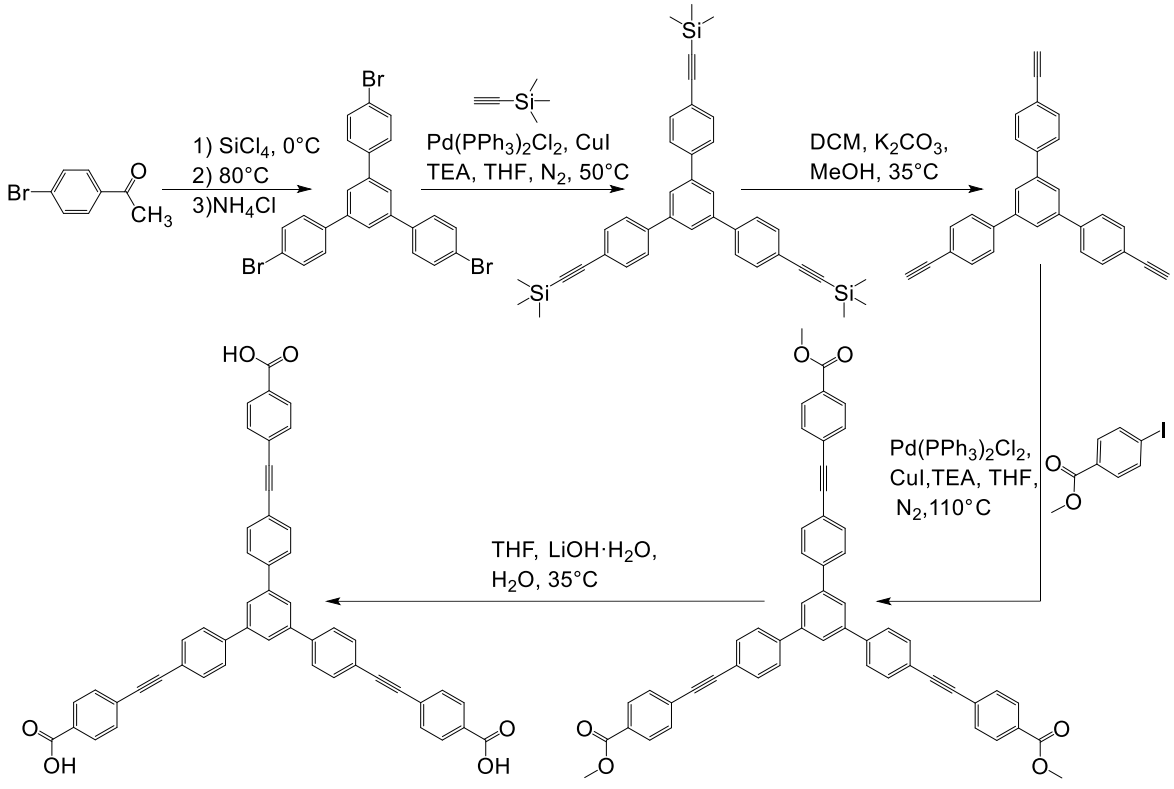

Scheme 5.2.1: Synthetic procedure used for the synthesis of **H_3L3**.

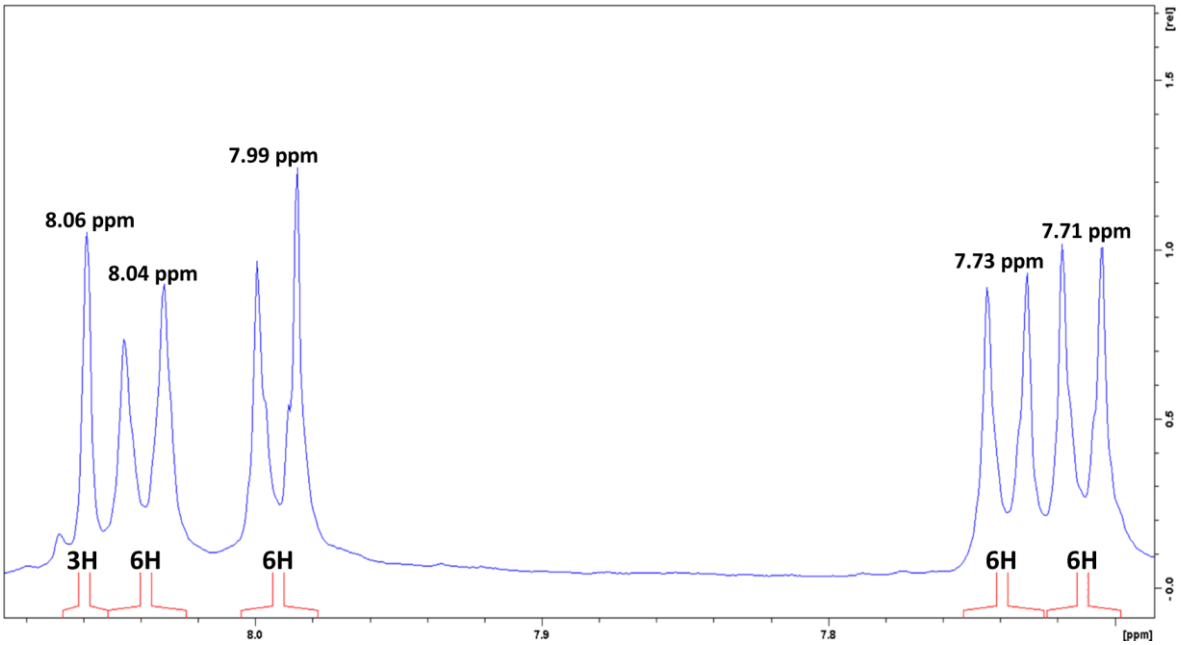

Figure 5.2.1: ^{1}H-NMR spectrum of **H_3L3** in DMSO-d_6.

5.3 $[Zn_4(\mu_4\text{-}O)(\mathbf{L3})_2]$ (**6**)

5.3.1 Synthesis and structural characterisation of $Zn_4(\mu_4\text{-}O)(\mathbf{L3})_2$ (**6**)

$[Zn_4(\mu_4\text{-}O)(\mathbf{L3})_2]$ (**6**) was synthesised by heating $Zn(NO_3)_2{\cdot}6H_2O$ and **H_3L3** (molar ratio of 1:1) in DMF at 100°C for 72 hours. Colourless square-prism crystals of **6** were obtained and characterised using single crystal XRD. **6** crystallises in the orthorhombic space group *P*mna and was found to have a molecular formula of $[Zn_4(\mu_4\text{-}O)(\mathbf{L3})_2]$.

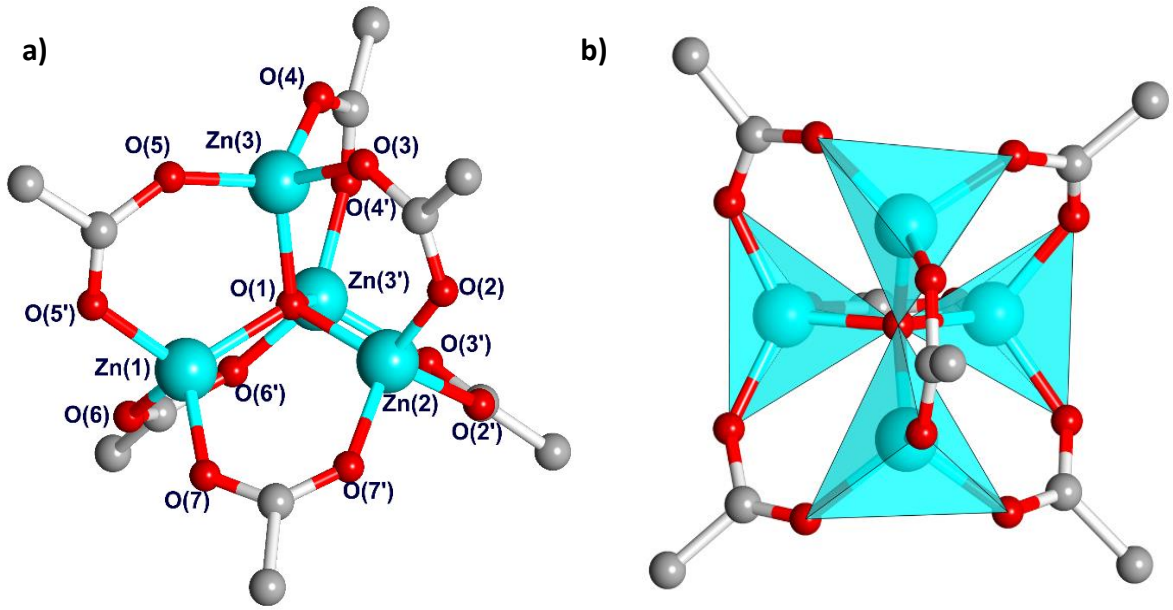

Figure 5.3.1: a), b) The $\{Zn_4O\}$ SBU stabilised by six carboxylate ligands. Colour key: Zn (turquoise), O (red), C (grey), H (white).

The asymmetric unit of **6** contains three crystallographically independent zinc atoms and two partially complete ligands. A forth Zn atom is generated by symmetry forming the well know $\{Zn_4O\}$ SBU.[6,7] The Zn^{II} atoms are tetrahedrally coordinated and are further arranged in a tetrahedral orientation around a central oxygen atom μ_4-O(1) (**Figure 5.3.1**). The Zn-O(1)-Zn angles vary between 109.48° and 110.03° and the O-Zn-O angles vary from 101.37° to 124.68°. Thus, the Zn-O(1)-Zn angles are close to the ideal tetrahedral value of 109.5°.

Each Zn atom is connected to the other three Zn^{II} atoms *via* syn, syn bidentate bridging carboxylate functionalities from each of the coordinating ligands (**$L3^{3-}$**). Six ligands are connected to each $\{Zn_4O\}$ SBU adopting a distorted octahedral orientation with angles

between *trans* located ligand carboxylate C-atoms and the central μ_4-O(1) varying from the ideal 180° angle to between 169.00° and 173.45° (**Figure 5.3.2**).

The carboxylate Zn-O bond lengths vary between 1.883(4) Å and 1.978(3) Å. These are typical lengths for bonds between carboxylate O-donors and Zn^{II} ions and are consistent with distances expected for this type of bonding. This SBU is one of the most well-known for Zn MOFs and has been used to synthesise a wide range of MOFs.[6,8–11]

Each SBU is connected to 10 additional {Zn_4O} SBUs *via* the six coordinating **L3^{3-}** ligands. Two symmetry equivalent nets are found in **6.** Thus the structure is two-fold interwoven whereby stabilising π-π interactions prevail between ligands of adjacent nets (**Figure 5.3.2**). The two edge to face π interactions have a distance of ca. 2.8 Å from the centre of the edge carbon atom to the centre of the adjacent phenyl ring. The parallel displaced π-π interaction has a distance of 4.1 Å. These are within the expected distances for these types of interactions.[12] π-π stacking interactions are known to add stability to the overall frameworks.[13]

Table 5.3.1: Selected bond distances and angles for the coordination environments found in **6**.

Atoms	Distance [Å] / Angle [°]	Atoms	Distance [Å] / Angle [°]
Zn(1)-O(1)	**1.922(3)**	O(1)-Zn(1)-O(6)	**115.89(10)**
Zn(2)-O(1)	**1.937(2)**	O(1)-Zn(1)-O(7)	**112.27(12)**
Zn(3)-O(1)	**1.9598(13)**	O(6)-Zn(1)-O(6)	**102.31(16)**
Zn(1)-O(6)	**1.945(2)**	O(6)-Zn(1)-O(7)	**104.55(10)**
Zn(1)-O(7)	**1.978(3)**	O(1)-Zn(2)-O(2)	**115.52(8)**
Zn(2)-O(2)	**1.922(2)**	O(1)-Zn(2)-O(8)	**110.94(13)**
Zn(2)-O(8)	**1.943(3)**	O(2)-Zn(2)-O(2)	**106.16(15)**
Zn(3)-O(3)	**1.977(3)**	O(2)-Zn(2)-O(8)	**103.71(10)**
Zn(3)-O(4)	**1.902(3)**	O(1)-Zn(3)-O(3)	**107.65(10)**
Zn(3)-O(5)	**1.883(4)**	O(1)-Zn(3)-O(4)	**111.66(12)**
		O(1)-Zn(3)-O(5)	**106.05(13)**
Zn(1)-O(1)-Zn(2)	**109.91(10)**	O(3)-Zn(3)-O(4)	**101.37(13)**
Zn(1)-O(1)-Zn(3)	**110.03(8)**	O(3)-Zn(3)-O(5)	**104.02(13)**
Zn(2)-O(1)-Zn(3)	**109.48(8)**	O(4)-Zn(3)-O(5)	**124.68(18)**

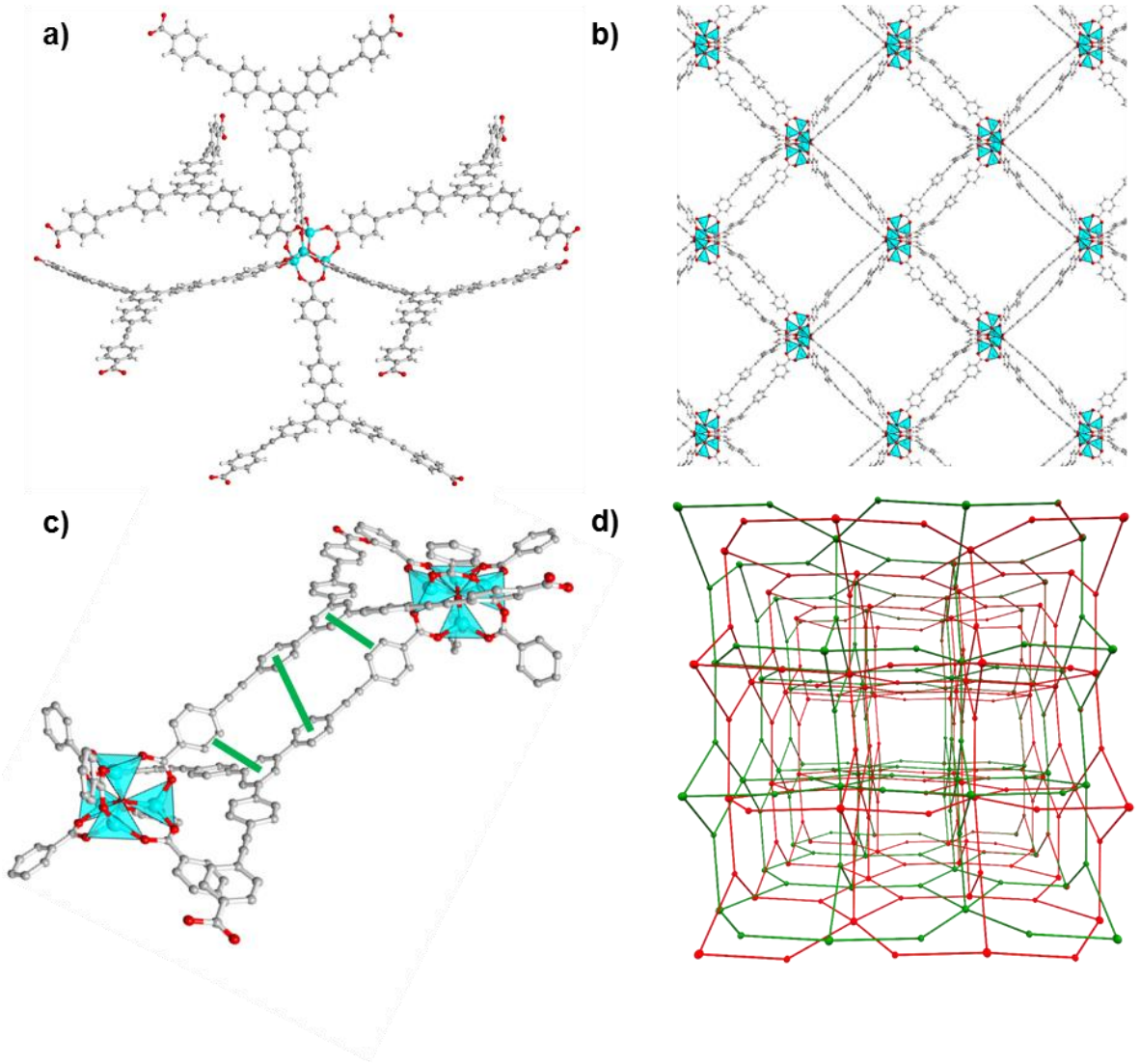

Figure 5.3.2: a) The $\{Zn_4O\}$ SBU showing all six ligands bound, **b)** View of **6** in the direction of the crystallographic *a*-axis, **c)** Structure showing two adjacent ligands from different nets highlighting the π-π interactions between them using green lines (H atoms are omitted for clarity). **a)**, **b)**, **c)** Colour key: Zn (turquoise), O (red), C (grey), H (white). **d)** Topological representation of **6** with view in the direction of the crystallographic *a*-axis showing both interpenetrated ***rtl*** nets in red and green. The six-coordinate nodes represent the $\{Zn_4O\}$ SBU and the three coordinate nodes represent the ligand ($\mathbf{L3^{3-}}$).

The topology of **6** was analysed using the TOPOSPRO software package v5.3.2.1 and a simplified representation was constructed (**Figure 5.3.2**, **d)**).[14] The trifunctional, triangular extended ligand gives rise to a neutral 3,6-connected {Zn_4O}-based structure with a **rtl** net.[15] The **rtl** net is related to the highly symmetric rutile structure of TiO_2.[16] This combination of triangles and octahedral building units could potentially give rise to three different net types which are affiliated to the distortion experienced at the octahedral node. These are, from most distorted to least distorted, **qom**, **pyr** and **rtl** nets.

When looking at other MOFs formed from the {Zn_4O} SBU and other triangular ligands, the **qom** net type appears to be favoured despite containing the most distorted octahedral SBU of all three nets. This often occurs for short ligands due to restrictions in the rotation of their peripheral phenyl rings. Surprisingly there are relatively few **rtl** nets known for MOFs compared to **pyr** and **qom** nets despite it being the most symmetric and therefore the most favoured topology.[7] The length of $\mathbf{L3^{3-}}$ means that the ligand is capable of additional bending compared to shorted tripodal ligands and this, combined with the fact that the alkyne bonds allow the free rotation of the terminal phenyl rings containing the carboxylate groups used for binding to the {Zn_4O} SBU, results in the formation of highly symmetric {Zn_4O} SBUs favouring the formation of an **rtl** net.

The void space was calculated using the RASPA software package and it was found to account for 87.9% of the unit cell volume of the crystal structure.[17] The void volume is filled by solvent molecules. The largest channels running through the structure have cross sectional diameters of 20 Å and extend parallel to the crystallographic *a*-axis (**Figure 5.3.3**, **a)** and **c)**). The use of the elongated ligand $\mathbf{L3^{3-}}$ results in these being significantly larger than the equivalent channel diameter of 9 Å in MOF-156-J.[7] Two smaller types of channels can also be found in the structure of **6**. These can be seen along the [111] and [011] directions and have diameters of *ca.* 11 Å and 13 Å, respectively (**Figure 5.3.3**, **b)** and **d)**).

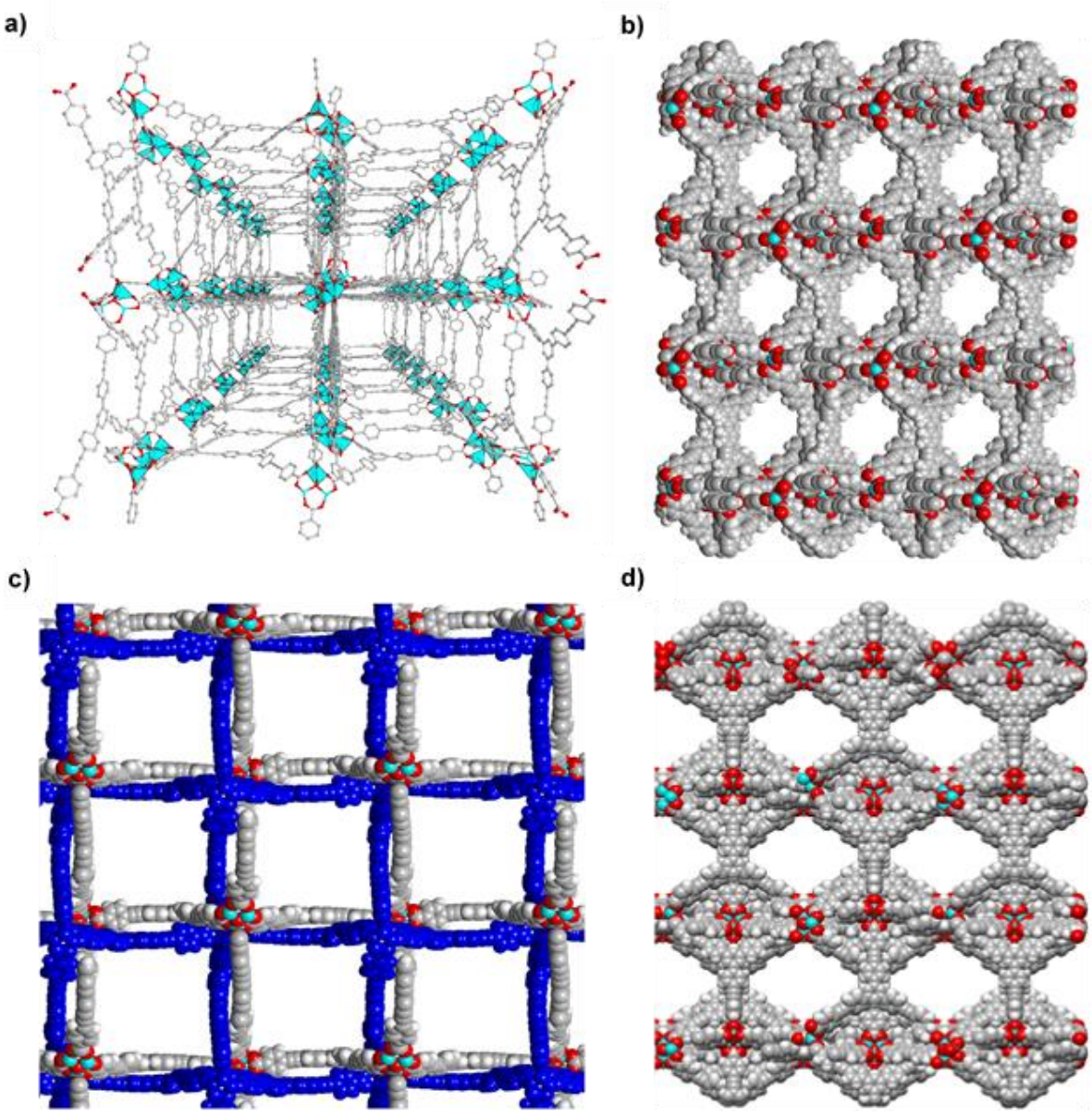

Figure 5.3.3: a) Ball and stick model showing a perspective view of **6** in the direction of the crystallographic *a*-axis. **b), c)** and **d)** Space filling models. **b)** View down the [111] direction **c)** View in direction of the crystallographic *a*-axis with one net highlighted in blue to highlight the interwoven structure of **6**. **d)** View in the [011] direction.

Table 5.3.2: Crystallographic details for compound **6**.

Identification code	**6**
Empirical formula	$C_{102}H_{54}O_{13}Zn_4$
Formula weight	1748.93
Temperature/K	215(2)
Crystal system	orthorhombic
Space group	*P*mna
a/Å	28.3602(19)
b/Å	39.029(3)
c/Å	39.481(3)
α/°	90
β/°	90
γ/°	90
Volume/Å^3	43701(5)
Z	4
ρ_{calc}g/cm^3	0.266
μ/mm^{-1}	0.351
F(000)	3560.0
Crystal size/mm^3	0.36 × 0.36 × 0.28
Radiation	CuKα (λ = 1.54184)
2Θ range for data collection/°	3.184 to 105.276
Index ranges	-29 ≤ h ≤ 27, -39 ≤ k ≤ 40, -34 ≤ l ≤ 40
Reflections collected	168605
Independent reflections	25476 [R_{int} = 0.0563, R_{sigma} = 0.0442]
Data/restraints/parameters	25476/15/551
Goodness-of-fit on F^2	1.063
Final R indexes [I>=2σ (I)]	R_1 = 0.0711, wR_2 = 0.2225
Final R indexes [all data]	R_1 = 0.0942, wR_2 = 0.2377
Largest diff. peak/hole / e Å^{-3}	0.68/-0.53

5.3.2 Physicochemical characterisation of **6**

5.3.2.1 X-ray powder diffraction

Crystals of **6** (**Figure 5.3.4**, ***inset***) were ground into a powder while kept in DMF to reduce the possibility of structure collapse and a PXRD pattern was measured using an APEX II DUO X-ray diffractometer to characterise the phase-purity of the synthesised material (**Figure 5.3.4**). The PXRD pattern was measured in a capillary to obtain low angle peaks and to avoid loss of crystallinity associated with solvent evaporation from the sample. The experimental pattern and a simulated PXRD pattern (based on the single crystal x-ray diffraction data) closely correspond confirming the crystalline phase purity of the synthesised material and in addition provide further evidence for the accuracy of the refined crystal structure. The pattern is characterised by a prominent diffraction peak at 3.23° in the measured and 3.18° in the simulated pattern. A weak peak is visible at 3.88° and 3.84° in the measured and calculated patterns, respectively. A third peak is seen at 4.53° in the measured and 4.45° in the simulated pattern. The next set of peaks in the measured pattern are at 5.95°, 6.34°, 7.09°, 7.42° and 7.72°. The first of these is clearly resolved in the simulated pattern at 5.91°. The second of these is split into two peaks at 6.23° and 6.34° in the simulated pattern. The two measured peaks are seen in the simulated pattern at 7.08° and 7.40°. The analysis suggests that the compound is phase-pure.

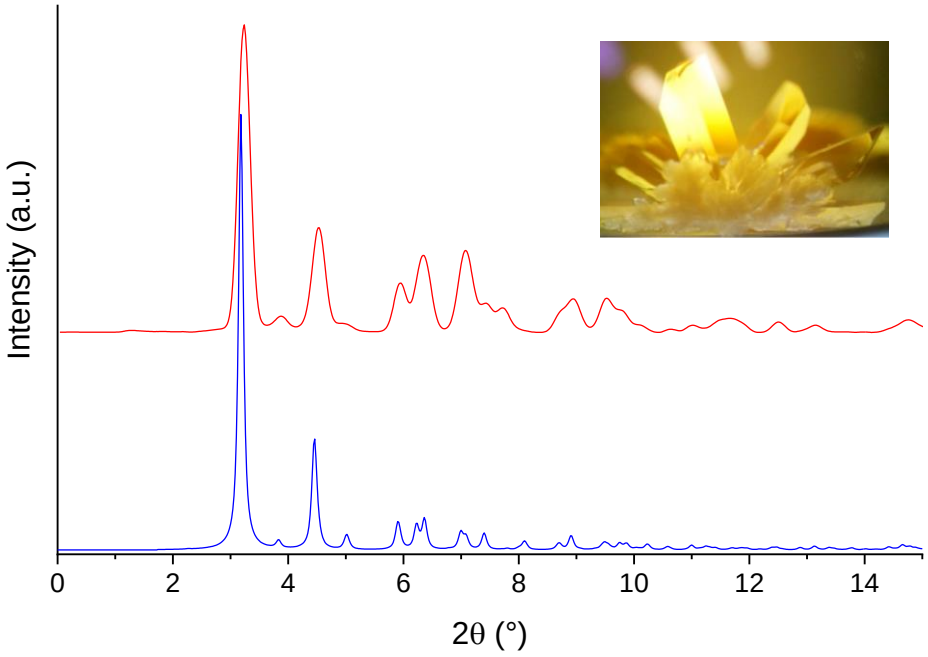

Figure 5.3.4: PXRD pattern of **6**, with the measured pattern in red and the calculated in blue. *Inset:* Image of the crystals of **6**.

5.3.2.2 Energy dispersive X-ray spectroscopy

Crystals of **6** in DMF were drop casted onto an aluminium SEM stub mount, dried in air for 24 hours and analysed using energy-dispersive X-ray spectroscopy (EDX) (**Table 5.3.3**). The EDX analysis was carried out using a 20 mm^2 Oxford Inca detector. All the elements seen in the crystal structure (C, O, Zn) were found and closely match with the expected values which were calculated based on the X-ray crystal structure data.

Table 5.3.3: Expected and observed atomic ratios by EDX.

Element	C	O	Zn
Expected Atomic %	78.7	18.9	2.4
Observed Atomic %	76.6	21.1	2.4

5.3.2.3 Raman and FT-IR spectroscopy

The Raman spectra of **6** is dominated by stretches derived from $\mathbf{L3^{3-}}$, further confirming the presence of the ligand in the MOF (**Figure 5.3.5**). There are three prominent signals in both spectra. The first is actually composed of two signals visible in **6** at 1135 and 1152 cm^{-1} and derive from C-C single bonds. These can be seen in the spectrum of $\mathbf{H_3L3}$ at 1129 and 1145 cm^{-1}, respectively. In **6** the most intense signal corresponds to the aromatic C=C stretch at 1606 cm^{-1} and in $\mathbf{H_3L3}$ this can be seen at 1605 cm^{-1}. The third of these signals is found at 2221 cm^{-1} and derives from the alkyne C≡C band in **6** and this shifts very slightly to 2220 cm^{-1} in $\mathbf{H_3L3}$. These strong signals match with the barely visible stretches in the FT-IR spectra of **6** and $\mathbf{H_3L3}$ further confirming the assignment as being correct.[18]

The FT-IR of **6** is characterised by signals which arise primarily from the organic ligand $\mathbf{L3^{3-}}$ (**Figure 5.3.6**). Analysis indicates that the weak vibration visible at 2214 cm^{-1} in **6** and 2209 cm^{-1} in $\mathbf{H_3L3}$ corresponds to the symmetric C≡C stretch. The signal at 1599 cm^{-1} in **6** and 1597 cm^{-1} in $\mathbf{H_3L3}$ comes from C=C stretching in phenyl rings. Below this in the spectrum of **6** the asymmetric stretch of the carboxylate COO^- is visible at 1558 cm^{-1} while the symmetric stretching is visible at 1420 cm^{-1}**.** The prominent band at 768 cm^{-1} in **6** and 777 cm^{-1} in $\mathbf{H_3L3}$ corresponds to C-H out of plane bending on the phenyl rings. Several bands can be seen in **6** that do not appear in $\mathbf{H_3L3}$. The most notable of these at can be seen at 1687 cm^{-1} which along with the broad signal at *ca.* 2990 cm^{-1} corresponds to DMF solvent molecules within the pores of the crystals of **6**.[19,20]

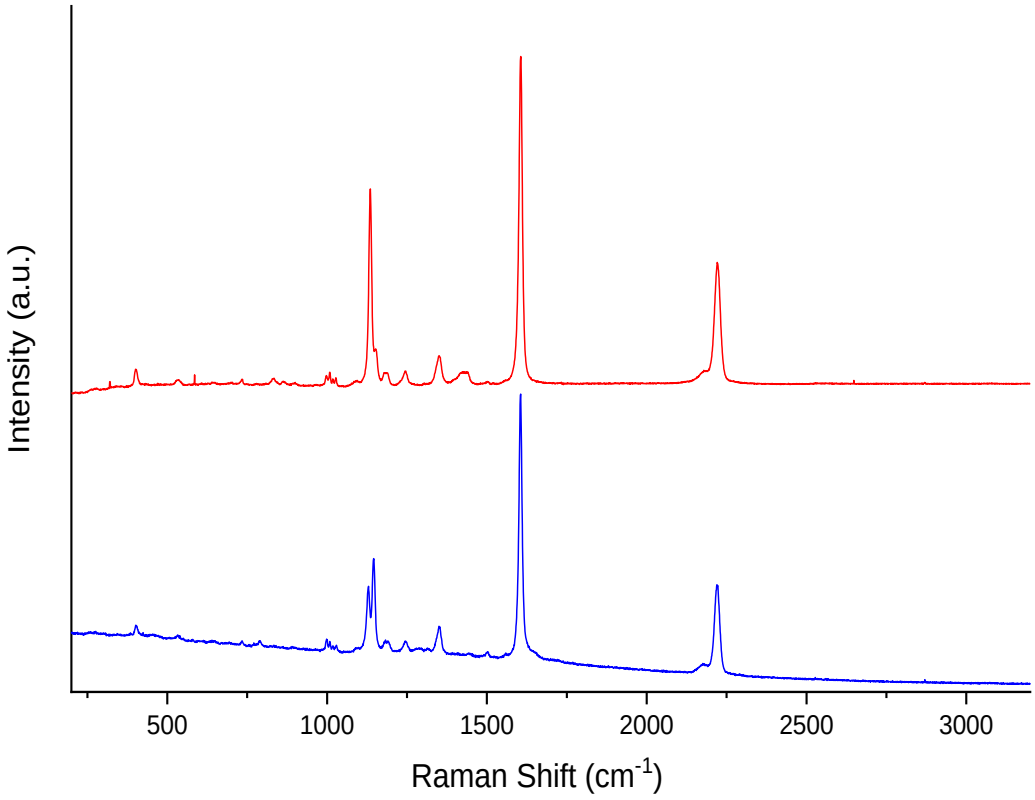

Figure 5.3.5: Raman spectrum of **6** (red) and **H_3L3** (blue).

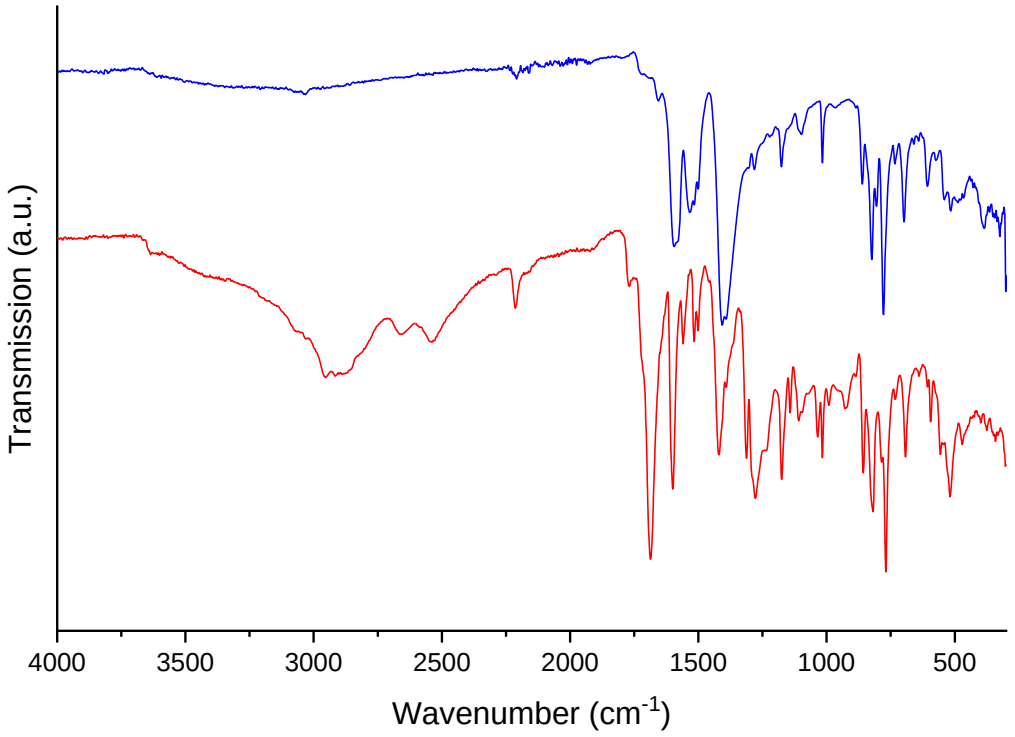

Figure 5.3.6: FT-IR spectrum of **6** (red) and **H_3L3** (blue).

5.3.3 Thermogravimetric and gas sorption characterisation of **6**

5.3.3.1 Thermogravimetric analysis

Thermogravimetric analysis (TGA) of **6** was performed in an N_2 atmosphere at a heating rate of 3°C per minute (**Figure 5.3.7**). The sample was initially removed from solvent and placed on filter paper to remove excess solvent outside the crystals. The crystals were then lifted onto the TGA crucible and the heating was applied. A weight loss of *ca.* 64% between 25 and 200°C was attributed to constitutional H_2O and DMF solvent molecules in the pores of **6**. This quantity of solvent could be expected given that the crystal structure contains a solvent accessible void volume of 87.9%. There is a steep drop in weight as soon as the measurement starts showing that even at temperatures from 25°C solvent is leaving the pores of the sample. Between 200 and 354°C there is almost no change in sample weight. There is a further weight loss of *ca.* 15% between 370 and 600°C showing the decomposition of the ligand.

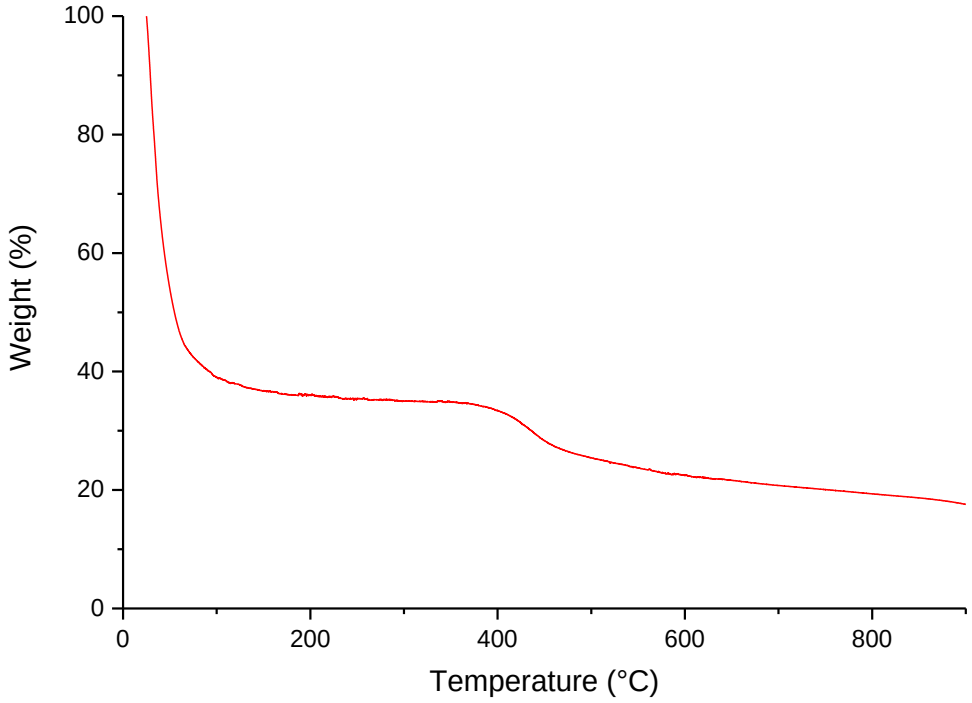

Figure 5.3.7: TGA of compound **6**.

5.3.3.2 Gas sorption experiments

Prior to conducting gas sorption experiments on **6** it was necessary to exchange the solvent. The DMF solvent of the reaction mixture was initially replaced by fresh DMF to remove unreacted materials. The DMF was then exchanged with $CHCl_3$ and left for three days, refreshing the solution once per day, followed by an exchange with decafluoropentane. This follows an established literature procedure.[21] The crystals were then transferred into a quartz measurement cell and the sample was activated by heating under vacuum at 25°C for 1 hour. A PXRD pattern of **6** was recorded after the activation of the sample (**Figure 5.3.8**). The measurement was performed on the dry activated material in a capillary on an APEX II DUO X-ray diffractometer to obtain low angle signals and provide a comparison to the pattern of the pristine sample of **6**. The measurement indicates that the materials undergoes some ordered structural changes during the activation process. However, the data also indicates that the crystalline 3D order of the material is maintained. Analysis shows that some signals at lower angles shifted slightly. The first and most prominent peak appears to have shifted from 3.23 to 3.61° indicating a change has occurred in relation to the size of the unit cell. Most of the remaining peaks appear to have also moved position.

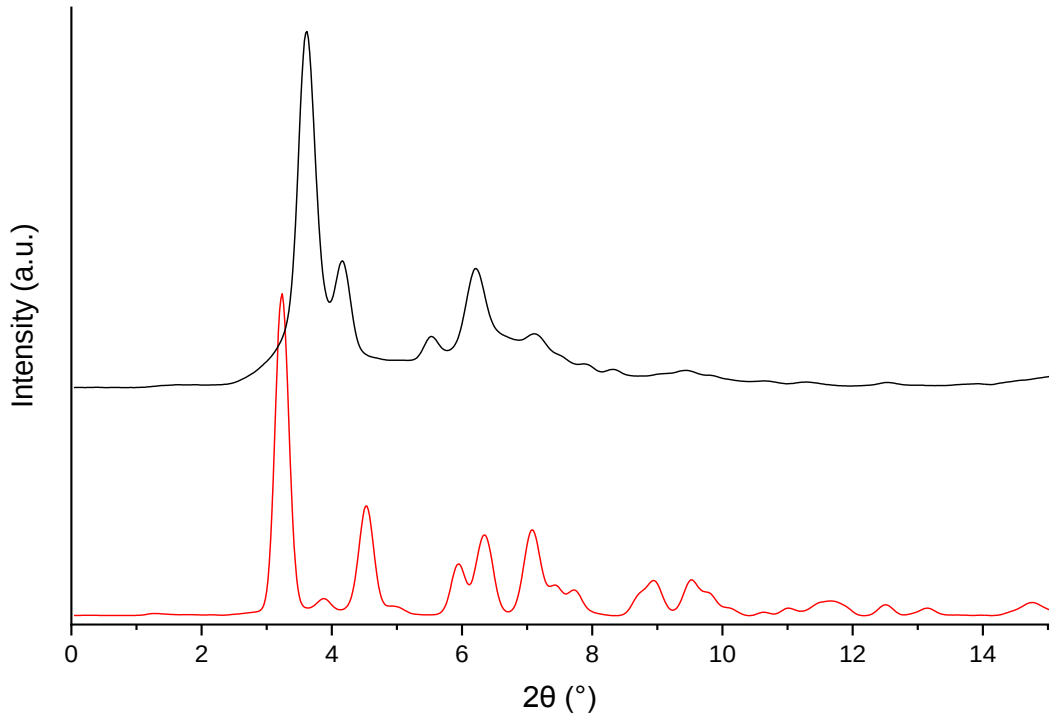

Figure 5.3.8: PXRD patterns of **6**, with the measured pattern before activation (red) and **6** after activation (black).

Based on similar structures in the literature[11,22–25] it was expected that **6** would give rise to a large surface area. The N_2 gas sorption shows a reversible type IV(b) isotherm[26] at 77 K (**Figure 5.3.9**) with a steep gas uptake at low partial pressures which corresponds to N_2 condensation in the accessible micropores in **6**. This is followed by condensation of N_2 into the accessible mesopores which is observed between 0.05 and 0.125 P/P_0. A maximum uptake of 983 cm^3/g of N_2 at 731 Torr was obtained, which corresponds to 1229 mg/g.

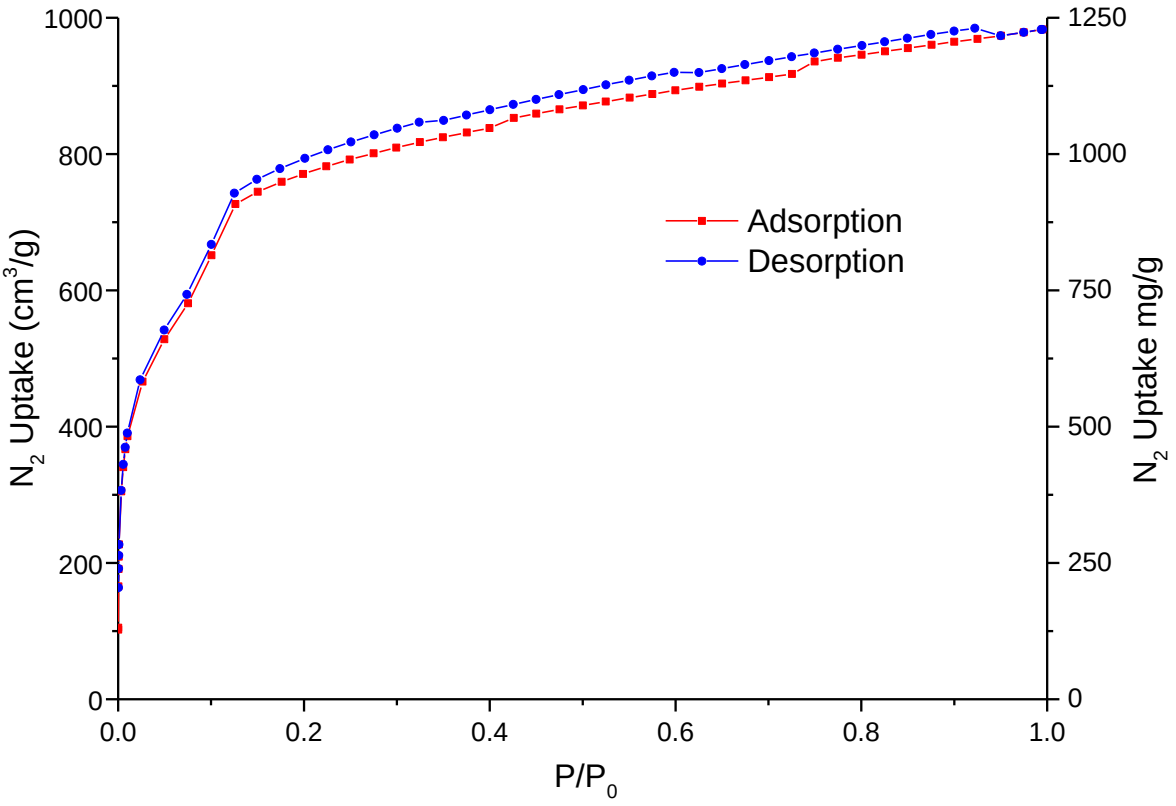

Figure 5.3.9: N_2 sorption isotherm of **6** measured at 77K.

The BET surface area derived from this isotherm gives a value of 3028 m^2/g (**Figure 5.3.10**). The points chosen for the BET calculation were selected according to the Rouquerol criteria.[27] The determined surface area renders **6**, as one of the materials with the highest reported surface areas. However, it appears lower than the crystal structure would indicate. This may be attributable to the structural changes upon activation.

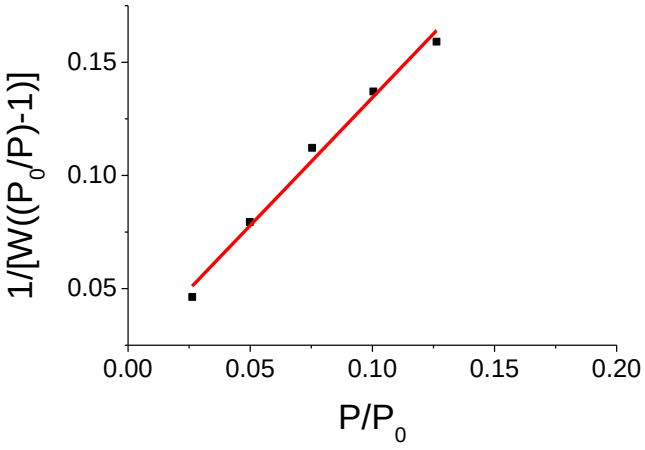

Figure 5.3.10: Plot of the linear region used to obtain the BET surface area of **6** and table of BET values obtained from the Plot.

Table 5.3.4: BET values obtained from the BET plot (**Figure 5.3.10**).

Slope	1.129
Intercept	0.02148
r (correlation coefficient)	0.994561
C constant	53.546
BET Surface Area (m^2/g)	3028

The pore size distribution of **6** was calculated from the N_2 isotherm using the Quantachrome AsiQwin software NLDFT using a cylindrical pore model with N_2 at 77 K as the adsorbate and carbon as the adsorbent (**Figure 5.3.11**, **red**).[28] This results in a distribution of pore sizes ranging from *ca.* 17 to 26 Å. The theoretical pore size distribution (PSD) was calculated following the method of Gelb and Gubbins,[29] in which the largest diameter spheres which may be successfully inserted into the structure without overlap with any of the framework atoms are recorded. This pore-size distribution gives well defined pores whose diameters range between *ca.* 19.7 to 21.0 Å (**Figure 5.3.11**, **black**).

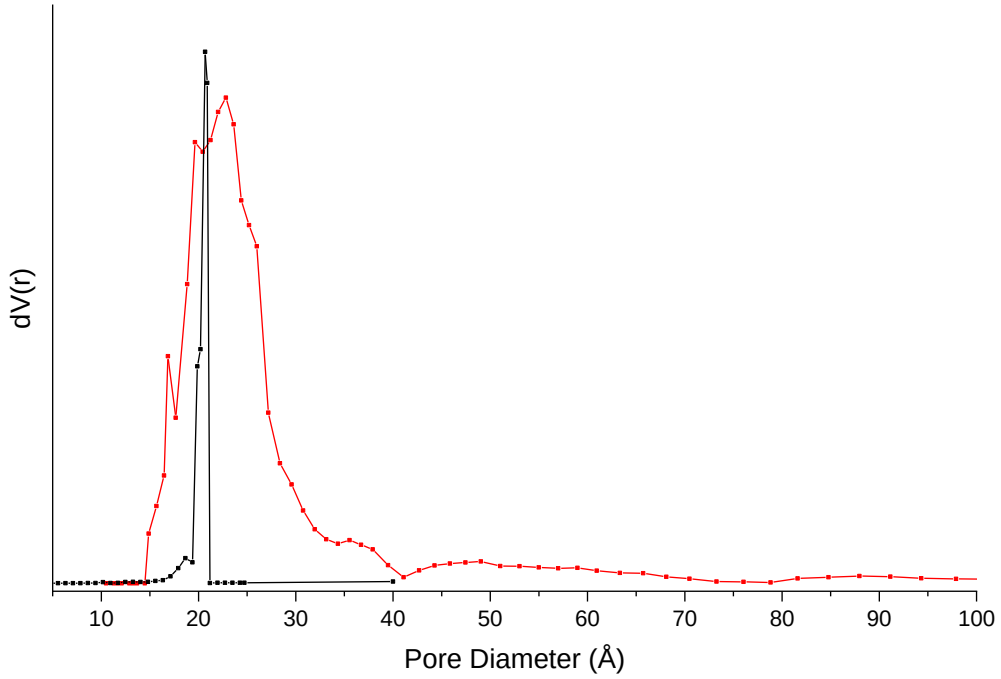

Figure 5.3.12: Pore size distribution plots of **6**. Calculated from the N_2 isotherm (red) and theoretical determination following the method of Gelb and Gubbins (black).

The H_2 gas sorption studies give rise to a reversible isotherm measured at 77 K (**Figure 5.3.12**). The MOF gives rise to an H_2 uptake of 332 cm^3/g at 756 Torr which corresponds to 2.9 wt%. This is notable when compared to literature values and is comparable to the uptake characteristics of HKUST-1, one of the best MOFs for low pressure H_2 sorption.[32] It should be noted that the density of this material is relatively low (0.266 g/cm^3) meaning that the volumetric uptake is 7.87 g/L which is less notable and would make this compound less advantageous when the volume of the storage container

is a consideration. The CO_2 gas sorption isotherm at 278 K shows an uptake of 140 cm^3/g at 754 Torr (**Figure 5.3.13**).

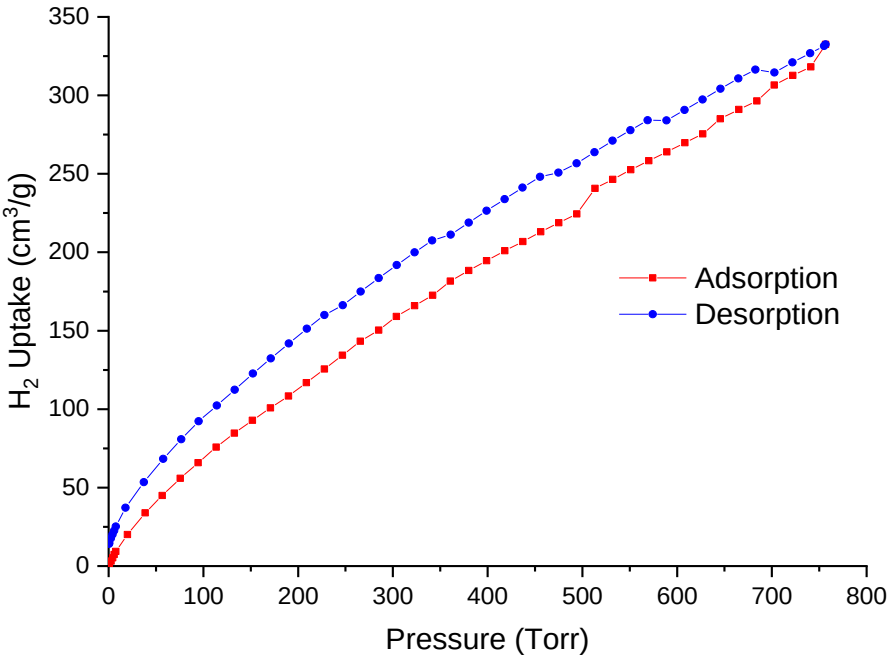

Figure 5.3.12: H_2 sorption isotherm of **6** measured at 77K.

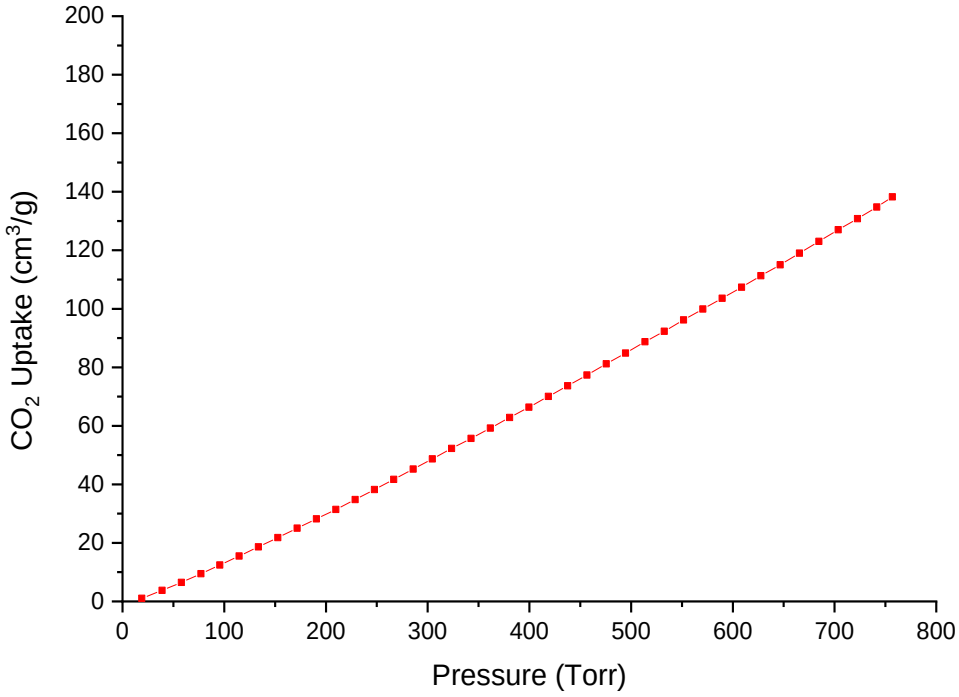

Figure 5.3.13: CO_2 isotherm of **6** measured at 278K.

5.4 Conclusion

The **H_3L3** ligand was chosen for a number of reasons. It provides an extended version of **H_3L2** thus it was envisaged to result in the synthesis of MOFs with increased pores-sizes and surface areas that can be advantageous for gas sorption and catalysis. The ligand was obtained in good yields involving a five step organic synthesis which consisted of one cyclisation reaction, two Sonogashira coupling reactions and two deprotection reactions.

A doubly interpenetrated Zn-based MOF was synthesised (**6**). It contains the well-established tetranuclear {Zn_4O}-based coordination clusters with octahedral topology that are linked by six **L3^{3-}** ligands. The **(6,3)** connectivity results in a rutile-based ***rtl*** net in which the Ti-atoms are formally replaced by the Zn-SBUs and the O-atoms by the trifunctional organic ligands. Thus the structure of **6** is significantly different to that of other MOFs that also employ the use of the octahedrally connected {Zn_4O} SBU linked by tripodal linkers such as MOF-177, MOF-180 and MOF-200 which all adopt the **qom** topology. The **qom** topology predominatly forms despite the fact that the **pyr** and **rtl** nets are theoretically favoured topologies and it occurs due to restrictions in the rotation of the peripheral phenyl rings in the ligands within these MOFs. There are relatively few examples of MOFs with either **pyr** or **rtl** topologies. Here we were able to overcome the rotational restrictions of the peripheral phenyl rings using the extended **L3^{3-}** ligands and provide one of the few examples of a MOF containing a **rtl** net.

6 adopts a two-fold interpenetrated structure in which the individual nets are interwoven; π-π stacking between the phenyl groups of the ligands adds stability to the overall framework structure. The compound is characterised by a solvent accessible void volume of 87.9% of the unit cell volume. The results of the thermogravimetric analysis are consistent with structural analysis and suggest that that the constitutional solvent molecules can be completely removed upon heating to *ca.* 200°C. **6** shows a moderately good thermal stability and undergoes ligand decomposition in N_2 at ca. 370°C.

The FT-IR and Raman spectra are consistent and are dominated by signals that result from the organic ligand vibrations. The EDX spectroscopy analysis fits closely with the theoretical expected values. The MOF retains a porous structure after desolvation and

activation but shows some ordered structural changes associated with the high void volume.

The MOF takes significant quantities of N_2 up. A steep N_2 uptake at 77 K at low partial pressures is observed. The structure reveals a type IV(b) isotherm giving rise to a BET surface area of *ca.* 3028 m^2/g, Noteworthy is the H_2 uptake of 332 cm^3/g at 756 Torr and 77 K which corresponds to 2.9 wt%. The pore size distribution reveals a broader than expected size distribution which may result from structural flexibility upon activation as demonstrated by XRD experiments after desolvation.

5.5 References

1 S. Sirilaksanapong, M. Sukwattanasinitt and P. Rashatasakhon, *Chem. Commun.*, 2012, **48**, 293–295.

2 Q. Yao, A. Bermejo Gómez, J. Su, V. Pascanu, Y. Yun, H. Zheng, H. Chen, L. Liu, H. N. Abdelhamid, B. Martín-Matute and X. Zou, *Chem. Mater.*, 2015, **27**, 5332–5339.

3 I. M. Hauptvogel, V. Bon, R. Grünker, I. a. Baburin, I. Senkovska, U. Mueller and S. Kaskel, *Dalt. Trans.*, 2012, **41**, 4172.

4 A. Zakaszewska, E. Najda-Mocarska and S. Makowiec, *New J. Chem.*, 2017, **41**, 2479–2489.

5 K. Sonogashira, *J. Organomet. Chem.*, 2002, **653**, 46–49.

6 H. Li, M. Eddaoudi, M. O'Keeffe and O. M. Yaghi, *Nature*, 1999, **402**, 276–279.

7 Y. B. Zhang, H. Furukawa, N. Ko, W. Nie, H. J. Park, S. Okajima, K. E. Cordova, H. Deng, J. Kim and O. M. Yaghi, *J. Am. Chem. Soc.*, 2015, **137**, 2641–2650.

8 H. Furukawa, K. E. Cordova, M. O'Keeffe and O. M. Yaghi, *Science*, 2013, **341**, 1230444.

9 N. Zhu, G. Tobin and W. Schmitt, *Chem. Commun.*, 2012, **48**, 3638–3640.

10 M. Eddaoudi, J. Kim, N. Rosi, D. Vodak, J. Wachter, M. O'Keeffe and O. M. Yaghi, *Science*, 2002, **295**, 469–472.

11 N. L. Rosi, *Science*, 2003, **300**, 1127–1129.

12 C. A. Hunter and J. K. M. Sanders, *J. Am. Chem. Soc.*, 1990, **112**, 5525–5534.

13 L. R. MacGillivray and C. M. Lukechart, *Metal-Organic Framework Materials*, 2014.

14 V. A. Blatov, A. P. Shevchenko and D. M. Proserpio, *Cryst. Growth Des.*, 2014, **14**, 3576–3586.

15 M. O'Keeffe, M. A. Peskov, S. J. Ramsden and O. M. Yaghi, *Acc. Chem. Res.*, 2008, **41**, 1782–1789.

16 U. Diebold, *Surf. Sci. Rep.*, 2003, **48**, 53–229.

17 D. Dubbeldam, S. Calero, D. E. Ellis and R. Q. Snurr, *Mol. Simul.*, 2016, **42**, 81–101.

18 E. Smith and G. Dent, *Modern Raman Spectroscopy - A Practical Approach*, John Wiley & Sons, Ltd, 2005.

19 A. Shastri, A. K. Das, S. Krishnakumar, P. J. Singh and B. N. Raja Sekhar, *J. Chem. Phys.*, 2017, **147**, 224305.

20 B. H. Stuart, *Infrared Spectroscopy: Fundamentals and Applications*, John Wiley & Sons, Ltd, 2005.

21 J. Ma, A. P. Kalenak, A. G. Wong-Foy and A. J. Matzger, *Angew. Chem. Int. Ed.*, 2017, **56**, 14618–14621.

22 H. Furukawa, N. Ko, Y. B. Go, N. Aratani, S. B. Choi, E. Choi, A. O. Yazaydin, R. Q. Snurr, M. O'Keeffe, J. Kim and O. M. Yaghi, *Science*, 2010, **329**, 424–428.

23 D. Yuan, D. Zhao, D. Sun and H. C. Zhou, *Angew. Chem. Int. Ed.*, 2010, **49**, 5357–5361.

24 R. Grünker, V. Bon, P. Müller, U. Stoeck, S. Krause, U. Mueller, I. Senkovska and S. Kaskel, *Chem. Commun.*, 2014, **50**, 3450.

25 H. Furukawa, M. A. Miller and O. M. Yaghi, *J. Mater. Chem.*, 2007, **17**, 3197.

26 M. Thommes, K. Kaneko, A. V. Neimark, J. P. Olivier, F. Rodriguez-Reinoso, J. Rouquerol and K. S. W. Sing, *Pure Appl. Chem.*, 2015, **87**, 1051–1069.

27 J. Rouquerol, P. Llewellyn and F. Rouquerol, in *Studies in surface science and catalysis*, Elsevier, 2007, vol. 160, pp. 49–56.

28 G. Horvath and K. Kawazoe, *J. Chem. Eng. Japan*, 1983, **16**, 470–475.

29 L. D. Gelb and K. E. Gubbins, *Langmuir*, 1998, **14**, 2097–2111.

30 L. Sarkisov and A. Harrison, *Mol. Simul.*, 2011, **37**, 1248–1257.

31 R. C. Reid, T. K. Sherwood and R. E. Street, *The Properties of Gases and Liquids*, McGraw-Hill, 1987.

32 H. W. Langmi, J. Ren, B. North, M. Mathe and D. Bessarabov, *Electrochim. Acta*, 2014, **128**, 368–392.

Chapter 6

Experimental

6 Experimental

6.1 Methods

Solvothermal synthesis was carried out using Parr stainless steel reactor autoclaves with 23 mL Teflon inserts in a standard chemical heating oven. Alternatively, 1.5 mL sealed rection/mass spectrometry vials from VWR were used in a Grant Instruments QBD4 series dry block heating system.

Nuclear magnetic resonance (NMR) spectroscopy was carried out using a Bruker DPX 400 spectrometer operating at 400 MHz for ^{1}H NMR spectra and 100 MHz for ^{13}C NMR spectra by Dr. John O'Brien and Dr. Manuel Rüther. Samples were prepared in deuterated solvents as mentioned. Standard abbreviations for spectra are used: s (singlet), d (doublet), t (triplet), q (quaternary), m (multiplet), sh (sharp) and br (broad).

Single crystal X-ray diffraction (SCXRD) refinement and analysis were performed by Dr. Nianyong Zhu, Dr. Amal Cherian Kathalikattil, Friedrich Steuber or Dr. Brendan Twamley, using a Bruker APEX2 Duo diffractometer. X-ray diffraction data were measured at 100 K using a MiTeGen micromount or at 215 - 220 K mounted in a glass capillary with a small amount of solvent, using an Oxford Cryosystem Cobra low temperature apparatus. Diffraction frames were integrated using the Bruker SAINT software package and absorption effects in the data were corrected for using the multi-scan method (SADABS).[1] Structures were solved by intrinsic phasing using XT[2] or by direct methods such as SHELXS and refined using Olex2[3] and XL[4] least squares refinement. Structures contain large void volumes in which ordered solvent molecules could not always be reliably located. To account for this, the Platon-SQUEEZE routine[5] was applied to calculate the void volumes of the structures and re-generate the reflection file through the exclusion of the diffraction contributions from these un-located solvent molecules.

Powder X-ray diffraction (PXRD) analysis was carried out using an APEX II DUO X-ray diffractometer by Dr. Nianyong Zhu, Dr. Amal Cherian Kathalikkattil or Dr. Brendan Twamley. Samples were ground under solvent and sealed inside 0.3 - 1.0 mm diameter borosilicate glass or "special glass" capillaries from WJM Glas Müller GmbH. The capillaries were mounted and centred on a goniometer head. The data were collected upon 360° φ

rotation frames at 2 values of 10° and 20°, with exposure times of 15 minutes per frame at a detection distance of 120 mm. Overlapping sections of data were then combined and the data was processed using the Bruker APEX2 routine XRD2-Eval subprogram. Analysis and background corrections were carried out using DIFFRAC.EVA software.[6]

Mass spectrometry was carried out on a Waters Maldi/ESI-QTOF Premier instrument by Dr. Martin Feeney and Dr. Gary Hessman. Samples were dissolved in HPLC grade solvents.

Raman spectroscopy was performed using a Renishaw Raman microscope. Samples were mounted on glass slides and measured at 20x magnification unless otherwise stated.

Fourier-transform infrared (FT-IR) spectroscopy was carried out using two different instruments. A PerkinElmer Spectrum One FT-IR spectrometer with data collected and processed using Spectrum v5.0.1 (2002 PerkinElmer Instrument LLC) software was used for most samples. A Bruker TENSOR II FT-IR Spectrometer with data collected and processed using Bruker OPUS software, was used for FT-IR measurements on compound **1**.

Scanning electron microscopy (SEM) was carried out on a Zeiss ULTRA plus scanning electron microscope using both InLens and SE2 detectors at a 5 kV acceleration voltage.

E*nergy-dispersive X-ray (EDX) spectroscopy* was carried out on samples within the microscope using a 20 mm^2 Oxford Inca EDX detector and a 20 kV acceleration voltage.

Transmission electron microscopy (TEM), *scanning transmission electron microscopy (STEM)* and *energy-dispersive X-ray (EDX) mapping* were carried out using a FEI Titan microscope at operating voltages of 80 kV and 300 kV.

Atomic force microscopy (AFM) analysis was performed using an Asylum Research AFM instrument. Samples were drop-casted from solution onto HOPG and imaged.

Dynamic light scattering (DLS) measurements were carried out on a Malvern instruments Zetasizer Nano series using a refractive index of 1.45 and a relative absorbance of 0.010 for $CHCl_3$.

Thermogravimetric analysis (TGA) was carried out on a PerkinElmer Pyriss 1 TGA under an N_2 gas flow (20 mL/min) using a ceramic crucible sample holder. Crystals of compounds **1**-**6** were removed from their DMF storage solutions and placed briefly onto filter paper to remove excess solvent prior to their addition to the TGA crucible. A heating rate of 3°C per minute was used as samples were heated from 20 - 30°C to 700 - 900°C. The instrument was calibrated to In and Ni standards in N_2.

Gas sorption analysis measurements were performed using a Quantachrome Autosorb iQ instrument. CP grade He, N_2, H_2 and CO_2 gases from BOC Gases Ireland used were used. Samples were activated under a secondary vacuum and heating mantle on the degasing port prior to conducting measurements. After activation, samples were transferred to the measurement port for analysis. The temperature was maintained at 77 K for N_2 and H_2 measurements using a liquid N_2 insulated bath and between 278 and 298 (± 0.1) K for CO_2 measurements using a circulating Dewar and a refrigerated/heated bath circulator (ISOTEMP 4100 R20, Fischer Scientific).

UV-visible-NIR spectroscopy was carried out on dissolved samples in 1 cm quartz cuvettes using a PerkinElmer Lambda 1050 UV/vis/NIR spectrophotometer. Baseline corrections were applied to all spectra.

Solid state UV-visible-NIR reflectance and transmission spectroscopy were measured on a Perkin Elmer Lambda 650 spectrometer using a 150 mm integrating sphere accessory. The samples were placed between two quartz slides for measurement. Transmission (T) measurements were performed with the sample positioned in front of the integrating sphere. Reflectance (R) measurements were carried out with the sample positioned at the rear of the integrating sphere. Spectra were corrected for the background of the quartz slide by measuring the transmission and reflectance spectra of single quartz slides.

The solid-state transmission spectra were converted to absorptance (A) spectra using the following formulae:

$$A = 1 - (R_{corrected} + T_{corrected})$$

$$T_{corrected} = \frac{T_{measured}}{\mathrm{T_{blank}}}$$

$$R_{corrected} = \frac{R_{measured} - \mathrm{R_{blank}}}{\mathrm{T_{blank}}}$$

The diffuse reflectance spectra were processed using the regression formula (F(R)):

$$F(R) = \left(1 - \frac{R_{corrected}}{100}\right)^{1/(\frac{Rcorrected}{100})}$$

Excitation and emission spectra as well as *fluorescence lifetime measurements* were performed using a Fluoromax 4 (Horiba-Jobin-Yvon) spectrometer and a Fluorolog, TCSPC system (Horiba-Jobin-Yvon) equipped with a 295 nm excitation source (nanoLED-295). Fluorescence decay curves were fitted using the Data Station DAS6 software package.

X-ray photoelectron spectroscopy (XPS) was performed under ultra-high vacuum conditions (<5 x 10^{-9} mbar) on a VG Scientific ESCAlab Mk II system equipped with a hemispherical analyser using Al Kα X-rays (1486.6 eV). The emitted photoelectrons were collected at a take-off angle of 90° from the samples surface. The analyser pass energy was set to 100 eV for survey scans and 40 eV for high-resolution core scans, yielding an overall resolution of 1.5 eV. Photoemission peak positions were corrected to C 1s at a binding energy of 248.8 eV. Prior to carrying out XPS measurements, the samples were loaded into a prep-chamber within the XPS instrument and kept under vacuum (<5 x 10^{-8} mbar) overnight to ensure that they were solvent free for XPS analysis.

Computational modelling was performed using simplified models chosen to explore possible SBU configurations and to assess the stabilities of different metal ion configurations. SBUs were modelled in a non-periodic environment using density function theory (DFT) at 0 K. The calculations were carried out with gaussian09[7] using PBE0[8,9] hybrid functional in conjunction with the SDDALL[10] basis set with an effective core potential for Co, Zn and Mn, a 6-31g(d)[11] basis set for C and O and a 6-31g(p)[12] basis set for H. The default convergence criteria and a larger integration grid containing 225 radial shells with each shell containing 974 angular points were used. Only the ferromagnetic configuration was modelled because the changes in energy due to spin interactions will be much less compared to that due to the changes in the coordination environment of the metals. To capture the proper electronic picture, the SBUs was truncated by replacing the **L2** ligands with benzoate ligands.

Electrochemical experiments were carried out using a Bio-logic Science Instrument VSP Potentiostat. A three electrode set-up was used in all experiments with further information detailed in the results sections for each experiment. A water bath was used to keep all reaction mixtures at 25°C during the experiments.

Photo-induced oxygen production experiments were performed using a Clarke type O_2 sensor. A 465 nm, 10 mW/cm^2 LED Prizmatix light source was used for these experiments. A water bath was used to keep all reaction mixtures at 25°C during experiments. Further experimental details can be found in the relevant results sections.

6.2 Materials

All chemicals and some solvents were purchased from Sigma-Aldrich Chem. Co. Ltd., Fluorochem Ltd. or VWR chemicals. Common solvents were obtained from local solvent suppliers at the hazardous materials facility in Trinity College Dublin and used as received unless otherwise stated. Water was deionised in house using a Millipore Synergy 185 water purification system.

6.2.1 Ligand Synthesis

Synthesis of 3,3',3''-(benzene-1,3,5-triyltris(ethyne-2,1-diyl))tribenzoic acid (**H_3L1**) was carried out in four steps using a modified literature procedure.[13]

Step 1: 1,3,5-Tris((trimethylsilyl)ethynyl)benzene was synthesised under an N_2 atmosphere by stirring 1,3,5-tribromobenzene (50.0 g, 0.16 mol), $Pd(PPh_3)_2Cl_2$ (2.0 g, 2.85 mmol), ethynyltrimethylsilane (53.0 g, 0.54 mol) and triethylamine (750 mL) in an round bottom flask (RBF) at 20°C. CuI (0.25 g, 1.31 mmol) was added to the RBF and the temperature was increased to 60°C for 24 hours. The inorganic salt was filtered off and the mixture was dried on a rotary evaporator to remove excess TEA. The crude product was dissolved in DCM (1 L) and washed with a saturated aqueous solution of NH_4Cl (3 x 1 L). The washed DCM fraction was dried under vacuum. The washed product was dissolved in hexane and filtered through a silica plug yielding a pale yellow solid. Yield: 56.253 g, 0.153 mol, 96.6%. ^{1}H NMR (400 MHz, DMSO-d, δ_H/ppm) 7.51(3H, s, CH), 0.25(27H, s, CH_3).

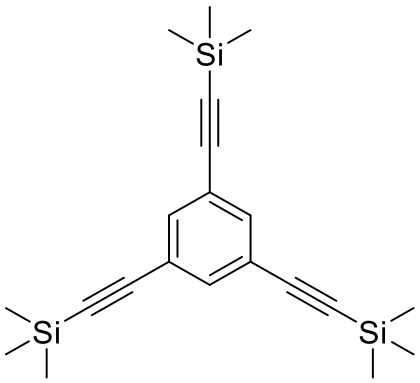

Figure 6.2.1: Structural representation of 1,3,5-tris((trimethylsilyl)ethynyl)benzene.

Step 2: 1,3,5-Triethynylbenzene was synthesised by stirring 1,3,5-tris((trimethylsilyl)ethynyl)benzene (18.336 g, 0.050 mol) in DCM (400 mL). K_2CO_3 (9.427 g, 0.168 mol) was dissolved in MeOH (100 mL) and added to the 1,3,5-tris((trimethylsilyl)ethynyl)benzene solution and the mixture was stirred at 35°C for 24 hours. The mixture was neutralised using a 1 M HCl solution. The reaction mixture was evaporated to dryness using a rotary evaporator. The crude product was purified using column chromatography (silica gel with a mobile phase of DCM). A yellow solid was obtained. Yield: 4.562 g, 0.030 mol, 60.8%. ^{1}H NMR (400MHz, $CDCl_3$-d, δ_H/ppm) 7.56(3H, s, CH), 3.10(3H, s, CH).

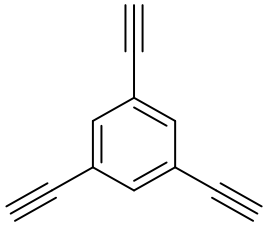

Figure 6.2.2: Structural representation of 1,3,5-triethynylbenzene.

Step 3: Triethyl-3,3',3''-(benzene-1,3,5-triyltris(ethyne-2,1-diyl))tribenzoate was synthesised under an N_2 atmosphere by stirring ethyl 3-iodobenzoate (7.19 g, 0.026 mol), $Pd(PPh_3)_2Cl_2$ (0.8 g, 1.1 mmol) PPh_3 (0.8 g, 3 mmol), 1,3,5-triethynylbenzene (1.185 g, 8 mmol) and triethylamine (50 mL) in a RBF at 20°C. CuI (0.75 g, 4 mmol) was added to the RBF and the temperature was increased to 35°C for 40 hours. The mixture was dried on a rotary evaporator and 15 mL of DCM was added to dissolve the crude product. The insoluble material was filtered off. The crude product was purified using column chromatography (silica gel with a DCM mobile phase). A white solid was obtained. Yield: 3.369 g, 0.006 mol, 71.8%. ^{1}H NMR (400 MHz, $CDCl_3$-d, δ_H/ppm) 8.22(3H, s, CH), 8.04(3H, d, J = 7.89, CH), 7.73-7.71(6H, m, CH), 7.46(3H, t, J = 7.81, CH), 4.41(6H, q, J_1 = 7.04, J_2 = 7.20, CH_2), 1.43(3H, t, J = 7.18, CH_3). ^{13}C NMR (150MHz, $CDCl_3$-d, δ_C/ppm) 165.9, 135.7, 134.4, 132.8, 130.9, 129.6, 128.6, 123.8, 123.1, 89.7, 88.4, 61.3, 14.3. HR-MS (ESI): m/z Calculated for $C_{39}H_{31}O_6$ $[M+H]^+$: 595.2121 ; Found: 595.2127.

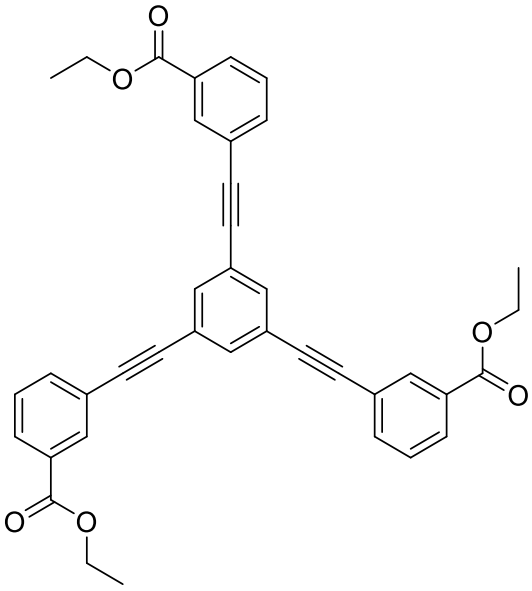

Figure 6.2.3: Structural representation of triethyl-3,3',3''-(benzene-1,3,5-triyltris(ethyne-2,1-diyl))tribenzoate.

Step 4: 3,3',3''-(Benzene-1,3,5-triyltris(ethyne-2,1-diyl))tribenzoic acid was synthesised by stirring triethyl-3,3',3''-(benzene-1,3,5-triyltris(ethyne-2,1-diyl))tribenzoate (3.2 g, 5.30 mmol) in anhydrous THF (60 mL) at 20°C. $LiOH{\cdot}H_2O$ (4.5 g, 0.11 mol) was dissolved in deionised H_2O (25 mL) and added to the triethyl-3,3',3''-(benzene-1,3,5-triyltris(ethyne-2,1-diyl))tribenzoate solution and the mixture was stirred for 24 hours. The mixture was concentrated using a rotary evaporator and was then acidified using aqueous HCl (40 mL, 3 M) until a brown precipitate formed. The precipitate was filtered off, washed with deionised H_2O (50 mL) and dried in air. The crude brown solid was purified using column chromatography (silica gel with a mobile phase of THF). A pale yellow solid was obtained. Yield: 2.267 g, 4.4 mmol, 82.5%. ^{1}H NMR (400 MHz, DMSO-d, δ_H/ppm) 8.11(3H, s, CH), 7.94(3H, d, J = 7.70, CH), 7.80(3H, s, CH), 7.62(3H, d, J = 7.54, CH), 7.43(3H, t, J = 7.62, CH). ^{13}C NMR (150 MHz, DMSO-d_6) δ_C/ppm) 166.4, 135.4, 134.2, 132.2, 131.5, 129.8, 129.2, 123.4, 122.0, 89.9, 88.1. HR-MS (ESI): m/z Calculated for $C_{33}H_{17}O_6$ $[M-H]^-$: 509.1025; Found: 509.1027.

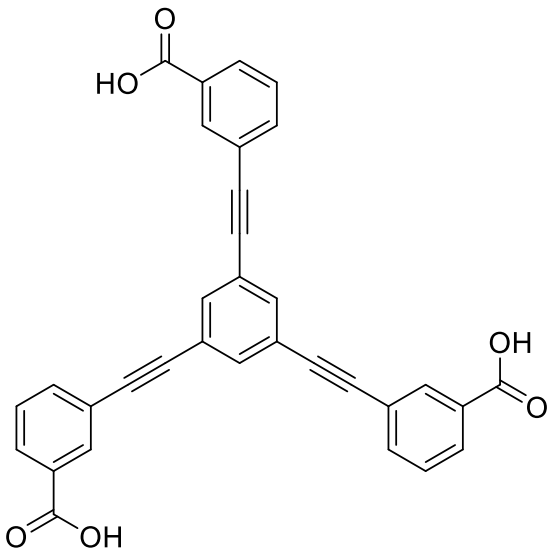

Figure 6.2.4: Structural representation of 3,3',3''-(benzene-1,3,5-triyltris(ethyne-2,1-diyl))tribenzoic acid.

Synthesis of 4,4',4''-(benzene-1,3,5-triyltris(ethyne-2,1-diyl))tribenzoic acid (**H_3L2**) was carried out in four steps. **Steps 1** and **2** are identical to the first two steps in the synthesis of **H_3L1** and **steps 3** and **4** are based on a known literature procedure.[13]

Step 3: Trimethyl-4,4',4''-(benzene-1,3,5-triyltris(ethyne-2,1-diyl))tribenzoate was synthesised under an N_2 atmosphere by stirring methyl 4-iodobenzoate (6.96 g, 26.5 mmol), $Pd(PPh_3)_2Cl_2$ (0.8 g, 1 mmol), PPh_3 (0.8 g, 3 mmol), 1,3,5-triethynylbenzene (1.242 g, 8.3 mmol) and triethylamine (50 mL) in an RBF at 20°C. CuI (0.75 g, 4 mmol) was added to the RBF and the temperature was increased to 35°C for 40 hours. The mixture was dried on a rotary evaporator and DCM (20 mL) was added to dissolve the crude product. The insoluble material was filtered off. The crude product was purified using column chromatography (silica gel with a mobile phase of DCM). A white solid was obtained. Yield: 3.354 g, 6 mmol, 72%. ^{1}H NMR (400 MHz, $CDCl_3$-d, δ_H/ppm) 8.04(6H, d, J = 8.48, CH), 7.70(3H, s, CH), 7.59(6H, d, J = 8.44, CH), 3.93(9H, s, CH_3).

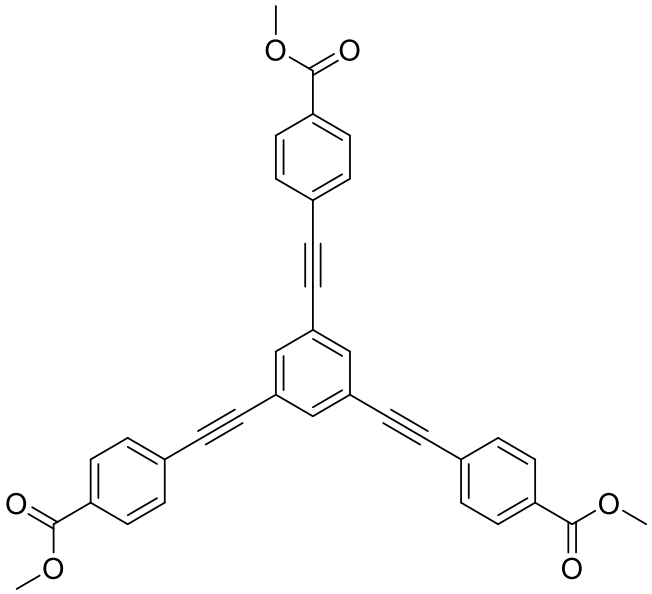

Figure 6.2.5: Structural representation of trimethyl-4,4',4''-(benzene-1,3,5-triyltris(ethyne-2,1-diyl))tribenzoate.

Step 4: 4,4',4''-(Benzene-1,3,5-triyltris(ethyne-2,1-diyl))tribenzoic acid (**H_3L2**) was synthesised by stirring trimethyl-4,4',4''-(benzene-1,3,5-triyltris(ethyne-2,1-diyl))tribenzoate (3.25 g, 5.9 mmol) in anhydrous THF (60 mL) at 20°C. LiOH.H_2O (4.5 g, 0.11 mol) was dissolved in deionised H_2O (25 mL) and added to the trimethyl-4,4',4''-(benzene-1,3,5-triyltris(ethyne-2,1-diyl))tribenzoate solution and the mixture was stirred for 24 hours. The mixture was concentrated using a rotary evaporator. The mixture was acidified using a 3 M HCl solution (65 mL) and a brown precipitate was formed. The precipitate was filtered off, washed with deionised H_2O (50 mL) and dried in air. The crude brown solid was purified using column chromatography (silica gel with a mobile phase of THF). A pale yellow solid was obtained. Yield: 1.997 g, 3.9 mol, 66%. ^{1}H NMR (400 MHz, DMSO-d, δ_H/ppm) 8.01(6H, d, J = 8.48, CH), 7.89(3H, s, CH), 7.72(6H, d, J = 8.48, CH). ^{13}C NMR (150 MHz, DMSO-d_6) δ_C/ppm) 166.7, 134.6, 131.8, 131.0, 129.6, 126.0, 123.3, 90.2, 89.7.

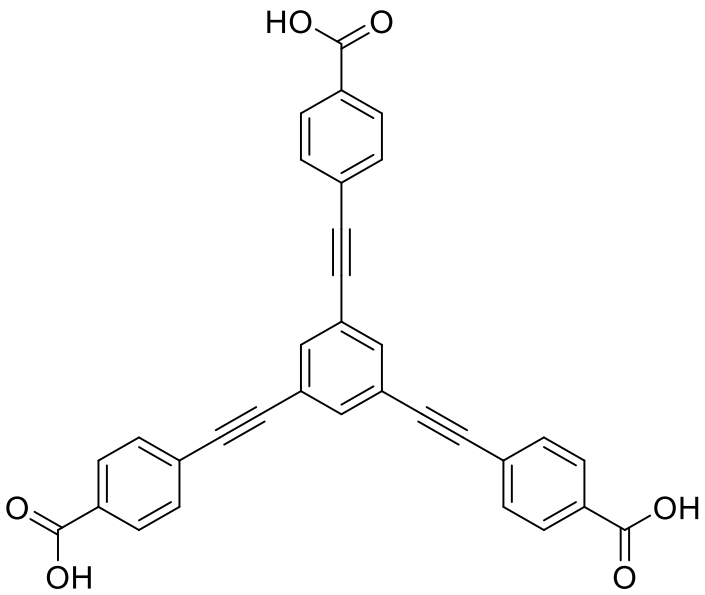

Figure 6.2.6: Structural representation of 4,4',4''-(benzene-1,3,5-triyltris(ethyne-2,1-diyl))tribenzoic acid (**H_3L2**)

Synthesis of 5,5'-((5'-(4-((4-carboxyphenyl)ethynyl)phenyl)-[1,1':3',1''-terphenyl]-4,4''-diyl)-bis(ethyne-2,1-diyl))benzoic acid (**H_3L3**) was carried out in five steps using a modified literature procedure.[14]

Step 1: 1,3,5-Tris(4-bromophenyl)benzene was synthesised by dissolving *p*-bromoacetophenone (40 g, 0.2 mol) in EtOH (320 mL). The solution was cooled using an ice bath and $SiCl_4$ (100 mL) was added dropwise over 30 minutes forming a red coloured solution. The mixture was heated for 20 hours at 80°C forming a yellow solution. The mixture was cooled to room temperature and a saturated aqueous NH_4Cl solution (400 mL) was added forming a yellow precipitate. The yellow precipitate was filtered off and washed with EtOH (300 mL) and DCM (150 mL). A white solid was obtained. Yield: 22.33 g, 41 mmol, 61.0%. ^{1}H NMR (400 MHz, $CDCl_3$, δ_H/ppm) 7.69(3H, s, CH), 7.61(6H, d, J = 8.44, CH), 7.53(6H, d, J = 8.44, CH).

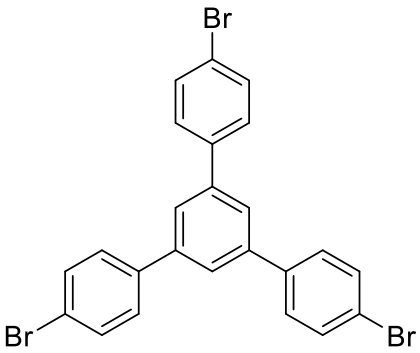

Figure 6.2.7: Structural representation of 1,3,5-tris(4-bromophenyl)benzene.

Step 2: Synthesis of 1,3,5-tris(4-(ethynyltrimethylsilane)phenyl)benzene was carried out by dissolving 1,3,5-tris(4-bromophenyl)benzene (20 g, 36.8 mmol) and ethynyltrimethylsilane (16.812 mL, 11.919 g, 121.4 mmol) in a THF:TEA mixture (200 mL: 200 mL). $Pd^{II}(PPh_3)_2Cl_2$ (2.584 g, 3.7 mmol) and CuI (0.584 g, 3.1 mmol) were added to the mixture and it was heated to 50°C for 16 hours under an N_2 atmosphere. The mixture was cooled and the solvent was removed under vacuum. The crude product was dissolved in DCM (400 mL) and washed with a saturated NH_3(aq) solution (330 mL x 3). Pure 1,3,5-tris(4-(ethynyltrimethylsilane)phenyl)benzene was obtained using a column chromatography (silica gel with a DCM mobile phase). Yield: 19.994 g, 0.0336 mol, 91%. ^{1}H NMR (400 MHz, DMSO-d, δ_H/ppm) 7.74(3H, s, CH), 7.63(6H, d, J = 8.44, CH), 7.57(6H, d, J = 8.44, CH), 0.28(27H, s, CH_3).

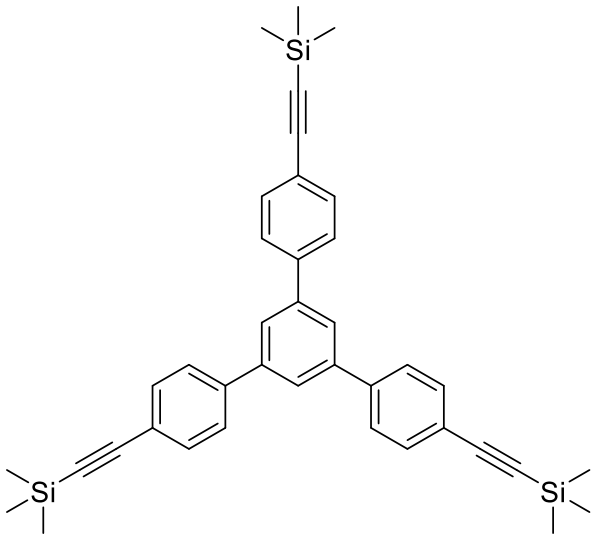

Figure 6.2.7: Structural representation of 1,3,5-tris(4-(ethynyltrimethylsilane)phenyl) benzene.

Step 3: 1,3,5-Tris(4-(ethynyl)phenyl)benzene was synthesised by dissolving the 1,3,5-tris(4-(ethynyltrimethylsilane)phenyl)benzene (5.00 g, 8.40 mmol) in DCM (250 mL). K_2CO_3 (6.97 g) was dissolved in MeOH (650 mL) and the solution was added to the 1,3,5-tris(4-(ethynyltrimethylsilane)phenyl)benzene solution in DCM. The mixture was stirred at 35°C for 4 hours. The solvent was removed under vacuum and the crude product was purified using a column chromatography (silica gel with a hexane 66% : DCM 33% mobile phase). A pale yellow solid was obtained. Yield: 2.10 g, 5.5 mmol, 66%. ^{1}H NMR (400 MHz, DMSO-d, δ_H/ppm) 7.76(3H, s, CH), 7.65(6H, d, J = 8.40, CH), 7.61(6H, d, J = 8.36, CH), 3.16(3H, s, CH).

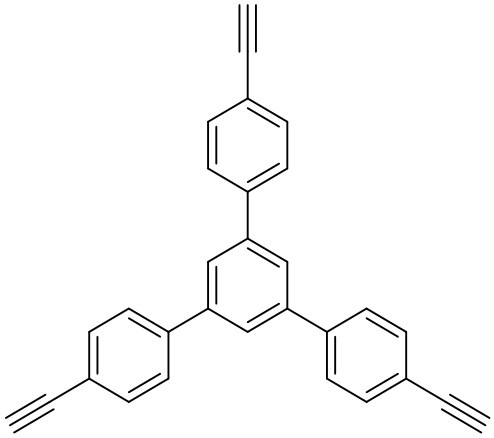

Figure 6.2.7: Structural representation of 1,3,5-tris(4-(ethynyl)phenyl)benzene.

Step 4: Trimethyl-4,4',4''-(benzene-1,3,5-triyltris(ethyne-2,1-diyl))tribenzoate was synthesised under an N_2 atmosphere by stirring methyl 4-iodobenzoate (8.662 g, 33 mmol), $Pd(PPh_3)_2Cl_2$ (0.694 g, 0.99 mmol), 4,4''-dibromo-5'-(4-bromophenyl)-1,1':3',1''-terphenyl (2.5 g, 6.6 mmol), THF (300 mL) and triethylamine (250 mL) in a RBF (1 L) at 20°C. CuI (0.015 g, 0.076 mmol) was added to the RBF and the temperature was increased to 80°C for 5 days. The mixture was dried on a rotary evaporator. The crude product was dissolved in DCM (200 mL) and washed with a saturated aqueous NH_3 solution (100 mL x 3). The DCM fraction was separated and collected and the solvent was removed using a rotary evaporator. The crude product was purified using column chromatography (silica gel with a DCM mobile phase). A pale yellow solid was obtained. Yield: 1.287 g, 1.648 mmol, 29.7%. ^{1}H NMR (400 MHz, DMSO-d, δ_H/ppm) 8.03(6H, d, J = 8.40, CH), 7.80(3H, s, CH), 7.70(6H, d, J = 8.44, CH), 7.65(6H, d, J = 8.40, CH), 7.61(6H, d, J = 8.44, CH), 3.92(9H, s, CH_3).

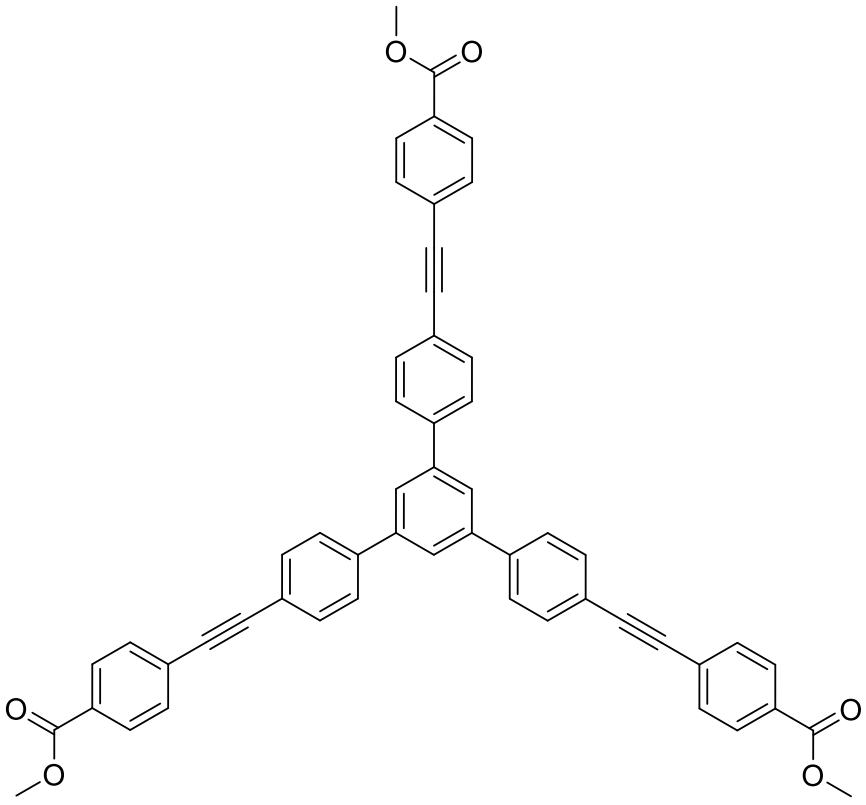

Figure 6.2.7: Structural representation of trimethyl-4,4',4''-(benzene-1,3,5-triyltris(ethyne-2,1-diyl))tribenzoate.

Step 5: 5,5'-((5'-(4-((4-Carboxyphenyl)ethynyl)phenyl)-[1,1':3',1''-terphenyl]-4,4''-diyl)-bis(ethyne-2,1-diyl))benzoic acid was synthesised by stirring trimethyl-4,4',4''-(benzene-1,3,5-triyltris(ethyne-2,1-diyl))tribenzoate (1.265 g, 1.620 mmol) in THF (150 mL) at 20°C. $LiOH{\cdot}H_2O$ (1.497 g, 35.68 mmol) was dissolved in deionised H_2O (75 mL) and added to the trimethyl-4,4',4''-(benzene-1,3,5-triyltris(ethyne-2,1-diyl))tribenzoate solution and the mixture was stirred at 35°C for 16 hours. The THF was removed using a rotary evaporator leaving a predominatly H_2O-based solution. The solution was acidified using an aqueous HCl solution (40 mL, 1 M) and a cream white precipitate formed. The precipitate was filtered off, washed with deionised H_2O (200 mL) and ethyl acetate (100 mL). The filtered material was washed with THF (500 mL). The filtrate was collected and dried on a rotary evaporator. A white solid was obtained. Yield: 0.835 g, 1.130 mmol, 69.8%. ^{1}H NMR (600 MHz, DMSO-d, δ_H/ppm) 8.06(3H, s, CH), 8.04(6H, d, J = 8.28, CH), 7.99(6H, d, J = 8.28, CH), 7.74(6H, d, J = 8.28, CH), 7.71(6H, d, J = 8.28, CH). ^{13}C NMR (150 MHz, DMSO-d_6, δ_C/ppm) 141.2, 140.8, 132.6, 132.0, 130.1, 128.1, 127.0, 125.4, 125.3, 121.7, 92.4, 90.0.

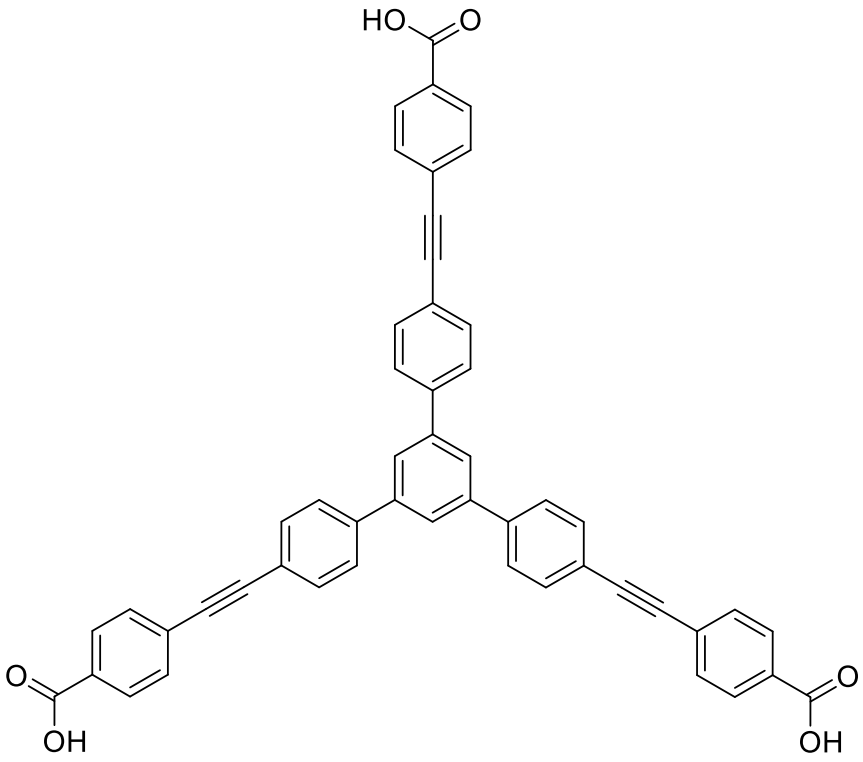

Figure 6.2.7: Structural representation of 5,5'-((5'-(4-((4-carboxyphenyl)ethynyl)phenyl)-[1,1':3',1''-terphenyl]-4,4''-diyl)-bis(ethyne-2,1-diyl))benzoic acid.

6.2.2 Coordination compound synthesis

Compounds **1**-**6** were synthesised according to the following procedures, for further analyses see the relevant results chapter:

[Cu_{36}(**L1**)$_{24}$(H_2O)$_{28}$(DMF)$_8$] (**1**)

H_3L1 (15 mg, 0.0294 mol) was added to a 1.5 mL reaction vial with DMF (0.6 mL). $Cu(NO_3)_2.3H_2O$ (7.0 mg, 0.029 mol) was dissolved in DMF (0.6 mL) and this was added to the reaction vial. The mixture was heated at 100°C for 120 hours. Pale blue crystals were obtained. The crystals were separated manually and washed with DMF. Yield: 0.4 mg.

(Me_2NH_2)[Co_5(**L2**)$_3$(μ_3-OH)$_2$(H_2O)$_2$(DMF)$_2$] (**2**)

H_3L2 (73 mg, 0.142 mol), $Co(NO_3)_2.6H_2O$ (136 mg, 0.467 mol) and DMF (10 mL) were added to a 23 mL Teflon insert. The mixture was sonicated for 15 minutes. The Teflon insert was placed inside a Parr stainless steel reactor autoclave and heated at 90°C for 48 hours. Dark purple crystals were obtained. The crystals were separated manually and washed with DMF. Yield: 12.49 mg. EDX analysis (atomic %): $C_{105}O_{24}Co_5$ (with 2 H_2O and 2 DMF constitutional solvent molecules per formula unit) –Calculated: C 78.4%, O 17.9%, Co 3.7%. Found: C 76.4%, O 19.5%, Co 4.2%.

[$MnCo_2$(**L2**)$_2$(H_2O)$_2$] (**3**)

H_3L2 (7.30 mg, 0.014 mmol), $MnCl_2{\cdot}2H_2O$ (2.50 mg, 0.015 mmol), $Co(NO_3)_2{\cdot}6H_2O$ (9.10 mg, 0.031 mmol) and DMF (1 mL) were added to a 1.5 mL reaction vial. The mixture was sonicated for 15 minutes followed by heating at 90°C for 72 hours. Bright blue crystals were obtained. The crystals were washed with DMF. Yield: 2.3 mg. EDX analysis (atomic %): $C_{72}O_{18}Mn_1Co_2$ (with 4 H_2O and 2 DMF constitutional solvent molecules per formula unit) – Calculated: C 75.8%, O 19.0%, Mn 1.1%, Co 2.1%. Found: C 74.9%, O 21.6%, Mn 1.2%, Co 2.2%.

[$CoZn_2$(**L2**)$_2$$(DMF)_2$] (**4**)

H_3L2 (7.3 mg, 0.0143 mmol), $Zn(NO_3)_2 \cdot 6H_2O$ (9.2 mg, 0.0309 mmol), $Co(NO_3)_2 \cdot 6H_2O$ (4.55 mg, 0.0156 mmol) and DMF (1 mL) were added to a 1.5 mL mass spec vial. The mixture was sonicated for 15 minutes followed by heating at 90°C for 72 hours. Pale pink crystals were obtained. The crystals were washed with DMF. Yield: 2.1 mg, 0.0016 mmol, 22%. EDX analysis (atomic %): $C_{72}O_{18}Co_1Zn_2$ (with 4 H_2O and 2 DMF constitutional solvent molecules per formula unit) – Calculated: C 77.42%, O 19.35%, Zn 2.15%, Co 1.07%. Found: C 77.73%, O 19.26%, Zn 2.12%, Co 0.89%.

[$ZnCo_2$(**L2**)$_2$$(DMF)_2$] (**5**)

H_3L2 (7.30 mg, 0.014 mmol), $Zn(NO_3)_2 \cdot 6H_2O$ (4.60 mg, 0.015 mmol), $Co(NO_3)_2 \cdot 6H_2O$ (9.10 mg, 0.031 mmol) and DMF (1 mL) were added to a 1.5 mL reaction vial. The mixture was sonicated for 15 minutes followed by heating at 90°C for 72 hours. Orange crystals were obtained. The crystals were washed with DMF. Yield: <5%. EDX analysis (atomic %): $C_{66}O_{20}Zn_1Co_2$ (containing 8 H_2O constitutional solvent molecules per formula unit) – Calculated: C 74.2%, O 22.5%, Zn 1.1%, Co 2.3%. Found: C 74.0%, O 22.7%, Zn 1.1%, Co 2.2%.

[Zn_4(μ_4-O)(**L3**)$_2$] (**6**)

H_3L3 (10.0 mg, 0.0135 mmol), $Zn(NO_3)_2 \cdot 6H_2O$ (4.02 mg, 0.0135 mmol) and DMF (1 mL) were added to a 1.5 mL reaction vial. The mixture was sonicated for 15 minutes followed by heating at 100°C for 72 hours. Pale yellow crystals were obtained. The crystals were washed with DMF. Yield: 1.5 mg, EDX analysis (atomic %): $C_{129}O_{31}Zn_4$ (containing 9 DMF and 9 H_2O constitutional solvent molecules per formula unit) – Calculated: C 78.7%, O 18.9%, Zn 2.4%. Found: C 76.6%, O 21.1%, Zn 2.4%.

6.3 References

1 G. M. Sheldrick, *SADABS, Univ. Göttingen, Ger.*, 1996.

2 G. M. Sheldrick, *Acta Cryst. A*, 2015, **71**, 3–8.

3 O. V. Dolomanov, L. J. Bourhis, R. J. Gildea, J. A. K. Howard and H. Puschmann, *J. Appl. Crystallogr.*, 2009, **42**, 339–341.

4 G. M. Sheldrick, *Acta Crystallogr. Sect. C Struct. Chem.*, 2015, **71**, 3–8.

5 A. L. Spek, *Acta Cryst. C*, 2015, **71**, 9–18.

6 EVA X-ray diffraction software, https://www.bruker.com/products/x-ray-diffraction-and-elemental-analysis/x-ray-diffraction/xrd-software/eva/overview.html.

7 M. J. Frisch, G. W. Trucks, H. B. Schlegel, G. E. Scuseria, M. A. Robb, J. R. Cheeseman, G. Scalmani, V. Barone, G. A. Petersson, H. Nakatsuji, X. Li, M. Caricato, A. Marenich, J. Bloino, B. G. Janesko, R. Gomperts, B. Mennucci, H. P. Hratchian, J. V. Ortiz, A. F. Izmaylov, J. L. Sonnenberg, D. Williams-Young, F. Ding, F. Lipparini, F. Egidi, J. Goings, B. Peng, A. Petrone, T. Henderson, D. Ranasinghe, V. G. Zakrzewski, J. Gao, N. Rega, G. Zheng, W. Liang, M. Hada, M. Ehara, K. Toyota, R. Fukuda, J. Hasegawa, M. Ishida, T. Nakajima, Y. Honda, O. Kitao, H. Nakai, T. Vreven, K. Throssell, J. A. Montgomery, J. E. P. Jr., F. Ogliaro, M. Bearpark, J. J. Heyd, E. Brothers, K. N. Kudin, V. N. Staroverov, T. Keith, R. Kobayashi, J. Normand, K. Raghavachari, A. Rendell, J. C. Burant, S. S. Iyengar, J. Tomasi, M. Cossi, J. M. Millam, M. Klene, C. Adamo, R. Cammi, J. W. Ochterski, R. L. Martin, K. Morokuma, O. Farkas, J. B. Foresman and D. J. Fox.

8 J. P. Perdew, K. Burke and M. Ernzerhof, *Phys. Rev. Lett.*, 1996, **77**, 3865–3868.

9 C. Adamo and V. Barone, *J. Chem. Phys.*, 1999, **110**, 6158–6170.

10 M. Dolg, U. Wedig, H. Stoll and H. Preuss, *J. Chem. Phys.*, 1987, **86**, 866–872.

11 M. M. Francl, W. J. Pietro, W. J. Hehre, J. S. Binkley, M. S. Gordon, D. J. DeFrees and J. A. Pople, *J. Chem. Phys.*, 1982, **77**, 3654–3665.

12 M. J. Frisch, J. A. Pople and J. S. Binkley, *J. Chem. Phys.*, 1984, **80**, 3265–3269.

13 R. K. Castellano and J. Rebek, *J. Am. Chem. Soc.*, 1998, **120**, 3657–3663.

14 S. Sirilaksanapong, M. Sukwattanasinitt and P. Rashatasakhon, *Chem. Commun.*, 2012, **48**, 293–295.

Chapter 7

Conclusion and future outlook

7 Conclusion and future outlook

In summary, within this research a number of synthetic strategies to produce novel advanced coordination materials have been developed. The compounds incorporate structurally related tri-functional carboxylate ligands in combination with a diverse set of transition metal ions. X-ray diffraction methods were used to analyse the structures of the resulting compounds and they were extensively characterised using a wide range of other analytical techniques. Some physico-chemical attributes including guest binding, guest encapsulation, gas sorption and catalytic OER activity, were investigated.

The ligand, 3,3',3''-(Benzene-1,3,5-triyltris(ethyne-2,1-diyl))tribenzoic acid (**H_3L1**) which contains *meta*-substituted benzoate functionalities used with Cu^{2+} ions in the synthesis of crystals of **1**, $[Cu_{36}(\mathbf{L1})_{24}(DMF)_8(H_2O)_{28}]$. X-ray structural analysis shows that **1** is composed of spherical coordination molecules **1A** and **1B**. A key characteristic of these molecules is that they are composed of $\{Cu_2\}$ paddle wheel SBUs that form inner octahedral assemblies composed of six SBUs and which are surrounded by outer cuboctahedral shells composed of the remaining twelve SBUs. Molecules **1A** and **1B** are structural isomers; their outer shells are identical but they are distinguished from each other by a 45° rotation of the inner octahedral assemblies shell. Thus, the coordination cages can be regarded as endohedral supramolecular cages which are composed of multiple smaller sub-cages providing numerous binding sites and contain well-defined cavities and pore openings of various sizes. The molecules have cross-sectional diameters of *ca.* 5 nm across and are among the largest synthetic coordination cage type molecules which are crystallographically characterised.

It is shown that by using post-synthetic modification methods, **1** can be solubilised through interactions at the labile coordination sites of the $\{Cu_2\}$ SBUs by 4-(3-phenylpropyl)pyridine making single molecules accessible. The structural integrity of the dissolved molecules is confirmed using a wide range of techniques including dynamic light scattering (DLS), transmission electron microscopy (TEM), energy dispersive X-ray (EDX) mapping and atomic force microscopy (AFM) analysis. Particularly noteworthy are the oppositely located labile coordination sites on the $\{Cu_2\}$ units that

may facilitate guest binding and which are known to perform as molecular traps. Initial photophysical studies were carried out using 7-amino-4-methylcoumarin (AMC) as a guest molecule. These suggest that the coordinatively labile sites on the $\{Cu_2\}$ SBU together with the intricate molecular structures give rise to guest-binding. Future work may feature reconstructing molecular cages with modified $\mathbf{L1^{3-}}$ ligands which include functional groups and exploring the use of a range of molecules that may bind to the apical sites on the SBUs, both of which should change the solubility as well as other properties of the molecular cages.

The ligand, 4,4',4''-(benzene-1,3,5-triyltris(ethyne-2,1-diyl))tribenzoic acid (**H_3L2**) which contains *para*-benzoate moieties, was used to synthesise **2**, $Me_2NH_2[Co_5(\mathbf{L2})_3(\mu_3\text{-}OH)_2(H_2O)_2(DMF)_2]$. Crystallographic X-ray analysis reveals the 3D MOF structure. The SBU of **2** is a pentanuclear $\{Co_5\}$ unit which is coordinated to by nine $\mathbf{L2^{3-}}$ ligands and four solvent molecules. The polymeric structure of **2** takes the form of a honeycomb-type network and the structure is twofold interpenetrated.

Gas sorption analysis confirms the stability of **2** upon activation. A type-I gas uptake isotherm is achieved for N_2 at 77 K with a BET surface area of 1755 m^2/g. A relative high uptake of H_2 gas of 1.84 wt% at 77 K and 756 Torr was reached. We surmise that the observed stability of the MOF may be due to a number of factors including the high connectivity of each $\{Co_5\}$ SBU, prevailing π-π interactions between phenyl rings in adjacent ligands, the noteworthy interpenetration and also the 1D pore structure of the compound. The hydrolytic stability was investigated by immersing crystals of **2** in deionised H_2O. Even after 18 months, X-ray photoelectron spectroscopy (XPS) of the solid material of the dispersion, revealed no changes.

With these characteristics in mind, it was decided to investigate the use of **2** as a catalyst for water oxidation at neutral pH, a condition at which many catalysts show low OER activity. Under photocatalytic conditions, high turnover frequencies and turnover numbers of 1.482 s^{-1} and 248 were achieved, respectively. Similarly, under electrocatalytic conditions in carbon paste (CP) electrodes, the compound reveals overpotentials of 0.405 and 0.755 V to reach 1 and 10 mA/cm^2, respectively (for the 40% **2**/CP electrodes). Tafel slopes varying between 133 and 176 mV/dec were obtained for the **2**/CP electrodes.

Further, It was then demonstrated that a material whose composition match closely to that of **2** could be synthesised under electrochemical conditions on the surface of fluorine doped tin oxide (FTO) glass electrodes. These **2**/FTO electrodes demonstrated catalytic activity in relation to electrochemical water oxidation. Bulk electrolysis experiments and the subsequent electrode characterisations on both the **2**/CP and **2**/FTO electrodes, show that these systems are exceptionally stable for prolonged periods of time under the applied conditions. While the formation of oxides has not been detected, their potential formation cannot be fully ruled out. Future work may investigate OER activities at basic and acidic pH values to evaluate the stability and efficiency of the compound at these alternative conditions. In addition it may be productive to synthesise **2** on the surfaces of other electronically conductive materials, such as Ni foam, to achieve higher current densities across the working electrode.

The use of various metal ions in the presence of **H_3L2**, lead to the synthesis of an isoreticular series of MOFs, [$MnCo_2$(**L2**)$_2$(H_2O)$_2$] (**3**), [$CoZn_2$(**L2**)$_2$(DMF)$_2$] (**4**) and [$ZnCo_2$(**L2**)$_2$(DMF)$_2$] (**5**). The trinuclear SBU found in all three MOFs, is composed of different metal configurations across one octahedral and two tetrahedral coordination positions. This mixture of coordination geometries in combination with the small size of the SBU, facilitated the accurate assignment of the relative metal ion positions in the structures.

This differentiation was performed using a range of complimentary techniques including single-crystal X-ray diffraction, EDX spectroscopy, UV-vis-NIR spectroscopic studies, XPS, and computational modelling. The combination of these techniques shows, that the metal arrangement in these coordination compounds are ordered and not randomly distributed. In each reaction solution the metal ions reveal clear preferences for either the octahedral or tetrahedral coordination environments. In these reaction solutions it was found that Mn(II) ions have a strong affinity for the octahedral position while the Zn(II) ions have strong preferences for the tetrahedral positions within each SBU. The Co(II) ions were shown to be adept at taking up either position depending on the composition of the reaction mixture.

Preliminary photo-induced water oxidation studies using **3** and **4** highlight their potential in this field of study. In particular the presence of **3** in a reaction mixture

showed significantly increased oxygen production. Compund 3 gave rise to a maximum TON of 6.4 and a TOF of 0.2 s^{-1}. Future studies may expand on the number of mixed-metal MOFs in this isoreticular series. The electro- and photocatalytic activities of these compounds may be explored in more detail.

5,5'-((5'-(4-((4-carboxyphenyl)ethynyl)phenyl)-[1,1':3',1''-terphenyl]-4,4''-diyl)-bis(ethyne-2,1-diyl))benzoic acid (**H_3L3**) which provides an extended version of the **H_3L2** ligand, was used to synthesise compound **6,** [$Zn_4(\mu_4$-O)(**L3**$)_2$]. This MOF readily forms large crystals under the applied reaction conditions. The structure was resolved using single crystal X-ray diffraction. **6** was found to be composed of two interwoven rutile (**rtl**) nets. This topology is indeed are rarely found when 6-connected {Zn_4O} SBUs are combined with 3-connecting ligands. The structure of **6** is facilitated by the rotational flexibility of the acetylene moieties of the ligand, bending effects and inter-ligand interactions. Particularly noteworthy are the low density (0.266 g/cm^3) and large pore sizes (up to *ca.* 22.8 Å) of this MOF. This was found to be stable on activation giving rise to a reversible type IV(b) isotherm for N_2 sorption at 77 K. The MOF reaches a maximum N_2 uptake of 983 cm^3/g at 731 Torr and is characterised by an experimental BET surface area of above 3000 m^2/g. The H_2 gas sorption studies give rise to a large H_2 uptake of 332 cm^3/g at 756 Torr and 77 K, which corresponds to an uptake of 2.9 wt% which is among the best gravimetric H_2 uptakes for MOFs at low pressures. Future work should investigate the gas sorption properties of **6** at higher pressures, whereby the H_2 adsorption properties will be of particular interest.

In conclusion, the synthesis of a number of distinctive MOPs and MOFs is demonstrated. Synthetic, structural and analytical challenges associated with the synthesis of highly augmented organic ligands and MOF structures were overcome. The presented compounds reveal fascinating structural attributes and unique physicochemical properties that derive form their intrinsic porosities. Further, the design principles at a molecular level, to allow preparation of new catalysts which reveal promising OER activity (see compounds **2** and **3**). It is noteworthy that such MOF-type compounds can also be synthesised electrochemically on electrodes.